

# **Magnetic structure in relation to the magnetic field induced ferroelectricity in Y-type hexaferrite $\text{Ba}_{2-x}\text{Sr}_x\text{Zn}_2\text{Fe}_{12}\text{O}_{22}$**

Von der Fakultät für Mathematik, Informatik und Naturwissenschaften der RWTH Aachen University zur Erlangung des akademischen Grades eines Doktors der Naturwissenschaften genehmigte Dissertation.

vorgelegt von  
Master of Science in Nanoscience and Technology

**Pankaj Thakuria**

aus Tezpur, Indien

Berichter: Juniorprofessor Dr. M. Angst  
Universitätsprofessor Dr. U. Klemradt

Tag der mündlichen Prüfung: 24. Mai 2017

Diese Dissertation ist auf den Internetseiten der Universitätsbibliothek online verfügbar.



I would like to dedicate this thesis to my  
loving mother who could not see this...



## Acknowledgements

It is a great pleasure for me to express my sincere gratitude to my supervisor Prof. Dr. Manuel Angst for giving me the opportunity to pursue my PhD within his young investigator group. He not only gave the valuable insights of physics but constantly remained enthusiastic on every single development in my work. The long lasting discussions to find out new ideas on what can be done and interpreting what is done is a big learning process for me. I would also like to express my sincere gratitude to the head of our group Prof. Dr. Thomas Brückel for allowing me to carry out my research work in the group and for offering valuable advice all along the way.

I would like to thank Dr. Enrico Schierle and Dr. Eugen Weschke for their help during resonant soft X-ray diffraction measurements in Helmholtz-Zentrum Berlin für Materialien und Energie Hahn-Meitner-Platz 1. I would like to thank Dr. Karel Prokeš and Dr. Slavomir Matas from Helmholtz-Zentrum Berlin für Materialien und Energie GmbH, Dr. Jürg Schefer from Paul Scherrer Institute, Dr. Yixi Su, Dr. Kirill Nemkovski, Dr. Tobias Schrader and Dr. Andreas Ostermann from FRM-II, JCNS for their help in neutron diffraction measurements. Special thanks to Dr. Shibabrata Nandi for his help in soft X-ray diffraction data analysis.

I would like to express my gratitude to Dr. Jörg Perßon for helping in sample preparation and in using Laue camera. I would like to thank Mr. Berthold Schmitz, Frank Gossen, Micha Hölzle for their technical support. I would also like to thank Dr. Emmanuel Kentzinger and Dr. Oleg Petravic for their great efforts in the maintenance and scheduling of the measurements at MPMS, PPMS and X-ray diffraction instruments. I would like to thank, Dr. Raphael Hermann, Dr. Werner Schweika, Dr. Karen Friese for valuable advises. I also would like to extend my thanks to all my colleagues at JCNS-2, PGI-4, Forschungszentrum Jülich GmbH. My great appreciations and thanks to secretary, Frau. Barbara Daeger. I like to express my gratitude to Dr. Artur Glavic for introducing me to soft X-ray beamline and teaching me the experimental knowhow.

I would like to thank Hemalatha Anepu for teaching me numerical analysis, and helping me carry out the numerical calculations in my thesis. Without her effort it would have been really a hard nut to crack. I would also like to thank Dr. Paul Zakalek for helping in the numerical calculations. I also like to express my gratitude to my long time office mates

Alice Klapper, Marcus Herlitschke, Paul Hering and my friends in the group for making my life very comfortable in the group. I would also like to thank Dr. Ashis Nandy for his valuable comments on the magnetic structures.

I am very grateful to the members of the young investigating group of Prof. Angst: Joost, Thomas, Shilpa, Hailey, Sabreen and Giorgi for valuable discussion on every topic ranging from experimental to data analysis.

I would like to thank my brother, sisters and all family members for their inspirational words to carry on my research. I appreciate the patience of my wife Nilima Gogoi for her enthusiastic words that kept me strong in difficult times. I am very thankful to my father who inspired me to pursue my dreams and stood by me always with his inspiring words.

I would also like to thank Dr. P. A. Joy of NCL Pune (India) for his valuable discussions. Finally, special thanks to all my friends in Jülich Jaydeep, Ranjita, Shymal, Sunil, Abhijit and family, Bhunesh, Naveen, Uday, Ankita, Sidhesh, Deep, Viplav etc., who are too many to name here, who are never forgettable.

## Abstract

This thesis consists of in depth study of spin structure of magnetoelectric Y-type hexaferrite  $\text{Ba}_{1-x}\text{Sr}_x\text{Zn}_2\text{Fe}_{12}\text{O}_{22}$  system. Magnetoelectric and multiferroic materials are of high interest from information technology point of view, but traditional mechanism of magnetism and ferroelectricity makes it rare to observe both in single phase materials. One of the most widely studied non conventional mechanism where cross coupling of magnetism and ferroelectricity takes place in non-collinear spin systems is spin driven ferroelectricity by inverse Dzyaloshinskii-Moriya (IDM) mechanism or spin current mechanism (SC). The spin frustration leading to non-collinear spin arrangements also leads to low magnetic ordering temperature hinders room temperature realization of magnetoelectric coupling effect. Hexaferrite systems are an answer to high temperature magnetoelectric behavior in single phase materials. Y-type hexaferrite with composition  $\text{Ba}_{1-x}\text{Sr}_x\text{Zn}_2\text{Fe}_{12}\text{O}_{22}$  was the first hexaferrite to show magnetoelectric behavior, where a 2-fan planar spin structure was proposed, not compatible with the magnetic field (H) induced ferroelectricity by IDM/SC mechanism. In depth investigation of the spin structure and its relationship with macroscopic field driven ferroelectricity was the central point of this thesis.

The widely accepted spin structure of Y-type hexaferrite is a spin block model with large (L) and small (S) spin blocks, collinear in spin arrangements inside the blocks but between the blocks arrangements changes from collinear to spiral depending upon the chemical composition. With change in the Sr content in the composition  $\text{Ba}_{1-x}\text{Sr}_x\text{Zn}_2\text{Fe}_{12}\text{O}_{22}$  spin structure was reported to change from collinear to in plane spiral in earlier studies. The change in spin structures were easily visible in magnetization curves, when magnetic field was applied perpendicular to c-axis. In three samples with  $x = 1.4, 1.18$  and  $0.72$  grown by flux methods, our refinement of single crystal x-ray diffraction data shows that Sr substitution causes local distortion and change in occupancies of Zn in the tetrahedral site which happens to be in the spin block boundary, accompanying a change in the Zn/Fe-O bond length. We speculate that the cumulative effect of local distortion, change in occupations of Zn and bond length change changes the superexchange interaction near the block boundary changing the spin structure.

The low field spin structure was studied by soft x-ray resonant magnetic scattering mea-

measurements in small horizontal applied field perpendicular to  $(0\ 0\ 1)$  in horizontal scattering geometry. The zero and very low field a helical incommensurate phase with circular dichroism in the diffraction conditions in the magnetic satellite was found. First metamagnetic transition took place from incommensurate to commensurate spin structure when a small magnetic field ( $< 100$  mT) was applied, characterized by  $(0\ 0\ 3/2)$  and  $(0\ 0\ 3/4)$  propagation. Equal intensity for incoming  $\sigma$  and  $\pi$  polarization for  $(0\ 0\ 3/2)$  reflection and absence of circular dichroism in both the satellite reflections leads to a non-chiral 4-fan structure as reported earlier. By fitting our calculated intensity ratios for linear and circular polarized x-ray shows coexistence of the 4-fan structure coexisting with the incommensurate low field phase and high field phase in some field ranges.

The high field phase, *i.e.* the ferroelectric phase was a commensurate phase characterized by presence of only  $(0\ 0\ 3/2)$  magnetic satellite. Difference in intensity for  $(0\ 0\ 3/2)$  reflection with incoming  $\sigma$  and  $\pi$  polarization singles out this phase from the low field 4-fan phase and circular dichroism in the same satellite reveals vector spin chirality in the scattering plane. Maps to circular dichroism produces some spin chiral domains with both chirality, which get inverted upon application of magnetic field in reverse direction. In vertical field perpendicular to scattering plane in horizontal scattering geometry the circular dichroism disappears establishing the direction of vector spin chirality. In addition a new phenomena, position dependent linear dichroism appears, which gives same domain configuration as that was observed in circular dichroism.

For the high field phase already proposed 2-fan model is non chiral and can neither give ferroelectric polarization by IDM/SC mechanism nor circular dichroism and new model is required. Numerical calculations on various probable models to fit our experimental data established the spin structure is a transverse conical structure with both in-plane and out of plane components for both the L and S spin blocks. This transverse conical spin structure with spin chirality in the direction of H can give ferroelectric polarization by IDM/SC mechanism in the direction perpendicular to c and H. Unpolarized neutron diffraction experiments in our sample in vertical magnetic field are also consistent with the proposed model.

The ferroelectric chiral phase is separated from the chiral zero field phase by a non chiral 4-fan phase in the magnetization process. The inversion of chirality by reverse magnetic field can be explained on the basis of absence of non chiral phase in the demagnetization process, facilitating the linkage between the chiral helical phase and the transverse conical phases. Inversion of chirality implies the flip of sign of polarization upon reversing magnetic field direction. Macroscopically no sign flipping was observed in previous reports which we attribute to the difference in composition of our samples.

The chiral transverse conical spin structure was found from low field close to 80 mT at 100 K predicting H induced ferroelectricity from this field, considerably lower than that reported by macroscopic measurements. At 300 K similar shape of spin chiral domains with circular dichroism as well as with linear dichroism also found, suggesting transverse conical spin structure at room temperature (RT). Presence of  $(0\ 0\ 3/2)$  propagation was also verified by in field unpolarized neutron diffraction at 300 K. With input from all the scattering experiments and macroscopic magnetization measurements a new phase diagram was constructed which suggested field induced ferroelectricity in this transverse conical spin structure can be realized at very low H and RT in highly resistive samples.

As a whole this thesis concludes that magnetic field induced ferroelectricity in y-type hexaferrite of composition  $\text{Ba}_{1-x}\text{Sr}_x\text{Zn}_2\text{Fe}_{12}\text{O}_{22}$  is by IDM/SC mechanism in a transverse conical spin structure available at very low H and up to RT.



## Zusammenfassung

Diese Dissertation beschreibt eine ausführliche Studie der Spin Struktur des magnetoelektrischen Y-Typ Hexaferriten  $\text{Ba}_{1-x}\text{Sr}_x\text{Zn}_2\text{Fe}_{12}\text{O}_{22}$ . Magnetoelektrische und multiferroische Materialien sind von hohem Interesse im Hinblick auf Anwendungen in der Informationstechnologie, aber die traditionellen Mechanismen von Magnetismus und Ferroelektrizität führen dazu, dass das simultane Auftreten in einem einphasigen Material selten ist. Einer der am ausführlichsten studierten nicht-konventionellen Mechanismen, bei dem eine Kopplung von nicht-kollinearem Magnetismus und Ferroelektrizität auftreten, ist eine spinbasierte Ferroelektrizität basierend auf dem inversen Dzyaloshinskii-Moriya (IDM) Mechanismus, respektive auf dem Spinstrom (SC) Mechanismus. Die Spin-Frustration, welche die nicht-kollinearen Spin Strukturen veranlasst führt jedoch üblicherweise zu sehr niedrigen Ordnungstemperaturen, weit unterhalb Raumtemperatur. Hexaferrite bilden eine Ausnahme, die magnetoelektrisches Verhalten bei hohen Temperaturen ermöglichen. Y-Typ Hexaferrit der Zusammensetzung  $\text{Ba}_{1-x}\text{Sr}_x\text{Zn}_2\text{Fe}_{12}\text{O}_{22}$  war der erste Hexaferrit, in welchem magnetoelektrisches Verhalten beobachtet wurde. Die vorgeschlagene Magnetstruktur ist jedoch nicht kompatibel mit Ferroelektrizität hervorgerufen durch den IDM/SC Mechanismus. Die ausführliche Untersuchung der Spin Struktur dieses Materials sowie deren Verbindung mit der makroskopisch beobachteten magnetfeld-induzierter Ferroelektrizität war der zentrale Punkt dieser Studie.

Es ist breit akzeptiert, dass die Spin Struktur in Hexaferriten in guter Näherung mit einem "Block-spin Modell" beschrieben werden kann, mit großen (L) und kleinen (S) Spin Blöcken, in denen die Spins jeweils kollinear angeordnet sind, wobei die Spins verschiedener Blöcke je nach chemischer Zusammensetzung nicht kollinear sein können. Mit einer Änderung des Sr Gehalts in  $\text{Ba}_{1-x}\text{Sr}_x\text{Zn}_2\text{Fe}_{12}\text{O}_{22}$  ändert sich die Spin Struktur von kollinear zu spiralförmig, gemäß früheren Studien. Magnetisierungsmessungen zeigen die Existenz verschiedener metamagnetischer Phasen auf für einkristalline Proben, gezüchtet aus Hochtemperaturlösungen, mit  $x = 1.4$  und  $1.18$ , nicht jedoch für  $0.72$ . Strukturverfeinerung von Einkristall-Röntgenbeugungsdaten zeigen, dass die Dotierung mit Sr lokale Verzerrungen sowie eine Änderung der Zn Besetzungen in den tetrahedrischen Plätzen verursacht, verbunden mit einer Änderung der Zn/Fe-O Bindungslänge. Wir spekulieren, dass der ku-

mulative Effekt dieser Änderungen zu einer Änderung der Superaustauschwechselwirkung an den Grenzen der Spin Blöcke führt, was zu den beobachteten Änderungen in der Spin Struktur führt.

Die Spin Struktur in niedrigen Magnetfeldern wurde mittels resonant-magnetischer Streuung von weichen Röntgenstrahlen untersucht, wobei das Magnetfeld horizontal und senkrecht zur [001] Richtung angelegt wurde und die Streuebene ebenfalls horizontal war. Die bei sehr kleinen Feldern stabile helikale Phase ist inkommensurabel moduliert, mit zirkularem Dichroismus in Streuung. Bereits bei einem kleinen angelegten Feld ( $<100$  mT) tritt ein metamagnetischer Übergang in eine kommensurable Spin Struktur auf, die durch Propagationsvektoren von  $(0,0,3/2)$  und  $(0,0,3/4)$  charakterisiert ist. Anpassung der Intensitätsverhältnisse für linear und zirkular polarisierte Röntgenstrahlen ergibt in bestimmten Feldbereichen eine Koexistenz dieser "4-Fächer" Spin Struktur mit der nicht-kollinearen Phase sowie mit einer weiteren Phase, die in höheren Feldern stabil ist.

Die Hoch Feld Phase, die ferroelektrisch ist, ist eine kommensurable Phase, welche durch die Präsenz von ausschließlich  $(0,0,3/2)$  magnetischen Satelliten charakterisiert ist. Die Intensitätsdifferenz dieses Reflexes zwischen sigma und pi Polarisierung der eingehenden Röntgenstrahlen unterscheidet diese Phase ebenfalls von der "4-Fächer" Spin Struktur. Des Weiteren wird ein zirkularer Dichroismus beobachtet, welche eine Vektor Spin Chiralität aufzeigt. Rasterung der Proben zeigt, dass Domänen mit umgekehrter Spin Chiralität existieren, welche durch Anlegen eines negativen Magnetfeldes invertiert werden können. Der zirkulare Dichroismus verschwindet, wenn das Magnetfeld vertikal (senkrecht zur Streuebene) angelegt wird. Dies fixiert die Richtung der Vektor Spin Chiralität. In einem vertikalen Magnetfeld wurde außerdem ein neues Phänomen, positionsabhängiger linearer Dichroismus, beobachtet. Rasterung ergibt eine Domänenkonfiguration, welche genau der im horizontalen Feld bestimmten Konfiguration der chiralen Domänen entspricht.

Die für die Hochfeldphase früher vorgeschlagene "2-Fächer" Spin Struktur ist nicht chiral und kann weder eine ferroelektrische Polarisation gemäß dem IDM/SC Mechanismus ergeben noch einen zirkularen Dichroismus in Streuung. Deshalb ist ein neues Modell nötig. Berechnungen verschiedener möglicher Spin Modelle und Anpassung an die experimentellen Daten ergeben, dass die tatsächliche Spin Struktur transversal-konisch ist, mit sowohl in c- als in ab-Richtung modulierten Spin Komponenten in beiden (L und S) Blöcken. Diese transversal-konische Spin Struktur kann nach dem IDM/SC Mechanismus eine ferroelektrische Polarisation ergeben, wobei die entsprechende Richtung der Polarisation mit der makroskopisch beobachteten Richtung übereinstimmt. Beugungsexperimente mit unpolarisierten Neutronen in vertikalen Magnetfeldern sind ebenfalls konsistent mit dem vorgeschlagenen Modell.

Die ferroelektrische chirale Phase ist getrennt von der ebenfalls chiralen Nullfeld Phase durch die nicht chirale "4-Fächer" Phase im Magnetisierungsprozess. Die Inversion der Chiralität durch Anlegen eines negativen Magnetfeldes kann erklärt werden durch die Absenz einer nicht-chiralen Phase im Demagnetisierungsprozess, was die Verbindung der chiralen helikalen Phase und der transversal-konischen Phase ermöglicht. Die Inversion der Chiralität impliziert eine Invertierung der Richtung der ferroelektrischen Polarisation durch Anlegen eines negativen magnetischen Feldes. In einer früheren makroskopischen Studie wurde ein solcher Polarisationsflip nicht beobachtet; wir führen das unterschiedliche Verhalten auf Abweichungen in der chemischen Zusammensetzung zurück.

Die chirale transversal-konische Spin Struktur wurde bereits bei tiefen Feldern ab  $\approx 80$  mT (bei 100 K) gefunden, was eine feld-induzierte Ferroelektrizität bereits in Feldern, die erheblich tiefer sind als aufgrund von makroskopischen Messungen berichtet. Bei 300 K konnten immer noch chirale Domänen beobachtet werden, mit ähnlichen Domänengrenzen wie bei tieferen Temperaturen. Des Weiteren wurde die  $(0,0,3/2)$  Propagation bei 300 K auch mit Neutronenbeugung verifiziert. Aus den Resultaten der verschiedenen Beugungsexperimente, verbunden mit makroskopischen magnetischen Messungen, wurde ein neues Phasendiagramm konstruiert, welches in Proben mit genügend hohem Widerstand das Auftreten von Ferroelektrizität in einem viel größeren Feldbereich sowie bis zu Raumtemperatur vorhersagt.

Zusammenfassend schließt die in dieser Dissertation vorgestellte Studie, dass die feld-induzierte Ferroelektrizität in Y-Typ Hexaferrit durch den IDM/SC Mechanismus in transversal-konischen Spin Strukturen verursacht wird, welche bereits in tiefen magnetischen Feldern und bei Raumtemperatur stabilisiert werden.



# Table of contents

<b>Table of contents</b>	<b>15</b>
<b>1 Overview</b>	<b>1</b>
<b>2 Introduction</b>	<b>3</b>
2.1 Magnetic interactions and order . . . . .	3
2.1.1 Magnetocrystalline anisotropy (MCA) . . . . .	6
2.1.2 Spin orbit interaction (SOI) . . . . .	6
2.1.3 Anisotropic exchange interaction . . . . .	7
2.2 Polar orders: Ferroelectrics . . . . .	11
2.3 Multiferroics: Interplay between spin and dipole . . . . .	11
2.4 Hexaferrites . . . . .	17
2.4.1 Magnetoelectric hexaferrites . . . . .	17
2.4.2 Crystal structure of hexaferrites . . . . .	18
2.4.3 Proposed spin structure of Y-type hexaferrite . . . . .	22
<b>3 Experimental techniques</b>	<b>27</b>
3.1 Sample synthesis . . . . .	27
3.1.1 Powder synthesis . . . . .	27
3.1.2 Single crystal growth . . . . .	28
3.2 Measurements of Macroscopic properties . . . . .	30
3.2.1 DC magnetization . . . . .	30
3.2.2 AC magnetic susceptibility . . . . .	32
3.3 Scattering theory . . . . .	33
3.4 X-ray scattering . . . . .	36
3.4.1 Thomson scattering . . . . .	37
3.4.2 Crystal structure determination: single crystal X-ray diffraction . . . . .	38
3.4.3 X-ray magnetic scattering . . . . .	39

3.4.4	Different scans used . . . . .	43
3.5	Experimental set-up for soft X-ray diffraction . . . . .	44
3.6	Neutron scattering . . . . .	45
3.6.1	TriCS . . . . .	47
3.6.2	E-4: 2-Axis-Diffractometer . . . . .	48
<b>4</b>	<b>Crystal growth and macroscopic characterization</b>	<b>49</b>
4.1	Crystal growth . . . . .	49
4.1.1	Sample preparation results . . . . .	51
4.2	Single crystal X-ray diffraction . . . . .	52
4.3	Macroscopic magnetization measurements . . . . .	55
4.3.1	Ferrimagnetic phase (BZY-1) . . . . .	56
4.3.2	The helical configuration BZY-2 and BZY-3 . . . . .	57
<b>5</b>	<b>Low <math>H</math> phases</b>	<b>71</b>
5.1	Zero $H$ magnetic structure . . . . .	71
5.2	In-field measurements with soft X-rays . . . . .	75
5.2.1	Discussion . . . . .	80
5.3	Circular polarization . . . . .	84
5.3.1	Spin chiral domains . . . . .	84
<b>6</b>	<b>Magnetic structure in the ferroelectric phase</b>	<b>91</b>
6.1	Horizontal magnet geometry . . . . .	92
6.1.1	Energy dependence in magnetic field . . . . .	92
6.1.2	Discussion . . . . .	99
6.1.3	Intensity calculations and circular dichroism mapping . . . . .	101
6.1.4	Model-A (2-fan structure) . . . . .	102
6.2	Vertical magnet geometry . . . . .	109
6.3	Calculations on possible models . . . . .	111
6.3.1	Model-B . . . . .	111
6.3.2	Model-C . . . . .	113
6.3.3	Model-D: The correct spin structure . . . . .	116
6.4	Experimental results in light of final model (model-D) . . . . .	119
6.4.1	Boundary between different phases . . . . .	119
6.4.2	Chirality inversion with reverse $H$ . . . . .	121
6.4.3	The room temperature magnetoelectric . . . . .	123
6.5	In field Neutron diffraction . . . . .	124

Table of contents	<b>17</b>
<hr/>	
6.5.1 Neutron scattering in $(0\ k\ l)$ plane . . . . .	127
6.5.2 The phase diagram . . . . .	129
<b>7 Summary and outlook</b>	<b>131</b>
<b>References</b>	<b>135</b>
<b>Appendix A</b>	<b>145</b>
A.1 Crystal structure refinement parameters . . . . .	145
<b>Appendix B</b>	<b>149</b>
B.1 4-fan structure . . . . .	149
B.2 Model-A . . . . .	150
B.3 Model-B . . . . .	151
B.4 Model-C . . . . .	156
B.5 Model-D . . . . .	162
<b>List of figures</b>	<b>167</b>
<b>List of tables</b>	<b>179</b>



# Chapter 1

## Overview

In condensed-matter physics various ordering phenomena have been studied extensively in the last two centuries and that led to many milestones in creating numerous novel devices. Out of all those ordering phenomena, magnetic and ordering of electronic degrees of freedom played a crucial role not only in basic science but in many applications. Extensive research on magneto-resistance, for example, discovered in the last two decades of the 20th century, in metallic multilayer changed the field of magnetic data storage explosively [1].

Unlike in conductors, in insulators there exists another ordering phenomenon, ordering of electric dipoles originating from the polar nature of chemical bonds. Materials with ordered magnetic properties leading to spontaneous magnetizations are classified as having ferroic properties (eg. ferro and ferrimagnets). Similarly, materials having ordered electric properties (spontaneous electrical polarizations) like dipole moments, are also considered to have ferroic properties (eg. ferroelectric or ferrielectric ). These ordering phenomena are also associated with strain in the lattice which in turn leads to phenomena like magnetostriction, piezoelectricity etc.

There are not many materials with both magnetic (spin) and electric dipole orders present simultaneously in a single phase. This has led to extensive studies on finding materials in which both orderings are simultaneously present either in single phase material (by unconventional mechanisms), composites or in thin films.

Unlike electromagnetism, which is a dynamic phenomenon, the electronic ordering phenomena like magnetism and ferroelectric properties, at a first glance, look mutually exclusive in periodically ordered condensed matter single phase systems. In conventional ferroelectric perovskite oxides such as  $\text{BaTiO}_3$ , the displacement of  $\text{Ti}^{4+}$  ions breaks the centrosymmetry. In other words polar structure needs space inversion symmetry breaking. This symmetry breaking is caused by the balancing forces due to hybridization of empty  $d$ -orbitals of  $\text{Ti}^{4+}$  with  $p$ -orbitals of  $\text{O}^{2-}$  and the short range Coulomb repulsions [2]. As

the temperature is lowered the bonding forces are stronger than the repulsive forces (ion-ion interactions), and a non-centrosymmetric phase is favored. Thus, empty d-orbitals are necessary to show conventional ferroelectric polarization where the space inversion symmetry is broken, making the structure non-centrosymmetric. On the contrary, magnetism is a phenomenon associated with partly filled d-orbitals, where, with reversal of time, the angular momentum associated with the spin is inverted and hence, time reversal symmetry is broken. In other words, magnetism requires time-reversal symmetry breaking. But it is very rare for both time-reversal symmetry breaking and space inversion symmetry breaking to occur happen simultaneously in conventional systems. This explains why there are only very few single phase materials containing both the orders [2].

Coexistence and interdependence of both of these orderings, leading to the phenomena called multiferroics and magnetoelectric, by different non-conventional routes, is discussed in the Chapter 2. Hexagonal ferrites were used in many permanent magnet applications for a long time due to their high magnetizations and insulating properties. Y-type hexagonal ferrite was the first hexaferrite to show magnetic field induced electrical polarization in 2005 [3], after that almost all the hexaferrites are found to display magnetoelectric behavior [4]. We synthesized some of these hexaferrite single crystals and used scattering methods to study the relationship of magnetic structure with already found macroscopic magnetoelectric properties. A brief introduction to crystal and magnetic structures of hexagonal ferrites and their magnetoelectric properties is also presented in this chapter.

Experiments are essential to understand structure and property relationships. Knowledge of experimental tools for synthesis, macroscopic measurements and scattering studies are essential to successfully conduct any experiment. In Chapter 3 we review the used lab-scale as well as large-scale experimental techniques and their principles. Growth results and lab scale characterization of samples are presented in chapter 4. Based on macroscopic data, the best samples were chosen for large scale facility experiments.

Y-type hexaferrite  $\text{Ba}_{2-x}\text{Sr}_x\text{Zn}_2\text{Fe}_{12}\text{O}_{22}$  was found to show magnetic field driven electrical polarization in magnetic field greater than 0.3 Tesla [3]. The magnetic structure of it was reported to comprise of different fan structures with magnetic moment in a plane perpendicular to c-axis. The rich meta magnetic phase diagram was studied by both neutron and soft X-ray resonance magnetic scattering techniques[5–11]. We studied the metamagnetic phases, both in low H and in H in the range of ferroelectric phase. Low H phases are presented in Chapter 5 and the magnetic structures in ferroelectric phase are discussed in chapter 6. We carried out simulations of intensity in our soft X-ray experiments to compare with our experimental data. In field neutron diffraction experiments were carried out to verify our models. Neutron diffraction results are presented in chapter 6.

# Chapter 2

## Introduction

Ordering of different degrees of freedom, such as lattice, spin, charge etc gives rise to different interesting physical properties in condensed matter systems. All these orderings are subjected to thermal energy. Above certain temperature a disordered state is reached. Out of all these ordering, our main concern is magnetic and ferroelectric ordering and their cross couplings.

### 2.1 Magnetic interactions and order

To put it simply, magnetic moment  $\mu_m$  is the magnetic dipole moment perpendicular to a current loop and its direction is given by the right hand thumb rule. In the case of atomic magnetism, orbital and spin rotation of electrons gives orbital and spin angular momentum. This angular momentum precesses in a magnetic field to give magnetic moment parallel to it as shown in Fig. 2.1. This automatically breaks the time reversal symmetry of the system as the sense of rotation of charge is reversed upon reversing time and so is the angular momentum and the corresponding magnetic moment.

In a crystalline solid atomic magnetic moments may order in a long range periodic fashion depending upon the exchange energy  $E_{ex}$ . This exchange energy is a measure of potential energy between two adjacent moments. For a one dimensional chain of magnetic atoms' system, the Hamiltonian for two adjacent atoms can be defined as:

$$H = - \sum_{i,i+1} J_{i,i+1} \mathbf{S}_i \cdot \mathbf{S}_{i+1} \quad (2.1)$$

where  $J_{i,i+1}$  is the exchange constant, originating from the *Pauli Antisymmetry Principle*, stating that the Eigen function of spin 1/2 indistinguishable particles should be antisymmetric with respect to the exchange of particles. Numerically  $J_{i,i+1}$  is half of the difference of energies between the singlet and the triplet states  $(E_s - E_T)/2$  found after exchange of

particles. In the case of ferromagnetic materials  $J_{i,i+1} > 0$  and therefore, singlet state has higher energy than the triplet state. In a single atom if spin  $i$  and  $i + 1$  are present, a triplet state is favored to minimize the Coulomb repulsion. When the spins are in two different atoms, either of the parallel or anti-parallel configurations may have lower energy (see following sections), as states of individual atoms couple together to give the final state. Nearest neighbor ferro and anti-ferromagnetic interactions may lead to different anti-ferromagnetic arrangement (for *e.g.* in a simple cubic lattice as shown in Fig. 2.2 [12]).

Direct exchange takes place when magnetic orbitals of neighboring atoms have sufficient overlap, but this is very rare in oxides, and in most cases indirect exchange take place. Exchange interaction mediated by a non magnetic atom, typically oxygen in oxides, bonded to two magnetic atoms is called *super-exchange interaction*. In super-exchange interaction (suppose mediated by O) between two iron atoms  $\text{Fe}^{3+}$  in  $d^5$  configuration, in an octahedral crystal field environment, there can be either ferromagnetic or anti-ferromagnetic coupling. Let us consider two ground states, (a) anti-ferromagnetic and (d) ferromagnetic, as shown in the Fig. 2.3. Both can mix with the excited states (b) and (e) due to successive hopping processes. In case of ferromagnetic ordering, the excited state (e) cannot mix with the excited states (f) and the excited states are reached only by spin forbidden hopping, which requires higher energy. Therefore, anti-ferromagnetic configuration has lower energy compared to ferromagnetic ordering in super-exchange mediated ordering when the bond angle is  $180^\circ$ . In case of  $90^\circ$  bond angle, where two different p-orbitals are involved, ferro-magnetism may also occur.

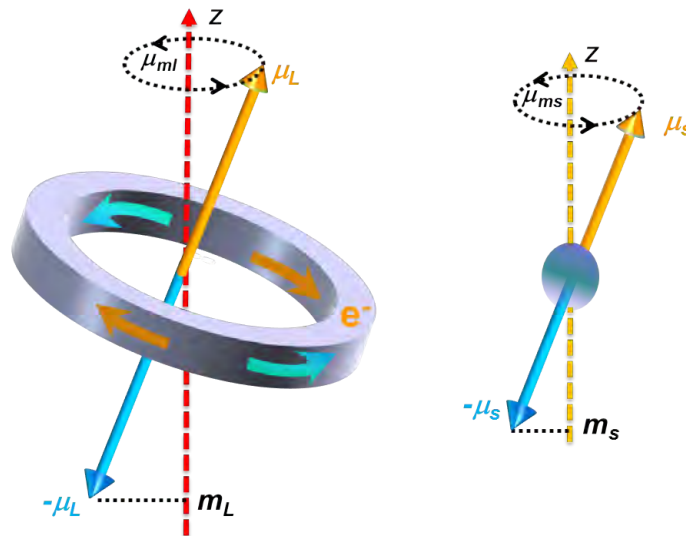


Fig. 2.1 Atomic magnetism (a) Orbital magnetic moment (b) Spin only moment.

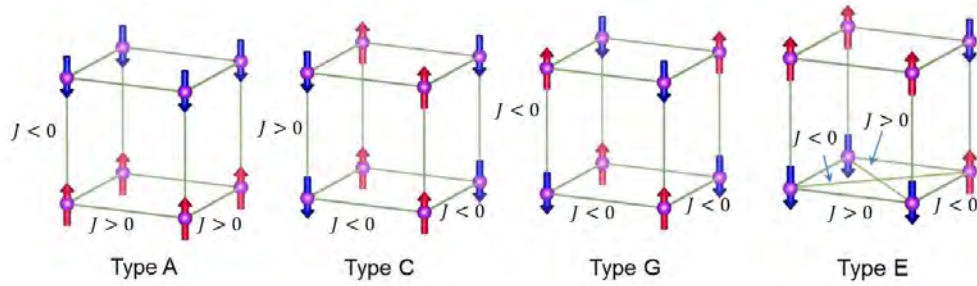


Fig. 2.2 Different types of anti-ferromagnetism in a cubic lattice due to positive and negative values of  $J$  in the nearest and the next nearest neighbors.

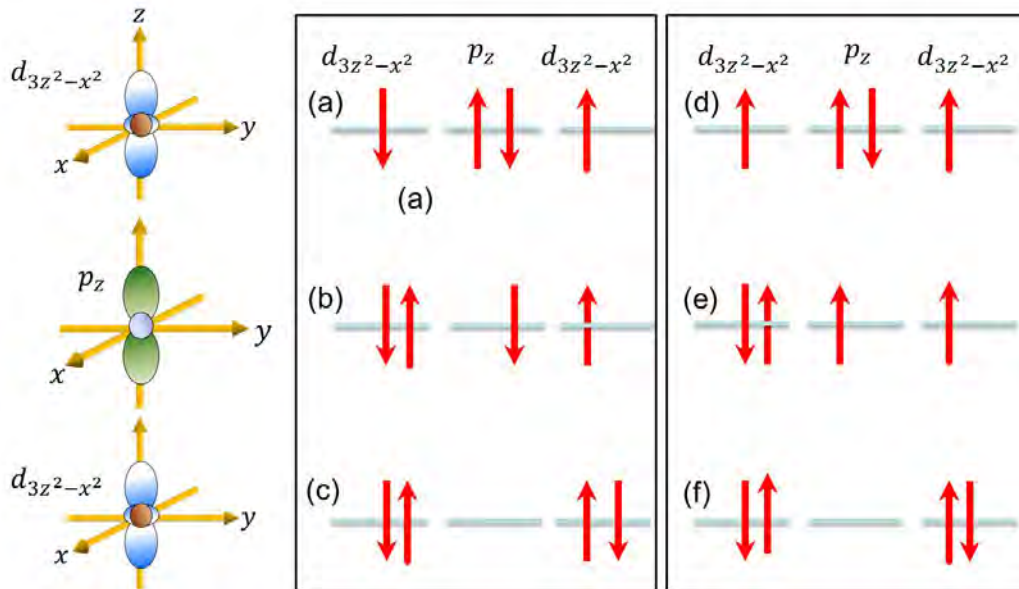


Fig. 2.3 Different intermediate steps in super-exchange interactions. Intermediates (d) and (e) are spin forbidden transitions.

There can be different kinds of super-exchange involving Mn as magnetic atoms in some perovskites like  $\text{La}_{1/3}\text{Sr}_{2/3}\text{MnO}_3$  (LSMO) and this mechanism is called *double exchange mechanism* [13, 14]. Various exciting phenomena, like metal insulator transition [15], colossal magnetoresistance (CMR)[16] [17] etc, take place near the magnetic ordering temperature of LSMO type materials. In mixed valence manganites, hopping of the  $e_g$  electron between  $\text{Mn}^{3+}$  ( $3d^4$ ) and  $\text{Mn}^{4+}$  ( $3d^3$ ) electrons takes place with equal energy before and after the hopping process, but the valence of both the manganites changes after it. During hopping the spin is conserved and hence, a ferromagnetic ordering takes place as shown in Fig. 2.4. This real hopping process is different from the super-exchange interactions where the exchange takes place through hypothetical excited states. Spin dependent hopping pro-

cess can explain some of the facts like colossal magnetoresistance, metal insulator transition etc, but is not enough to explain all the exciting phenomena.

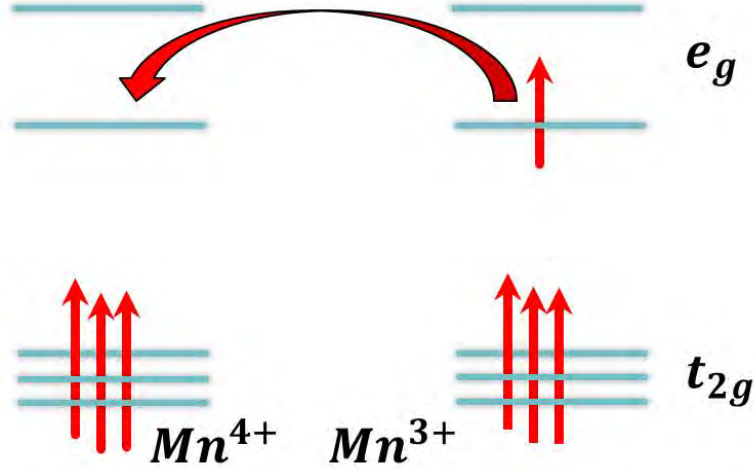


Fig. 2.4 Mechanism of double exchange.

### 2.1.1 Magnetocrystalline anisotropy (MCA)

Magnetocrystalline anisotropy (MCA) originates from coupling between the spin and orbital motion of electrons in the crystal lattice. As the magnetocrystalline anisotropy is strongly related to the lattice symmetry, this gives a preferred crystallographic direction to the magnetic moment to align. The simplest case of MCA can be considered as uniaxial anisotropy which can be written in the form of anisotropy energy (up to fourth order terms) as [18]:

$$E_{anis} = K_{u1} \sin^2 \theta + K_{u2} \sin^4 \theta \quad (2.2)$$

where,  $\theta$  is the angle between anisotropy axis and magnetization direction. Positive large values of  $K_{u1}$  favor easy axis. For hexagonal systems, for positive values of  $K_{u1}$ , if  $K_{u2} > -K_{u1}$  c-axis is the easy axis and if  $K_{u2} < -K_{u1}$  basal plane is the easy plane. For negative values of  $K_{u1}$ , if  $K_{u2} < -K_{u1}/2$  basal plane is the easy plane and if  $2K_{u2} > -K_{u1}$  an easy cone is observed.

### 2.1.2 Spin orbit interaction (SOI)

Spin orbit interaction is a relativistic term, originates from the relative motion of electrons in the lattice, and is the primary contributor to magnetocrystalline anisotropy. We can write a simple Hamiltonian as:

$$H_{SO} = \lambda L \cdot S \quad (2.3)$$

Here,  $\lambda$  is the spin orbit interaction coefficient, the strength of which depends upon the symmetry of the crystal and orbital moment in the crystal. The degeneracy of the term is given by  $(2J + 1)$ . In most of the systems orbital angular momentum is not observed and is said to be quenched. Orbital angular momentum operator is purely imaginary. In the absence of possibilities of linear combinations of them, mostly orbital angular momentum is quenched, *i.e.* the expectation value,  $\langle \psi | L | \psi \rangle = 0$ . If the crystal field does not remove the degeneracy completely, there can be linear combinations which give real values of the expectation value (for *e.g.*  $\text{Fe}^+$  in octahedral high spin state). In systems where complete quenching of orbital angular momentum takes place, SOI can have an effect on higher order perturbation theory and may lead to new excited states. SOI restores the quenched orbital moment to some extent, leading to preferred magnetization direction.

**Competing interaction** In the case of two competing exchange integrals, *e.g.* nearest neighbor  $J_1$  and next nearest neighbor  $J_2$ , other non-collinear orderings like screw type, helical or cycloidal are possible for suitable values of  $J_1$  and  $J_2$ . The total Hamiltonian for competitive interactions can be written as:

$$\begin{aligned} H &= \sum_{ij} (J_1 \mathbf{S}_i \mathbf{S}_{i+1} + J_2 \mathbf{S}_i \mathbf{S}_{i+2}) \\ &= -2NS^2 (J_1 \cos\theta + J_2 \cos 2\theta) \end{aligned} \quad (2.4)$$

Minimizing the energy in Eq. 2.4 we can have the following condition:

$$\cos\theta = -\frac{J_1}{4J_2}, \quad \text{for } |J_1| > 4|J_2| \quad (2.5)$$

Depending upon the values of  $J_1$  and  $J_2$ , ferromagnetic, anti-ferromagnetic or helimagnetic ordering can be found as shown in the Fig. 2.5. The angle  $\theta$  between the nearest neighbor spins is given by Eq. 2.5.

### 2.1.3 Anisotropic exchange interaction

All the exchange interactions described above are isotropic as, with respect to the crystal axis, they do not depend upon the moments. Spin orbit interaction, when included in the exchange interaction, becomes anisotropic and the excited states are allowed to mix with the ground state, which makes them sensitive to the local crystal environment. The total Hamiltonian for the exchange interactions of two spins in atoms  $a$  and  $b$  can be written as:

$$H = \sum_{ij} J(\mathbf{S}_i \mathbf{S}_j) + \frac{1}{2} \sum_{ij} D_{ij} [\mathbf{S}_{a,i} \mathbf{S}_{b,j} + \mathbf{S}_{a,j} \mathbf{S}_{b,i}] + d[\mathbf{S}_i \times \mathbf{S}_j] \quad i, j = x, y, z \quad (2.6)$$

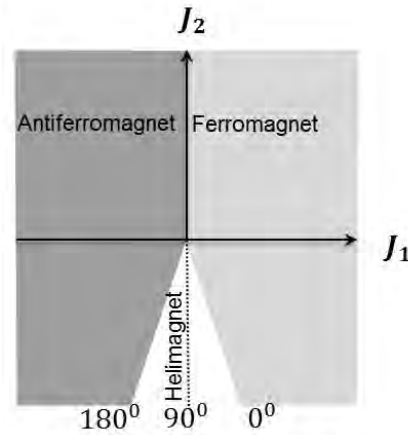


Fig. 2.5 Competing ferromagnetic and anti-ferromagnetic interactions between  $J_1$  and  $J_2$ , leading to helical magnetic order [19].

First term represents the isotropic exchange discussed so far and the remaining two terms represent the anisotropic exchange interactions. The anisotropic exchange is a small correction to the isotropic exchange and is often neglected. Physical interpretation of the anisotropic exchange can be viewed as the change in charge distribution around magnetic atom as a result of change in spin direction caused by SOI. As a consequence there is a change in the orbital overlap and this leads to a different strength of exchange interaction with the direction of spontaneous magnetization [20].

The anisotropic part has a symmetric and an antisymmetric contribution. Symmetric exchange takes place when the energy of the right-handed ( $\nearrow \searrow$ ) and left-handed ( $\searrow \nearrow$ ) magnetic configurations are the same, else it may be antisymmetric exchange. The second term in Eq. 2.6 represents symmetric anisotropic exchange and the third term represents the antisymmetric anisotropic exchange interactions. Single on-site excitations due to SOI contribute the antisymmetric part and two excitations due to SOI contribute the symmetric part of anisotropic exchange. This is explained in Fig. 2.6 by considering the states for atoms  $a$  as  $[\eta, \varphi$  and  $\xi]$  and for atom for  $b$  as  $[\zeta, \theta$  and  $\lambda]$ .

### Symmetric anisotropic exchange

This type of exchange interactions are predominant in systems with orbital order and reduced dimensionality. Some of the transfer processes due to hopping in symmetric exchange are shown in Fig. 2.6(a). Electron from the ground state  $\eta$  is first excited via SOI to  $\varphi$  state and then comes back to the ground state  $\zeta$  at  $b$ . Same thing can happen in atom  $b$ . There exist some other pathways also which are discussed in detail elsewhere [21]. Here the exchange constant  $D_{ij}$  has the same magnitude for processes  $a \rightarrow b$  or the reverse process.

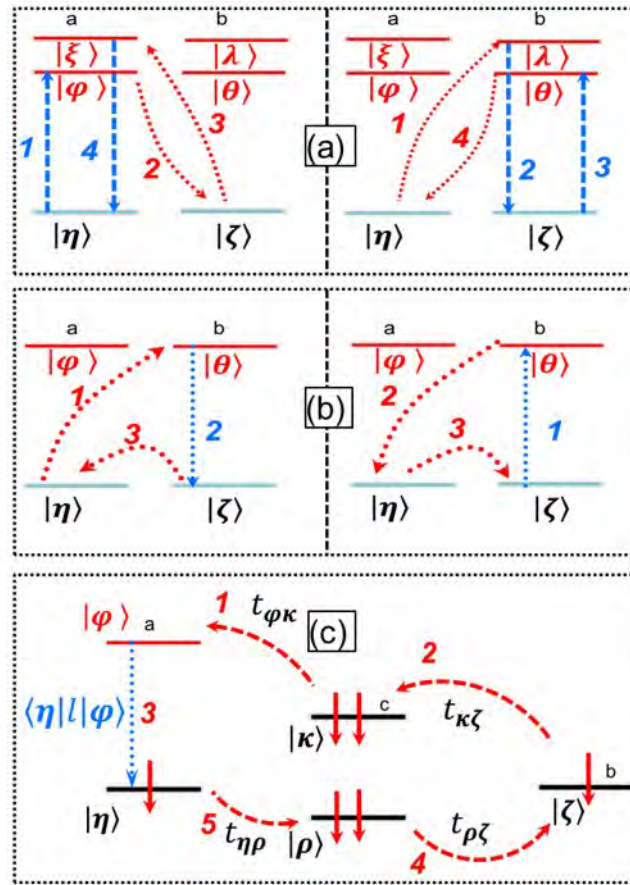


Fig. 2.6 Schematic of (a) Symmetric anisotropic exchange (b) Antisymmetric anisotropic exchange interactions. Blue lines represent transitions with the excited state due to SO coupling while the red arrows represent electron hopping via the transfer integral. There can be some other excited states also. Only one excited state is represented here. (c) Possible hopping and transfer processes when two magnetic atoms  $a$  and  $b$  are connected via a non magnetic atom  $c$ . Redrawn after [21].

Therefore, the process is symmetric.

## Antisymmetric anisotropic exchange

### Dzyaloshinskii-Moriya interaction

For explaining the weak ferro-magnetism in  $\text{Cr}_2\text{O}_3$  type oxides Dzyaloshinskii [22] and later Moriya [23] used anisotropic exchange interaction (the third term in Eq. 2.6).  $d$  is a constant vector and comes into existence after the spin-orbit-interaction (SOI). Normally the anisotropic term  $d$  is very small compared to isotropic term  $J$  ( $\frac{d}{J} \sim 10^{-2}$ ). Antisymmetric exchange is illustrated in Fig. 2.6(b). SOI breaks the degeneracy and the ground states  $\eta$  and  $\zeta$ , of the individual atoms  $a$  and  $b$  respectively, can interact via the excited state  $\theta$  as

shown in Fig. 2.6(b) [21]. Electrons excited from the ground state  $\eta$  of one atom  $a$  can be excited to the excited state  $\theta$  in atom  $b$  and then it comes back to ground state  $\zeta$  of atom  $b$  by transfer integral and finally to the initial state. Hopping and transfer integrals for two magnetic atoms bonded to a central nonmagnetic atoms are shown in Fig. 2.6(c). The charge transfer energy from atom  $a$  to atom  $b$  is very large compared to that from crystal field splitting or to that from the charge transfer to nonmagnetic atoms in the middle of magnetic atoms.

The Hamiltonian for DM interaction can be written as:

$$H_{DM} = \sum_{ij} d_{ij} \cdot (\mathbf{S}_i \times \mathbf{S}_j) \quad (2.7)$$

The energy  $H_{DM}$  depends upon the symmetry of the system, spatial directions of spins  $i$  and  $j$ , value and direction of  $d_{ij}$  depends upon the symmetry of the system. Because of DM interaction, collinear ferrimagnetic structure becomes unstable and a new non-collinear canted magnetic structure arises. This may lead to chiral structures with a specific chirality  $C$  given by  $c = \mathbf{S}_i \times \mathbf{S}_j$ . The chirality can be defined depending upon the sign of  $c$  *i.e.* for  $c > 0$  it right handed and for  $c < 0$  it is left handed. The canting angle can be estimated from the two site model:

$$H_{DM} = JS_1 \cdot \mathbf{S}_2 + d \cdot (\mathbf{S}_1 \times \mathbf{S}_2) \quad (2.8)$$

The angle  $\theta$  between the two spins determines the energy  $E$  of the system as:

$$E = JS^2 \cos \theta + dS^2 \sin \theta \quad (2.9)$$

and the angle  $\theta$  is given by  $\tan(\pi - \theta) = |d/J|$ .

Moriya [23] generalized the directions of the vector  $d$  after introducing SOI in Anderson's formalism [24] for two atoms in points A and B in a straight line and C is the point bisecting them. For  $d = 0$  inversion symmetry is present between the interacting atoms or a mirror plane ( $\perp$  AB). This implies that the interacting atoms must be different or have different chemical environments. Moriya [23] gave the following rules for determining the directions of  $d$ .

1. when there is an inversion center I at C:  $d = 0$ .
2. if a mirror plane exists perpendicular to A and B through C:  $d \parallel$  mirror plane or  $d \perp$  mirror plane.
3. if a mirror plane including A and B exists:  $d \perp$  mirror plane.

4. a two fold rotation axis  $C_2 \perp AB$  passes through  $C$ :  $d \perp$  two fold axis
5. if an  $n$  fold axis  $C_n$  along  $AB$  exists:  $d \parallel AB$

A necessary condition for  $d$  to have a finite value and hence a finite contribution from DM term to total energy, is the breaking of inversion symmetry. This breaking of space inversion symmetry may lead to electric polarization, which will be discussed in section 2.3. A small value of  $d$  has been measured by [25] very recently using resonance x-ray scattering technique.

## 2.2 Polar orders: Ferroelectrics

Ferroelectrics are insulators that have spontaneous polarizations, *i.e.* they exhibit ordering of their electrical dipole moments or inducing of new dipole moments even in the absence of an applied external electric field. Possibility of switching of polarizations by external electric field is one of the conditions for materials to be called ferroelectrics.

For materials to show polarization primary condition is to have a non-centrosymmetric structural arrangement. The competition between short range repulsions favoring symmetric structure and the bonding forces favoring non-centrosymmetric state determines the polarity. A ferroelectric is characterized by an order-disorder transition at Curie temperature ( $T_c$ ), above which the short range repulsion is the dominant force favoring symmetric arrangements [2]. Below the ordering temperature the bonding forces dominates the repulsive forces and a non-centrosymmetric structure is favored. Local ordering of the dipole moments can act in a cooperative way to give polar order and thus, a net polarization is observed.

A common example of ferroelectricity in transition metal systems is BaTiO<sub>3</sub> (BTO). According to the accepted theory, local force causing the off-center distortion of the Ti<sup>4+</sup> ion is considered to be due to the hybridization of the empty  $3d$  orbitals and  $2p$  orbitals in oxygen [2]. In this mechanism  $d^0$  state in the transition metal is a necessary condition. There are other ways to break the inversion symmetry, which will be discussed in the following sections.

## 2.3 Multiferroics: Interplay between spin and dipole

As discussed in section 2.1, magnetism is a phenomenon solely by unpaired electrons. In section 2.2 we found that empty  $d$  states are essential for transition metal oxides to show conventional polar orders. On a first glance, spin and conventional ferroelectric polar orders appear to be mutually exclusive [2]. Only very few materials exist in which intrinsically both the orders coexist. Therefore, some alternative mechanisms have been looked for in

the last decade. The term *multiferroic* was coined to define a material that has more than one ferroic property associated with it [26]. This is pictorially represented in Fig. 2.7. Multiferroics have been classified into two broad types by Daniel Khomshkii [27].

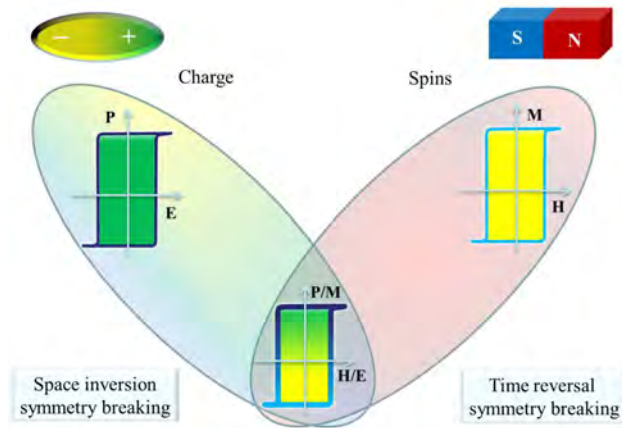


Fig. 2.7 Multiferroics: coupling between different order parameters.

1. **Type-I:** These are ferroelectrics where ferroelectric property is independent of magnetic structure, in many cases origin of both magnetism and ferroelectricity are due to different atoms. Cross coupling between both the spin and polar orders are not observed in many cases. A typical example is  $\text{BiFeO}_3$ , where magnetism is due to  $3d^5$  high spin moments of  $\text{Fe}^{3+}$  and electric polarization is due to the 6s lone pair of electrons present in  $\text{Bi}^{3+}$ , which modifies the hybridization to break the inversion symmetry. Although both the orderings occur above room temperature, the G-type anti-ferromagnetic structure (see Fig. 2.2) does not allow net magnetization. This net magnetization was overcome in thin films and nanostructures [28, 29]. A different class of materials exists, where ordering of charge in the metal ions can lead to ferroelectricity. In this case, spins are free [30] with charged valence states to contribute to magnetism. Very high cross coupling can be expected from this type of materials as a small change in charge configuration can lead to a considerable change in magnetization. However, out of the many predicted charge ordered multiferroics, macroscopic evidences are not many.  $\text{LuFe}_2\text{O}_4$  was proposed to have charge order based ferroelectric ordering [31] but recent works have proved it to be not ferroelectric [32–34]. In magnetite, although polar structure was found below Verwey transition [35], only recently it has been proved that switching of charge orders can be achieved by applying electric field [36].

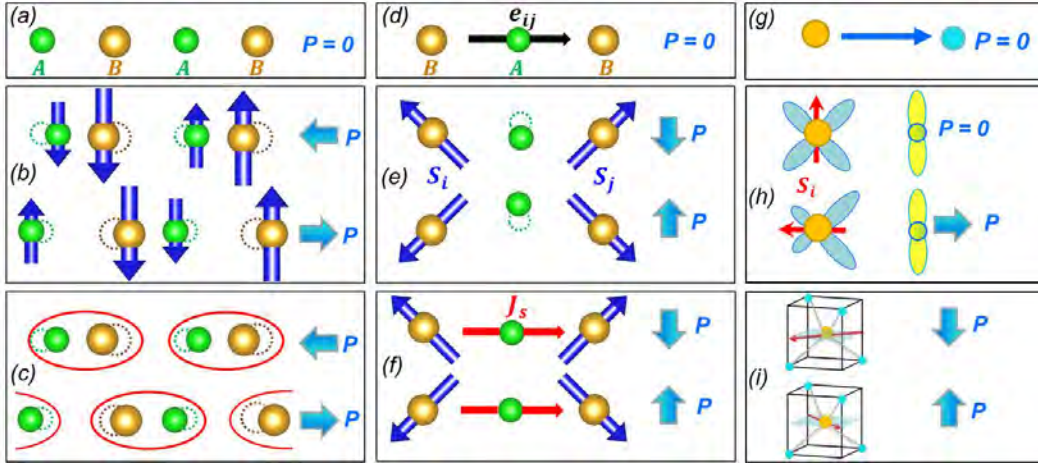


Fig. 2.8 Mechanism of multiferroicity [37].

2. **Type-II:** In this type of multiferroics polar order originates from magnetic ordering, for example. Certain non-collinear magnetic ordering leads to space inversion symmetry breaking and a net polarization can be obtained. After the discovery of ferroelectric polarization associated with a magnetic transition in  $\text{TbMnO}_3$  [38], the research area called *magneto-electric* gained considerable interest [37, 39–43]. For spin based magneto-electrics, different mechanisms have been proposed as listed below:

- (a) **Symmetric exchange striction mechanism:** In a typical exchange striction mechanism, ferroelectricity is induced by symmetric exchange interaction. In Fig. 2.8(a), (b) and (c) the symmetric exchange interaction between *down-down*, *down-up*, *up* and *up-down*, *up-down* spins  $\mathbf{S}_i$  and  $\mathbf{S}_j$  in two atoms A and B of different charges leads to displacement of the atoms due to striction associated with the spin configuration (see Fig.2.8(b) and (c)). Finite electric polarization in a certain crystallographic direction  $\Pi_{ij}$  can be found from the following equation:

$$P_{ij} \propto \Pi_{ij}(S_i \cdot S_j) \quad (2.10)$$

A primary condition for exchange striction mechanism is the requirement of commensurate spin order [37], so that the displacement due to striction is not canceled out after summing out over the entire lattice. Magneto-electric effect in some of the orthorhombic rare-earth manganites  $\text{RMnO}_3$  (where  $R$  is Ho, Y, Tm, Yb or Lu) can be explained on the basis of this exchange striction mechanism in

E-type magnetic ordering [44–46].

- (b) **Inverse DM interaction (IDM):** We found earlier (see subsection 2.1.3) that in anisotropic antisymmetric exchange interaction absence of center of inversion leads to non zero  $d$  vector. In other words, we can say that DM interaction leads to non-collinear spin arrangement. After formation of a spiral spin structure, for example, as a result of competitive nearest and next nearest neighbor interaction (see 2.1.2), as a reaction to it the system can minimize its energy by lattice deformation that creates a non zero  $d$  vector consistent with the non-collinear spin order already formed. Therefore, inverse DM interaction can be considered as the lattice relaxation to minimize the energy by atomic displacement of the center atom as a result of DM interaction. This, in turn, results in a net polarization in the direction as shown in Fig. 2.9.

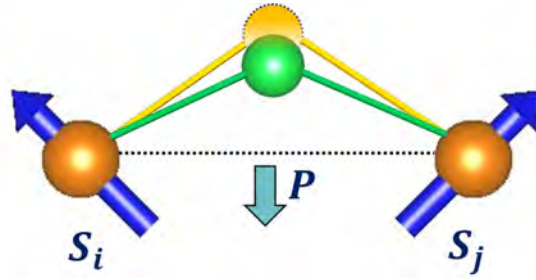


Fig. 2.9 Inverse DM interaction.

To explain the magnetic structure of  $\text{Cr}_2\text{O}_3$  system, Cox introduced some terminology regarding the spiral spin ordering which was later modified by Kimura [39] and Tokura [37, 40] and is shown in Fig. 2.10. A generalized expression for the induced polarization in these compounds due to magnetic spiral ordering was obtained [47, 48] from the Hamiltonian Eq. 2.7. The net polarization is given as:

$$\mathbf{P} = a \sum_{i,i+1} \mathbf{e}_{i,i+1} \times (\mathbf{S}_i \times \mathbf{S}_{i+1}) \quad (2.11)$$

$\mathbf{e}_{i,i+1}$  is the unit vector in the propagation direction connecting the two adjacent spins.

- (c) **Spin current mechanism:** Similar to the spin polarized current in semiconductors, a new mechanism has been proposed for spin induced ferroelectricity [49]. This mechanism can be explained with the help of Fig. 2.11 [49]. As can

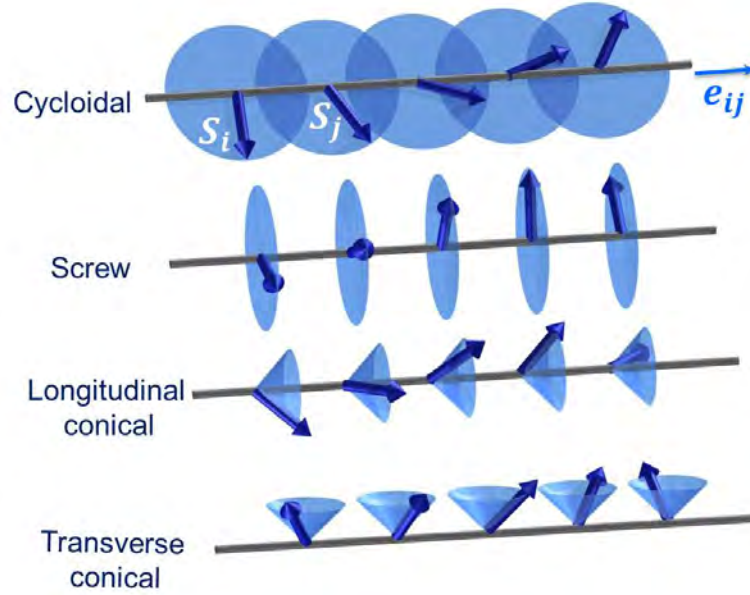


Fig. 2.10 Different types of spiral orders.

be seen in the figure, two magnetic atoms  $M_1$  and  $M_2$ , with oxygen in between them, carry non-collinear moments  $\vec{S}_1$  and  $\vec{S}_2$ . A spin current  $\vec{J}_s$  is proposed to exist in the direction shown by the green arrow. This spin current  $\vec{J}_s$  is proportional to  $\vec{S}_1 \times \vec{S}_2$ . The direction of the electrical polarization is proportional to the vector product of the spin current  $\vec{J}_s$  and a unit vector  $\vec{e}_{ij}$  along propagation vector direction. Therefore, the net polarization is given in the same direction as the polarization by DM mechanism by the same Eq. 2.11. On a phenomenological level both the mechanisms are equivalent, with the difference that, in *spin current mechanism* polarization is from electronic contribution from spin current (which changes electron density) whereas in *DM interaction* shift of nonmagnetic atoms contributes to polarization. Spin current mechanism can also be called as *inverse DM interaction (IDM)*.

**Macroscopic polarization in different spirals** Although microscopically local breaking of inversion symmetry takes place in IDM interaction, for macroscopic polarization different symmetry considerations should be accounted for:

- i. **Cycloidal spin structure:** As can be seen from Fig. 2.10 and Fig. 2.11, in the cycloidal spin configuration the vector product of the adjacent spin vectors  $\vec{S}_i$  and  $\vec{S}_j$  is not parallel to the unit vector  $\vec{e}_{ij}$  connecting the two adjacent sites or to the propagation vector direction. Therefore, a net polar-

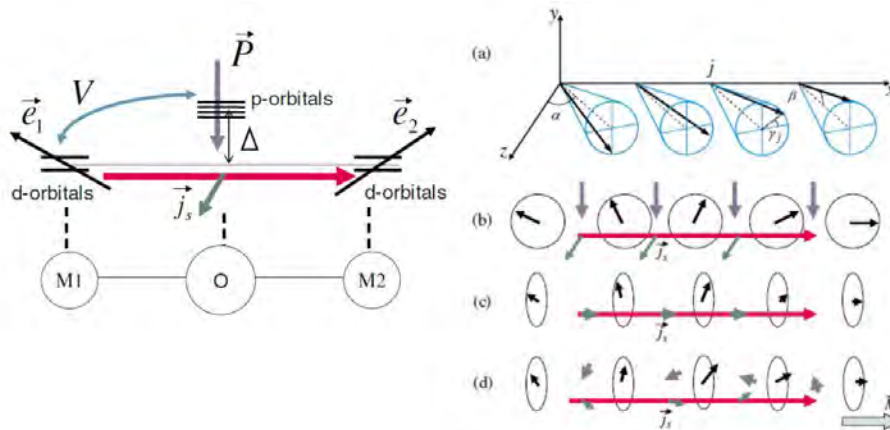


Fig. 2.11 Spin current mechanism of multiferroicity after [49].

ization can be realized according to Eq. 2.11 in a direction perpendicular to both the propagation vector and the cross product of the spins.

- ii. **Proper screw structure (helical):** In the proper screw structure, according to IDM or spin current mechanism, net polarization is zero. The vector product of two adjacent spins is always parallel to the propagation vector direction.
  - iii. **Longitudinal conical structure:** In longitudinal conical spiral also, like proper screw spiral, net polarization is zero.
  - iv. **Transverse conical spiral:** In transverse conical spiral the vector product of the spins is not parallel to propagation direction and so, a nonzero final vector product can be reached according to Eq. 2.11. Therefore, macroscopically, polarization is possible. Transverse conical structure can be decomposed into ferromagnetic and cycloidal structure. In our compound of interest Y-type hexaferrite with composition  $\text{Ba}_{(2-x)}\text{Sr}_x\text{Zn}_2\text{Fe}_{12}\text{O}_{22}$  a proper-screw magnetic structure was reported. Magnetic field driven ferroelectric polarization was found in this compound. So, according to above rules it can not be due to IDM mechanism. Therefore, we investigated the magnetic structure using several scattering techniques and macroscopic measurements.
- (d) **The p-d hybridization mechanism:** In this mechanism a single magnetic site coupled with a ligand atom can produce a local dipole moment. Via SOI, the ionic character of the covalent bond between the metal and ligand is modulated depending upon local spin moment direction. This produces a dipole moment

in the bond direction. This mechanism is very rare and is found only in some selective compounds like  $\text{CuFeO}_2$  [50],  $\text{MnI}_2$  [51] etc.

## 2.4 Hexaferrites

In the previous chapter we have discussed about different spin based magneto-electric materials. When we compare different spin based multiferroics, it can be seen that most of them have either of the ferroic ordering temperatures far below room temperature. For example, orthorhombic manganites have spin based ferroelectricity only below 28 K [52]. Transverse conical spin spiral  $\text{CoCr}_2\text{O}_4$  has magnetic field driven ferroelectricity below 26 K [53]. In case of cycloidal  $\text{MnWO}_4$  the ferroelectricity is observed below 12.5 K [42]. In case of  $\text{CuO}$  relatively high temperature (230 K) ferroelectricity is observed in the spiral phase because of the high super-exchange interaction near  $180^\circ$  bond angle [54]. To explore the magneto-electricity in single phase oxides the super-exchange interaction should be strong enough to have a magnetic order at room temperature that favors the magneto-electric coupling. Mostly spiral order is due to the nearest neighbor and next nearest neighbor competitive super-exchange interaction, causing the frustration, which lowers the magnetic transition temperature. Therefore, strong super-exchange interaction is a necessary step for material design for multiferroics based on spin order at room temperature. An overview of materials showing spin based multiferroics can be found in ref. [37, 39, 40].

### 2.4.1 Magnetoelectric hexaferrites

Hexaferrites are one of the oldest and the most extensively used magnetic materials in permanent magnet applications. In the last decade hexaferrites have been found to show promise for tuning magneto-electric coupling to room temperature. In fact, this class of materials are the only materials having magnetic ordering above 100 K with spiral spin based multiferroicity. Moreover, high magnetic moments are observed in all the classes of hexaferrites (see following sections for various classes of hexaferrites), high ferrimagnetic moments are observed which favor practical applications. In the year 2005, a class of hexaferrite, called 'Y-type' hexaferrite, was found to display magnetic field driven ferroelectricity below 130 K and the maximum of the field-driven polarization was near 1 Tesla [3]. In the year 2008, low field ( $\pm 30$  millitesla) magneto-electric coupling was found in Mg and small amount of Al substituted 'Y-type' hexaferrite [55, 56]. In the year 2010, Sc and Mg substituted for Fe in another class of hexaferrite, the 'M-type' hexaferrite, was found to show magnetic field driven ferroelectricity [57]. In the same year, room temperature magneto-electric coupling was demonstrated in the class called 'Z-type' hexaferrite [58, 59] powders. These hexaferrites are difficult to classify in a generalized way on the

basis of their magnetic structures as they range from proper screw to longitudinal conical, transverse conical and ferrimagnetic spin structures. With little modification in the transition metal site (by substituting other magnetic or nonmagnetic ions) and in the alkaline earth metal site (by the same group elements of different sizes), magnetic structures can be changed from one to another. Magnetic field driven ferroelectricity is observed in almost all of the hexaferrite structure types. Most importantly, spontaneous magnetization is found near room temperature and above it. Therefore, hexaferrites are one of the most promising materials for room temperature applications.

### 2.4.2 Crystal structure of hexaferrites

Hexaferrites are known by different names such as Ferroxdure, Barium Hexaferrite, Barium Ferrite etc. and are used extensively for permanent magnet applications. All the hexaferrites crystallize in hexagonal structures with hexagonal or rhombohedral space group. In table 2.1 different types of hexaferrites are shown. There are different ways to classify all the hexaferrites, one of them is based on the three constituent blocks: spinel, M-type and Y-type hexaferrite. All other hexaferrites are constituted with these three units, as shown in table 2.1. Other classifications are discussed in successive sections.

Table 2.1 Different hexaferrites with their structural blocks

Name	Molecular formula	Molecular units	Blocks	C Å(Approx)	Space group
S	$MeFe_2O_4$	S	1/2S		
M	$RFe_{12}O_{19}$	M	SR	23.2	$P6_3/mmc$
W	$RMe_2Fe_{16}O_{27}$	M+2S	SSR	32.8	$P6_3/mmc$
X	$R_2Me_2Fe_{28}O_{46}$	2M+2S	SRS*S*R*	84.1	$R\bar{3}m$
Y	$R_2Me_2Fe_{12}O_{22}$	Y	STSTST	43.5	$R\bar{3}m$
Z	$R_3Me_2Fe_{24}O_{41}$	Y+M	STSR	52.3	$P6_3/mmc$
U	$R_4Me_2Fe_{36}O_{60}$	Y+2M	SRS*R*S*T	38.16*3	$R\bar{3}m$

#### M-type hexaferrite

Apart from simple spinel, the least complex structure is M-type hexaferrite. To understand the structure let us start from a layer of oxygen called layer-A as shown in Fig. 2.12. There are two ways in which the next layer of oxygen is placed: one is layer-B as shown by blue triangle and the other is layer-C as shown by the red triangle in the Fig. 2.12. There are four oxygen atoms per projected unit cell in the layers B and C. One of these four oxygen atoms is replaced by an alkaline earth metal ion, such as Ba or Sr, to form the B' and C' layers. These layers A, B, C, B', and C' can be organized in different ways to form different hexaferrites [60].

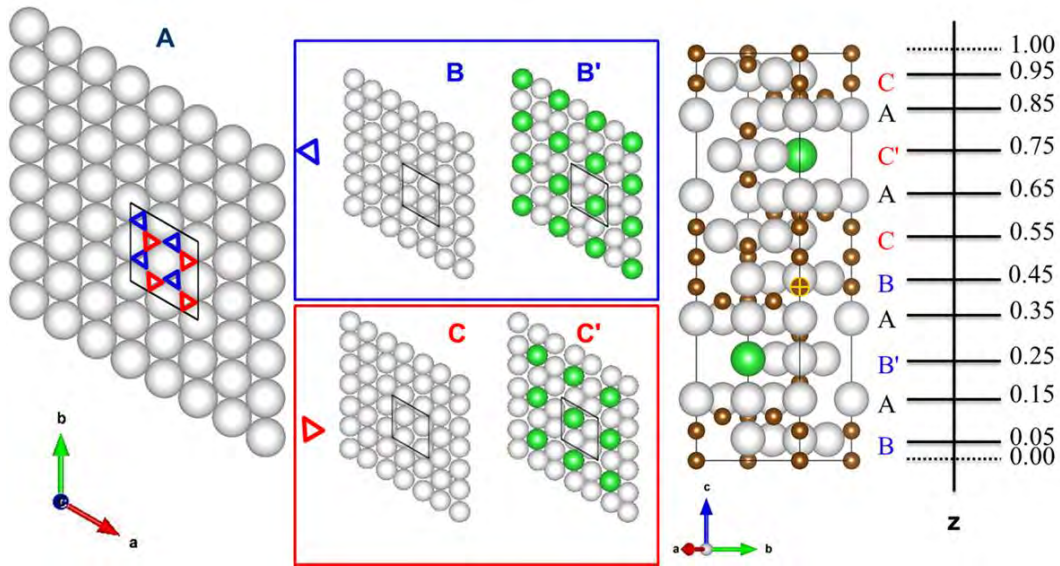


Fig. 2.12 Different close packed layers in hexaferrite. Gray colored atoms are oxygen, greens are alkaline earth metals and brown are transition metals.

M-type hexaferrite crystallizes in  $P6_3/mmc$  (194) space group. The first layer (the B-layer of oxygen) starts at  $z = 0.05$  and the sequence goes on as:  $BAB'ABCAC'AC$ .

### The $B_1S_4$ model for M-type hexaferrite

In the nomenclature for this hexaferrite, a single barium containing layer is called as  $B_1$ -layer as shown in Fig. 2.13. The  $B_1$ -layer is sandwiched between the  $ABCA$  type cubic blocks called the  $S_4$ -blocks and contain four layers of oxygen. This  $B_1$ -layer shows a three fold symmetry between two spinel plates. Apart from the Ba atom, the other oxygen atoms form two triangles as shown in blue lines in the right side of the Fig. 2.13. The Ba atom marked X in yellow is above the plane and the one opposite to it is below the plane. Spinel planes can be reflected through this  $B_1$  layer.

### The R-S model for M-type hexaferrite

In this widely accepted form of nomenclature, R refers to the hexagonal packing such as  $AB'AB'$  or  $AC'AC'$  and S is the cubic packing such as ABC. This is a much superior way compared to  $B_1S_4$  model to define the hexaferrite, as each block contains distinct magnetic characteristics which gives rise to saturation magnetization.

The S-block consists of two ABC type oxygen layers having spinel units with unit formula  $Me_2Fe_4O_8$ . In between the oxygen layers there are four octahedral sites and two tetrahedral sites with coordination numbers 6 and 4 respectively with oxygen co-ordination environment.

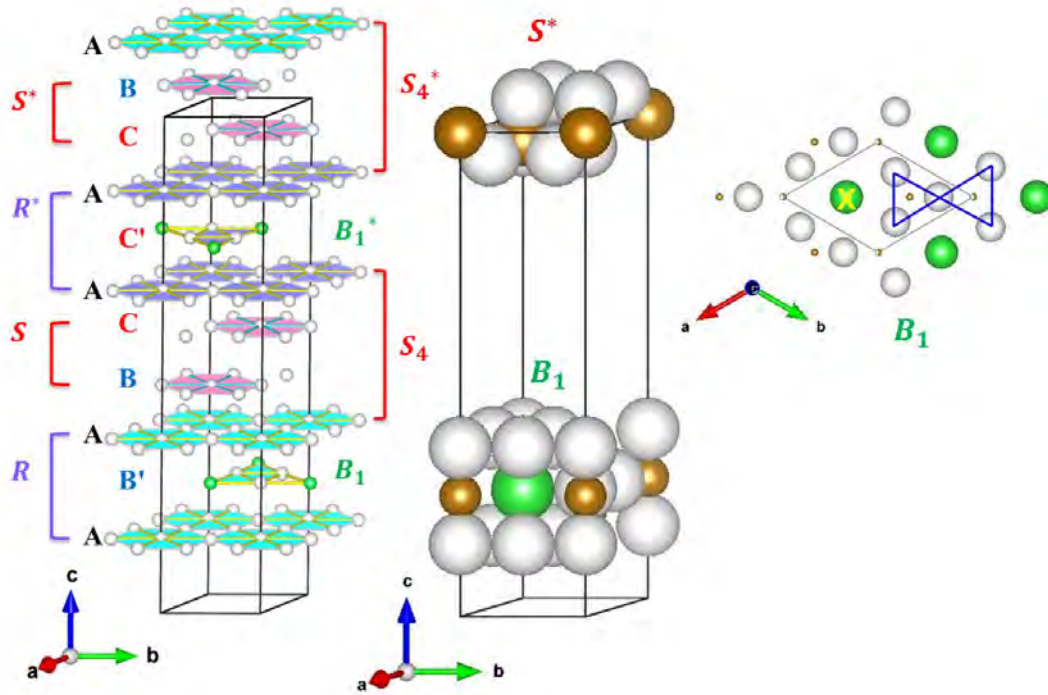


Fig. 2.13 B-S and RS blocks in M-type hexaferrite.

The R-block (rhombohedral) consists of three layers of oxygen but the middle layer is a  $B_1$  layer as discussed in  $B_1S_4$  model, with a formula unit of  $BaFe_6O_{11}$ . There is an asymmetry in the co-ordination environment of the transition metal ions in the R-block because of the  $Ba^{2+}$  ion and therefore, a 5 co-ordinated trigonal bi-pyramidal site exists in the R-block with Fe(2) ions in it (as can be seen in Fig. 2.14(b)).

There are different types of voids in the closed packing, like tetrahedral, octahedral, trigonal bipyramidal etc. Iron atoms Fe(1), Fe(4) and Fe(5) with Wyckoff positions 2a, 4f<sub>2</sub> and 12k occupy the octahedral sites as shown in Fig. 2.14(b). Fe(3) with Wyckoff position 4f<sub>1</sub> has a tetrahedral ligand environment. Fe(2) with Wyckoff position 2b goes to the trigonal bi-pyramidal site as shown in Fig. 2.14(c).

### Y-type hexaferrite

Y-type hexaferrites, which constitute the main topic of research in this thesis, like M-type, have distinct features. Using various combinations of Y-type and M-type hexaferrite and spinel type structures all the other hexaferrites can be built. Y-type hexaferrite crystallizes in  $R\bar{3}m$  space group. Y-type hexaferrites have a general formula of  $Ba_2Me_2Fe_{12}O_{22}$  where Ba can be substituted by similar sized alkaline earth metal ions and  $Me$  is a bivalent transition metal ion.

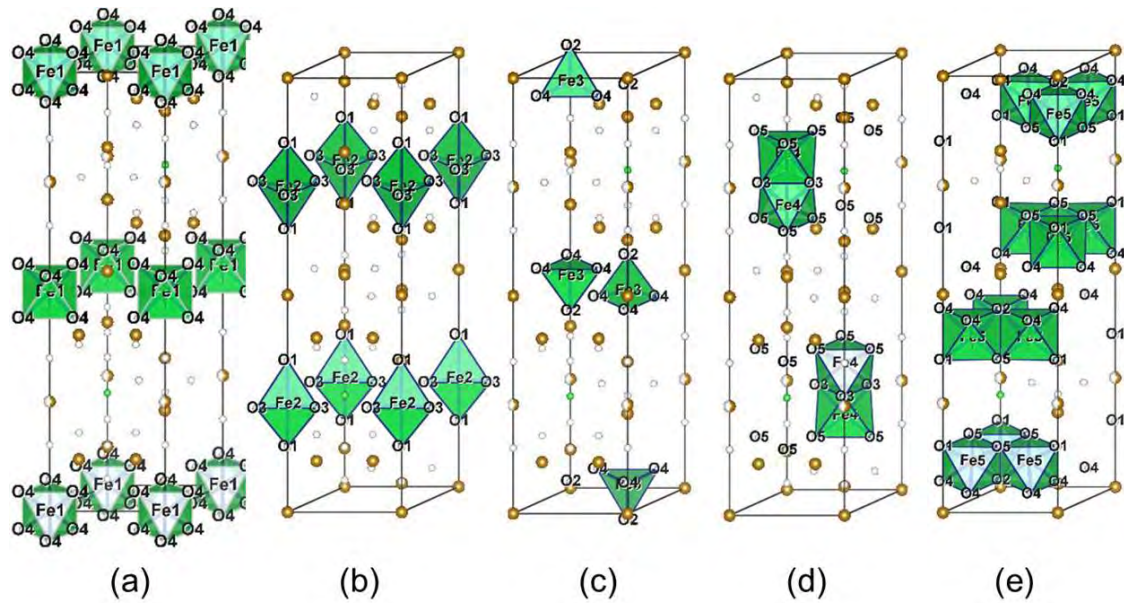


Fig. 2.14 Polyhedra in M-type hexaferrite.

### $B_2S_4$ model for Y-type hexaferrite

The crystal structure of Y-type hexaferrite can be described similar to that of M-type hexaferrite in light of the  $S_4$  blocks sandwiching barium containing layers. The  $S_4$  layer in Y-type hexaferrite is also a 4-layered ABCA type spinel layer. The Ba containing layer has two layers of oxygen, where one out of four oxygen is replaced by a Ba or any other alkaline earth metal ion (as shown by the green layer in Fig. 2.15).

### The T-S model for Y-type hexaferrite

Similar to M-type hexaferrite with R-S model, Y-type hexaferrites can be modeled by TST-STST blocks (see Fig. 2.15). The spinel blocks are same as in M-type but the T-block contains four layers of oxygen of ABAB types, where, in the central two layers one of the four oxygen anions is replaced by an alkaline earth metal ion. T-block has a general formula  $Ba_2Fe_8O_{14}$ . One major difference in the transition metal sites in the T-block, compared to R-block in M-type hexaferrite, is that the trigonal bi-pyramidal site is absent in T-block (see Fig. 2.16).

### Other hexaferrites

Other hexaferrites can be constructed with the help of spinel blocks, M-type and Y-type hexaferrites as shown in Table 2.1. For example, Z-type hexaferrite is a stacking of  $1/2$  M-type and  $1/3$  Y-type hexaferrites. In terms of blocks it can be considered as  $RSTSR^*S^*T^*S^*$  as shown in Fig. 2.17. Similarly, U-type hexaferrite also can be constructed by using M and

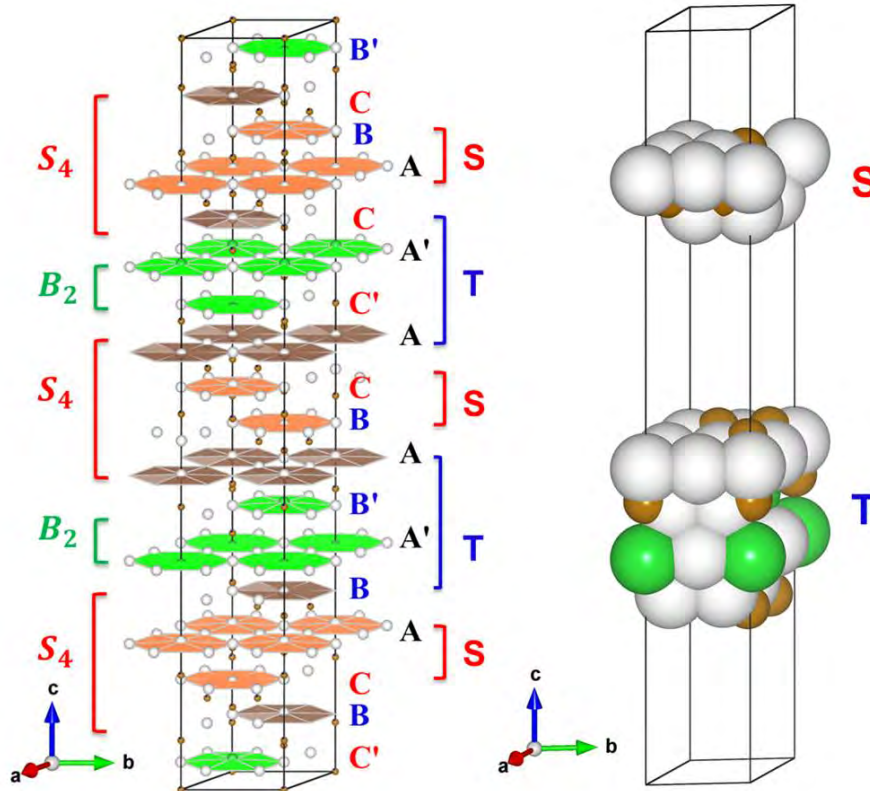


Fig. 2.15  $B_2S_4$  and T-S model for Y type hexaferrite.

Y-type hexaferrites.

### 2.4.3 Proposed spin structure of Y-type hexaferrite

$Ba_{(1-x)}Sr_xZn_2Fe_{12}O_{22}$  A planar proper screw spin structure was proposed [3, 5, 7, 8, 61] for intermediate values of  $x$  for all fields applied perpendicular to  $c$  axis. The crystal is divided into two spin blocks, large spin blocks and small spin blocks.

Magnetic structures of  $[Ba_{(1-x)}Sr_x]_2Zn_2Fe_{12}O_{22}$ , depending upon  $x$ , were studied by Utsumi *et al.*[62]. A unit cell contains 6 different types of Fe atoms as shown in Table 2.2.  $Zn^{2+}$  ions are located at the two tetrahedral (6c) sites. We will use the formalism used by Utsumi *et al.*[62]. A variable  $\gamma$  is defined where, occupation of Zn(1) is  $\gamma$  and that of Zn(2) is  $(1 - \gamma)$ , however, total occupation of  $Zn^{2+}$  does not add up to 2 in stoichiometric formula for different values of  $x$  [63, 64]. We also carried out refinement of single crystal X-ray diffraction data and found the same and these results are presented in Chapter-3. For  $x = 0$  individual spin directions of  $Fe^{3+}$  atoms in the 6c sites are opposite in direction to that of 3b, 18h and 3a sites.

Let us consider the first 12 layers of atoms, from height  $z = 0$  of the unit cell, along [001] as shown in Fig. 2.18(b). The most widely accepted spin structure [5] is of block

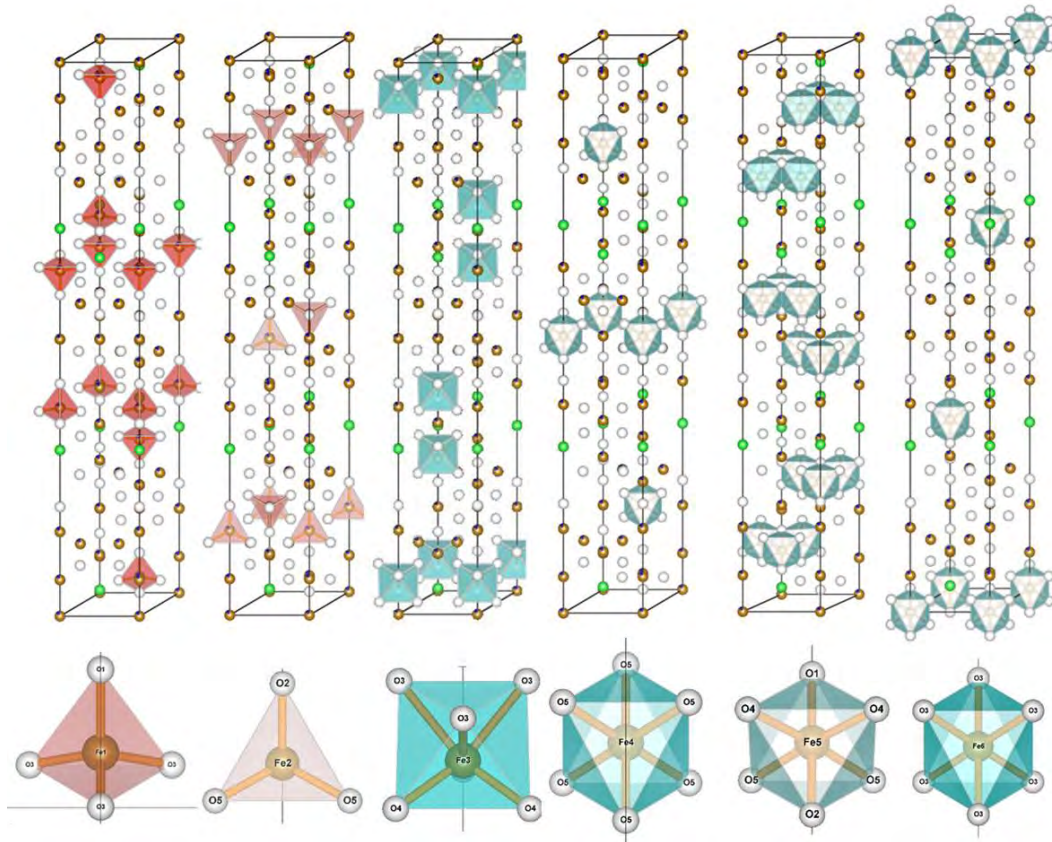


Fig. 2.16 Transition metals sites in Y-type hexaferrite.

spin models which turns from helical to cycloidal [56, 65, 66] to ferrimagnetic structures depending upon the composition and  $H$ . Based on refinements of single crystal neutron diffraction data the boundary ( $T_{1/2}ST_{1/2}$ ) between the blocks were proposed by Momozawa *et al.*[7]. Within each block collinear ferrimagnetic ordering was proposed. This block model makes it easier to model the magnetic structure. The spin structure in between the blocks changes depending upon composition. For  $Ba_{(1-x)}Sr_xZn_2Fe_{12}O_{22}$ , it changes from proper screw to collinear ferrimagnetic [3, 5, 7, 8, 61] depending upon  $x$ . In the available model for describing the magnetic structure based on spin block model, the whole unit cell is divided into two types of spin blocks along  $[001]$  as small S and large L (in later sections S represents small spin blocks rather than spinel structural blocks, unless specified otherwise), stacked one over the other alternately. These spin blocks are of two distinct configurations as shown in Fig. 2.18(a). The boundary between the spin blocks are in the middle of the tetragonal T crystallographic block and a large spin block can be called ( $T_{1/2}ST_{1/2}$ ) [7]. In terms of layer number, boundary between the spin blocks is found to be between  $j = 4$  and  $j = 5$  layers as shown in Fig. 2.18(b) [5]. Values of  $\gamma$  were found to vary with  $x$ , which has

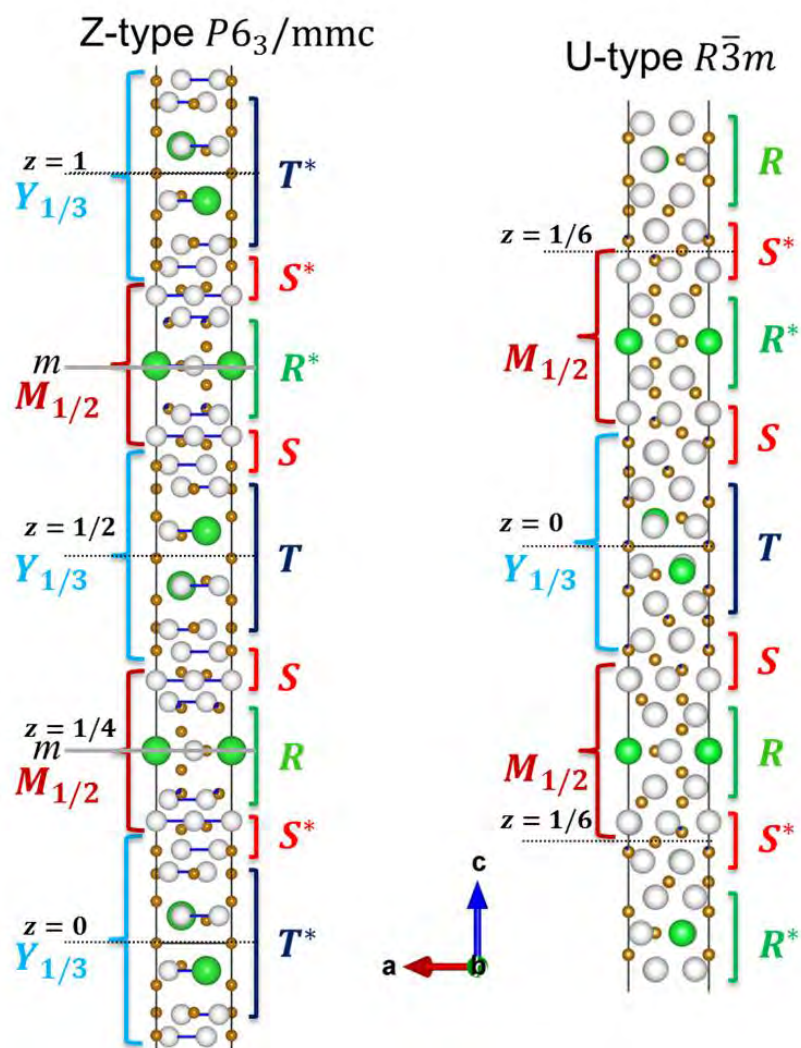


Fig. 2.17 Crystal structure of Z-type and U-type hexaferrite.

an important role in determining whether the structure will be ferrimagnetic or non-collinear [62].

Table 2.2 Different types of  $\text{Fe}^{3+}/\text{Zn}^{2+}$  in unit cell of  $\text{Ba}_2\text{Zn}_2\text{Fe}_{12}\text{O}_{22}$

Atom (label)	Wyck	structural block	Magnetic block	spin	$C_{Fe}$	Coordination
Fe(1) (Zn(1))	6c	T	$\mu_S$	$\uparrow$	$\gamma$	Td
Fe(2) (Zn(2))	6c	S	$\mu_L$	$\uparrow$	$1 - \gamma$	Td
Fe(3)	6c	T	$\mu_L$	$\uparrow$	1	Oh
Fe(4)	3b	S	$\mu_L$	$\downarrow$	1	Oh
Fe(5)	18h	T,S	$\mu_L$	$\downarrow$	1	Oh
Fe(6)	3a	T	$\mu_S$	$\downarrow$	1	Oh

Table 2.3 Superexchange interaction in the first 12 layers of the unit cell from  $z = 0$ , for  $x = 0$ . Numbers in superscript represent the layer number and that in parentheses represent Wyckoff positions.

$\text{Fe}^j\text{-O}^j\text{-Fe}^j$	Exchange integral [62]	Strength [67]
$\text{Fe}^1(6)\text{-O}^2(3)\text{-Fe}^4(1)$		very strong
$\text{Fe}^4(1)\text{-O}^2(3)\text{-Fe}^5(3)$	-0.365	weak
$\text{Fe}^4(1)\text{-O}^6(1)\text{-Fe}^8(5)$	-0.503	medium
$\text{Fe}^5(3)\text{-O}^7(4)\text{-Fe}^8(5)$	-1	strong
$\text{Fe}^8(5)\text{-O}^{10}(5)\text{-Fe}^{11}(2)$		medium
$\text{Fe}^{11}(2)\text{-O}^{10}(5)\text{-Fe}^{12}(4)$		medium

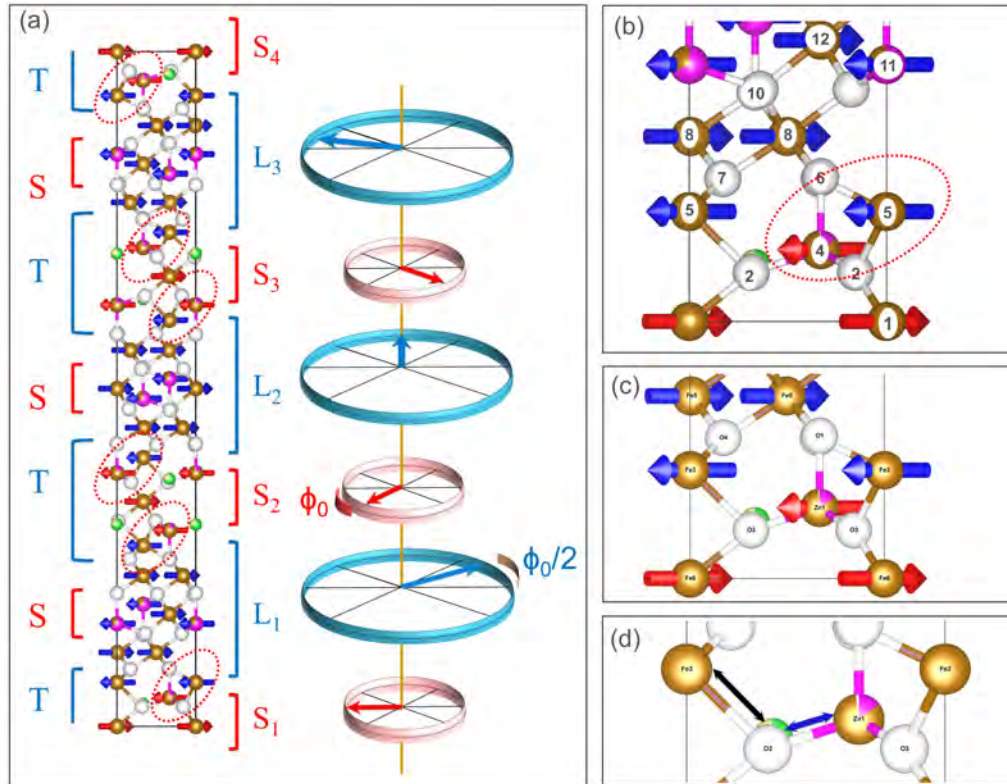


Fig. 2.18 (a) Crystal and spin structure of  $[\text{Ba}_{(1-x)}\text{Sr}_x]_2\text{Zn}_2\text{Fe}_{12}\text{O}_{22}$  in the ferrimagnetic phase. On the left side of the structure, crystallographic T and S blocks are shown as discussed in 2.4.2. On the right side, small S (red) and large L (blue) spin blocks are shown. (b) First 12 layers of atoms along  $[0 0 1]$ . (c) Expanded region of the boundary between spin blocks. (d) Enlarged view of the boundary region without the spins.

Table 2.3 shows some super-exchange interactions and their strength. It is seen that the ferromagnetic  $\text{Fe}^4\text{-O}^2\text{-Fe}^5$  super exchange interaction is weak.  $\text{Fe}^4$  is not pure  $\text{Fe}^{3+}$  but partially substituted by  $\text{Zn}^{2+}$ . A close look at the spin structure reveals that all the

super-exchange interactions lead to anti-ferromagnetic ordering, except  $\text{Fe}^4\text{-O}^2\text{-Fe}^5$  which is shown by dotted ellipse in Fig. 2.18(a) and (c). Bond length between  $\text{Fe}/\text{Zn}^4(1)\text{—O}^3(3)$  (blue) and  $\text{Fe}^5(3)\text{—O}^3(3)$  (brown) is modified by  $\gamma$ . The bond length  $\text{O}^2(3)\text{-Fe}^5$  is much longer compared to that of average Fe-O bond length. This will be discussed in detail in Chapter-3. Change in bond length modifies the strength of the concerned super-exchange interaction. This change in super-exchange interaction can explain the transition from ferromagnetic to the non-collinear spin structure. This can also be viewed as a competing exchange interaction between nearest neighbor  $\text{Fe}^4\text{-O}^2\text{-Fe}^5$  ferromagnetic and next nearest neighbor anti-ferromagnetic  $\text{Fe}^5\text{-O}^7\text{-Fe}^8$ .

# Chapter 3

## Experimental techniques

### 3.1 Sample synthesis

#### 3.1.1 Powder synthesis

Solid state synthesis is one of the most widely used techniques, where reactants are mixed in solid state and heated to high temperatures, very often above 1000° C. Both thermodynamic and kinetic aspects are important in solid state reactions [68]. Decrease in the Gibbs free energy favors the reaction to occur, which is determined by thermodynamic factors, whereas the rate at which the reaction will occur is determined by the kinetic aspects. Solid state reaction between two reactant species A and B to a thermodynamically stable species C takes place via diffusion of reactants to the interfaces where nucleation of C takes place as schematically shown in Fig. 3.1 (a). This process requires higher temperatures as the crystal structure of the reactants and products in most cases are not similar and a lot of bond breaking and making takes place. The rate of diffusion can be obtained from Fick's first law as:

$$J = -D \left( \frac{\partial c}{\partial x} \right) \quad (3.1)$$

Here,  $D$  is the diffusion coefficient,  $J$  is flux of diffusing species and  $\frac{dc}{dx}$  represents the concentration gradient. The average distance that a species will be able to travel is given by:

$$\langle x \rangle = (2Dt)^{1/2} \quad (3.2)$$

For a reaction to occur in a given time and at a particular temperature, therefore, average crystallite size of the reactant should be smaller than  $\langle x \rangle$ . The rate of a solid state reaction

can be controlled by controlling the following aspects:

- Grinding the reactants to smaller particles. In case of smaller particles, the reaction rate is enhanced in two ways: first, the species have to travel shorter distance for completion of reaction and second, higher surface area is provided.
- Proper mixing and pelletization of the reactant mixture is helpful for efficient reaction.
- Rate of diffusion depends upon temperature. Therefore, elevated temperature is required for a solid state reaction to take place.

### 3.1.2 Single crystal growth

The availability of good quality single crystals is essential in understanding many properties of matter, most importantly the tensor properties. Single crystals also help in avoiding any effects arising from grain boundaries. Crystal growth can be considered as a phase transformation from either liquid, solid or gas phase to solid phase. Solid-solid phase transformation is a rare practice but gas to solid and liquid to solid are well established methods for crystal growth. There are different methods of crystal growth. Therefore, in our work we used optical floating zone and flux method of crystal growth. There are three basic steps for crystal growth [69]:

- Supersaturation or supercooling.
- Nucleation.
- Growth of a particular phase of single crystal favoring the above two aspects.

**Flux growth method** Flux growth is primarily characterized by crystal growth from high temperature solutions. In flux growth, initial task is to melt the constituents. Many of the reactants have very high congruent melting points and very often melt incongruently at low temperatures. Therefore, in flux growth they are melted with the help of a binary, ternary or higher mixture, where one or more constituents is the flux. The mechanism of melting materials, whose melting points are individually high, at lower temperature is explained in Fig. 3.1(b). Practically, phase diagrams are more complex. For example, a more complex phase diagram can be seen in [70]. Fluorides and oxides are commonly used as flux for preparing oxide materials. Some examples are, PbO, PbF<sub>2</sub>, BaO, BaF<sub>2</sub>, Bi<sub>2</sub>O<sub>3</sub>, Li<sub>2</sub>O, Na<sub>2</sub>O, K<sub>2</sub>O, KF, B<sub>2</sub>O<sub>3</sub>, P<sub>2</sub>O<sub>5</sub>, V<sub>2</sub>O<sub>5</sub>, MoO<sub>3</sub> etc or mixtures of these.

In flux growth, nucleation may take place at the wall of the crucible or a seed crystal can also be used instead. The molten flux can be decanted or the crystals can be removed from the cold solid mixture by using suitable chemicals like acids which can dissolve the

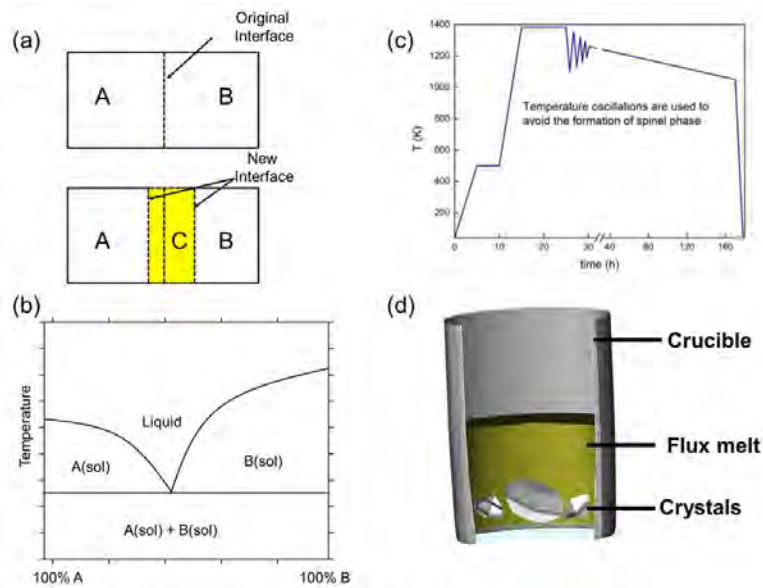


Fig. 3.1 (a) Mechanisms of solid state reactions (b) Lowering of melting point on mixing different constituents (c) Temperature profile in the crystal growth, and (d) Schematics of crystal growth inside a platinum crucible.

flux and other reactants [69]. Sometimes, to avoid some phases, some temperature recycling processes are adopted which suppress the crystallization of that phase [71]. A typical temperature recycling process is shown in Fig. 3.1(c).

**Floating zone crystal growth** Optical floating zone method compared to flux growth is a faster method. In floating zone method, at 10 atm  $O_2$  pressure M-type hexaferrite was prepared [57, 72] and in a recent report Y-type hexaferrite [73] was synthesized. A schematic of optical floating zone method is shown in Fig. 3.2. Two sintered ceramic rods of desired composition, one feed at top and other seed at bottom (see Fig. 3.2) are mounted in a way such that their tips meet at the heating zone. Elliptical mirrors focus heat from halogen lamps to the heating point to melt both the rods in the floating zone. After melting in the zone the rods are moved either up or down in a controlled way and the the melt cools down to form the single crystal. Rods are rotated in same or opposite direction during growth to avoid nonuniform heating. Our trial on Y-type hexaferrites produced M-type hexaferrite. Our speculation is that this may be due to nonavailability of 10 atm of oxygen pressure. Therefore, in this thesis all the samples were prepared by flux method.

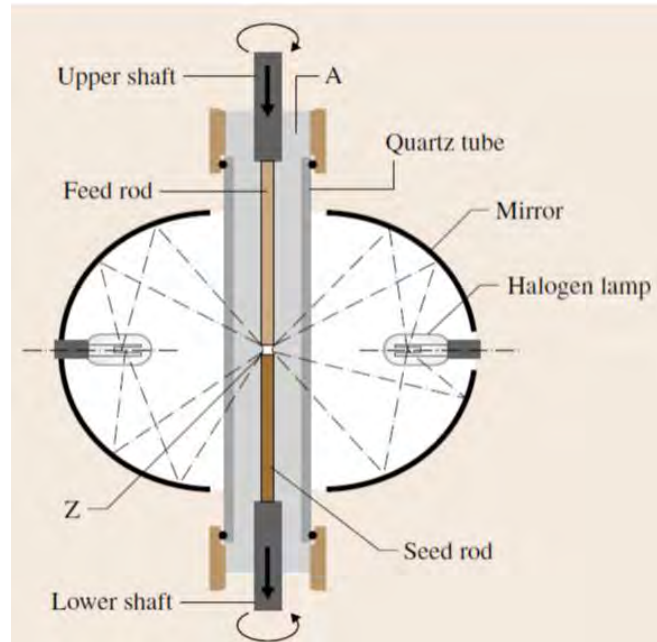


Fig. 3.2 Schematics of an optical floating zone crystal growth chamber from [69].

## 3.2 Measurements of Macroscopic properties

### 3.2.1 DC magnetization

Macroscopic magnetization of the samples was performed using SQUID (Superconducting Quantum Interference Device) magnetometer (Quantum Design Magnetic Property Measurement System MPMS) and VSM (Vibrating Sample Magnetometer) options of a Quantum Design PPMS (Physical Property Measurement System). Either the temperature or the magnetic field is varied in the measurement while keeping the other constant.

**SQUID magnetometer** Underlying principle of a SQUID is a loop with two Josephson junctions, as shown in Fig. 3.3(c), which act as a magnetic flux-to-voltage transducer. The sensitivity is defined by the magnetic flux quantum. In a magnetic property measurement instrument, a SQUID does not determine the magnetic moment directly. The sample is allowed to pass through a series of detection coils of superconducting wires and the current from the detection coils is coupled to the squid sensor, as schematically shown in Fig. 3.3(a) [74]. This type of coil is called second order gradiometer coil, which excludes flux contributions that are constant, and is thus more sensitive to localized moment (*i.e.*, the sample's). A second order gradiometer is more sensitive than a first order gradiometer coil with two coils but is less sensitive than a third order gradiometer coil where four coils are used. A SQUID sensor works as a linear current to voltage converter: change in current in the detection coil is proportional to the change in SQUID output voltage which in turn is proportional to the

magnetic moment in the sample.

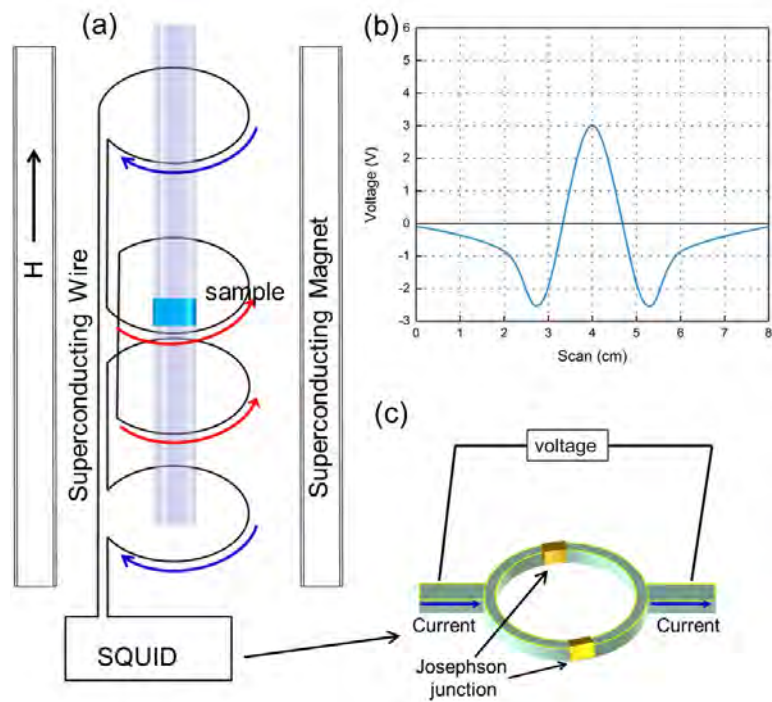


Fig. 3.3 (a) Configuration of SQUID detection coils in a SQUID magnetometer (b) SQUID output voltage as a function of scan length of the sample and (c) DC SQUID with two Josephson Junctions.

As the sample is scanned through the detection coil the magnetic flux changes, and hence the voltage through the detection coil changes. This can be traced as a function of the sample position. The sample moment is then obtained by fitting the response as point-like dipole moments. The SQUID magnetometer used in this study is made by Quantum Design Inc [75]. and is capable of measuring magnetic properties in the temperature range 1.8 K to 400 K in standard setting and up to 800 K with oven option. Magnetic field range is  $\pm 7$  Tesla. Two different options are available: one is DC and the other is RSO (Reciprocating Sample Transport Option). DC measurement is characterized by sample transport in discrete steps while RSO motor oscillates the sample rapidly with a small amplitude of 5 mm. The RSO option is helpful when a very fast measurement is required. SQUID is a very sensitive magnetometer with sensitivity of the order of  $5 \times 10^{-8}$  emu. Samples are mounted to the sample rod by glues with negligible magnetic moment and this does not effect our results as the samples measured have comparatively high magnetic moments.

**VSM option in PPMS** Compared to DC measurement in SQUID magnetometer, Vibrating sample magnetometer (VSM) is a faster measurement option. The sample to be

measured is mounted in between two pick-up coils by a linear motor head. The sample is vibrated with 40 Hz in vertical direction. Change in magnetic moment with vibration induces an electric current in the pick up coil. Lock in technique is used to separate the sample moment from the electrical noise. The instrument used has a sensitivity of about  $10^{-6}$  emu.

### 3.2.2 AC magnetic susceptibility

AC magnetic measurement (ACMS) is a tool to study the magnetization dynamics where the induced moment is a time dependent phenomenon. We used the ACMS option in PPMS, where the sample is centered within the coil and a small external AC field is superimposed on the DC field. This produces a change in moment in the detection coil. The AC moment is given by:

$$M_{AC}(t) = \frac{dM}{dH} H_{AC} \sin(\omega t) \quad (3.3)$$

where,  $H_{AC}$  is the amplitude of the driving field,  $\omega$  is the driving frequency,  $\chi_{AC} = \frac{dM}{dH}$  is the slope of the M-H curve and is called *AC susceptibility*.

From ACMS measurement, information about relaxation process, relaxation time and spin glass nature of the magnetic systems can be studied. The AC susceptibility,  $\chi_{AC}$ , is a complex quantity and can be written as:  $\chi_{AC} = \chi - i\chi'$ . The real part,  $\chi$ , is related to the reversible magnetization process with oscillating magnetic field  $H(t) = H_0 + A \cos 2\pi\omega t$  and the imaginary part,  $\chi'$ , is the irreversible magnetization process, which corresponds to energy absorbed from the field. For phase shift  $\theta$ , magnetization is given as:

$$M(t) = M_0 + \cos(2\pi\omega t - \theta) \quad (3.4)$$

Thus, we can write the values of  $\chi$  and  $\chi'$  as:

$$\chi = m \cos \theta / A \quad (3.5)$$

$$\text{and } \chi' = m \sin \theta / A \quad (3.6)$$

$\chi$  and  $\chi'$  of a sample depend mainly upon the temperature, frequency  $\omega$  and amplitude  $A$  of the driving field. Other parameters such as static bias, applied pressure and other external parameters may also influence it. Compared to DC susceptibility, temperature dependent AC susceptibility gives sharp transition temperature values and it separates out the order disorder transitions from the local short range orderings [76] (which will be discussed in Chapter4).

### 3.3 Scattering theory

Scattering methods of characterization are unique tools to determine the microscopic characteristics of a sample, which in turn give valuable correlation to the macroscopic properties of interest. Scattering theory provides a background to understand the actual scattering process and design experiments. A scattering event is a quantum mechanical event and so should be treated quantum-mechanically. A scattering event for a particular scattering probe with wave function  $\psi$  can be described by the following Hamiltonian, considering only the elastic scattering and ignoring the spin (for details see ref [77]):

$$i\hbar \frac{d\psi}{dt} = \left[ -\frac{\hbar^2}{2m} \Delta^2 + V(\vec{r}) \right] \psi \quad (3.7)$$

$$V(\vec{r}) = 0 \quad \text{except inside the target.}$$

For an incoming plane wave  $\psi_k(\vec{r}) = e^{ikr}$ , the time independent stationary *Schrodinger equation* can be written as:

$$\left[ -\frac{\hbar^2}{2m} \Delta^2 + V(\vec{r}) \right] \psi(\vec{r}) = E \psi_k(\vec{r}) \quad (3.8)$$

The energy  $E$  is given by the plane wave energy  $E_k = \frac{\hbar^2}{2m} k^2$ . We can introduce the Green function  $G_o$  to Eq. 3.8 by defining:

$$\left[ \frac{\hbar^2}{2m} \Delta^2 + E \right] G_o(\vec{r}, \vec{r}' | E) = \delta(\vec{r} - \vec{r}') \quad (3.9)$$

We can consider the function  $\psi_o$  equal to the incoming wave to be the solution for  $V(\vec{r}) = 0$  i.e.,  $\psi_k^{(0)} = \psi_k(\vec{r}) = e^{ikr}$ . This equation can now be transformed to an integral equation, as given below and is called the *Lippmann-Schwinger equation*:

$$\psi_k'(\vec{r}) = \psi_k^{(0)}(\vec{r}) + \int d^3 r' G_o(\vec{r}, \vec{r}' | E) V(\vec{r}') \psi_k'(\vec{r}') \quad (3.10)$$

By defining the boundary condition such that  $\psi_k'(\vec{r})$  is the outgoing scattered wave, Green function is:

$$G_o(\vec{r}, \vec{r}' | E) = -\frac{2m}{\hbar^2} \frac{1}{4\pi} \frac{e^{ik|\vec{r}-\vec{r}'|}}{|\vec{r}-\vec{r}'|} \quad (3.11)$$

$$\text{where } k = \sqrt{\frac{2m}{\hbar^2} E}$$

Since the *Lippmann-Schwinger equation* contains  $\psi_k'$  on both the sides, we make a few approximations for getting non-trivial solution. Let us consider the scattered wave function for zeroth order ( $V = 0$ ) be a plane wave  $\psi_k^{(0)}(\vec{r}) = e^{ik\vec{r}}$ . So the Eq. 3.10 can be written as:

$$\psi_k^{(n+1)}(\vec{r}) = e^{ik\vec{r}} + \int d^3\vec{r}' G_0(\vec{r}\vec{r}' | E) V(\vec{r}') \psi_k^{(n)}(\vec{r}') \quad (3.12)$$

Now, by Born expansion, we get:

$$\psi_k' = \psi_k^{(0)} + \psi_k^{(1)} + \psi_k^{(2)} + \psi_k^{(3)} + \dots \quad (3.13)$$

The first term in the Eq. 3.13 stands for no scattering event, second term represents single scattering event and the rest of the terms represent multiple scattering. The second term is called the *first Born approximation*. In a real scattering event, the distance between scatterers ( $\vec{r}'$ ) is much smaller than the distance ( $\vec{R}$ ) of detectors from the sample. This condition is the *Fraunhofer Approximation*. Experimentally, this far field limit is a good approximation as we place the detector and source at a distance much larger than the volume of the sample. For small volumes of samples multiple scattering can be neglected. Moreover, in soft X-ray resonance diffraction, which is extensively used in our experiments, multiple scattering can be potentially neglected as the scattering is observed from only a few unit cells on the surface. Neglecting multiple scattering from first Born approximation and Fraunhofer approximation for  $|\vec{R}| = |\vec{R} - \vec{r}'|$  and  $\vec{Q} = \vec{k}' - \vec{k}$ , we can approximate Eq. 3.10 as:

$$\psi_k^{(1)}(\vec{r}) = \underbrace{e^{i\vec{k}\vec{R}}}_{\text{Incoming}} + \underbrace{-\frac{2m}{\hbar^2} \frac{1}{4\pi R} e^{ikR} \int e^{i\vec{Q}\vec{r}'} V(\vec{r}') d^3r'}_{\text{Scattered}} \quad (3.14)$$

The second term in Eq. 3.14 represents the scattered wave in the direction of  $\vec{k}'$ . The intensity, collected in the detector place in the direction of  $\vec{k}'$ , is a square of the absolute value of it and is given as:

$$I(\vec{Q}) \propto |F(\vec{Q})|^2 = \left| \frac{m}{2\pi\hbar^2} \int V(\vec{r}) e^{i\vec{Q}\vec{r}} d^3r \right|^2 = |F[V(\vec{r})]|^2 \quad (3.15)$$

$F$  is the Fourier transform of the scattering potential. In most experiments the intensity of the scattered beam is measured and phase information is not measured. Therefore, obtaining scattering potential from the simple inverse Fourier transformation is not possible, and this is referred to as the famous *phase problem*.

Replacing  $\vec{r}'$  to single scattering particles in spatial distribution, we can rewrite Eq. 3.15

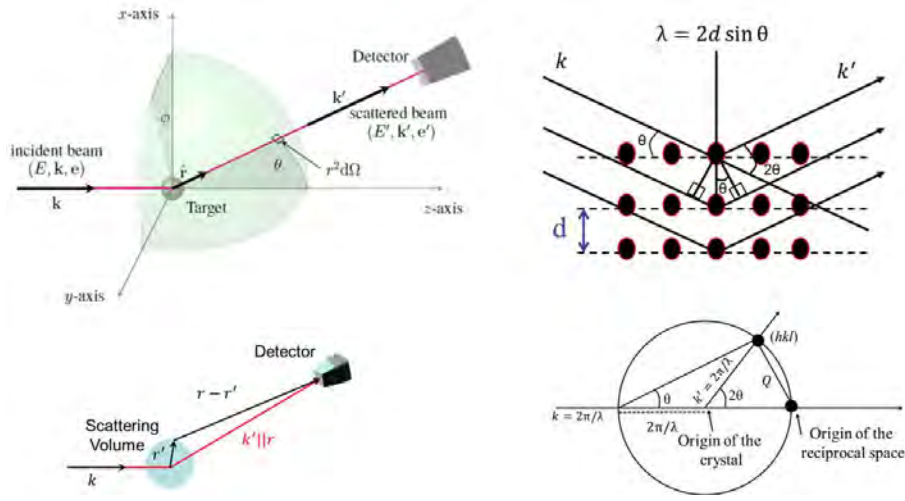


Fig. 3.4 Diffraction [78].

as:

$$\int V(\vec{r}) e^{i\vec{Q}\cdot\vec{r}} d^3 r = \sum_{j=1}^N e^{i\vec{Q}\cdot\vec{r}_j} \int V(\vec{r}') e^{i\vec{Q}\cdot\vec{r}'_j} d^3 r' \quad (3.16)$$

The scattering potential  $V(\vec{r}')$  depends upon the probed material and the radiation used.

**Bragg scattering** For a periodic crystal, the scattering potential is to be invariant under the translation vector  $\vec{t} = u\vec{a}_1 + v\vec{a}_2 + w\vec{a}_3$ , where  $u$ ,  $v$  and  $w$  are integers and  $\vec{a}_i$  are fundamental lattice vectors. Therefore, the scattering potential  $V(\vec{r}) = V(\vec{r} + \vec{t})$  can be expanded as a Fourier series as:

$$V(x) = \sum_{\vec{t}} V_{\vec{t}} e^{i\vec{t}\cdot\vec{x}} \quad (3.17)$$

We can introduce the reciprocal lattice vector  $\vec{G} = h\vec{b}_1 + k\vec{b}_2 + l\vec{b}_3$  and  $\vec{G} \cdot \vec{t} = 2\pi n$  (where,  $n$  is an integer).  $h$ ,  $k$  and  $l$  are integers such that they satisfy for all  $\vec{t}$ , producing plane waves having the same periodicity as that of the concerned Bravais lattice.

The distance between two planes defined by *Miller indices*  $(hkl)$  is related to  $G$  as follows:

$$d_{(hkl)} = \frac{2\pi}{|\vec{G}(hkl)|}$$

The situation  $\vec{G}(hkl) = \vec{Q}(hkl)$ , known as *Laue Condition*, states that scattered intensity can be observed only if the scattering vector  $\vec{Q}$  is equal to a reciprocal lattice vector, and

otherwise averages to zero due to destructive interference from high number of scatterers. For an observed reflection, the scattering amplitudes interfering constructively along the direction of  $\vec{k}'$ , means that the phase factors of the waves scattered at lattice points of the crystal differ only by a factor  $e^{2\pi in}$  along  $\vec{k}'$  (where  $n$  is an integer). Mathematically, we have the famous *Bragg equation* as follows:

$$2d_{(hkl)} \sin \theta = n\lambda$$

where,  $2\theta$  is the angle between the incident and the scattered wave, and  $n$  is the order of reflection.

**Ewald sphere** The condition for appearance of a Bragg reflection can be determined by an *Ewald Sphere*. An Ewald sphere is a imaginary sphere drawn with radius equal to the wave vector  $|k| = 2\pi/\lambda$  and the origin of the crystal as origin of the reciprocal space (as shown in Fig. 3.4(d)). Only those reciprocal lattice points which coincide with the surface of the Ewald sphere give constructive interference and hence, only those reflections are observed.

In a good approximation, the scattered intensity can be calculated by putting atoms in the respective lattice points  $x$ ,  $y$  and  $z$ . The amplitude of the scattered beam can be calculated as a combination of the scattering potential and the atomic position as:

$$F_{(hkl)} = \sum f_a(Q) e^{-2\pi i(hx+ky+lz)} \quad (3.18)$$

where,  $t = x\vec{a}_1 + y\vec{a}_2 + z\vec{a}_3$

$f_a(Q)$  is the atomic scattering factor. This atomic scattering factor is different for different probes as explained in the following sections.

### 3.4 X-ray scattering

Before going to details of x-ray scattering, let us define the scattering geometry and various co-ordinate systems used as shown in Fig. 3.5. The three Cartesian coordinates are along  $U_1$ ,  $U_2$  and  $U_3$  as shown in the Fig. 3.5. Linear polarization in the scattering plane, *i.e.*  $U_1 - U_3$  plane, is defined as  $\pi$  and that perpendicular to the scattering plane is defined as  $\sigma$ . This geometry and nomenclature will be followed in rest of this thesis. Now, we can see the

following relations for the scattering geometry:

$$\hat{U}_1 = (\vec{k} + \vec{k}')/|\vec{k} + \vec{k}'| = (\hat{k} + \hat{k}')/2 \cos \theta$$

$$\hat{U}_2 = (\vec{k} \times \vec{k}')/|\vec{k} \times \vec{k}'| = \hat{k} \times \hat{k}'/\sin 2\theta$$

$$\hat{U}_3 = (\vec{k} - \vec{k}')/|\vec{k} - \vec{k}'| = (\hat{k} - \hat{k}')/2 \sin \theta$$

and

$$\sigma = \hat{U}_2 \quad \sigma' = -\hat{U}_2$$

$$\pi = \hat{U}_1 \sin \theta - \hat{U}_3 \cos \theta \quad \pi' = -(\hat{U}_1 \sin \theta - \hat{U}_3 \cos \theta)$$

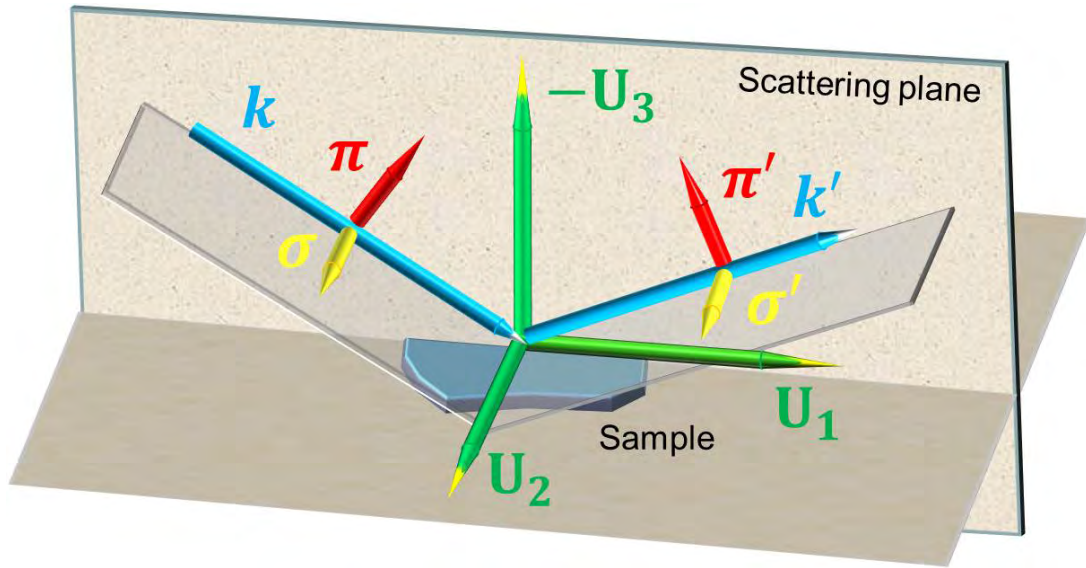


Fig. 3.5 Scattering geometry, coordinate system with polarization.

### 3.4.1 Thomson scattering

The common scattering of x-rays on matter, at not too high energies, can be well described within a simple classical picture called the Thomson scattering. Oscillating electric fields, perpendicular to the propagation direction in electromagnetic radiations, can polarize electrons bound to atoms, in the direction of the electric field of the incoming radiation. This oscillatory motion of the electrons causes emission of electromagnetic radiation with electric field perpendicular to the oscillation of charge (see Fig. 3.6(b)). This type of scattering events are called the *Thomson Scattering*.

Total cross section for the elastic Thomson scattering is found as:

$$\sigma_T = \frac{8\pi}{3} r_0^2$$

where,  $r_0$  is the classical electron radius. Polarization dependence of Thomson scattering is given by the first term in equation 3.25. Intensity is observed in only the  $\sigma \rightarrow \sigma$  and  $\pi \rightarrow \pi$  channels and in the later channel intensity is reduced by a factor of  $\cos 2\theta$ .

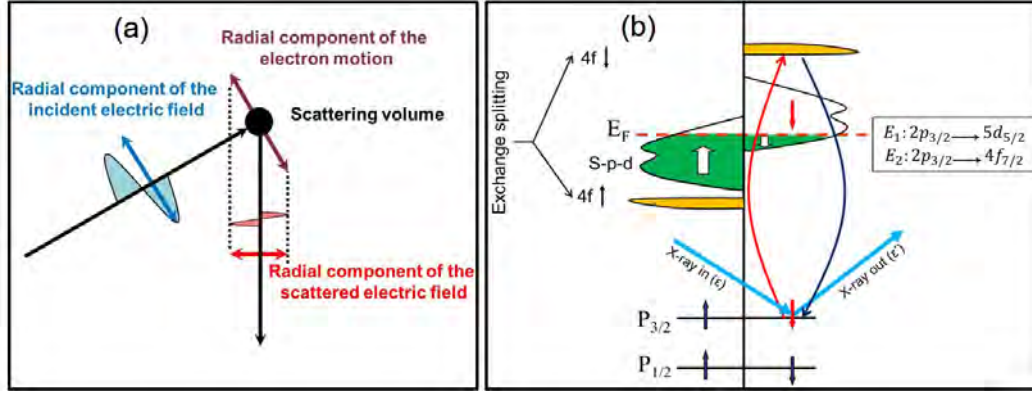


Fig. 3.6 (a) Schematic of Thomson scattering and (b) X-ray resonance scattering.

### 3.4.2 Crystal structure determination: single crystal X-ray diffraction

In any study with single crystals, the preliminary experiment is to solve the crystal structure. Intensity of a reflection ( $hkl$ ) can be calculated by squaring the absolute value of amplitude in Eq. 3.18 by putting atoms in the lattice points. However, for intensity in the detector, we use particle nature of the radiation and the phase information is lost, which is the famous phase problem. The phase problem does not allow us to go back directly from the intensity to crystal structure. Therefore, intensities calculated from a structural model are compared to the experimentally measured intensities and parameters such as atomic positions ( $x, y, z$ ), lattice parameters, isotropic ( $U$ ) and anisotropic ( $U_{ij}$ ) are varied for  $\chi^2$  minimization.  $\chi^2$  is given by:

$$\chi^2 = \sum_i w(hkl)(F_{obs}^2 - F_{calc}^2) \quad (3.19)$$

The quality of the solution is defined by values of the parameters  $R_1$ ,  $wR_2$  and  $Goof$  which are defined below.

$$R_1 = \frac{\sum ||F_{obs}| - |F_{calc}||}{\sum |F_{obs}|} \quad (3.20)$$

$wR_2$  is square of  $F$  values convoluted with refining weighting scheme  $w$ . It is in most cases about double the value of  $R_1$ .  $Goof$  is the goodness of fit for the solution which uses difference in  $R$  values, number of reflections observed and the number of parameters used.  $Goof$  value ideally approaches 1 at the end of refinement.

### 3.4.3 X-ray magnetic scattering

Magnetic scattering by X-rays are of two types based on the principle of interaction. First one is non resonant magnetic scattering, and in the second one the energy of the X-rays used is tuned to the energy required to knock out one electron from a core shell to a shell that contains magnetic information. In non-resonant magnetic scattering, weak  $\approx 10^{-6}$  (compared to Thomson scattering or charge scattering) magnetic signal is overcome by using high brilliance of synchrotron radiation [79–88].

We used resonant magnetic scattering so we will confine our discussion with the resonant process only.

#### Resonant magnetic X-ray scattering

In the photoelectric effect, an electron from core state is excited to an unoccupied state above the Fermi level by tuning the X-ray energy to the corresponding energy difference. The core hole can be filled by various processes, such as fluorescence, or the excited electron can fall back to its original place. This later process, which is coherent, as the state of the atom is unchanged, is called resonant X-ray scattering and is shown in Fig. 3.6(c). In the case of magnetically ordered materials, this resonant scattering may carry the magnetic information as the unoccupied states are spin polarized. To determine the cross section, let us write the total elastic scattering amplitude as:

$$f = f_0 + f' + if'' + f_{spin} \quad (3.21)$$

where,  $f_0 \propto zr_0$  is the Thomson charge scattering amplitude, ( $z$ ) is the atomic number. At the resonance energy, electric dipole ( $\Delta l = 1$ ) and multiple transition ( $\Delta l > 1$ ) contribute through the  $f'$  and  $f''$  terms. For the dominant electric dipole,  $E_1$  transition in the magnetic ion, the coherent resonant elastic scattering amplitude  $f_{EL}^e$  can be written after [82, 85] as:

$$f_{EL}^e(\omega) = \frac{4\pi}{k} f_D \sum_{M=-L}^L \left[ \hat{\epsilon}'^* \cdot Y_{LM}^{(e)}(\vec{k}') Y_{LM}^{(e)*}(\vec{k} \cdot \hat{\epsilon}) \right] F_{LM}^{(e)}(\omega)$$

where,

$Y_{LM}^{(e)}$  = vector spherical harmonics

$f_D$  = Debye-Waller factor and

$$F_{LM}^{(e)} = \sum_{a,n} \left[ \frac{p_a p_a(n) \Gamma_x(aMn; EL) / \Gamma(n)}{x(a, n) - i} \right]$$

$\hat{\epsilon}$  and  $\hat{\epsilon}'$  are the unit vectors in polarization directions of electric field for incoming and scattered photons.  $F_{LM}^{(e)}$  determines the strength of resonance.  $p_a$  is the probability of an ion to exist in an initial state  $|a\rangle$  and  $p_a(n)$  is the probability of transition to a final state  $|n\rangle$ .  $F_{LM}^{(e)}$  depends upon probability of transition  $P_a(n)$  from initial state  $|a\rangle$  to a final state  $|n\rangle$  and probability  $p_a$  of the ion existing in the initial state, which in turn depends upon the overlap integral between both the states (for details see [85]).

The ratio  $\Gamma_x/\Gamma$  is the partial line width of the excited state due to a pure electric dipole radiative decay for all radiative and non-radiative processes. The Debye-Waller factor  $f_D$  is the  $Q$  dependent thermal parameter. These transitions are magnetically sensitive because of the difference in occupation of the minority and majority bands in exchange split bands, where the excited state  $|n\rangle$  lies. Resonance occurs at the absorption edges of the elements and this enhances the intensity of magnetic reflections. The strength of the enhancements are tabulated in Table 3.1 [82, 89, 90].

Table 3.1 Resonance enhancement of scattering amplitude for some elements. Weak =1, medium =  $10^2$  and strong  $> 10^3$

Elements	Edge	Transition	Energy range(KeV)	Resonance strength	Comment
3d	K	1s $\rightarrow$ 4p	5-9	weak	small overlap
3d	$L_I$	2s $\rightarrow$ 3d	0.5-1.2	weak	small overlap
3d	$L_{II}, L_{III}$	2p $\rightarrow$ 3d	0.4-1.0	strong	dipolar, large overlap, high spin polarization of 3d
4f	K	1s $\rightarrow$ 4p	40-63	weak	small overlap
4f	$L_I$	2s $\rightarrow$ 5d	6.5-11	weak	small overlap
4f	$L_{II}, L_{III}$	2p $\rightarrow$ 5d 2p $\rightarrow$ 4f	6-10	medium	dipolar, quadrupolar
4f	$M_I$	3s $\rightarrow$ 5p	1.4-2.5	weak	small overlap
4f	$M_{II}, M_{III}$	3p $\rightarrow$ 5d 3p $\rightarrow$ 4f	1.3-2.2	medium to strong	dipolar, quadrupolar
4f	$M_{IV}, M_V$	3d $\rightarrow$ 4f	0.9-1.6	strong	dipolar, large overlap, high spin polarization of 4f
5f	$M_{IV}, M_{II}$	3d $\rightarrow$ 5f	3.3-3.9	strong	dipolar, large overlap, high spin polarization of 5f

From the Table 3.1, following broad observations about resonant enhancement can be made:

1. Resonance enhancement depends upon the magnitude of the transition matrix elements.  $\Delta l = 1$  dipole transitions are stronger than the  $\Delta l = 2$  quadrupole transitions.

Transitions from  $s$ -core levels to non- $s$  higher levels exhibit small resonance as the overlap between the wave functions are small.

2. Differences between occupations of the majority and minority carriers in the exchange split bands above Fermi level also influence resonance enhancement. For example, in first rare earth elements, because of small exchange splitting in the spin polarized  $5d$  bands compared to  $4f$  bands,  $2p \rightarrow 5d$  dipole transition is weaker than that of  $2p \rightarrow 5f$  quadrupole transition.
3. Spin orbit coupling strength in ground and excited states.

Let us consider the  $L_3$  edge of  $\text{Fe}^{3+}$  high spin ion, *i.e.*  $2p_{3/2} \rightarrow 3d$  transition. Vector spherical harmonics can written as [85]:

$$\begin{aligned}
 &\text{For } L = 1 \text{ and } M = \pm 1 \\
 &\left[ \hat{\epsilon}'^* \cdot Y_{1\pm 1}^{(e)}(\hat{k}') Y_{1\pm 1}^{(e)*}(\hat{k}) \hat{\epsilon} \right] = (3/16\pi) \left[ \hat{\epsilon}' \cdot \hat{\epsilon} \mp i(\hat{\epsilon}' \times \hat{\epsilon}) \cdot \hat{z}_n - (\hat{\epsilon}' \cdot \hat{z}_n)(\hat{\epsilon} \cdot \hat{z}_n) \right] \\
 &\text{For } L = 1 \text{ and } M = 0 \\
 &\left[ \hat{\epsilon}'^* \cdot Y_{10}^{(e)}(\hat{k}') Y_{10}^{(e)*}(\hat{k}) \hat{\epsilon} \right] = (3/8\pi) \left[ (\hat{\epsilon}' \cdot \hat{z}_n)(\hat{\epsilon} \cdot \hat{z}_n) \right]
 \end{aligned} \tag{3.22}$$

Here  $\hat{z}_n$  is a unit vector in the direction of magnetic moment of the  $n^{\text{th}}$  atom. So, by combining both these equations and for charge scattering we can write the amplitude as:

$$f_{nE1}^{XRMS} = \left[ (\hat{\epsilon}' \cdot \hat{\epsilon}) F^0 - i(\hat{\epsilon}' \times \hat{\epsilon}) \cdot z_n F^{(1)} + (\hat{\epsilon}' \cdot \hat{z}_n)(\hat{\epsilon} \cdot \hat{z}_n) F^{(2)} \right] \tag{3.23}$$

Here,  $F^0$  term is the charge scattering term as defined earlier. The second term  $F^{(1)}$ , which is linear in magnetic moment component, contributes towards the first harmonic magnetic satellite and the second term  $F^{(2)}$ , which is quadratic in magnetic moment component, contributes towards the second harmonic magnetic satellites. We can define three unit vectors  $z_1, z_2$  and  $z_3$  parallel to the Cartesian co-ordinate axes  $U_1, U_2$  and  $U_3$  representing magnetic moment component of the  $n^{\text{th}}$  atom. Now we can write the terms of Eq. 3.23 in a  $2 \times 2$  matrix as follows:

$$f_{nE1}^{XRMS} \rightarrow \begin{vmatrix} \sigma \rightarrow \sigma & \pi \rightarrow \sigma \\ \sigma \rightarrow \pi & \pi \rightarrow \pi \end{vmatrix}$$

In the following equation all the terms in the matrices are of this above mentioned format

e.g.  $\sigma \rightarrow \pi$  represents incoming  $\sigma$  polarized photon and scattered  $\pi$  polarized photon.

$$f_{nE1}^{XRMS} = F^{(0)} \begin{vmatrix} 1 & 0 \\ 0 & \cos 2\theta \end{vmatrix} - iF^{(1)} \begin{vmatrix} 0 & z_1 \cos \theta + z_3 \sin \theta \\ z_3 \sin \theta - z_1 \cos \theta & -z_2 \sin 2\theta \end{vmatrix} + F^{(2)} \begin{vmatrix} z_2^2 & -z_2 [z_1 \sin \theta - z_3 \cos \theta] \\ z_2 [z_1 \sin \theta + z_3 \cos \theta] & -\cos^2 \theta [z_1^2 \tan^2 \theta + z_3^2] \end{vmatrix} \quad (3.24)$$

The first sub matrix, as discussed earlier, represents charge scattering and the other two matrices contain magnetic information. Following observations can be made on the above equation:

- Linear in the components of magnetization term, *i.e.* the second term contributes towards the magnetic satellite  $\vec{r}$ . It produces the first harmonic satellite. Second quadratic in magnetic moment component term  $F^{(2)}$  contributes towards second harmonic satellite as well as towards the charge Bragg peak. For ferromagnets, both the terms contribute to allowed charge reflections.
- With the help of linearly polarized synchrotron radiation and careful selection of scattering geometry, magnetic moments in all directions can be probed.
- Scattering angle depends on Bragg angle, therefore, by analyzing different reflections (if accessible) validity of a particular model can be tested.

Let us now consider the magnetic structure factor for dipole resonant magnetic scattering for the first harmonic satellite:

$$F^{XRMS} = \sum f_{nE1}^{XRMS} e^{iQr} \quad (3.25)$$

Intensities can be calculated by taking the absolute square value of the structure factors  $F^{XRMS}$ .

**Circular dichroism** The intensity in circular polarization without polarization analysis of outgoing beam is given by [9] by the following equation:

$$I_{\chi}^{XRES} = \frac{1}{2} [I_{\sigma \rightarrow \sigma} + I_{\sigma \rightarrow \pi} + I_{\pi \rightarrow \sigma} + I_{\pi \rightarrow \pi}] + \chi \text{Im} [F_{\pi \rightarrow \sigma}]^* [F_{\sigma \rightarrow \sigma}] + [F_{\sigma \rightarrow \pi}] [F_{\pi \rightarrow \pi}] \quad (3.26)$$

where,  $\chi$  is  $\pm 1$  for  $P$  and  $M$  polarizations.

This intensity is measured when we use either of the  $P$  and  $M$  polarizations of the incoming beam. This intensity contains the contribution from the intensities in the linear channels also. The difference between these two intensities gives the absolute circular dichroism. To normalize it, we divide it by the sum. The difference of  $P$  and  $M$  corresponds to only

the imaginary part of the cross terms  $[\overline{F_{\pi \rightarrow \sigma}}][F_{\sigma \rightarrow \sigma}] + [F_{\sigma \rightarrow \pi}][\overline{F_{\pi \rightarrow \pi}}]$ , whereas their sum is independent of the cross terms and is the total intensity in the linear channels, as can be seen from the following equation:

$$\begin{aligned} I(p) - I(M) &= 2 * \text{Im}([F_{\pi \rightarrow \sigma}]^* [F_{\sigma \rightarrow \sigma}] + [F_{\sigma \rightarrow \pi}] [F_{\pi \rightarrow \pi}]^*) \\ &= 2 * \text{Im}[F_{\sigma \rightarrow \pi}] [F_{\pi \rightarrow \pi}]^* \quad ; \text{since } [F_{\sigma \rightarrow \sigma}] = 0 \end{aligned}$$

After separating out only the imaginary part, we have:

$$I(p) - I(M) = 2 * ([F_{\sigma \rightarrow \pi}] [F_{\pi \rightarrow \pi}]^* - [F_{\sigma \rightarrow \pi}]^* [F_{\pi \rightarrow \pi}]) \quad (3.27)$$

Now we define the relative circular dichroism (Rel\_Circ) as follows:

$$\begin{aligned} \text{Rel\_Circ} &= I_{\chi}^{\text{rel}} = \frac{(I(p) - I(M))}{(I(p) + I(M))} \\ &= \frac{2 * ([F_{\sigma \rightarrow \pi}] [F_{\pi \rightarrow \pi}]^* - [F_{\sigma \rightarrow \pi}]^* [F_{\pi \rightarrow \pi}])}{[I_{\sigma \rightarrow \sigma} + I_{\sigma \rightarrow \pi} + I_{\pi \rightarrow \sigma} + I_{\pi \rightarrow \pi}]} \end{aligned} \quad (3.28)$$

This equation 3.28 will be used for the calculation of circular dichroism.

**Linear dichroism** For the calculation of linear dichroism we used the following equation:

$$\text{Rel\_lin} = \frac{I_{\pi \rightarrow \sigma} - I_{\sigma \rightarrow \pi}}{I_{\pi \rightarrow \sigma} + I_{\sigma \rightarrow \pi}} \quad (3.29)$$

Experimentally, we measured the following parameters:

$$I_{in,\pi,\sigma}^L = \frac{(I_{\pi \rightarrow \sigma} + I_{\pi \rightarrow \pi}) - I_{\sigma \rightarrow \pi}}{I_{\pi \rightarrow \sigma} + I_{\sigma \rightarrow \pi} + I_{\pi \rightarrow \pi}} \quad (3.30)$$

### 3.4.4 Different scans used

In a typical X-ray diffraction experiment we look through the reciprocal space and collect the intensity in the detector. The intensity detected in the detector depends upon the type of scans we used. We used the following rotational degrees of freedom in our experiments and these are depicted in Fig. 3.7:

- **$\omega - 2\theta$  scans:** It is also the  $(00l)$  scan in our experiment, where we scan through the specular line along Q, moving both  $\omega$  and the detector angle  $2\theta$  proportionally and simultaneously. This is longitudinal scan and probes reciprocal space parallel to Q.
- **$2\theta$  scan:** In this scan, at a particular value of  $\omega$ , detector angle is scanned for a particular Q.

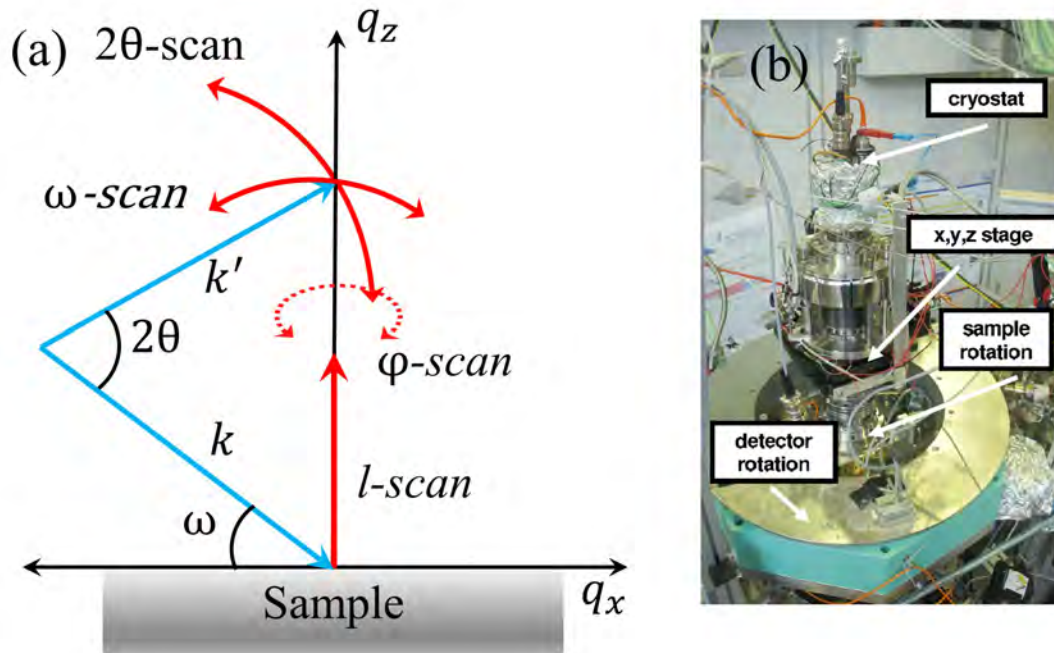


Fig. 3.7 (a) Different scans used to measure the reciprocal lattice vector length and intensity (b) Two permanent end-stations, the XUV diffractometer and the high-field diffractometers in the UE46\_PGM-1 beamline.

- **Rocking curve:** Here,  $\omega$  is scanned keeping the detector angle constant.
- **Energy scan at fixed  $Q$ :** Here, energy is scanned, with the value of  $Q$  fixed, by simultaneously moving the  $\omega$  and  $2\theta$  corresponding to the  $Q$ .

In the low  $Q$   $l$ -scans polarization dependence of specular reflectometry contribution may be significant, which in turn depends upon the magnetization components in plane and out of plane.

### 3.5 Experimental set-up for soft X-ray diffraction

Experimental set up for soft X-ray resonance diffraction used is the UE46\_PGM-1 beamline of BESSY-II (Helmholtz Zentrum Berlin), which is one of two beamlines situated at the elliptical undulator UE46 of BESSY-II. It has the capability of tuning the polarization of the incoming beam, the linear as well as circular, in the energy range 120 eV to 2000 eV. Polarization analysis of scattered beam is not performed in any of the experiments. Two permanent end-stations, the XUV diffractometer and the high-field diffractometer, are used in our experiments (see Fig. 3.7(b)).

Most of the zero field diffraction studies were carried out in the XUV diffractometer. The XUV diffractometer end-station is a UHV-compatible two-circle diffractometer with

horizontal scattering geometry and permits movement of  $\omega$  and  $2\theta$  with the highest accuracy and stability. It is versatile for high quality diffraction experiments over the entire angular range of the detector in the temperature range from 4 K to 320 K. A XUV100-type photodiode point detector is used with a set of changeable slits in the front for optimizing the q-resolution. The detector can be scanned in vertical direction also to compensate possible Chi-misalignment. The beam spots used are varied from experiment to experiment and is mentioned in respective sections.

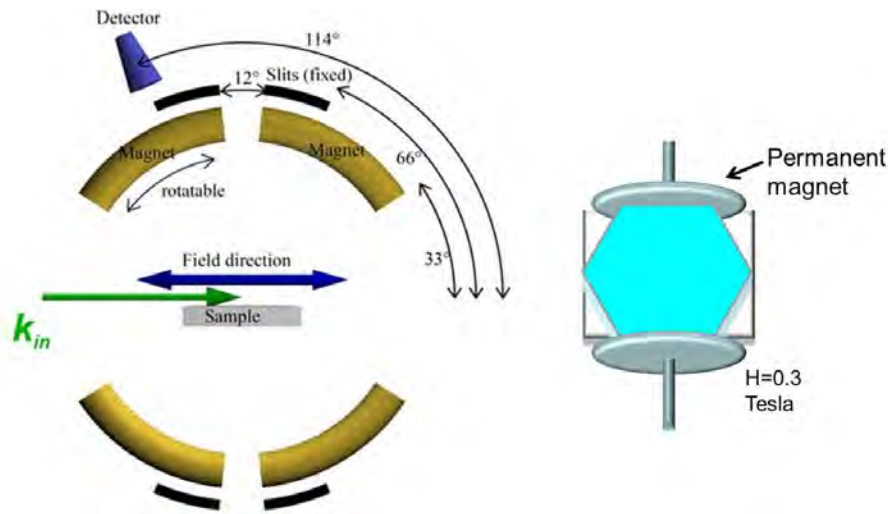


Fig. 3.8 *Left*: Schematic of high field chamber with the openings of the magnets. *Right*: Schematic of permanent magnet assembly in the zero field chamber.

The high-field diffractometer end-station is equipped with a horizontal magnet capable of generating fields up to 7 Tesla and temperatures down to 4 K. Therefore, it is a suitable source to study metamagnetic transitions in solids. In the end-station there is a superconducting coil for magnetic field that can be rotated independent of the sample. Out of the dark angles in the magnet, there are four openings which cover detector angles  $66^\circ$  and  $12^\circ$  in  $2\theta$ . The magnet can be rotated by  $33^\circ$  to use this whole  $66^\circ$  of detector angles (see Fig. 3.8).

In the XUV diffractometer we used two permanent magnets as shown in the right side of Fig. 3.8. In this case, the sample is mounted in between two permanent magnets with an applied strength of 0.3 Tesla at the center of the sample and it is fixed by screw assembly. Diffractions are performed through the openings of the screw assembly.

### 3.6 Neutron scattering

Neutrons are subatomic elementary particles with mass  $m_N = 1.675 \times 10^{-24}$  kg, whose wave length ( $\lambda$ ) is given by de Broglie wave particle duality ( $\lambda = h/\sqrt{2mE}$ );  $E$  is the kinetic

energy. A neutron is a spin 1/2 particle with magnetic moment  $-1.91 \mu_N$  making it additionally sensitive to magnetic environment in the sample. The scattering potential  $V_n(\vec{r})$  for a neutron can be expressed as a sum of nuclear ( $V_N(\vec{r})$ ) and magnetic ( $V_M(\vec{r})$ ) contribution.

**Nuclear scattering** For a neutron of  $\approx 25$  meV kinetic energy and mass  $m_N$  the wave length is  $\approx 1$  Å. In Nuclear scattering neutrons interact with the nucleus of the atoms via the nuclear forces. The potential  $V_N(\vec{r})$  is Fermi pseudo potential. For a single particle it can be written as  $b_j \delta(r - r_j)$ . Here, for a nucleus  $j$ , located at position  $r_j$ ,  $b_j$  is the scattering length of the nucleus and  $\delta$  is the Dirac delta function. Using Fermi pseudo potential for a crystal the nuclear scattering the scattering potential can be written as the sum of individual nuclear interaction [91] :

$$V_N(\vec{r}) = \frac{2\pi\hbar^2}{m_N} \sum_j b_j \delta(\vec{r} - \vec{r}_j) \quad (3.31)$$

In contrast to x-ray scattering the form factor for nuclear neutron scattering is independent of  $Q$ , as the nucleus is much smaller compared to electron clouds and the scattering amplitude can be written as:

$$N(\vec{Q}) = \sum_j b_j \cdot e^{i\vec{Q}\vec{r}_j} \quad (3.32)$$

The value of  $b_j$  is different for same atoms with different isotopes. A list of neutron scattering length for different elements and isotopes can be found here [92]. To account for different distribution of different isotopes in nature we have to consider the average isotope distribution [93]. So the differential scattering cross section can be written as

$$\frac{d\sigma}{d\Omega} = \left\langle \sum_j b_j e^{i\vec{Q}\vec{r}_j} b_j^* e^{-i\vec{Q}\vec{r}_j} \right\rangle = \langle b \rangle^2 \left| \sum_j e^{i\vec{Q}\vec{r}_j} \right|^2 + N \langle (b - \langle b \rangle)^2 \rangle \quad (3.33)$$

Only the first term in Eq. 3.33 contains phase information (coherent scattering) and the second term is the incoherent scattering term contributing to the isotropic background.

**Magnetic scattering** The intrinsic magnetic moment of a neutron  $\mu_N$  makes it possible to interact with the magnetic field produced by unpaired electrons in atoms. The magnetic scattering potential ( $V_M = -\vec{\mu}_N \cdot \vec{B}$ ) for neutron is due to interaction with spin ( $\vec{B}_{spin}$ ) and unquenched orbital ( $\vec{B}_{orbital}$ ) moments. In the scattering process a neutron changes its spin moment in its quantization axis  $z$  from  $\sigma_z$  to  $\sigma_z'$  ( $\sigma$  is spin operator) as wave vector changes from  $k$  to  $k'$ . The magnetic scattering cross section can be expressed as below: (for further

details see [94] )

$$\frac{d\sigma}{d\Omega} \propto \left| -\frac{1}{2\mu_B} \langle \sigma_z' | \hat{\sigma} \cdot \vec{M}_\perp(\vec{Q}) | \sigma_z \rangle \right|^2 \quad (3.34)$$

Only  $\vec{M}_\perp(\vec{Q})$  contributes to magnetic scattering.  $\vec{M}_\perp(\vec{Q})$  is the Fourier transformed magnetization component perpendicular to  $\vec{Q}$ .

$$\begin{aligned} \vec{M}_\perp(\vec{Q}) &= \hat{Q} \times \vec{M}(\vec{Q}) \times \hat{Q} \\ \vec{M}(\vec{Q}) &= \int \vec{M}(\vec{r}) e^{i\vec{Q} \cdot \vec{r}} d^3r \\ \vec{M}(\vec{r}) &= \vec{M}_S(\vec{r}) + \vec{M}_L(\vec{r}) \end{aligned} \quad (3.35)$$

In contrast to nuclear scattering magnetic scattering of neutron has a form factor. In most of the transition metal compounds orbital magnetic moment is quenched. Contributions to  $\vec{M}(\vec{Q})$  is only from the spin part.

$$\begin{aligned} \vec{M}(\vec{Q}) &= -2\mu_B \cdot f_m(\vec{Q}) \sum_i e^{i\vec{Q} \cdot \vec{r}_i} \cdot \vec{S}_i \\ f_m(\vec{Q}) &= \int_{atom} \rho_s(\vec{r}) e^{i\vec{Q} \cdot \vec{r}} d^3r \end{aligned} \quad (3.36)$$

$f_m$  is the magnetic form factor which is the Fourier transformation of the spin density  $\rho_s$  distribution of a single atom. The magnetic scattering takes place at the outer unpaired electrons, so form factor falls with  $\vec{Q}$  similar to X-ray scattering. However, in magnetic scattering contributions are from only unpaired outer shell electrons whereas in x-ray all electrons contribute. The form factor fall is much faster in neutron magnetic scattering compared to that of X-ray scattering.

### 3.6.1 TriCS

The single-crystal diffractometer TriCS at the Swiss Continuous Spallation Source (SINQ) is used to carry out temperature dependent neutron diffraction experiments. TriCS is installed at the Swiss spallation neutron source (SINQ) at the Paul Scherrer Institute (PSI, Villigen, Switzerland). TriCS is designed for investigations of commensurate and incommensurate crystal and magnetic structures as well as phase transitions driven by temperature, magnetic field or pressure. The flux is  $\approx 1.02 \times 10^5$  n/cm<sup>2</sup> sec.

### 3.6.2 E-4: 2-Axis-Diffractometer

The E-4 2-axis diffractometer is installed at research reactor BER II of Helmholtz-Zentrum Berlin für Materialien und Energie Hahn-Meitner-Platz-1. The instrument is primarily suited for magnetic structure determination under various conditions. This includes magnetic fields up to 17 T and temperatures down to 30 mK. The monochromator shielding is at  $2\theta_M = 42.5^\circ$  most of the time. This position corresponds to the incident wavelength of 0.244 nm. We used only the vertical field as our interested reflections are in the dark angle range caused by the magnets in horizontal field geometry. The field values of the superconducting magnets have considerable error bars at lower field values which will be discussed in experimental results section.

# Chapter 4

## Crystal growth and macroscopic characterization

### 4.1 Crystal growth

As described in the previous chapter, we have used flux growth technique for synthesizing our single crystals (see section 3.1.2). To obtain high quality single crystals by flux method, steady-state slow-cooling is very much needed to be maintained during crystal growth. M-type hexaferrite single crystals are prepared extensively by using different fluxes. Even floating zone method is also used [57]. In fact, only M-type hexaferrites have been reported to be prepared by floating zone method. Small crystals were prepared from molten salts of 1:1 NaCl and KCl mixtures [95]. Altogether different fluxes are used for preparing hexaferrite single crystals like BaO-B<sub>2</sub>O<sub>3</sub> [60, 96, 97], PbO [98], BaCl<sub>2</sub> [99], Bi<sub>2</sub>O<sub>3</sub> [100], PbO-PbF<sub>2</sub> [98], PbO-B<sub>2</sub>O<sub>3</sub> [101, 102], Na<sub>2</sub>O-B<sub>2</sub>O<sub>3</sub> [103]. In most of the reports, Na<sub>2</sub>O-Fe<sub>2</sub>O<sub>3</sub> flux was preferred over other fluxes [104–109].

For M-type hexaferrite it was found that 20 to 26.3 mole% of Na<sub>2</sub>O and 10 to 20 mole% of BaO are a good starting composition for crystal growth [105]. Here, Na<sub>2</sub>O and Fe<sub>2</sub>O<sub>3</sub> act as flux, with the latter one acting as self flux as it participates as a reactant for crystal growth. With NaFeO<sub>2</sub>, flux content plays a vital role in the type of crystal formed as major product. As shown in the Table 2.1, other hexaferrites can be built by three constituents: M-type hexaferrite, Y-type hexaferrite and the spinel blocks. In most of our experiments, Y-type and M-type hexaferrites are the most favored phases.

It was found that for BaO:*Me*O ratio of 1:1 with 30 mole% or more NaFe<sub>2</sub>O<sub>4</sub> instead of Fe<sub>2</sub>O<sub>3</sub>, only spinel phase *Me*Fe<sub>2</sub>O<sub>4</sub> is formed [110]. Therefore, we tried to avoid this composition. For the synthesis of Y-type single crystals, the best Y-type hexaferrite was reported to be below 5 % of flux content [110] (see Fig. 4.1). Out of the different hexaferrites, the

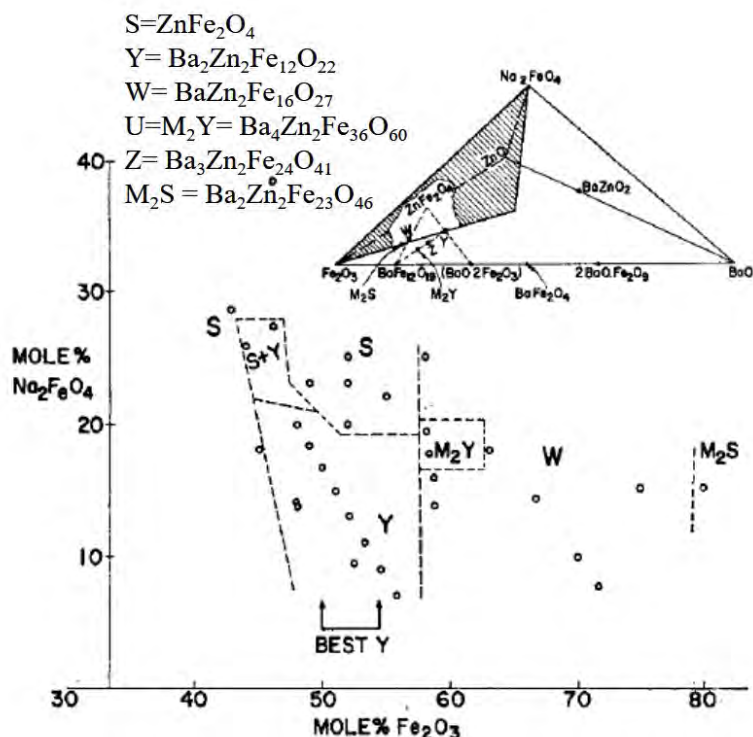


Fig. 4.1 BaO:ZnO = 1:1 plane single crystal fields. Inset shows the composition tetrahedron for BaO:ZnO plane. From: [110].

BaO:MeO ratio determines which hexaferrite will crystallize in the growth process [111]. All these hexaferrites lie very close to each other in the compositional tetrahedron as can be seen from the inset of Fig. 4.1. Therefore, they are thermodynamically and kinetically very close to each other in single crystal synthesis. From previous reports, the following observations can be made regarding the factors determining the type of hexaferrite going to crystallize from NaFeO<sub>2</sub> flux:

- BaO:MeO ratio.
- Type of Me atom[96].
- Temperature from which slow cooling down takes place[105].
- Amount of NaFeO<sub>2</sub> flux used.

Y-type hexaferrites have BaO and MeO ratio of 1:1. For this initial composition of 1:1, Tauber *et al.* studied the growth of Y-type hexaferrite [110] using NaFeO<sub>2</sub> flux. They found that Y-type hexaferrites are major product only in a very narrow range of 5 mole% of Fe<sub>2</sub>O<sub>3</sub>. Small ZnFe<sub>2</sub>O<sub>4</sub> crystals or polycrystalline powders were the by-product in most

of the cases. For high flux concentration, but lower than 30% (mole) and low  $\text{Fe}_2\text{O}_3$ , good quality crystals were found. The window for Y-type crystal is different for different  $Me$  ( $\text{Zn}^{2+}$ ) ions. To avoid the spinel phase, a temperature cycling process with rapid cooling and heating was found to be helpful [71].

In all our syntheses, Ba: $Me$  ratio is maintained to be 1:1 for Y-type hexaferrite. Momozawa also found that in the case of partial substitution of Ba by Sr, viscosity increases with Sr content and, nucleation temperature decreases for both high and low values of Sr content.

We used a platinum and a platinum-rhodium crucible for the crystal growth. Respective reactants and flux are mixed together, after weighing, by grinding using a mortar pestle, followed by ball-milling. A Nebertherm furnace is used for programmable cooling during the growth. Cooling rates ranging from  $1^\circ\text{C}$  to  $2^\circ\text{C}$  per hour are used for the synthesis.

We used  $\text{NaFeO}_2$  as self flux in our synthesis. Starting materials are mixed properly by grinding in a mortar followed by ball milling for 12 hours. The final mixture is placed in the platinum crucible and heated to a temperature above the melting point. After temperature recycling, as explained in section 3.1.2, it is slowly cooled to certain low temperature ( $\approx 950^\circ\text{C}$ ) and then to room temperature. The compositions listed in Table 4.1 are used for the synthesis.

Table 4.1 Composition of starting materials used for crystal growth (composition in mole%), details parameters can be found in Appendix-A.

$\text{BaCO}_3$	$\text{SrCO}_3$	$\text{ZnO}$	$\text{Fe}_2\text{O}_3$	$\text{Na}_2\text{CO}_3$	$\text{Co}_3\text{O}_4$	$\text{NiO}$	Code
9.845	9.845	19.69	53.61	7.01			BZY-1
3.938	15.752	19.69	53.61	7.01			BZY-2
5.907	13.783	19.69	53.61	7.01			BZY-3
2.04	10.02		59.18	20.41		8.16	BNZ-1
3.938	15.752		53.61	7.01	19.69		BCZ-1

### 4.1.1 Sample preparation results

Single crystals are formed at different places of the crucible, ranging from the center to the side walls. Therefore, nucleation centers can be considered to be on the walls of the crucible. While using a crucible of Pt-Ir alloy, it was found that the flux overflows through the wall of the crucibles. This could be due to higher affinity of the flux to stick to the walls and then overflow due to capillary action. The first three compositions listed in Table 4.1 were targeted for Y-type hexaferrite as reported in [71]) and we obtained single crystals of Y-type with various sizes. For BZY-1,  $6\text{mm} \times 4\text{mm} \times 4\text{mm}$  size was obtained. For BZY-2 and BZY-3, most of the crystals were plate like, and the biggest one was found to be  $10\text{mm} \times$

8mm × 2mm. All the hexaferrites are found to be flat plate type with  $[0\ 0\ 1]$  perpendicular to the flat surface.

Recently, Z-type hexaferrite was found to show magneto-electric properties at room temperature in polycrystalline materials [58]. With the only available single crystal growth reported, four state memory at room temperature was seen [59]. Therefore, we attempted the synthesis of Z-type single crystals. Attempt to prepare Z-type hexaferrite with Co (BCZ-1) and Ni (BNZ-1) failed as preliminary X-ray investigations found the formed crystals to be of M-type hexaferrites. Compositions for Z-type hexaferrites were taken from ref [111]. Z-type hexaferrites, as mentioned in Section 2.4, consist of alternating blocks of 1/3 of Y-type and 1/2 of M-type hexaferrites, stacked one above the other (see Fig. 2.17). Therefore, we believe that further fine tuning of thermodynamic and kinetic parameters with more experiments are necessary to synthesize Z-type hexaferrites.

Samples with code BZY-1, BZY-2 and BZY-3 are used for further characterization. Single crystals are seen as shiny black plate-like  $(0\ 0\ 1)$  facets buried inside the crucible. Hot dil.  $\text{HNO}_3$  is used to get the crystals out of the crucible. In certain cases, concentrated  $\text{HNO}_3$  is used (65-70%) and heated to 60° C. Some photographs of as grown crystals are shown in Fig. 4.2

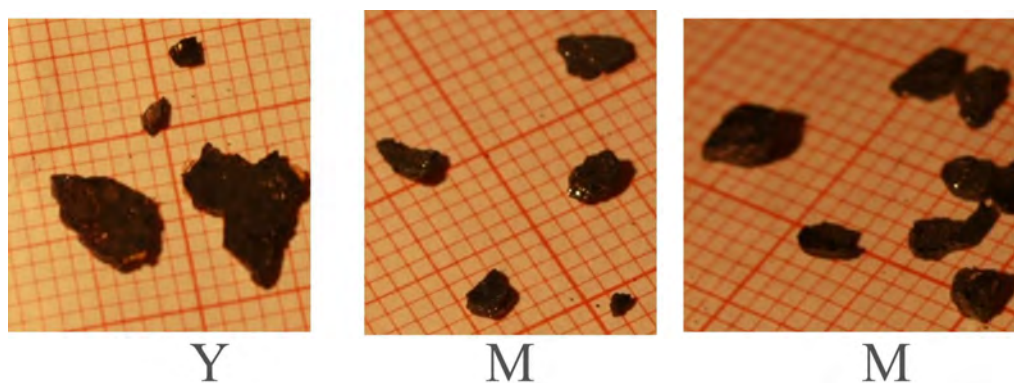


Fig. 4.2 Some of the as grown crystals with  $[0\ 0\ 1]$  perpendicular to the plane of the paper.

## 4.2 Single crystal X-ray diffraction

After the synthesis of the crystals, primary characterization was performed for phase purity and crystal structures were determined. Single crystals were cleaved for a microscopic part for use in single crystal X-ray diffraction studies in the supernova single crystal diffractometer from Rigaku. Following the data reduction, in the CrysAlis<sup>pro</sup> [112], refinement of the structure is performed using JANA2006 [113].

From the previous refinement studies it was found that Zn atoms are located in two

tetrahedral sites [63, 64]. Therefore, we restricted Zn in our refinement to only 6c tetrahedral sites.

From single crystal X-ray diffraction, refinement compositions are found out to be as shown in Table 4.2. The Sr composition ( $x$ ) given in the reactant mixture is different from that found from the refinement of X-ray diffraction. These types of differences were reported previously also [5]. Therefore, for the precise determination of  $x$ , we need to depend upon the composition from refinement rather than predicting it from the composition initially used in the reactant mixture. Discrepancies, in the value of  $x$ , may arise with results from other studies also. Therefore, we compared the values from only those previous studies where compositions were taken from refined data of scattering studies.

$\text{Zn}^{2+}$  is restricted in two tetrahedral sites with Wyckoff position 6c in our refinement. Zn(1) is partially occupied by Fe(1) and, Zn(2) by Fe(2). The occupations are found to vary with  $x$ . The occupancies of Zn, defined as  $\gamma$ , in the 11<sup>th</sup> layer (*i.e.* Zn(2)) decreases as  $x$  increases (see Fig. 2.18). In the earlier studies, no clear trend was observed for  $\gamma$  with  $x$  [62]. Therefore, with only three compositions it is difficult to find a conclusive fitting for  $\gamma$  with  $x$ . Moreover, since the difference between the electron content in  $\text{Zn}^{2+}$  and  $\text{Fe}^{3+}$  is just 6 electrons, so with X-rays which are sensitive to the number of electrons, it is difficult to precisely determine  $\gamma$ . Partial occupancies of Zn(1) and Zn(2) are graphically shown in Fig. 4.3(b). The occupancies of Zn(1) increase as we go higher in  $x$  and that of Zn(2) decrease. The sum of occupancies of Zn1 and Zn2 are less than unity. That is why in the overall composition we have less Zn than the nominal stoichiometry. Earlier refinements also reported similar findings [63, 64].

Table 4.2 Composition and partial occupancies of Zn(1) and Zn(2) from single crystal X-ray diffraction refinements at room temperature

Code	R	Stoichiometric formula	Zn(1)	Fe(1)	Zn(2)	Fe(2)
BZY-1	1.41	$\text{Ba}_{1.28}\text{Sr}_{0.72}\text{Zn}_{1.52}\text{Fe}_{12.48}\text{O}_{22}$	0.11	0.89	0.65	0.35
BZY-2	1.42	$\text{Ba}_{0.58}\text{Sr}_{1.4}\text{Zn}_{1.66}\text{Fe}_{12.28}\text{O}_{22}$	0.14	0.84	0.68	0.31
BZY-3	1.83	$\text{Ba}_{.8}\text{Sr}_{1.18}\text{Zn}_{1.56}\text{Fe}_{12.38}\text{O}_{22}$	0.12	0.85	0.66	0.33

From the refinement we calculated the bond length of all the transition metal-O bonds. Zn(1) in layer number 4 to O(1) in layer 6 are the shortest in the range of 1.9 Å. Fe(3) in layer 5 to O(3) in layer 2 has the longest bond length ( $\approx 2.25\text{\AA}$ ) compared to other average bond lengths of  $\approx 2\text{\AA}$ . All the bond lengths are tabulated in Table 4.3. The bond lengths for all the three samples can be seen in Fig. 4.3(a). Significant change in bond length is observed with change in  $x$  for the bonds shown with ellipse in the Fig. 4.3(a). Changes in bond length with change in  $x$  can be attributed to difference in the Shannon radius of  $\text{Ba}^{2+}$

Table 4.3 Different transition metal-O bond lengths from single crystal X-ray refinements of samples BZY-1, BZY-2, BZY-3 at room temperature.  $x$  is given in the formula  $\text{Ba}_{1-x}\text{Sr}_x\text{Zn}_{1-p}\text{Fe}_{6+p}\text{O}_{11}$

	BZY-1	BZY-2	BZY-3
Bond type	$x=0.36$	$x=0.59$	$x=0.70$
Zn(1)-O(1)	1.906	1.913	1.899
Zn(1)-O(3)	1.890	1.877	1.883
Zn(2)-O(2)	1.985	1.989	1.989
Zn(2)-O(5)	1.939	1.928	1.941
Fe(3)-O(3)	2.255	2.251	2.233
Fe(3)-O(4)	1.940	1.925	1.933
Fe(4)-O(5)	2.008	2	2.002
Fe(5)-O(1)	2.004	1.999	2.008
Fe(5)-O(2)	2.005	2	2.006
Fe(5)-O(4)	1.975	1.981	1.983
Fe(5)-O(5)	2.049	2.054	2.045
Fe(6)-O(3)	2.024	2.023	2.021

and  $\text{Sr}^{2+}$  [114].  $\text{Ba}^{2+}/\text{Sr}^{2+}$  in layer-3 is connected to the  $\text{O}^{2+}$  in layer-2 which is bonded to the  $\text{Fe}^{3+}$  in layer 4 and 5, see Fig. 2.18. Smaller size of Sr can cause local distortion, which affects the Zn distribution in layer 4.

From section 2.4.3 we have seen that the boundary between the spin blocks is dominated by ferromagnetic super-exchange interaction in Zn(1)-O(3)-Fe(3). In Zn(1)-O(3)-Fe(3), one bond length Zn(1)-O(3) is smaller than the average bond length and one bond length Fe(3)-O(3) is longer. This makes the super-exchange interactions different from the rest and we have a ferromagnetic interaction in the collinear phase. Change in  $x$ , and hence change in occupancies in Zn(1), has significant effect on this super-exchange interaction not only because bond lengths vary significantly but also because the strength depends upon the magnetic  $\text{Fe}^{3+}$  content. Change in Zn occupancies in the Zn(1) sites not only changes the bond length associated with Zn(1) but also the bonds associated with Fe(3) *i.e.* Fe(3)-O(4). Therefore, we can claim that one of the reasons for spin structure change from collinear to spiral with change in  $x$ , is the change in partial occupancies of Zn in Zn(1) site which in turn changes the bond length. With change in bond length the unusual ferromagnetic interaction of Zn(1)-O(3)-Fe(3) no longer remains collinear. However, changes in bond lengths are do not qualitatively follow the same trend as that of  $x$  and this can be seen clearly from the Fig. 4.3(a).

Momozawa *et al.*[5] found out that there are three types of magnetic ordering depending upon the Sr content in the crystals of  $\text{Ba}_{(1-x)}\text{Sr}_x\text{ZnFe}_6\text{O}_{11}$ : ferrimagnetic ordering for  $0 \leq x \leq 0.5$ , helical magnetic ordering for  $0.5 \leq x \leq 0.8$  and collinear commensurate order-

ing for  $0.8 \leq x \leq 1$  were reported. From our samples we have three  $x$  values: one in the ferrimagnetic range (BZY-1) and others in the non-collinear range (BZY-2 and BZY-3). We used magnetization measurements on the samples to find out if they display the signature metamagnetic features reported [3, 5].

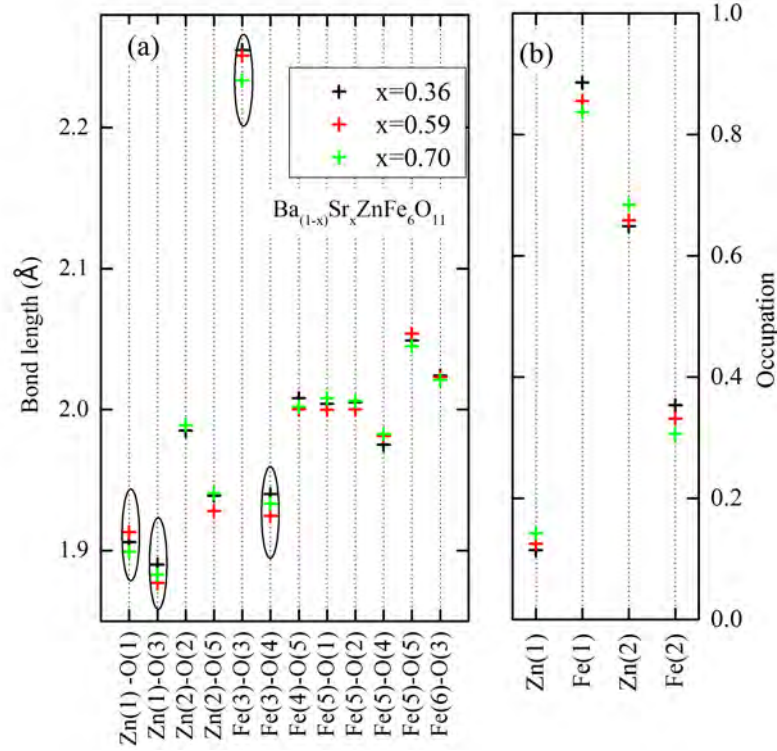


Fig. 4.3 (a) Different Fe/Zn-O bond lengths and (b) Partial occupancies of Zn(1) and Zn(2) for BZY-1, BZY-2 and BZY-3.  $x$  is given in the formula  $\text{Ba}_{1-x}\text{Sr}_x\text{ZnFe}_6\text{O}_{11}$

## 4.3 Macroscopic magnetization measurements

### Magnetization change with composition

We plotted the magnetization curves for all the three samples, normalized to magnetization at 6 T, in Fig. 4.4. It can be seen that, unlike BZY-2 and BZY-3, no indications of metamagnetic transitions are present in BZY-1. Step-like behavior in magnetization curves in BZY-2 and BZY-3 corresponds to different metamagnetic transitions as reported earlier [5]. Metamagnetic and composition dependent magnetic behavior of our samples are so interesting that it is imperative to discuss them separately for each sample in the following subsections.

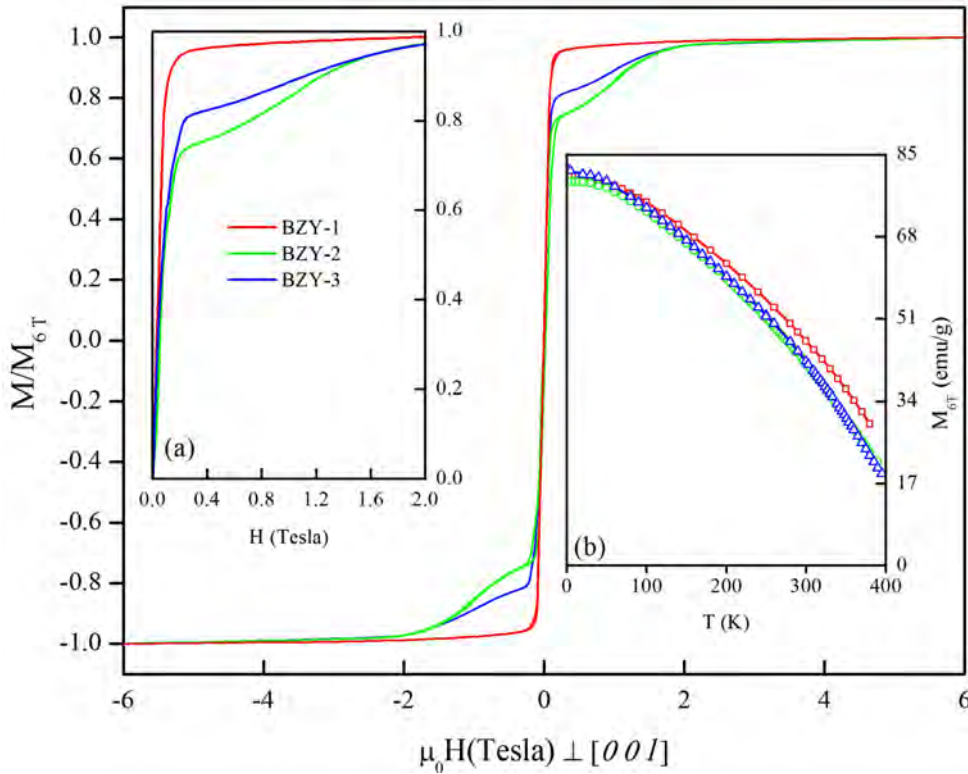


Fig. 4.4 (a) DC magnetization vs applied external magnetic measurements of all the three samples  $H \perp [001]$ , normalized to magnetization at 6 T at 10 K. Inset (a) shows the enlarged view of low field region. (b) Magnetization at 6 Tesla as a function of temperature.

### 4.3.1 Ferrimagnetic phase (BZY-1)

For the low Sr content  $\text{Ba}_{0.64}\text{Sr}_{0.36}\text{Zn}_{0.76}\text{Fe}_{6.24}\text{O}_{11}$  samples, an easy plane of magnetization  $\perp [001]$  ( $M_{\perp}$ ) as well as a hard direction  $\parallel [001]$  ( $M_{\parallel}$ ) is found. From torque measurements it was argued that anisotropy energy can be expressed as simple function of  $K_1 \cos \theta$  [115, 116]. In Fig. 4.5 (red curve) it can be seen that along the easy plane of magnetization, no distinct metamagnetic anomalies can be found up to 380 K in 6 T which is a rather high H. Magnetization curves at low temperature appear to reach saturation at pretty low H for  $H \perp [001]$ , but at higher temperatures saturation is not reached completely even at 6 Tesla. Magnetization at 6 Tesla for  $H \parallel [001]$  is equal to that of  $H \perp [001]$  at low temperatures, but at higher temperature, from the converging nature of both the curves, it can be expected to meet at higher field than 6 Tesla. The saturation magnetization, calculated using the block spin model (see section 2.4.3)  $17.6 \mu_B/\text{formula unit}$ , is close to experimental magnetization at 6 Tesla  $17.45 \mu_B/\text{formula unit}$  at 10 K.

Zero-field-cooled (ZFC) curves, field-cooled curves (FC) and measured while warming (FCW) curves at  $H=10$  mT for BZY-1 are shown in the inset of Fig. 4.5. In the ZFC

curve, for both  $H \perp [001]$  and  $H \parallel [001]$ , it is seen that magnetization drops sharply after 360 K and the straight line extrapolation of the drop meets at 380 K with  $M = 0$ . This temperature is close to the reported Curie temperature measured by temperature dependent magnetization as well as Mössbauer spectroscopy [5, 117, 118]. Many substitution studies are carried out in  $\text{Ba}_2\text{Zn}_2\text{Fe}_{12}\text{O}_{22}$  for Ba as well as for both the transition metal sites, and  $T_C$  is reported to be varying from 300 K to 800 K by different methods of measurements.  $\text{Ba}_2\text{Zn}_2\text{Fe}_{12}\text{O}_{22}$  has a  $T_C$  around 392 K [117]. The initial magnetization curve at 380 K can be seen clearly to be different from that of 360 K. Therefore, we can consider 380 K to be the transition temperature.

A thermal irreversibility  $T_{irr}$ , *i.e.* difference between ZFC and FC curves, are seen below 50 K, where ZFC  $M \parallel$  declines and FC increases. For Co<sub>2</sub>Y hexaferrite, it was proved on the basis of the magnetic hyperfine field that, this temperature is related to a spin reorientation or spin transition temperature where a helical magnetic to ferrimagnetic transition takes place [118]. For  $H \perp [001]$  below 360 K,  $M_{\perp}$  remains almost constant up to 50 K before dropping down near 50 K. On the other hand, for  $H \parallel [001]$ , below 360 K  $M_{\parallel}$  goes on increasing steadily up to 50 K for ZFC and up to base temperature 10 K for FC. In the case of helical phase,  $M_{\perp}$  is found to display metamagnetic steps in the magnetization vs  $H$  measurements (see Fig. 4.4). Although we observed such  $T_{irr}$  in M-T measurements,  $M_{\perp}$  does not show any anomalies up to 5 K. Therefore, such ferrimagnetic to helical-magnetic transition can not be interpreted based only on temperature dependent magnetization measurements. This needs further microscopic scattering studies to find out the origin of observed  $T_{irr}$ . It can be assumed that the anisotropy field parallel to  $[001]$  decreases with temperature whereas, in perpendicular direction it remains constant above 50 K to  $T_C$ . Decrease in anisotropy field  $H \parallel [001]$  also opens up a possibility of some magnetic moments in  $[001]$  direction.

### 4.3.2 The helical configuration BZY-2 and BZY-3

#### $H_{\perp c}$ and $H_{\parallel c}$

Let us come to the higher Sr containing samples *i.e.* BZY-2 and BZY-3. In Fig. 4.4 for BZY-2 and BZY-3 it is seen that  $M_{\perp}$  ( $M$  measured for  $H_{\perp}[001]$ ) follows a step-like behavior in the low field region. This type of behavior was studied by Enz [115], who found that the magnetization ( $M_{\perp}$ ) with applied magnetic field  $H \perp (00l)$  shows step-like behavior, while, for  $H \parallel [001]$  ( $M_{\parallel}$ ) no distinct steps were found. According to Enz, there is a competing nearest-neighbor ferromagnetic ( $J_1 > 0$ ) and next nearest-neighbor anti-ferromagnetic interaction ( $J_2 < 0$ ) that leads to helical configuration with angle  $\alpha$  where,  $\cos \alpha = -\frac{J_1}{4J_2}$  and  $|4J_2| > |J_1|$  (as discussed in section 2.1). Here,  $J_i$  represents the exchange interactions between total moments in either L or S block. Beyond a certain critical field  $H_k$ , helical

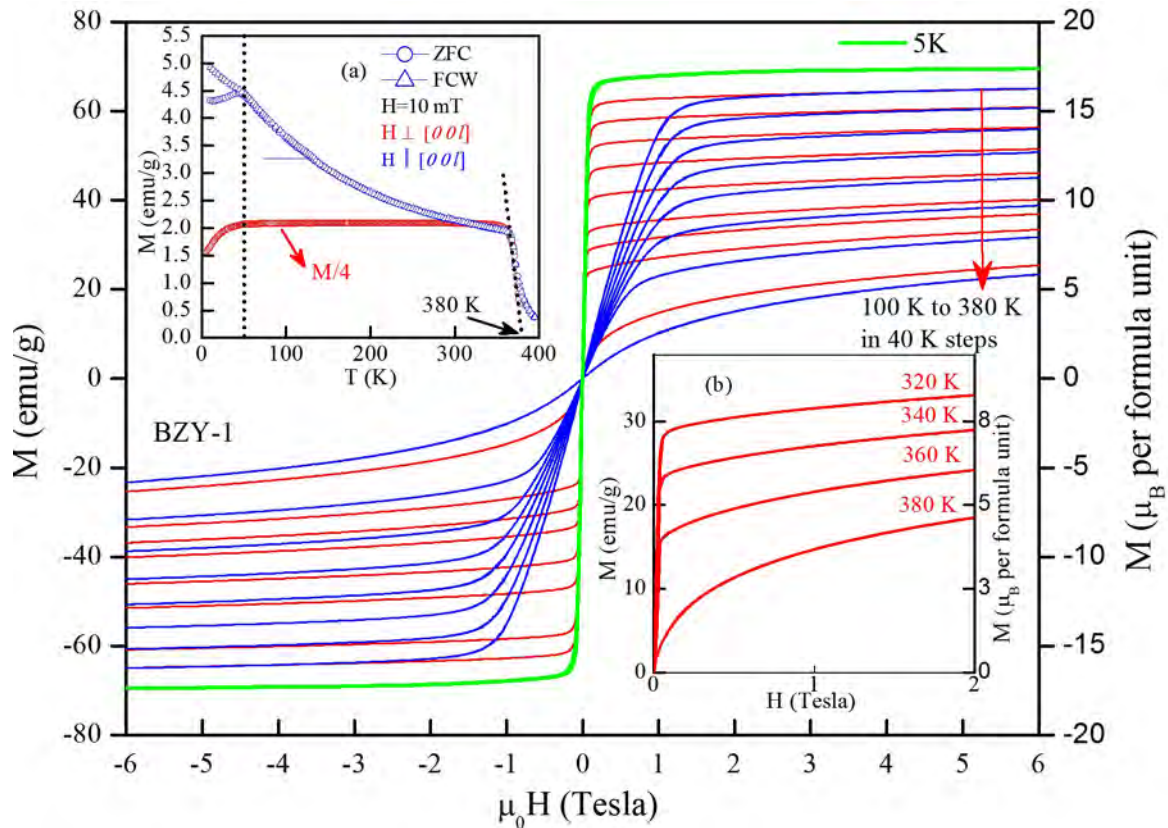


Fig. 4.5 DC Magnetization vs applied external magnetic measurements of BZY-1 in  $H \perp [001]$  as well as  $H \parallel [001]$ . (a) ZFC and FC curves for  $H \parallel [001] = 10$  mT and ZFC for  $H \perp [001]$ . (b) comparison of initial magnetization curves near the transition temperature for  $H \perp [001]$ .

magnetic order is stabilized and upon increasing  $H$ , the magnetization increases sharply through  $H_k$ . A strong magneto-crystalline anisotropy term in the basal plane ( $k_3$ ) (weaker than anisotropy in  $\parallel [001]$ ) and a magnetostriction energy ( $E_m$ ) was introduced to account for the different metamagnetic structures.

For BZY-2 and BZY-3 samples, as can be seen in Fig. 4.6 saturation is reached below 2.5 Tesla for  $T < 200$  K for  $H \perp [001]$ . Above 220 K, the S-shaped curves of magnetization indicate a high saturation field.  $H_{th}$ , the meeting point for  $M_{\perp}$  and  $M_{\parallel}$ , is near the saturation field. From the upper portion of this figure it can be seen that  $H_{th}$  is near 3 Tesla up to 180 K and then it increases up to 6 Tesla. At low  $H$ , at 340 K and 380 K, it is seen that  $M_{\perp}$  is lower than the  $M_{\parallel}$  but with increase in  $H$ , this is reversed. It indicates that anisotropy (MCA) field  $\parallel [001]$  becomes weaker near 340 K (see section 2.1.1 for MCA).

Both BZY-2 and BZY-3 behave similarly for  $M_{\parallel}$  and  $M_{\perp}$ , when normalized to the magnetization at 6 Tesla (see Fig. 4.7). In  $M_{\perp}$ , step-like features suggest metamagnetic transi-

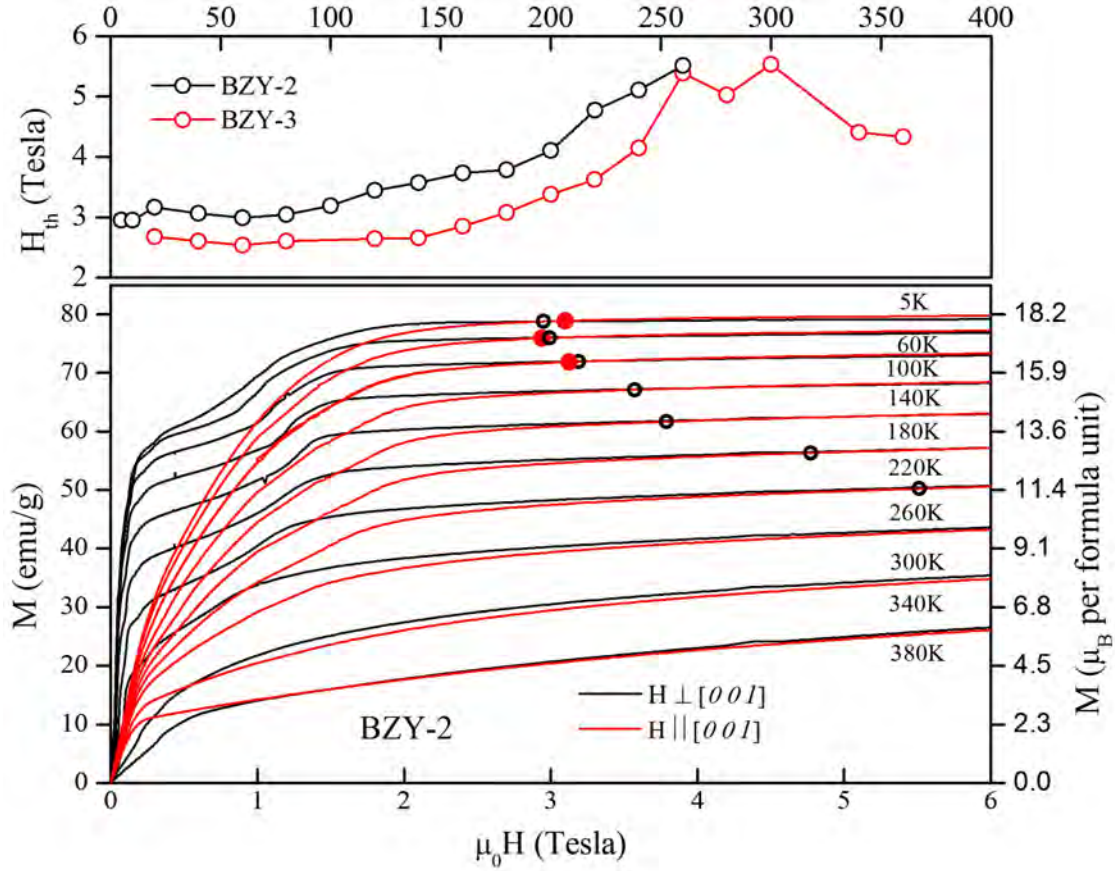


Fig. 4.6 (below) DC Magnetization vs applied external magnetic measurements of BZY-3 in both  $H \perp [001]$  (black) and  $H \parallel [001]$  (red) configuration. The dots indicate the threshold fields where the magnetization curves, measured both parallel and perpendicular directions, meet. (above) Variation of threshold field  $H_{th}$  with  $T$ .

tions and  $M_{\parallel}$  follows a similar path to saturation but with no visible step-like features. No spontaneous magnetization was found to be present in the samples.

### $M_{\perp}[001]$ detailed investigation

Momozawa [61] reported six metamagnetic transitions corresponding to six magnetic fields for a crystal of composition  $\text{Ba}_{0.504}\text{Sr}_{1.496}\text{Zn}_2\text{Fe}_{12}\text{O}_{22}$ . Following Momozawa we use the following notation for these phases and fields:

- *Slightly modified helix*  $\rightarrow 0 \leq H \leq H_1$ .
- *Intermediate-I*  $\rightarrow H_2 \leq H \leq H_3$ .
- *Intermediate-II*  $\rightarrow H_4 \leq H \leq H_5$ .
- *Intermediate-III*  $\rightarrow H_5 \leq H \leq H_6$ .

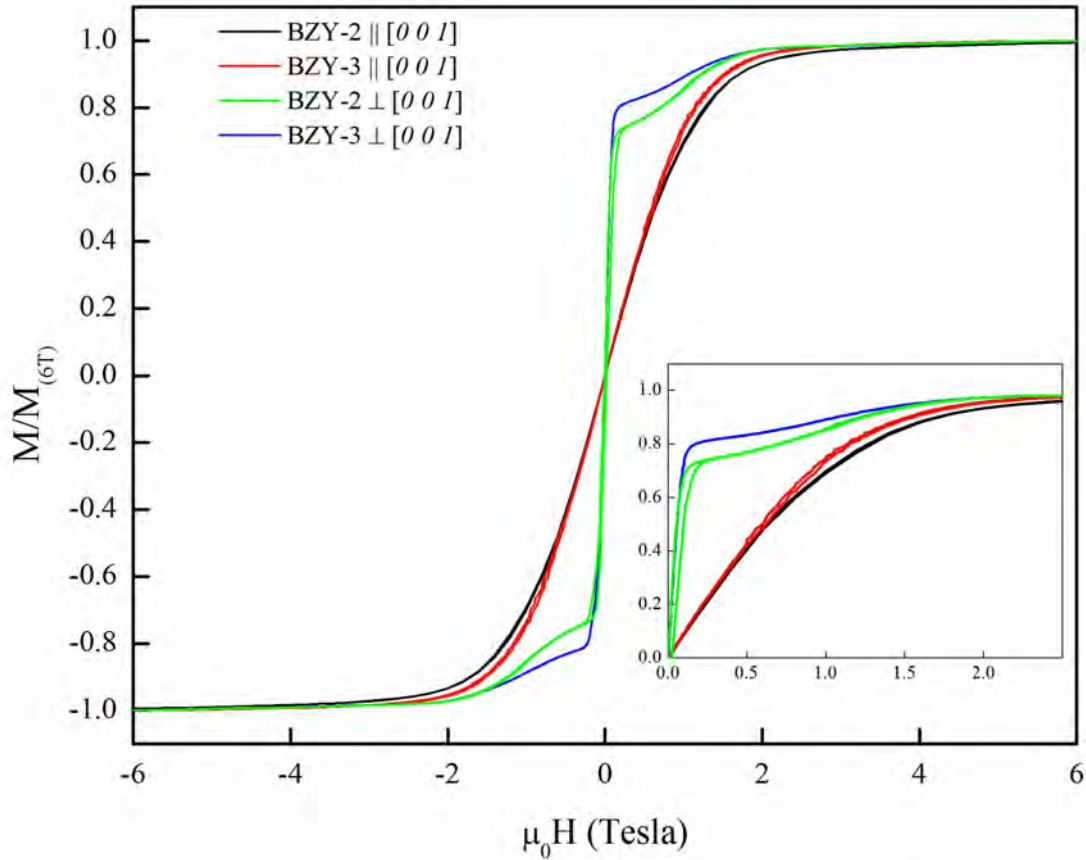


Fig. 4.7 DC Magnetization vs applied external magnetic measurements of BZY-2 and BZY-3 in a SQUID magnetometer, normalized over magnetization at 6 Tesla. For BZY-2 and BZY-3, both perpendicular to  $[0 0 1]$  and parallel to  $[0 0 1]$   $H$  is applied. Inset shows the enlarged region of low applied  $H$  in positive quadrant.

- *Ferrimagnetic*  $\rightarrow H_6 \leq H$ .

The values of these metamagnetic fields are reported to change with composition within the helical phase [61, 62]. There exist three  $H \perp -T$  phase diagrams in literature for helical phase for close to  $(\text{Ba}_{0.5}\text{Sr}_{1.5})\text{Zn}_2\text{Fe}_{12}\text{O}_{22}$  compositions. Initial magnetization, neutron scattering and magnetoelectric measurements were used to determine these phase diagrams. Momozawa used magnetization measurements as well as neutron scattering at particular fields to validate the phase diagram [8]. Kimura *et al.*[3] also used the initial magnetization curves and later used magnetic field induced polarization and magnetoelectric current to validate his model. This phase diagram was refuted by Chai *et al.*, who claimed that the boundary for the intermediate-III phase moves towards lower field with oxygen sintered highly resistive samples [119]. However, no quantitative analysis of oxygen content was done in that work.

On a first look at the initial magnetizations of our samples, broad regions in  $H$  can be considered as metamagnetic phase boundaries. As can be seen in Fig. 4.8, the red and blue dots can be put to determine by eye the field for  $H_5$  and  $H_6$ . For *e.g.*, the blue dots denote the field where complete ferrimagnetic saturation occurs; is not just a single point in the curve but can be considered as a broad region. We have used two different approaches to determine the metamagnetic transitions.

- First derivative of  $M$  with respect to  $H$   $\left(\frac{\partial M}{\partial H}\right)$  and the second derivative  $\frac{\partial^2 M}{\partial H^2}$ .
- Intersection of the extrapolated straight lines from the steps of magnetization corresponding to different transitions.

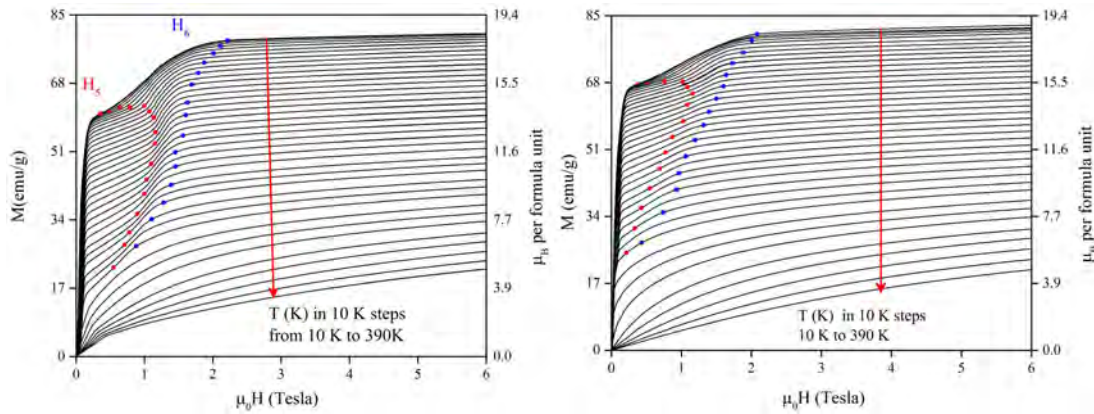


Fig. 4.8 (a) Initial magnetization curves of both BZY-2 and BZY-3 samples for  $H \perp [001]$ . Red dots indicate  $H_5$  and blue dots indicate  $H_6$ . Dots are put with accuracy of eyes.

The second method gives the middle point of transition whereas second and first derivatives are used to determine the broadness of the transition. In Fig. 4.9 the region of sharp increase in first derivative corresponds to the flat region in the second derivative. This flat region is considered as broadness of the transition.

The first four metamagnetic transitions with temperature are plotted in the bottom panel of Fig. 4.10.  $H_1$  and  $H_4$  begin to appear from 318 K down to 4 K, the lowest temperature measured, for BZY-2.  $H_2$  and  $H_3$  are visible only for  $T < 280$  K. For  $280 \text{ K} < T$ , it was not possible to resolve both as no distinct steps are visible.  $H_1$  appears at higher field  $\approx 60$  mT near 300 K and decreases to  $\approx 20$  mT at 50 K and then again a small increase is seen. Similar behavior was seen in earlier studies [8]. For BZY-3 all the metamagnetic transitions start appearing at 303 K.  $H_1$  and  $H_3$  get smeared out (can not be determined) at low temperature and could not be resolved. In both cases, all the transitions are situated close to each other at higher temperature but become separated from each other gradually as temperature is

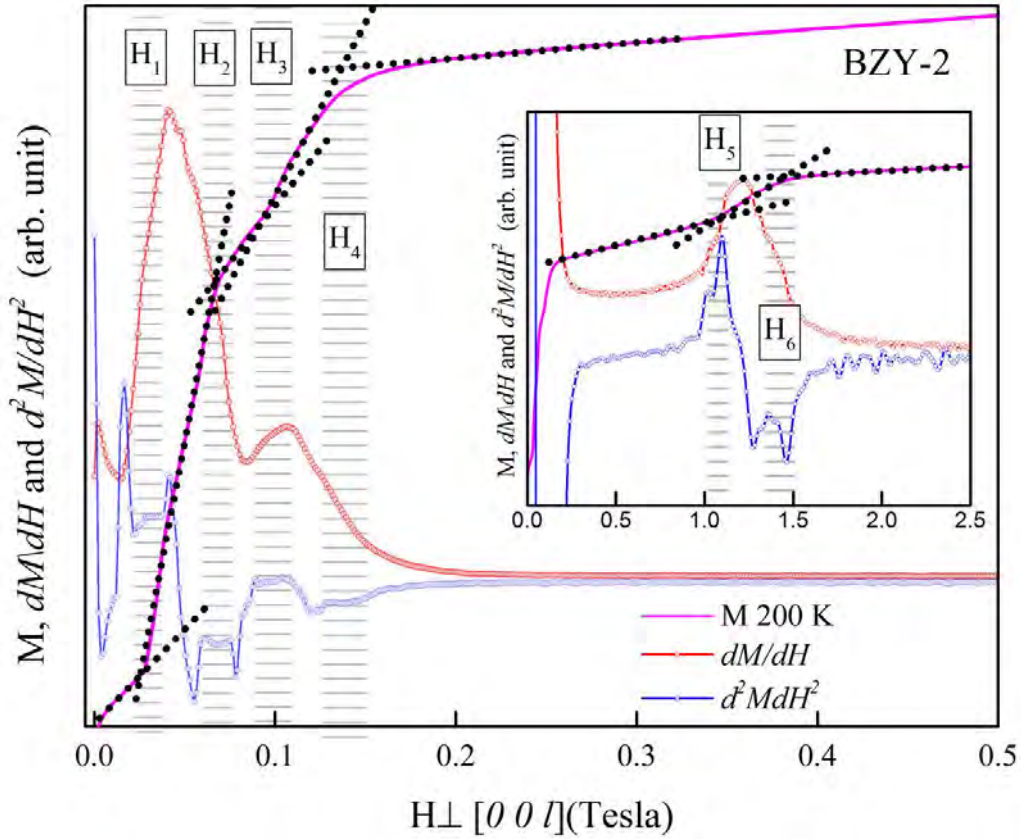


Fig. 4.9 Magenta curve shows the  $M$  vs  $H \perp [0 0 l]$  at 200 K (initial magnetization). Red curve shows the first derivative of  $M_{\perp}$  and the blue curve shows the second derivative. Horizontal grid lines are the broad metamagnetic transitions. Black dotted lines are the extrapolation of regions where  $M_{\perp}$  has the steepest change. The crossing points are considered to be the points of metamagnetic transitions.

lowered.  $H_1$  in both cases is very narrow while  $H_3$  has the broadest transition as can be inferred from the vertical bars attached to the symbols.

$H_5$  and  $H_6$  are also plotted against temperature in Fig. 4.10(b). Both transitions appear in the lower field at high temperature. For BZY-2,  $H_5$  starting at lower  $H$  goes to higher  $H \approx 1.1$  T at 150 K and starts decreasing again. The same features are observed for BZY-3 also but with different  $H$ . At higher and lower  $T$ ,  $H_5$  appears to be broader while in the intermediate temperature range it is very sharp. For BZY-2,  $H_6$  reaches as high as  $\approx 2.2$  Tesla at low temperature, whereas for BZY-3 it is  $\approx 2.1$  Tesla. For both BZY-2 and BZY-3,  $H_6$  decreases continuously. Variation of  $H_5$  and  $H_6$  are also consistent with those reported in the literature [3, 8, 119]. Kimura *et al.* argued that the region between  $H_5$  and  $H_6$  (Intermediate-III) is the region where magnetic field induced ferroelectricity occurs. Chai *et al.* found that the phase boundary found by magnetoelectric measurements in highly resistive sample corresponds

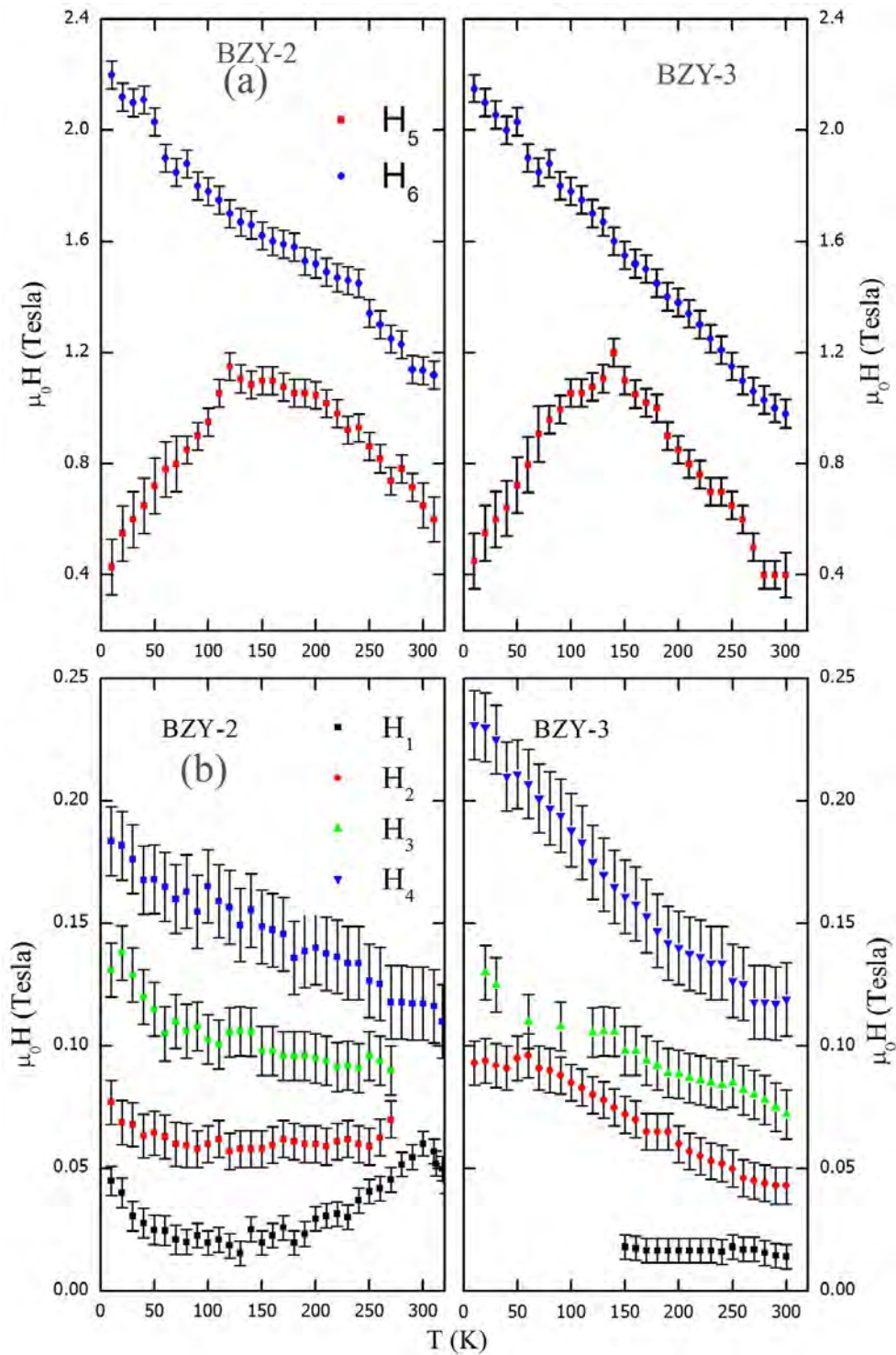


Fig. 4.10 Metamagnetic fields (a)  $H_1$ ,  $H_2$ ,  $H_3$  and  $H_4$  and (b)  $H_5$  and  $H_6$  are plotted against temperature for BZY-2 (left) and BZY-3 (right). Error bars indicate the broadness of transitions as determined by the first and second derivatives of initial magnetization.

to a wider region than the phase boundary of  $H_5$  and  $H_6$ . Intermediate-III is considered as a transient metamagnetic phase connecting ferrimagnetic and intermediate-II phase [61]. Therefore, a detailed investigation is required to determine the relation between magnetic structure and macroscopic magnetic field induced ferroelectric polarization (see Chapter-5 and Chapter-6).

### Transition temperatures BZY-2 and BZY-3

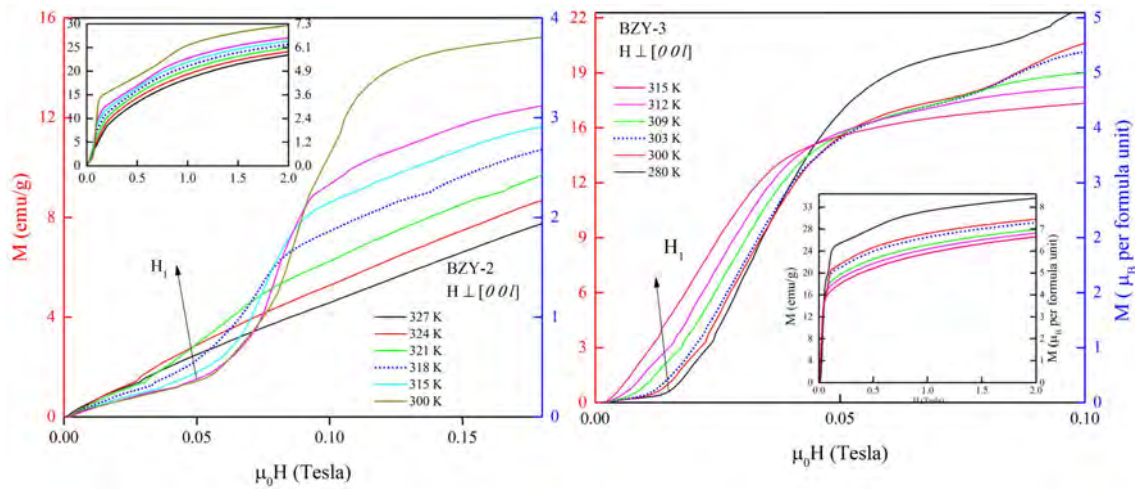


Fig. 4.11 Initial magnetization curves near spin reorientation temperature of BZY-2 and BZY-3. Inset for both cases show the high  $H$  regions.

Some of the initial magnetization curves for BZY-2 and BZY-3 near the temperature where  $H_1$  appears are shown in Fig. 4.11. Higher temperature initial magnetization curves were measured first. After each measurement an oscillatory field is applied to demagnetize the sample. The residual magnetic field in the instrument is below 0.5 mT. As mentioned above, no spontaneous magnetization is observed within the error of the instrument. As seen in both the cases of BZY-2 and BZY-3, at certain temperature the metamagnetic transition starts appearing. Above 290 K we have measured the curves in 3 K intervals. In case of BZY-2, near 318 K (the dotted blue curve) the metamagnetic transition corresponding to  $H_1$  starts appearing. For BZY-3, it is near 303 K. It can be seen that other distinct metamagnetic transitions start appearing at this temperature.

Although it is assigned 318 K for BZY-2, the data for 321 K also have some signature of step-like behavior. Moreover, we have measured the initial magnetization curves in 3 K steps, so it is apparently difficult to assign an exact temperature where the metamagnetic transition start to appear.

In Fig. 4.12 ZFC and FC curves are shown. FC curves are measured in two different

ways: one, while heating in the presence of  $H$  after cooling with applied  $H$  and the other one is measuring while cooling in  $H$ . In case of low field measurements ( $H = 3$  mT, 7.5 mT, 30 mT and 50 mT), magnetization seems to increase very sharply upon warming above  $\approx 318$  K, and reaches its maximum ( $T_p$ ) at 332 K and then sharply decreases. In fact, the  $T_p$  region is slightly broader as can be seen in the bottom right corner Fig. 4.12 for 326 K to 337 K. Below 318 K, after a dip, the magnetization again increases with decrease in temperature and reaches a maximum at around 100 K and decreases again on further lowering the temperature (particularly, for ZFC). Such a peak ( $T_p$ ) like behavior (*Hopkinson's peak*) just below the ordering is found to arise in materials with strong magneto crystalline anisotropy [120]. Below the ordering temperature  $T < T_c$ , when the coercive field equals to or becomes less than the applied field, in ZFC measurement, such peak like behavior is observed. In many soft magnetic materials a broad peak is observed while in some cases it becomes sharper.

This effect is treated differently by different people. From  $M(T)$  measurements Lee *et al.* found 382 K as the Curie temperature of  $\text{Ba}_2\text{Zn}_2\text{Fe}_{12}\text{O}_{22}$  and it increases to 615 K with Co replacing Zn [121]. Some authors considered the peak ( $T_p$ ) as a spin reorientation temperature, *i.e.*, below this temperature a canted conical state is possible in very low  $H$  [119]. In polycrystalline samples of  $\text{BaSrCoZnFe}_{11}\text{O}_{22}$ , at 365 K the helical phase is considered to appear [122]. For  $(\text{Ba}_{(1-x)}\text{Sr}_x)_2\text{Zn}_2\text{Fe}_{12}\text{O}_{22}$ ,  $x = 0.748$ , 319 K was considered as the spin reorientation temperature and 337 K as the Neel temperature ( $T_N$ ) of an antiferromagnetic transition [5, 8] based on neutron diffraction and  $M(T)$  measurements. For  $\text{Ba}_2\text{Mg}_2\text{Fe}_{12}\text{O}_{22}$  single crystals, 195 K is a spin reorientation temperature and 553 K is the ferrimagnetic to paramagnetic transition [65]. Similar situation was encountered for Al-doped samples [66] and  $M(T)$  measurements were shown to be misleading in determining the spin-reorientation temperature.

Compared to  $M(T)$  measurements, initial magnetization curves near 332 K ( $T_p$ ) do not show any anomalies within our experimental resolution conditions (see Fig. 4.13). The dotted pink curve around 333 K do not have any visible anomaly. The first visible anomaly in initial magnetization curves appears at 318 K. Therefore, to know the transition temperature and the type of transition, we need to see if there is any frequency dependence in AC magnetic susceptibility (ACMS) measurements. In case of spin glass or any spin frozen system, frequency dependence in the ACMS measurements is a standard tool to distinguish between spin frozen transition and other types of transition [76].

AC magnetic susceptibility of the samples was measured in a Quantum Design PPMS. Samples were cooled to low temperature and then at each temperature, with different frequencies, measurements are performed and then swept to next temperature at 1 K/min rate.

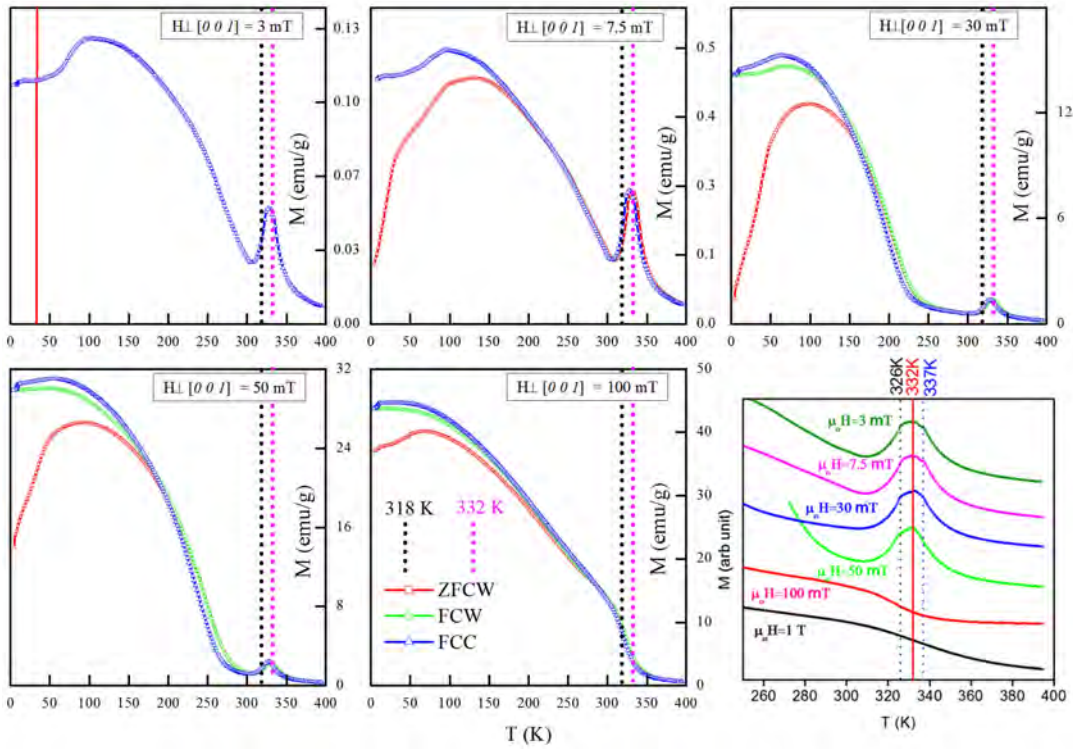


Fig. 4.12 Zero-field-cooled curves (red), field-cooled curves measured while warming curves (green) and field-cooled curves measured while cooling curves (blue) at different applied  $H_{\perp} [001]$  for BZY-2. Vertical dotted pink line corresponds to the  $T_p$  of the ZFC curve at 332 K and the black line is at 318 K (determined as the spin reorientation temperature from the initial magnetization curves). Bottom right figure shows enlarged view of the  $T_p$  region.

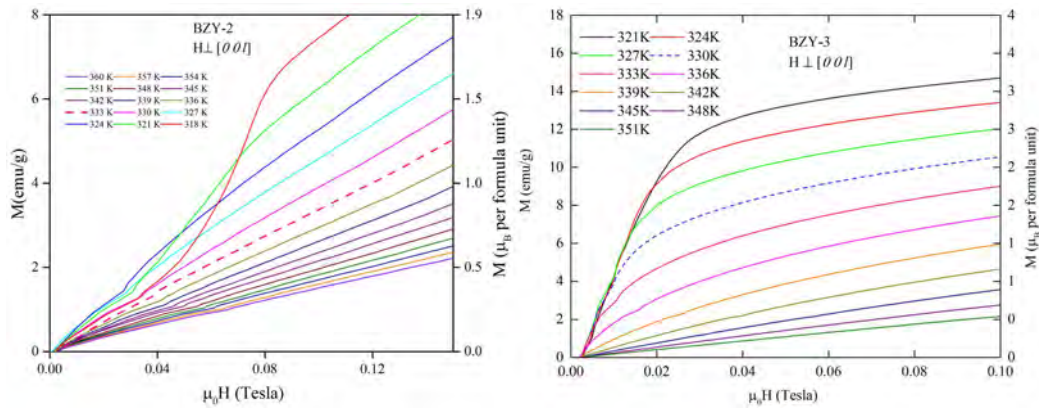


Fig. 4.13 Initial magnetization curves near  $T_p$ . *Left:* for BZY-2 and *Right:* for BZY-3. Inset shows the expanded region near low field.

ACMS measurements shows similar peak like feature as seen in low field ZFC curves but at 324 K and this is sharp compared to the broad maxima in low  $H$  ZFC curves. This corre-

sponds to the rising part of the peak in the ZFC curve in DC-magnetization and most likely is the real transition temperature below which is the helical phase. There is no frequency dependence near the peak at 324 K. Frequency dependence in the real part of the ACMS starts appearing in nearly the same region where difference between the ZFC and FC curves is observed in low  $H$  measurements. The frequency dependence are considered to be the signature of glassy nature or frustration in magnetic ordering. In our case of ordered system, this can amount to transient metamagnetic phases with different spin spiral states, as is seen from the DC magnetization process. In fact, ZFC-FC bifurcation temperature is found to have a field dependence.

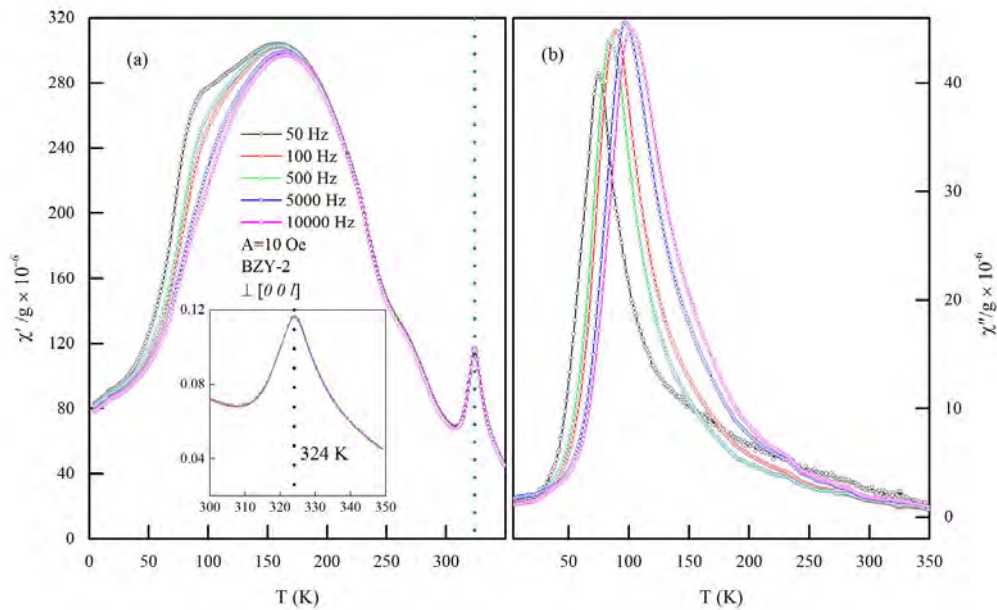


Fig. 4.14 (a) Real and (b) Imaginary part of the AC magnetic susceptibility of BZY-2. Inset shows the region near ordering temperature.

In case of BZY-3 samples the two corresponding temperatures are 329 K and 303 K. As can be seen from the Fig. 4.15, at low field a strong peak type behavior is observed at 331 K, which drops down at 303 K and starts increasing again with decreasing temperature. Compared to BZY-2, the  $T_p$  region is found to be very sharp in BZY-3.

Initial magnetization curves near 330 K were found to have a steep increase, in fact, at 333 K also it has slight step increase compared to that of higher temperature at lower field. Such features were not observed in case of BZY-2. In the ACMS measurement of BZY-3, a sharp frequency-independent peak is observed at 331 K. It is at the same temperature where the same peak was observed for low  $H$  ZFC curves. The frequency dependent region is also at the same temperature where ZFC and FC curves bifurcate.

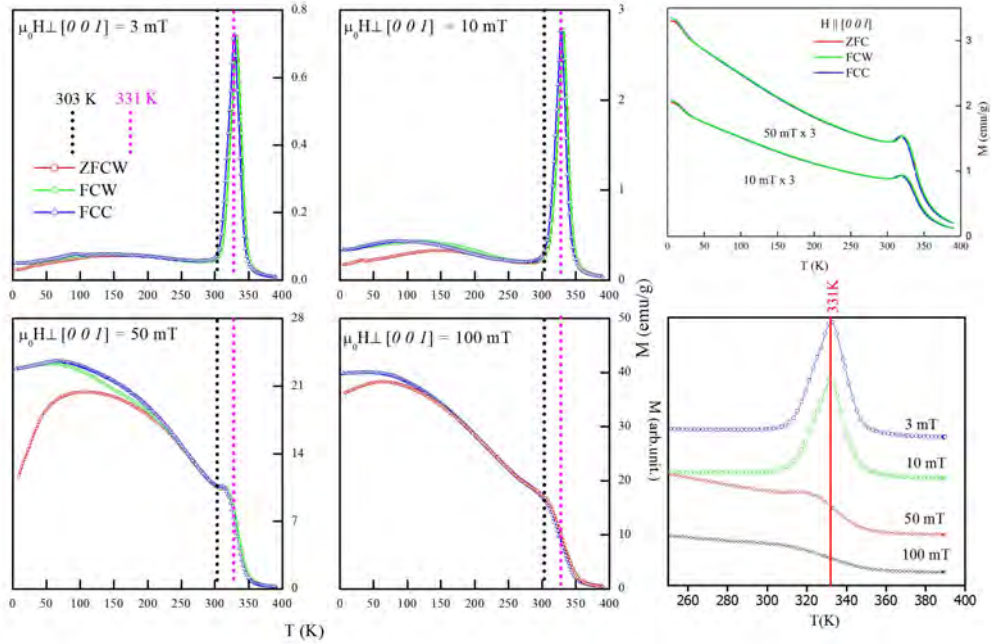


Fig. 4.15 ZFC (red), FCW (green) and FCC (blue) at different applied  $H_{\perp} [001]$  for BZY-3. Vertical dotted pink line corresponds to the ZFC curve at  $331 \text{ K}$  and the black line is at  $303 \text{ K}$ , determined as the spin reorientation temperature from the initial magnetization curves. Bottom right figure shows enlarged view of the  $T_P$  region.

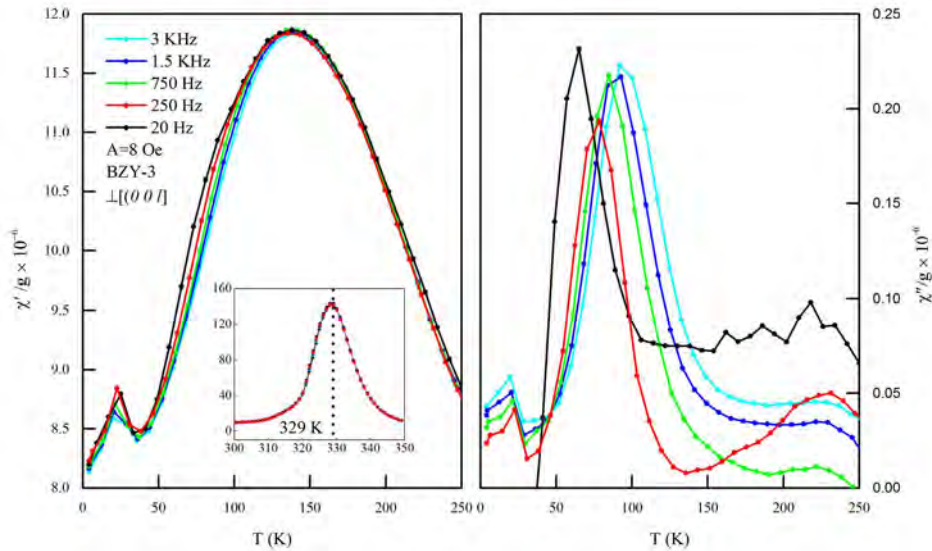


Fig. 4.16 (a) Real and (b) Imaginary part of the AC magnetic susceptibility of BZY-3. Inset shows the region near ordering temperature.

Sharp peak like behavior at the transition temperature and absence of frequency dependence in the ACMS measurements shows that this transition is not some local order to dis-

order transition. Still it is not clear whether it is ordered magnetic to paramagnetic transition or a transition from one magnetic order to other. However, from the virgin magnetization measurements it is clear that metamagnetic signatures are retained to room temperature and above to 318 K and 303 K for BZY-2 and BZY-3 respectively. If magnetic field induced ferroelectricity is due to the spin order below this transition temperature, then a possibility to observe such phenomenon up to room temperature can be predicted from the magnetic data. However, because of the leakage current it was not possible to measure above 130 K [3].



# Chapter 5

## Low $H$ phases

### 5.1 Zero $H$ magnetic structure

The long  $c$  lattice parameter ( $\approx 43.5\text{\AA}$ ) of Y-type hexaferrite and magnetic propagation along  $[0\ 0\ l]$  makes it easy to study with soft X-ray resonant scattering technique. There are few studies on the magnetic structures of Y-type hexaferrite using Fe  $L_3$  edge photon energy [6, 9–11, 123]. Very large enhancement in magnetic scattering intensity at resonance was observed in these studies. All those studies were concentrated on structures in zero field or small magnetic fields. We extensively used soft X-ray resonance technique to determine the magnetic structure of the different metamagnetic phases as shown in Chapter-4. This chapter will deal with only the low  $H$  phases, *i.e.* up to  $H_4$ . Magnetic structures of the phases in between  $H_5$  and  $H_6$  will be discussed in the next chapter. Neutron diffraction experiments will also be discussed in relevant sections.

The zero- $H$  structure was studied by Momozawa [5, 62] by neutron diffraction. Mulders *et al.* studied the zero- $H$  structure by circular and linear polarization of Fe  $L_3$  edge X-ray resonant diffraction. Hiraoka [10, 11] studied the spin chiral domains and the effect of temperature on them. The only in-field study was carried out by Hearmon *et al.* [6], but the maximum applied field value was limited by the electromagnet (150 mT), where they could reach hardly near  $H_3$ .

**Temperature dependence of zero field structure** For soft X-ray experiments we used surfaces either as grown or cleaved ex-situ. In  $(0\ 0\ l)$  scans with  $\sigma$  and  $\pi$  polarizations of incoming photons (see Fig. 3.5 for  $\sigma$  and  $\pi$  polarizations) two incommensurate satellite reflections are observed at  $(0\ 0\ 3\pm\delta)$ ,  $\delta = 0.38$  as shown in Fig. 5.1(a).

We know from the matrix Eq. 3.25 that for incoming  $\pi$  polarized photons, the intensity is sensitive to moment components in all  $z_1$ ,  $z_2$  and  $z_3$  directions, whereas, for  $\sigma$  polarized photons  $z_2$  moment components are not observed. For a helical structure, where  $z_3$  moments

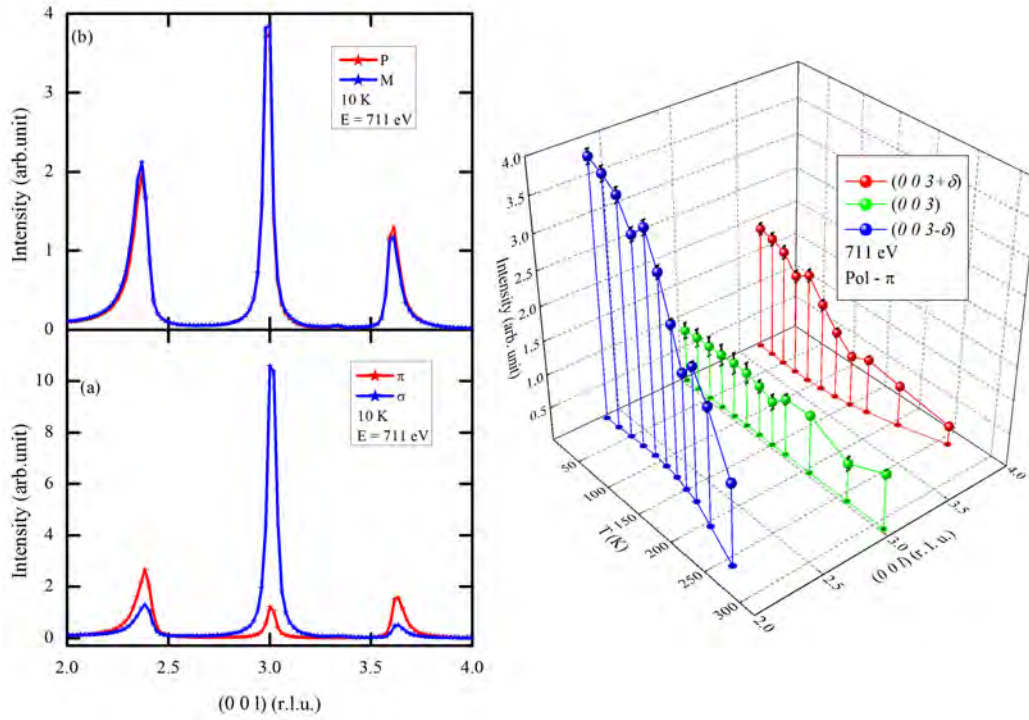


Fig. 5.1  $(0\ 0\ l)$  scan at 10 K with 711 eV energy (a) with  $\pi$  and  $\sigma$  polarizations and (b) with  $P$  and  $M$  polarizations, (right:) temperature dependence of incommensurate satellite with nuclear  $(0\ 0\ 3)$  reflection, intensity and position in reciprocal space.

are absent,  $\pi \rightarrow \sigma$  and  $\sigma \rightarrow \pi$  intensities are equal. Intensity in  $\sigma \rightarrow \sigma$  is zero for purely magnetic scattering. The  $\pi \rightarrow \pi$  intensity adds up in the total incoming  $\pi$  channel. As a result, intensity of the  $(0\ 0\ 3 \pm \delta)$  in  $\pi$  channel is higher than that of the  $\sigma$  channel. We can see this in Fig. 5.1(a) that for both the satellites, intensity in the  $\pi$  channel is greater than that of  $\sigma$  channel.

For nuclear Thomson scattering  $(0\ 0\ 3)$  nuclear reflection reverse order is observed as shown in Fig. 5.1(a). In Thomson scattering,  $\sigma \rightarrow \pi$  and  $\pi \rightarrow \sigma$  off-diagonal channel intensities are not observed while, in diagonal channels  $\sigma \rightarrow \sigma$  to  $\pi \rightarrow \pi$  ratio is given by  $\cos^2 2\theta$  as can be seen in Eq. 3.25. Our experimental ratio 10 is somewhat lower than the calculated 14 ratio. We found that the full width at half maximum is the same for both the channels for Thomson scattering. Therefore, the penetration depth calculated for both the channels are similar, *i.e.*  $\approx 85$  nm. Intensity ratios  $\pi/\sigma$  for  $(0\ 0\ 3 + \delta)$  and  $(0\ 0\ 3 - \delta)$  reflections are 3.65 and 1.87 respectively. We have intensity ratios  $\pi/\sigma$  in our experiment comparable to that of Mulders *et al.* group's experimental values of 3.375 and 2.17 and calculated values of 3.125 and 1.96 for  $(0\ 0\ 3 + \delta)$  and  $(0\ 0\ 3 - \delta)$  respectively. Few more intensity ratios are tabulated in Table. 5.1. It would be wrong to directly compare exact ratios of intensities, as

the propagation vector in the reference [9] is smaller than that of ours. Both the ratios  $\pi/\sigma$  for  $(0\ 0\ 3+\delta)$  and  $(0\ 0\ 3-\delta)$  are  $\theta$  dependent and hence, have different values.

Circular polarized X-ray resonance diffraction provides information about the chirality of the sample. Intensity in the two incoming polarization of photons  $P$  and  $M$  is distinguished from each other by the chiral term  $\chi = \pm 1$  in the following equation [9] (for details see section 3.4.3):

$$I_{\chi}^{XRES} = \frac{1}{2}[I_{\sigma \rightarrow \sigma} + I_{\sigma \rightarrow \pi} + I_{\pi \rightarrow \sigma} + I_{\pi \rightarrow \pi}] + \chi \text{Im} \left[ \overline{[F_{\pi \rightarrow \sigma}]} [F_{\sigma \rightarrow \sigma}] + [F_{\sigma \rightarrow \pi}] \overline{[F_{\pi \rightarrow \pi}]} \right] \quad (5.1)$$

$\chi$  is  $\pm 1$  for  $P$  and  $M$  polarizations

Value of  $\chi$  ( $=\pm 1$ ) determines the intensity in both the channels depending on whether the second term is added or subtracted from the linear total average intensity given by the first term. Since,  $[M_{\sigma \rightarrow \sigma}]$  is zero according to Eq. 3.25, the second term in Eq. 5.1 determines the intensity of chiral scattering. This second term involves all the three moments ( $z_1$ ,  $z_2$  and  $z_3$ ).

In our experimental data which is presented in Fig. 5.1(a), the contrast between circular  $P$  and  $M$  is very weak compared to that reported in [9]. This can be explained in the light of the beam spot used and size dependent populations of chiral domains. In the cited experiment,  $1\text{ mm}^2$  of sample surface area was illuminated, but we used a  $120\ \mu\text{m}$  horizontal beam and  $400\ \mu\text{m}$  vertical beam compared to experimental sample surface of  $8\text{ mm}^2$ . With small beam spots Hiraoka *et al.* found that, for circular polarization, spin chiral domains with variable sizes exist. Therefore, with small beam spots different ratios of the intensities can be observed for both  $P$  and  $M$  satellites. This is discussed in section 5.3.1. However, as observed in earlier cases [9],  $(0\ 0\ 3-\delta)$  is comparatively more intense in  $M$  and  $(0\ 0\ 3+\delta)$  is more intense in  $P$ , which is consistent with chiral structures.

In Fig. 5.1(c) it can be seen that the incommensurate propagation vector  $(0\ 0\ \delta)$  increases with increasing temperature. At 10 K,  $\delta = 0.62$  and it reaches to  $\delta = 0.87$  at 260 K. No satellite reflections can be observed at 320 K and above. With increase in temperature, the intensity of the nuclear reflection decreases marginally but the intensity of the satellite decreases considerably. The ratio of the intensities between  $(0\ 0\ 3-\delta)/(0\ 0\ 3+\delta)$  is plotted in Fig. 5.3(a). This ratio follows the same trend as that of the propagation vector. Intensities of  $(0\ 0\ 3-\delta)$  and  $(0\ 0\ 3+\delta)$ , for a particular temperature, are distinct from each other by position in reciprocal space  $Q$ . Since they are following the same trend, we can assume that there are no anomalies with respect to  $Q$  in the range of the temperatures shown in the Fig. 5.1.

For comparison, neutron diffraction experiment was also carried out in TRICS at The Paul Scherrer Institute, Villigen, Switzerland. In case of neutron diffraction, the incommen-

surate propagation vector  $(0\ 0\ 9\pm\delta)$  is also changing with temperature and the intensity, as expected, drops with increase in temperature, see Fig. 5.2. Integrated intensities are calculated by Gaussian fitting of the reflections. In right side figure of Fig. 5.2, integrated intensities with position in reciprocal space are plotted with respect to the temperature. Smooth change in position and intensity in neutron as well as resonant X-ray diffraction data rules out any phase transition at zero  $H$  from 290 K to 10 K. However, above 290 K we have measurements only at 320 K, where no satellite was observed. Therefore, we can say from the present data that at 320 K helical configuration disappears, but we can not say at which temperature in the range 320-290 K this transition takes place.

Table 5.1 Comparison of the ratio of intensities of our experiment to that of experimental and calculated one by Mulders *et al.*[9]

Polarization	$(0\ 0\ 3+\delta)$			$(0\ 0\ 3-\delta)$			$(0\ 0\ 3-\delta)/(0\ 0\ 3+\delta)$		
	Exp.	Ref [9]	Calc. [9]	Exp.	Ref [9]Exp.	Calc. [9]	Exp.	Ref [9]	Calc. [9]
$\pi/\sigma$	3.65	3.375	3.125	1.87	2.173	1.96			
$\pi$							2.05	1.85	2.04
$\sigma$							4.02	2.875	3.25

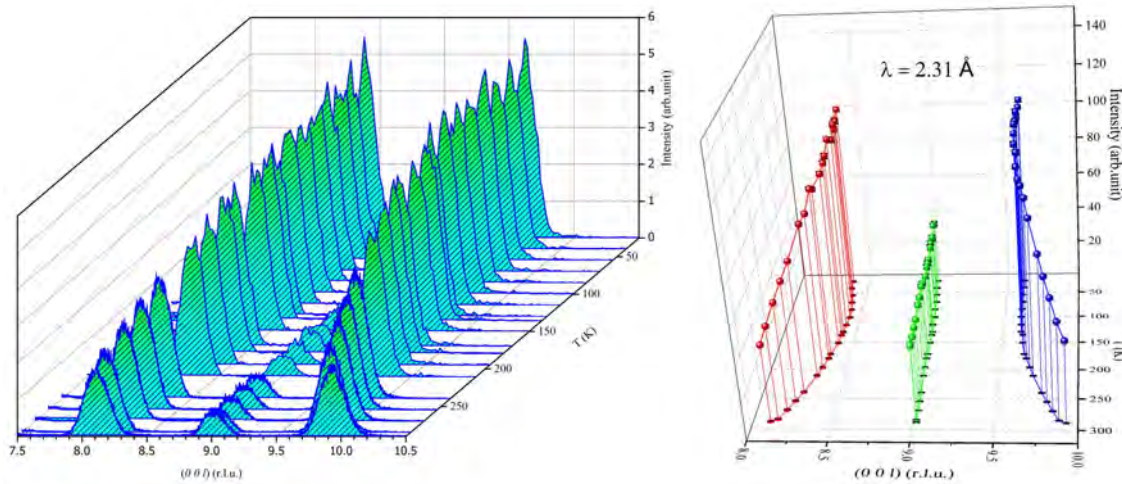


Fig. 5.2 *Left:*  $(0\ 0\ l)$  scans at different temperatures with neutron of wavelength  $\lambda = 2.31\text{\AA}$ . *Right:* temperature dependence of incommensurate satellite with nuclear  $(0\ 0\ 9)$  reflection, intensity and position in reciprocal space are shown.

In Fig. 5.3(a) propagation vector parameter  $\delta$  from  $(0\ 0\ 3n\pm\delta)$  for both X-ray and neutron diffractions is plotted with respect to the temperature. A small difference in the value of  $\delta$  is observed for neutron and resonant X-ray measurements. Such differences

were observed earlier also [9] and this can be because two samples from same growth are used for measurements. A small change in Sr content changes  $\delta$  and the qualitative the change in  $\delta$  is in agreement with the previously reported studies [62].

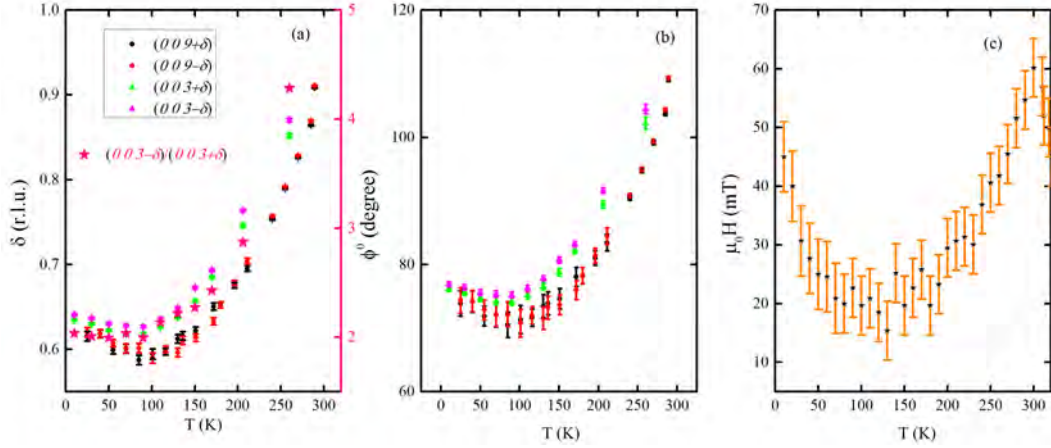


Fig. 5.3 (a) change in propagation vector with temperature for both neutron and X-ray measurements, with X-ray  $(003 \pm \delta)$  is measured, while with neutron  $(009 \pm \delta)$  is measured. The ratio of  $(003 - \delta)/(003 + \delta)$  is also plotted (pink curve) with a different scale (right-side). (b) Turn angle ( $\phi$ ) calculated from X-ray and neutron experiments (c)  $H_1$  field from magnetic measurement with temperature.

The value of  $\delta$  can be related to the turn angle ( $\phi$ ) between large (L) and small (S) spin blocks as  $\phi = 2/3\pi\delta$  considering equal angles between the adjacent spin blocks.  $\phi$  calculated from the position of the incommensurate reflection is plotted as a function of temperature in Fig. 5.3 (b).  $\phi$  changes from near  $140^\circ$  at 10 K to  $135^\circ$  at 300 K. It was found earlier that the value of  $\delta$  follows the first critical field for metamagnetic transition  $H_1$  [5], and our result also shows the changes in  $H_1$  follows same trends as that of  $\delta$  (see Fig. 5.3(c)).

## 5.2 In-field measurements with soft X-rays

We carried out our experiments in detail at two temperatures 100 K and 10 K in the high field chamber. The high field chamber, as mentioned in 3.5, has an opening of  $66^\circ$  in between the horizontal magnets. This provides us access to a maximum of  $(002.5)$  in the reciprocal space at the Fe  $L_3$  edge energy. Therefore, higher energy is used for orienting the samples. In Fig. 5.4 some fixed-Q energy scans at zero  $H$  for two Q values, incommensurate  $(002.38)$  and commensurate  $(001.5)$ , are shown. For these two Q values we have magnetic satellites at  $H = 0$  and at higher  $H$  respectively. Resonance of Fe  $L_3$  edge is found to be in a broad range from 704 eV to 714 eV. Similar broad energy spectrum was observed

by Mulders *et al.*[9] also. For the incommensurate reflection  $(0\ 0\ 2.38)$ , two maxima at 707.5 eV and 711 eV are observed in the energy scans and as expected,  $\pi$  is more intense than  $\sigma$ . A new satellite  $(0\ 0\ 1.5)$  is observed at higher  $H$  (discussed later), therefore, at zero  $H$  also fixed  $Q$  energy scan is measured for all the polarizations for  $(0\ 0\ 1.5)$ . In this case,  $\sigma$  channel intensity is more than that of  $\pi$ , which is not possible in case of magnetic reflections. In zero  $H$ , no  $(0\ 0\ 1.5)$  satellite is observed, therefore, this can be attributed to the reflectometry contribution in the background when incident angle  $\theta$  is very small. Energy curves at different  $H$  will be treated in Chapter-6.

Therefore, we used different energies from 707.5 eV to 711 eV to study the in-field magnetic structures which are shown as dashed lines in Fig. 5.4.

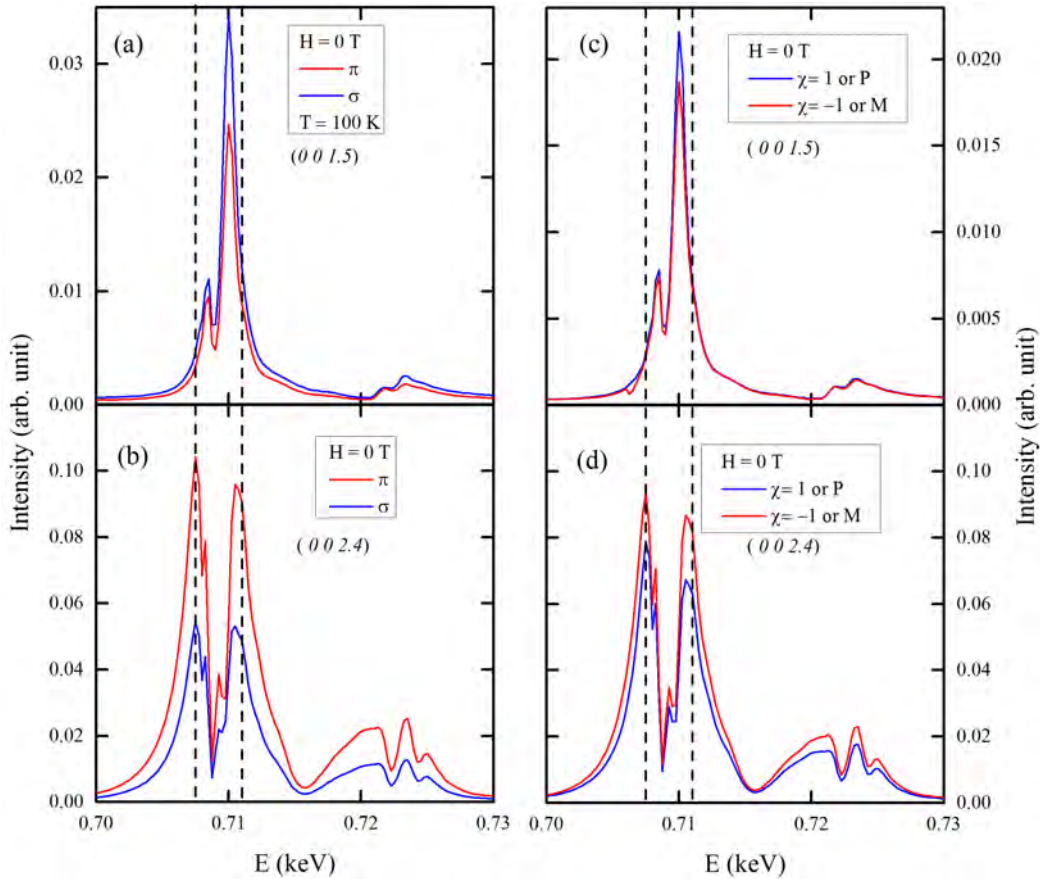


Fig. 5.4 Energy scans with fixed  $Q$  at  $H = 0$ . (a) and (b) are energy scans for  $\sigma$  and  $\pi$  polarizations at  $Q = (0\ 0\ 1.5)$  and  $Q = (0\ 0\ 2.4)$  respectively. (c) and (d) are for  $P$  and  $M$  polarizations with the same  $Q$  respectively.

Fig. 5.5 shows some of the  $(0\ 0\ l)$  scans at 100 K with  $E=707.5$  eV. In zero  $H$ , incommensurate  $(0\ 0\ 3-\delta)$  reflection becomes asymmetric, with a small kink at very low  $H$ . The origin of this kink is unknown, probably a small modification in the turn angle  $\phi$  which can

not be resolved with the present resolution at the present detector distance. It can be due to small modification in the helix as pointed out to be the so called *slightly modified helix* [8]. The small kink disappears around 9 mT (not observed for  $H = 0$ ). A new small satellite  $(0\ 0\ 2.25)$  appears with a commensurate propagation vector  $(0\ 0\ 0.75)$  in the  $\pi$  channel at 20 mT. At the same field a small peak develops  $(0\ 0\ 1.5)$  with equal intensity in  $\sigma$  and  $\pi$  channels. At 25 mT, only in  $\pi$  channel  $(0\ 0\ 2.25)$  is observed but  $(0\ 0\ 1.5)$  is observed in both the channels. With increase in  $H$  further at 30 mT, small intensity in  $(0\ 0\ 2.25)$  is also observed in  $\sigma$  channel. This intensity is so small that it may be due to imperfect polarizations also, so we will neglect it. At 40 mT, only the two commensurate reflections are observed and  $(0\ 0\ 3-\delta)$  incommensurate reflection disappears. After 50 mT,  $(0\ 0\ 2.25)$  reflection appears only in the  $\pi$  channel along with  $(0\ 0\ 1.5)$  in both the channels with equal intensity.

The intensity of the reflections from all the  $(0\ 0\ l)$  scans are integrated by using a Lorentzian fit and plotted against applied magnetic field and shown in Fig. 5.6. At 100 K the incommensurate reflection  $(0\ 0\ 3-\delta)$ , corresponding to helical phase, disappears near 40 mT in both the channels. Ratio between  $\pi$  and  $\sigma$  channel remains close to 2 (see Fig. 5.6), as is found in zero  $H$  measurements. Both the commensurate reflections start appearing at the same  $H = 20$  mT. The horizontal bars in Fig. 5.6 refer to the  $H$  values taken from  $M$  vs  $H$  curves as discussed in Chapter-4. Considerable intensity of  $(0\ 0\ 3-\delta)$  remains above  $H_1$  but the commensurate reflections starts appearing at  $H_1$ . Hearmon *et al.* observed that at 165 K and at 50 K both  $(0\ 0\ 1.5)$  and  $(0\ 0\ 3-\delta)$  are present up to 70 mT. In our case they are observed up to 40 mT. In contrast with Hearmon *et al.*'s result, we did not observe any commensurate reflections at  $(0\ 0\ 2)$ .

Table 5.2 Different satellite reflections observed for different fan structures and comparison with reference [6]. In this reference, apart from main phase satellites other satellites were also found, indicating mixture of phases.

	Our experiment		Ref.[6]		
	10 K	100 K	50 K	165 K	295 K
Helix	$(0\ 0\ 3-\delta)$	$(0\ 0\ 3-\delta)$	$(0\ 0\ 3-\delta)$ $(0\ 0\ 1.5)$	$(0\ 0\ 3-\delta)$ $(0\ 0\ 1.5)$	$(0\ 0\ 3-\delta)$ $(0\ 0\ 2)$ $(0\ 0\ 1.5)$
6 fan	absent	absent	$(0\ 0\ 3-\delta)$ $(0\ 0\ 2.25)$ $(0\ 0\ 2)$ $(0\ 0\ 1.5)$	$(0\ 0\ 3-\delta)$ $(0\ 0\ 2.25)$ $(0\ 0\ 2)$ $(0\ 0\ 1.5)$	$(0\ 0\ 3-\delta)$ $(0\ 0\ 2.25)$ $(0\ 0\ 2)$ $(0\ 0\ 1.5)$
4 fan	$(0\ 0\ 2.25)$ $(0\ 0\ 1.5)$	$(0\ 0\ 2.25)$ $(0\ 0\ 1.5)$	$(0\ 0\ 2.25)$ $(0\ 0\ 1.5)$	$(0\ 0\ 2.25)$ $(0\ 0\ 1.5)$	$(0\ 0\ 2.25)$ $(0\ 0\ 1.5)$
2 fan	$(0\ 0\ 1.5)$	$(0\ 0\ 1.5)$	$(0\ 0\ 1.5)$	$(0\ 0\ 1.5)$	$(0\ 0\ 1.5)$

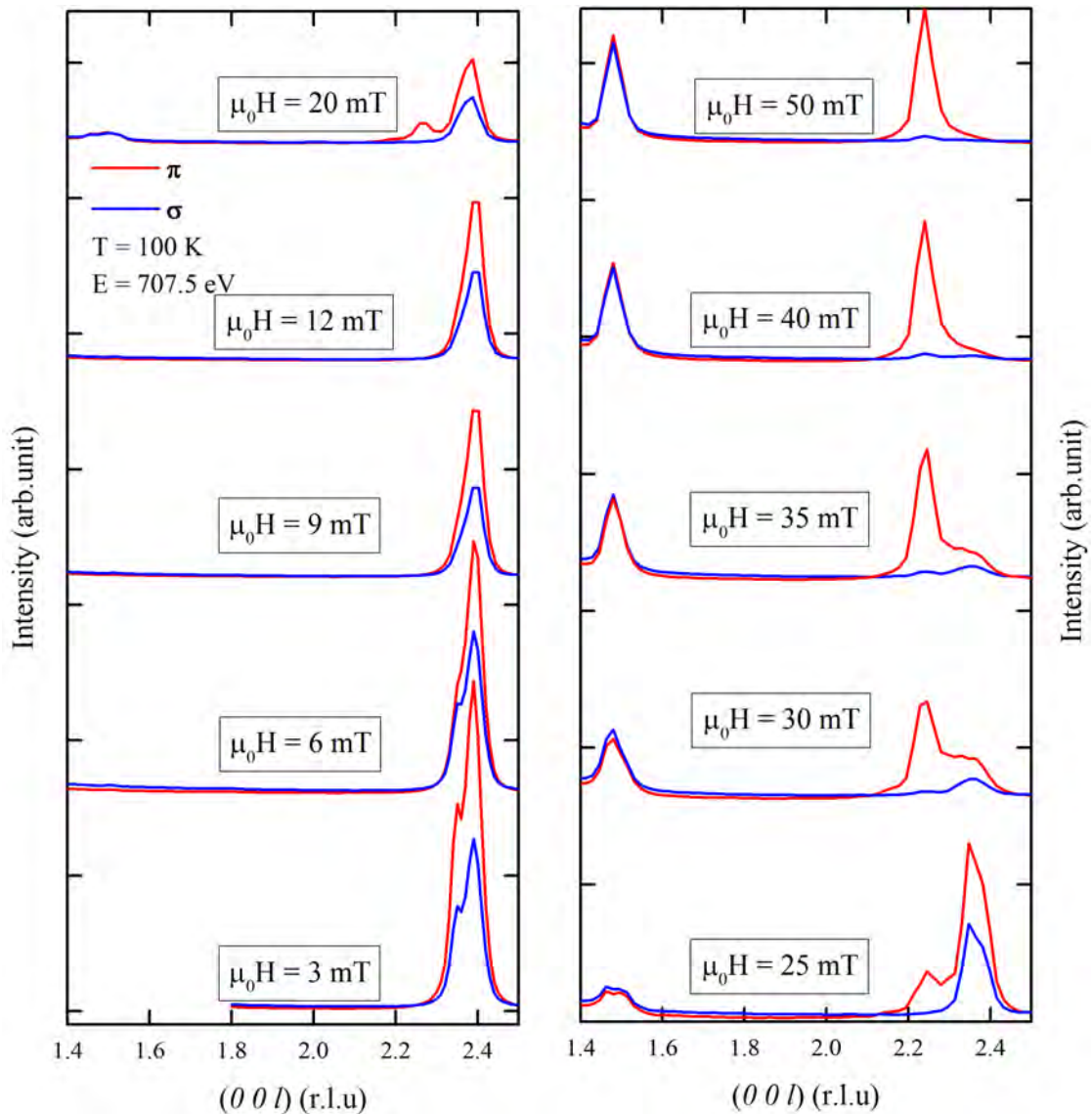


Fig. 5.5  $(00l)$  scans at different magnetic fields at 100 K with  $\sigma$  and  $\pi$  polarizations of incoming photons.

At 10 K only the incommensurate  $(003-\delta)$  reflection is observed up to 50 mT, see Fig. 5.7. Above 50 mT the  $(003-\delta)$  reflection becomes highly asymmetric and a shoulder starts appearing at  $(002.25)$ . The intensity at  $(003-\delta)$  gradually decreases in the  $\pi$  channel, whereas, at 100 mT in both  $\sigma$  and  $\pi$  channels it completely disappears. At the same  $H$ ,  $(001.5)$  reflection also starts appearing. Integrated intensity vs  $H$  curve shows that unlike 100 K, at 10 K the  $(003-\delta)$  persists above  $H_2$  and disappears before  $H_3$ . Both  $(001.5)$  and  $(002.25)$  are observed in between  $H_1$  and  $H_2$  and  $(002.25)$  disappears before  $H_3$ , whereas,  $(001.5)$  intensity increases. To get more accurate idea of the intensity, it is better

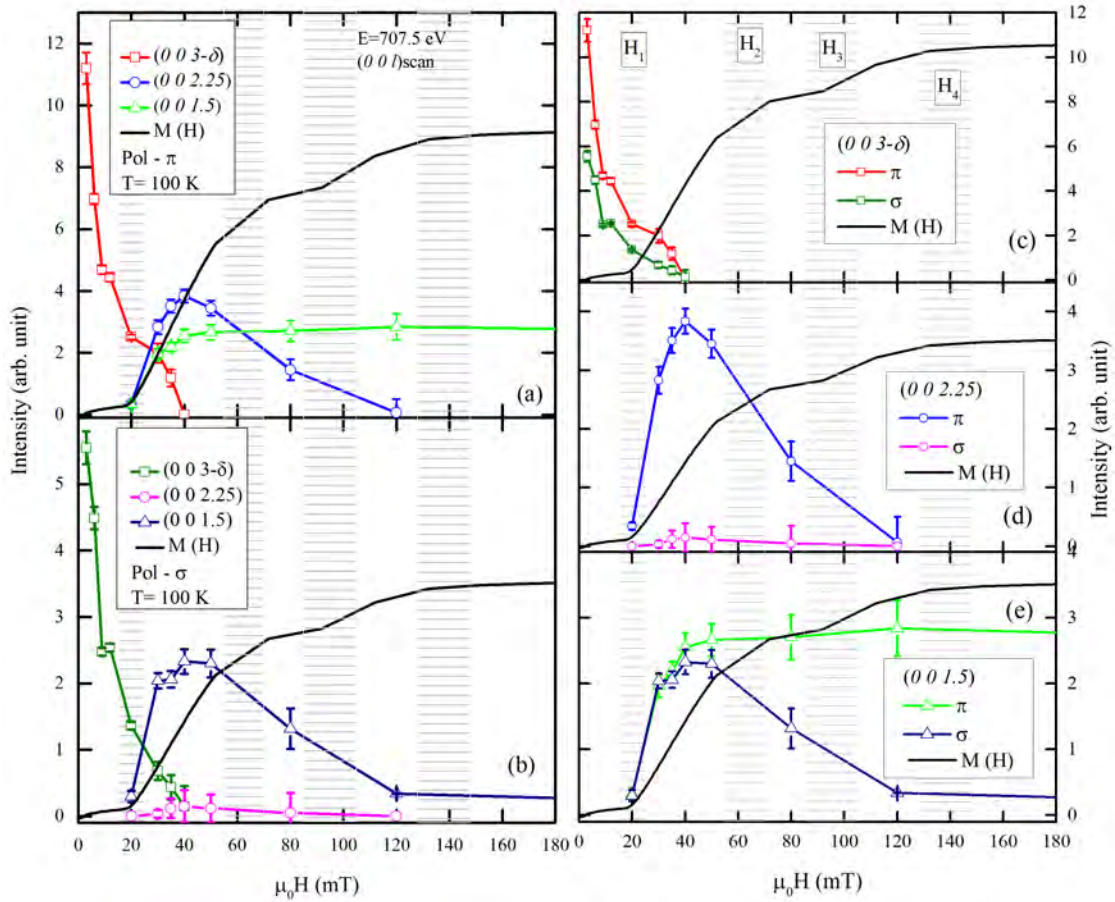


Fig. 5.6 Integrated intensity from the Lorentzian fitted peaks of  $(0 0 l)$  scans as shown in Fig. 5.5. (a) Incommensurate  $(0 0 3-\delta)$ , commensurate  $(0 0 0.75)$  and  $(0 0 1.5)$  reflections with  $\pi$  polarization. Initial magnetization curves at 100 K (arbitrary unit) are also shown for comparison. Horizontal gray bars refer to the metamagnetic transition fields at 100 K as explained in the previous chapter. (b) same as (a), but with  $\sigma$  polarization and (c), (d) and (e) are individual reflections shown separately. All measurements are performed in increasing field after zero-field cooling. Error in  $H$  is  $\approx 5$  mT.

to do transverse scans or omega scans rather than specular longitudinal scans (as discussed in section 3.4.4). In the omega-scan-measurement integrated intensity shows similar trends as that of the  $(0 0 l)$  scans. The  $(0 0 2.25)$  reflection is found between  $H_2$  and  $H_3$ , see Fig. 5.8.

As reported earlier, rather than sharp metamagnetic transitions, the microscopic magnetic structures coexist within large field regions [6]. Different reflections with different metamagnetic phases are tabulated in the Table 5.2 along with those observed in reference [6]. In our case, no reflection at  $(0 0 2)$  is observed at either of the temperatures 10 K or 100 K. This can be because of the close energy associated with adjacent metamagnetic structures

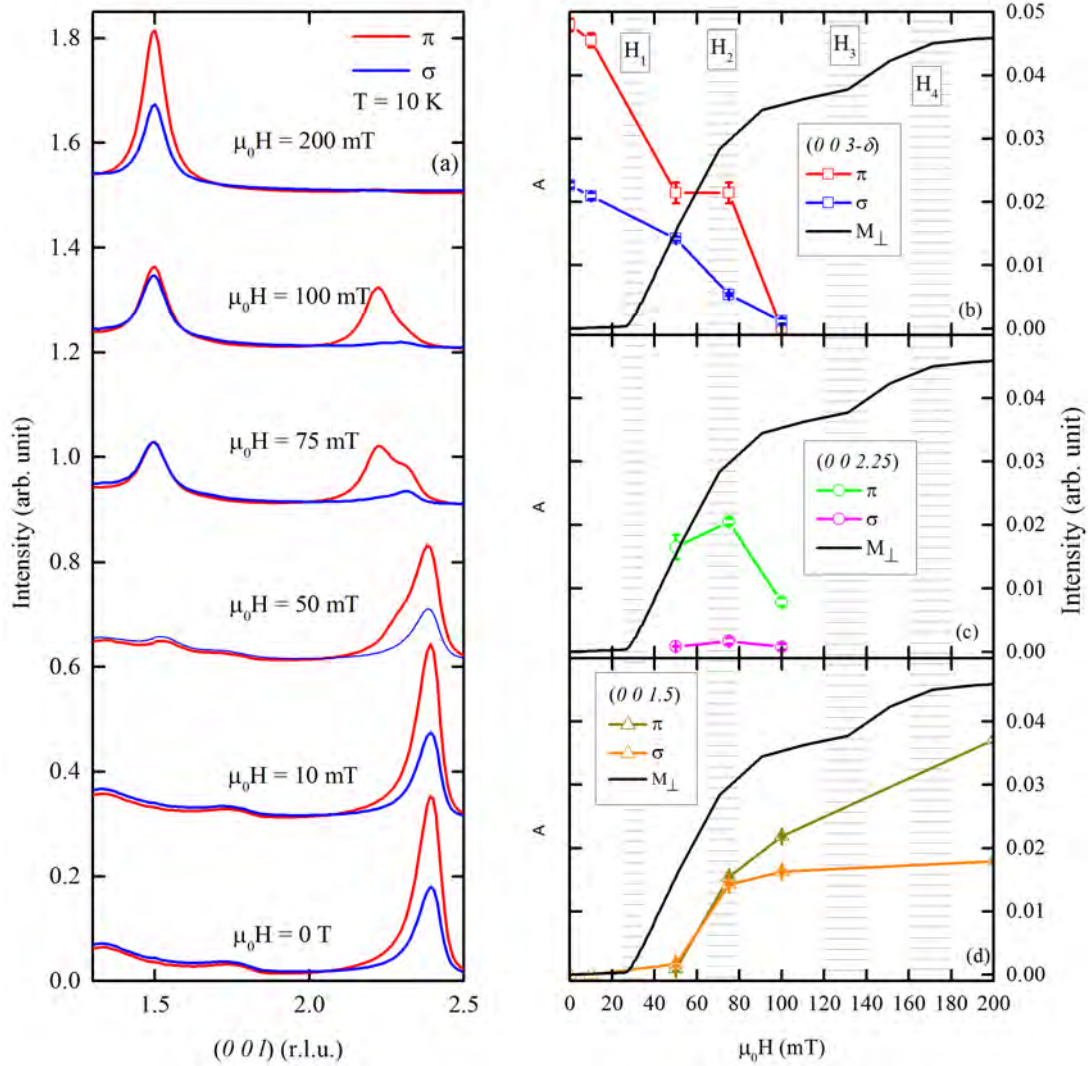


Fig. 5.7 (a) Some of the  $(00l)$  scans at different magnetic fields at 10 K and  $E = 711$  eV. (b) Integrated intensity from the Lorentzian fitted peaks of  $(00l)$ . Incommensurate  $(003-\delta)$  reflection with both  $\sigma$  and  $\pi$  polarizations, initial magnetization curves at 10 K (arbitrary unit) are also shown for comparison. Horizontal gray bars refer to the metamagnetic transition fields at 10 K as explained in the previous chapter. (c) is the same as (b) with  $(002.25)$  (d) with  $(001.5)$  reflections. All measurements are performed in increasing field after zero-field cooling. Error in  $H$  is  $\approx 5$  mT.

[6].

### 5.2.1 Discussion

There are various fan structures reported previously. From neutron diffraction, after helical phase, so called *4-fan* and *2-fan* structures were proposed for higher fields [8, 61]. *Intermediate-I*, which is the region between  $H_2$  and  $H_3$ , is primarily proposed to be consist-

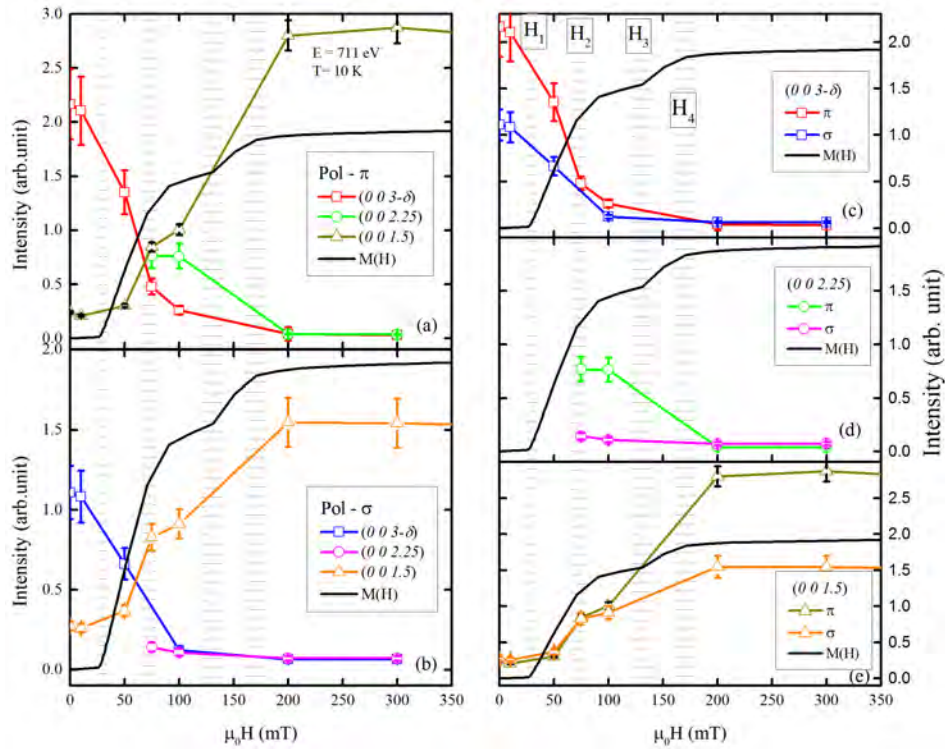


Fig. 5.8 Integrated intensity by Lorentzian fitting of the omega scans for  $\sigma$  and  $\pi$  polarizations. Initial magnetization curves at 10 K (arbitrary unit) are also shown for comparison. (a) and (b) are integrated intensities at different field of  $(0\ 0\ 3-\delta)$ ,  $(0\ 0\ 2.25)$  and  $(0\ 0\ 1.5)$  with  $\pi$  and  $\sigma$  polarization respectively. In (c), (d), and (e) individual reflections are shown separately for both the polarizations.

ing of the 4-fan structure. Another new 6-fan phase was found by soft X-ray diffraction [6] at lower  $H$ . These fan structures are shown in Fig. 5.9.

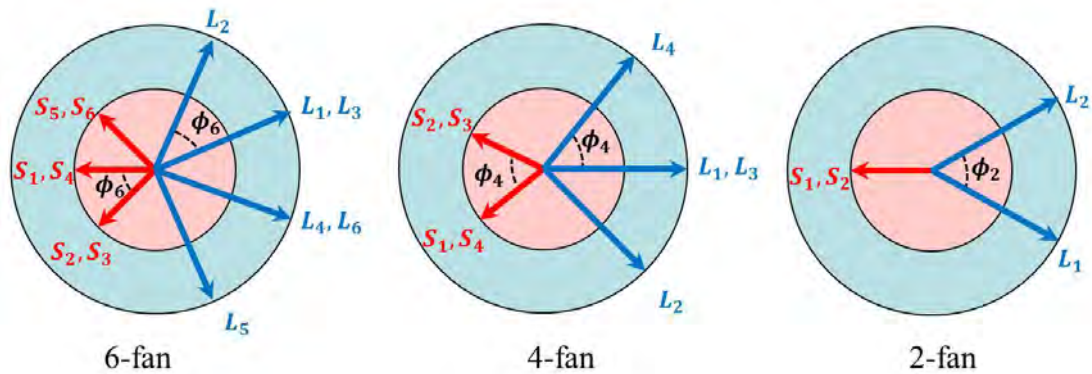


Fig. 5.9 Various fan structures reported in the literature. Large ( $L_k$ ) and small ( $S_k$ ) are stacked as  $L_k S_k L_{k+1} S_{k+1} \dots$  for  $k = 1, 2, 3, \dots$

Let us consider the 4-fan structure. We can resolve the components along the field direction  $H$  and perpendicular to it in a plane  $\perp[0\ 0\ 1]$ . For the components in the field direction, large spin blocks have a periodicity of  $2c/3$  in real space, which corresponds to a satellite reflection  $(0\ 0\ 3/2)$ . The small spin blocks have ferromagnetic contribution and it contributes towards the nuclear reflection. In case of perpendicular to field direction, both the large and small spin blocks have periodicity of  $4c/3$  in real space, which corresponds to satellite reflection  $(0\ 0\ 3/4)$ . Now, as a whole, for the 4-fan structure we can have magnetic contribution in the reflections  $(0\ 0\ 0) \simeq (0\ 0\ 3)$ ,  $(0\ 0\ 3-3/4)$  and  $(0\ 0\ 3-3/2)$ . Now if we see particularly, for the  $(0\ 0\ 2.25)$  reflection, it is the modulated moments that have only perpendicular to  $H$  components. Within our scattering geometry (see Fig. 3.5) it is the  $z_2$  component that contributes towards this magnetic reflection. In the matrix Eq. 3.25 only the  $\pi \rightarrow \pi$  channel probes the moment along  $z_2$ . Therefore, we should observe intensity in the  $\pi \rightarrow \pi$  channel only for  $(0\ 0\ 3/4)$  and it has contribution from both the L and S spin block components along  $z_2$ .

For the  $(0\ 0\ 3/2)$  reflection, modulated moments in the field direction contribute. For  $z_3 = 0$  we have contribution from  $z_1$  moments only and there is no intensity in  $\pi \rightarrow \pi$ . This makes intensity in incoming  $\sigma$  and  $\pi$  channels equal. For the 2-fan structure we have intensity in only  $\pi \rightarrow \pi$  channel (see section 6.1.4 for details). Therefore, higher intensity in incoming  $\pi$  channel than  $\sigma$  channel is due to 2-fan structure or other complex structures.

For our structure, considering the atomic coordinates and value of  $\gamma$  (see section 4.2), from our X-ray structural refinement we calculated the intensities in various channels. We used  $4/3$  unit cells to calculate the intensity for both  $(0\ 0\ 2.25)$  and  $(0\ 0\ 1.5)$  reflections. In our experimental limitations we could not measure the  $(0\ 0\ 3)$  reflection, therefore,  $(0\ 0\ 3)$  is not calculated.

In Fig. 5.11 calculated intensities in individual channels are plotted against the angle  $\phi$ . For the  $(0\ 0\ 2.25)$  reflection as can be seen in the  $\sigma \rightarrow \pi$  and  $\pi \rightarrow \sigma$  channel no intensity is observed. For  $z_3 = 0$  both the channels are sensitive to  $z_1$  moments. As we saw in Fig. 5.10 there is no contribution to the modulated moments along  $[0\ 0\ 1]$  corresponding to  $(0\ 0\ 2.25)$  reflection from the  $z_1$  components from both S and L spin blocks. Therefore, according to our calculations, we have intensity in only the  $\pi$  channel for  $(0\ 0\ 2.25)$  reflection. Intensity in the  $\pi$  channel increases as we increase  $\phi$ . For the  $(0\ 0\ 1.5)$  reflection, only the  $z_1$  components have periodicity along  $(0\ 0\ 1)$  equal to  $Q$ . As can be seen from the Fig. 5.11, we have equal intensity in  $\sigma \rightarrow \pi$  and  $\pi \rightarrow \sigma$ .  $\pi \rightarrow \pi$  intensity is almost zero for an entire range of  $\phi$ , except for some small values. Therefore, we can expect equal intensity in both the  $\sigma$  and  $\pi$  channels. With increase in  $\phi$  value,  $\sigma \rightarrow \pi$  and  $\pi \rightarrow \sigma$  intensities also increase.

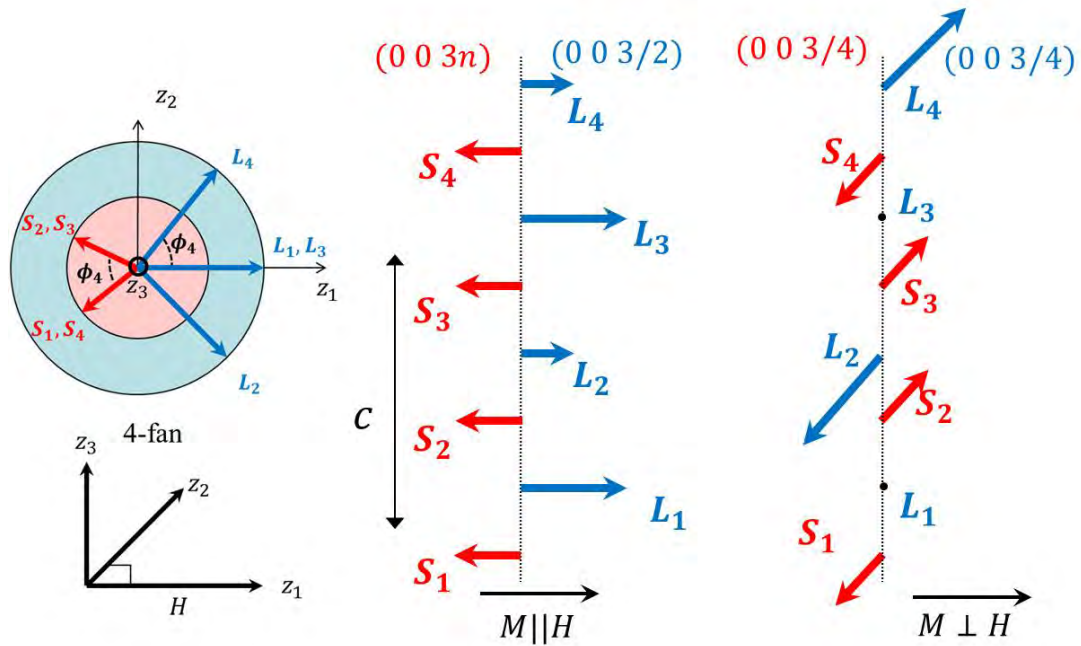


Fig. 5.10 Component of spin block moments ( $\perp c$ ) L and S of 4-fan structure along field direction and perpendicular to it. Corresponding satellite reflections due to the components are also shown.

It is difficult to compare direct values of the intensities with our experimental data as there are many other parameters like absorption, penetration depth etc involved. Therefore, we plotted the ratios of some of the parameters from our calculations in Fig. 5.11. For the  $(0\ 0\ 2.25)$  reflections,  $I_\pi/I_\sigma$  ratio makes no sense as  $I_\sigma$  is very small. For the  $(0\ 0\ 1.5)$  reflection, apart from very small values of  $\phi$ ,  $I_\pi/I_\sigma$  is equal to 1 for the entire range. As mentioned earlier, only the  $z_1$  components of the L-blocks contributes to intensity of  $(0\ 0\ 1.5)$  reflections in both the channels. Hence, equal intensity in both the channels will be one of the criteria for the 4-fan structure. Ratio of intensity of the  $(0\ 0\ 1.5)/(0\ 0\ 2.25)$  reflections can be a good tool to estimate the angle  $\phi$ . For  $I_\pi$  the ratio is smaller than unity. This means that for the 4-fan structure, intensity in  $(0\ 0\ 2.25)$  should be higher than that of  $(0\ 0\ 1.5)$ . The ratio varies smoothly from 0 to 1 with  $\phi$ . In Fig. 5.11(c) we plotted the calculated relative circular dichroism for both the  $(0\ 0\ 2.25)$  and  $(0\ 0\ 1.5)$  reflections and this will be discussed later in this chapter.

For the 6-fan structure, four propagation vectors were reported:  $(0\ 0\ 1/2)$ ,  $(0\ 0\ 1)$ ,  $(0\ 0\ 3/2)$  and  $(0\ 0\ 0)$ . We did not observe the first two propagation vectors in our sample. Therefore, presence of 6-fan structure in our sample can be ruled out. The 2-fan structure will be dealt with in detail in the next chapter.

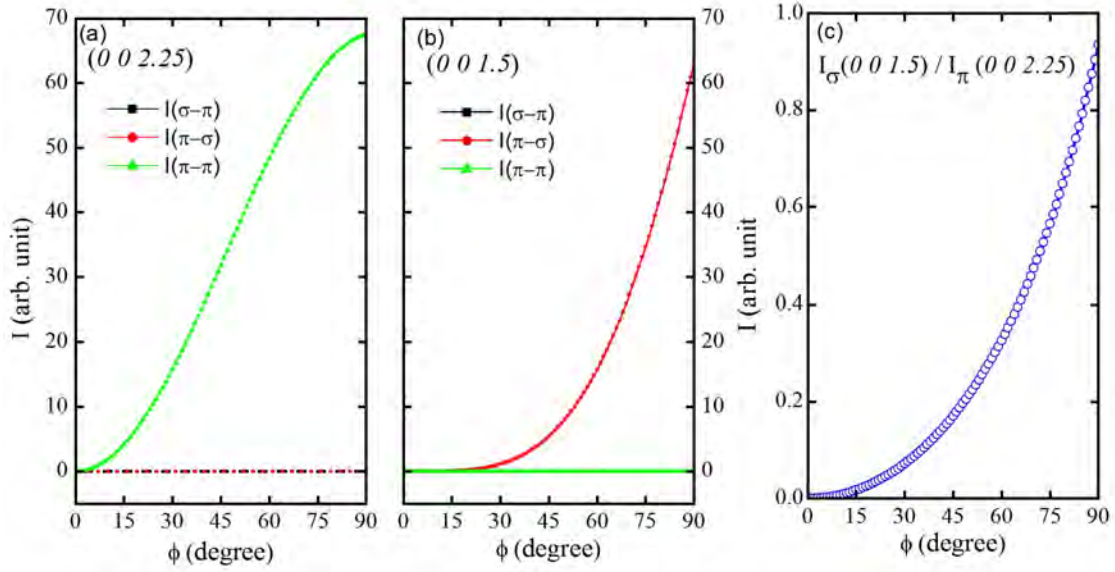


Fig. 5.11 Calculated intensity as a function of  $\phi$  for 4-fan structure for both (a)  $(0\ 0\ 2.25)$  (b)  $(0\ 0\ 1.5)$  reflections and (c) ratio of intensities of the  $(0\ 0\ 1.5)$  in  $\sigma$  channel to that of  $(0\ 0\ 2.25)$  in  $\pi$  channel.

## 5.3 Circular polarization

### 5.3.1 Spin chiral domains

As seen in Eq. 5.1, scattered intensity in the case of circular polarized light is determined by the sign of  $\chi$ . Chirality in the non-centrosymmetric (see section 2.1.3) sample determines the sign of  $\chi$ . For the same sample there can be a region with different chirality [124, 125]. Therefore, using beam-spots that are smaller than the regions of sample having same chirality, can give better estimation of the  $P$  and  $M$  intensities. The regions with the same chirality will be called as spin chiral domains after [10].

Hiraoka *et al.*[10] studied the spin chiral domains at zero  $H$ . Very recently, the effect of cooling in electric and magnetic field was also studied by the same group [11]. We used the same technique of mapping the sample surface with resonant diffraction using circular polarizations. For that we place the detector and sample orientation corresponding to a particular reflection and mapped the sample by measuring  $y$  scans at different  $z$ . Beam spots ( $100\ \mu\text{m} \times 150\ \mu\text{m}$ ) are optimized with scan parameters to avoid any dark regions in the sample.

In Fig. 5.12(a) and (b) a map of the sample surface with  $P$  and  $M$  polarizations is shown. In zero  $H$ , sitting at  $(0\ 0\ 3-\delta)$  (fixed  $Q$ ), sample surface is scanned by moving in in-plane direction ( $\perp z_1$ ) using step motors. Different high intensity and low intensity regions are

found in the sample surface. There are regions ranging from 0.2 mm to 2 mm distance with higher intensity in either of the polarizations. There is considerable contrast between  $P$  and  $M$  polarizations in the observed domains. The size of these spin chiral domains are comparable to those of earlier studies [10, 11].

In Fig. 5.12(c) the ratio between  $P$  and  $M$  is plotted. As mentioned earlier (see Fig. 5.1), we did not observe significant circular dichroism in our earlier  $(0\ 0\ l)$  scans because of the larger beam spots used. From the maps with smaller beam spots, ratio of  $P/M$  is found to range from 2 to 0.5, indicating that our results are very close to those of Mulders *et al.*[9]. It is a little smaller than the highest value observed by Hiraoka *et al.*( $\approx 5.8$ ). In Fig. 5.12(d) we normalized the difference of  $P$  and  $M$  with their sum to enhance the contrast between them.

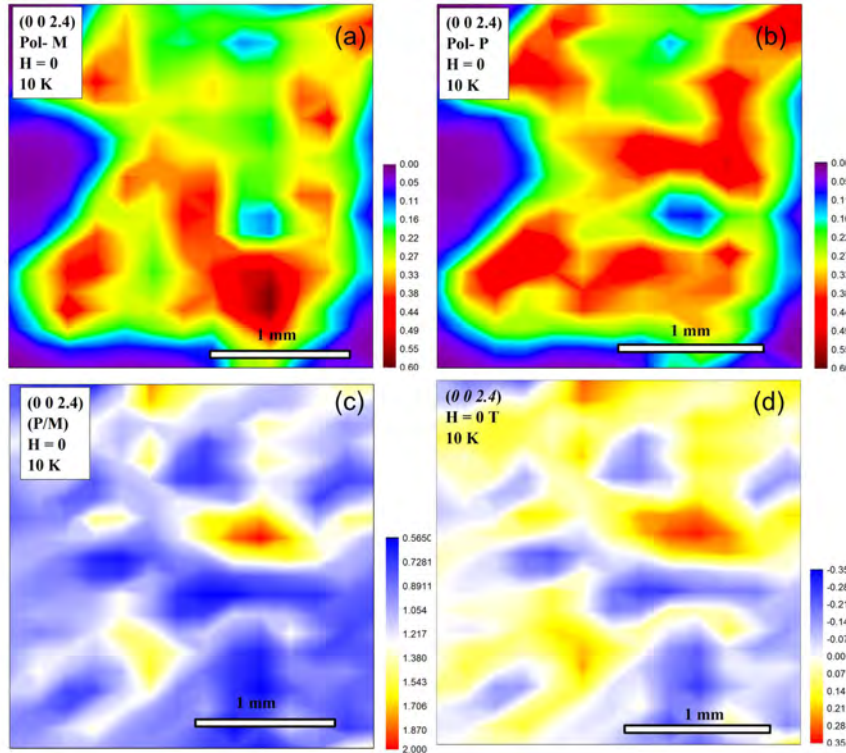


Fig. 5.12 (a) and (b) are maps of the sample surface with  $M$  and  $P$  polarizations respectively. (c) is the map of the ratio between  $P$  and  $M$  over the sample surface and (d) is difference between  $P$  and  $M$  normalized by their sum ( $\frac{P-M}{P+M}$ ).

The shape of the Chiral domains is arbitrary at  $H = 0$ . In different samples domains with different sizes are observed. In Fig. 5.13 two domain patterns of the same sample are compared at zero  $H$ . Here, (a) is measured at zero  $H$  after coming down from 340 K in zero  $H$ . (b) is same sample but a saturation field  $\mu_0 H = 3.5$  T is applied and after that  $H$  is

ramped back to 0 and the measurement is performed. It can be clearly seen that the sample does not remember the domain pattern corresponding to zero  $H$  for  $(0\ 0\ 3-\delta)$  reflection after applying a saturation field. It was already found that demagnetizing the sample by heating it above ordering temperature also produces different domain patterns [6].

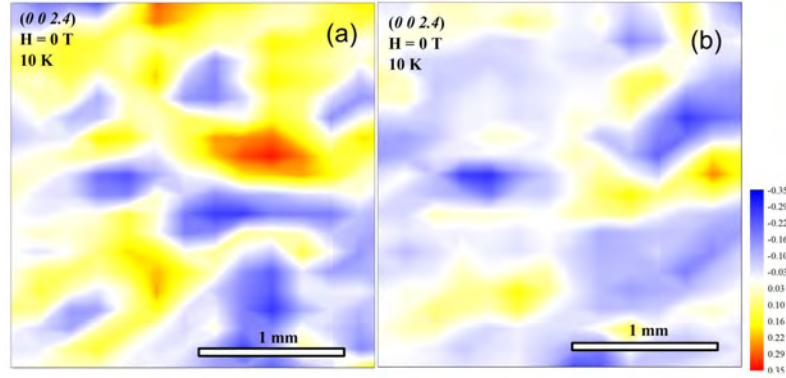


Fig. 5.13 (a) Same as Fig. 5.12 (d), (b) after applying saturation magnetic  $H$ .

We also tried to find out the intensity with circular polarizations for bigger sample volume. Comparatively larger beam spots ( $400\mu m \times 400\mu m$ ) are used for determining the changes in circular dichroism with  $H$ . From Fig. 5.14 it is seen that appearance and disappearance of reflections with  $H$  are the same as that for linear polarizations. At 100 K,  $P/M$  ratio is found to be in between 1.35 to 1.4 for the  $(0\ 0\ 3-\delta)$  reflection. This is relatively smaller compared to the values observed by Mulders *et al.* and Hearmon *et al.*

From Fig. 5.14 it can be seen that both the  $(0\ 0\ 2.25)$  and  $(0\ 0\ 1.5)$  reflections start appearing at the same  $H$ , just above  $H_1$ . Considerable intensity in the  $(0\ 0\ 3-\delta)$  reflection is found in the region  $H_1 < H_2$ . For the  $(0\ 0\ 2.25)$  reflection, in fields close to zero, the relative circular dichroism ( $I_\chi$ ) is observed up to 30 mT and it increases to 12 % at 80 mT. The increase in  $I_\chi$  starts before the critical field  $H_2$  determined from the macroscopic magnetization measurements. For the  $(0\ 0\ 1.5)$ ,  $I_\chi$  is near 10 % up to 50 mT but starts increasing afterwards.

At 10 K also  $P/M = 2$  for  $(0\ 0\ 3-\delta)$  at low  $H$ , but this decreases to 1 and then to less than 1 with increase in  $H$ . The  $(0\ 0\ 2.25)$  reflection has considerable intensity above  $H_2$ . It is difficult to draw conclusive evidence as there are not enough data points measured at low  $H$ .

From the calculations we have seen that, for the  $(0\ 0\ 1.5)$  reflection the intensities in the  $\sigma$  and  $\pi$  channels are equal for the 4-fan structure (see Fig. 5.11). From our integrated intensity we plotted the  $I_\pi/I_\sigma$  ratio in Fig. 5.16. At 100 K,  $I_\pi/I_\sigma$  is close to 1 up to  $H_2$  but after that it starts increasing. There is a normal increase after  $H_3$  due to change in the energy

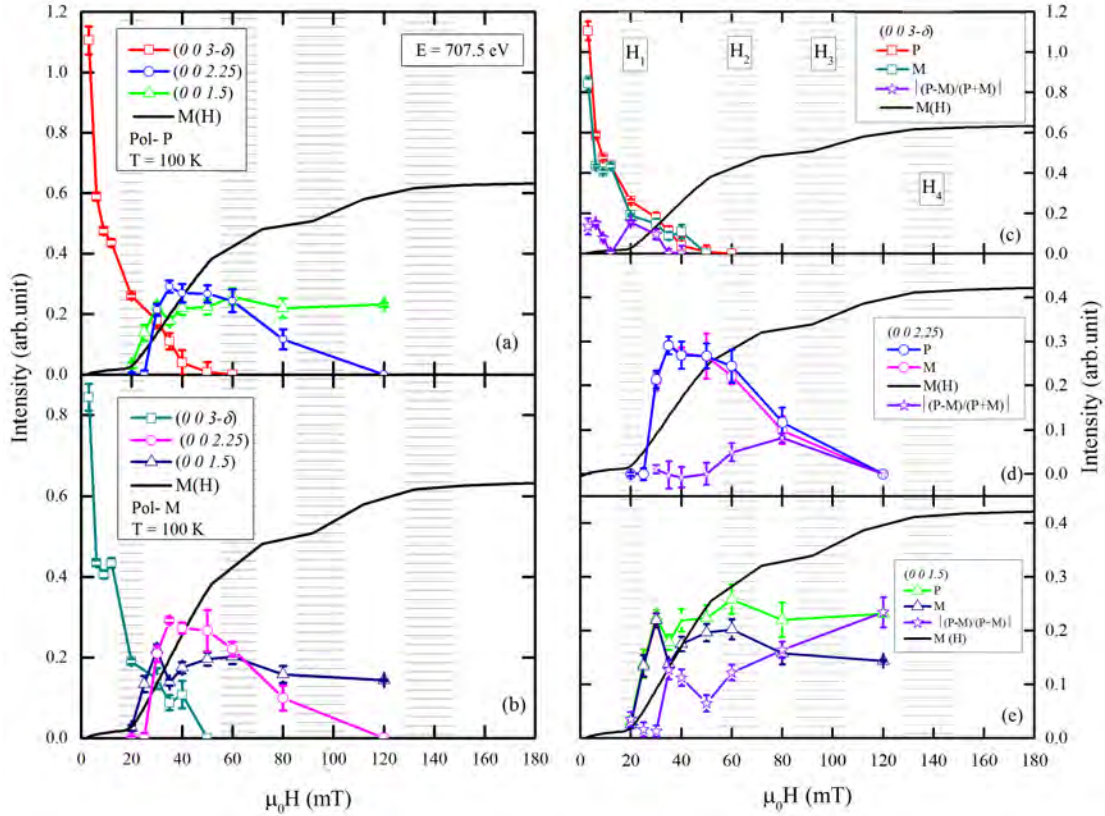


Fig. 5.14 Integrated intensity from the Lorentzian fitted peaks of  $(0 0 l)$  scans. (a) Incommensurate  $(0 0 3-\delta)$ , commensurate  $(0 0 0.75)$  and  $(0 0 1.5)$  reflections with circular  $p$  polarization. Initial magnetization curves at 100 K (arbitrary unit) is also shown for comparison. Horizontal gray bars refer to the metamagnetic transition fields at 100 K as explained in the previous chapter. (b) is the same as (a) with circular  $M$  polarization. (c), (d) and (e) are individual reflections shown separately for both the polarizations with  $I_\chi = \frac{I(P) - I(M)}{I(P) + I(M)}$ .

profile at this field, which is discussed in section 6.1.1. The ratio of the intensity in the  $\pi$  channel for  $(0 0 1.5)/(0 0 2.25)$  should be below 1 for all angles  $\phi$ . We can extract the angle  $\phi$  between the large spin blocks from this ratio. Our calculated value of  $\phi$  ranges from  $76^\circ$  to  $85^\circ$  as plotted in Fig. 5.16. From neutron diffraction  $\phi$  was estimated to be  $81.5^\circ$  at the onset of intermediate-I structure, which is the 4-fan structure [8].

In contrast to neutron scattering, where the 4-fan structure is in the field range  $H_2 < H_3$  [8], we observe both  $(0 0 1.5)$  and  $(0 0 2.25)$  reflections below  $H_3$ , but the intensity ratio does not fit above  $H_2$  for the 4-fan structure. Moreover, we have some small values ( $\approx 10\%$ ) of circular dichroism in this region. In addition, the  $(0 0 3-\delta)$  reflection does not disappear completely at  $H_1$  but extends above it. Therefore, we can anticipate that several phases co-exist. Above  $H_1$ , modified helix and 4-fan structure coexist and below  $H_2$ , the 2-fan structure and the 4-fan structure coexist.

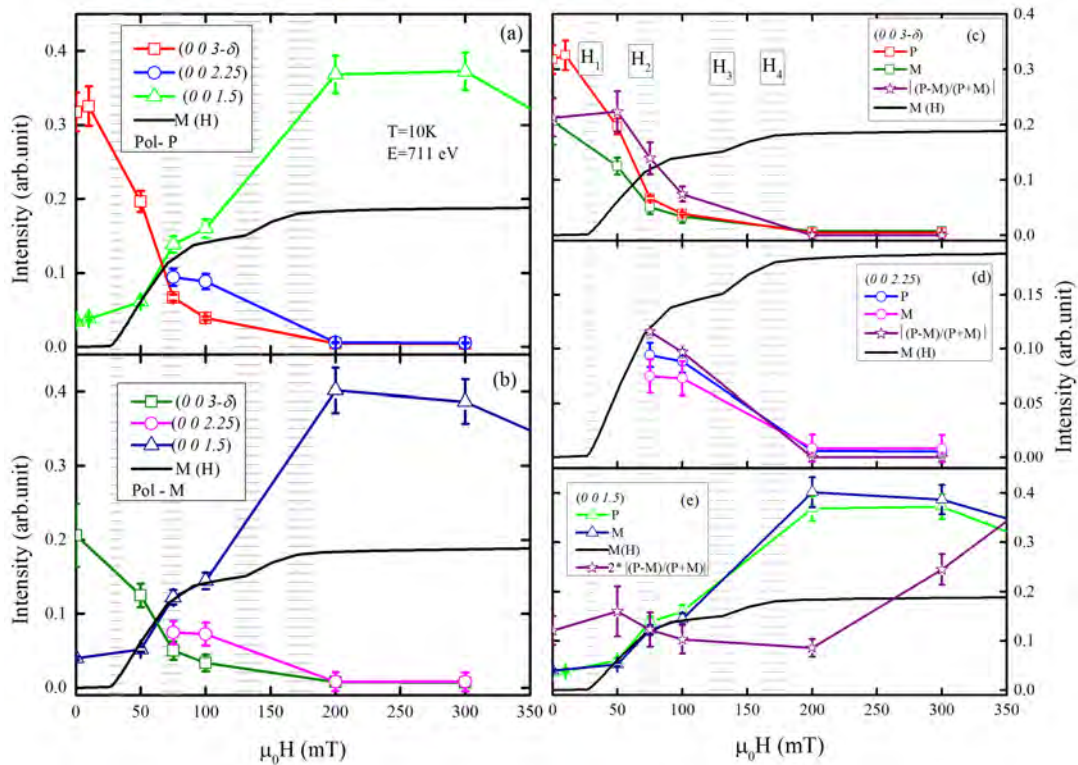


Fig. 5.15 Integrated intensity by Lorentzian fitting of the omega scans for  $P$  and  $M$  polarizations. Initial magnetization curves at 10 K (arbitrary unit) are also shown for comparison. (a) and (b) are integrated intensities at different fields of  $(0\ 0\ 3-\delta)$ ,  $(0\ 0\ 2.25)$  and  $(0\ 0\ 1.5)$  with  $P$  and  $M$  polarization respectively. In (c), (d), and (e) the individual reflections are shown separately for both the polarizations.

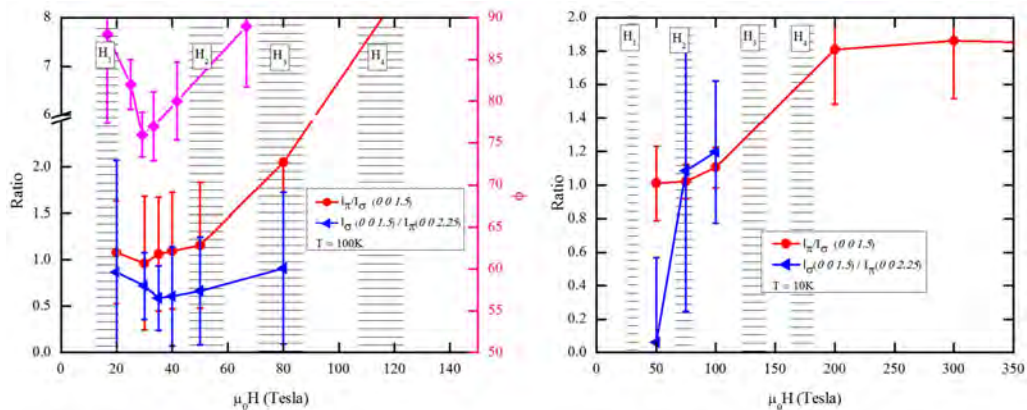


Fig. 5.16 The ratios on intensities in the  $\sigma$  and  $\pi$  channels for  $(0\ 0\ 1.5)$  reflection and ratio of intensity of  $(0\ 0\ 1.55)$  and  $(0\ 0\ 2.25)$  reflections in the  $\pi$  channels for different  $H$  at 100 K and 10 K.

At 10 K we do not have enough data points near low  $H$ . As seen in Fig. 5.7, for 50 mT ( $0\ 0\ 1.5$ ) intensity is much much lower than that of ( $0\ 0\ 2.25$ ) and ( $0\ 0\ 3-\delta$ ). Therefore, the ratio ( $0\ 0\ 1.5$ )/( $0\ 0\ 2.25$ ) for  $I_\pi$  channel is very small. We can assume this field to be the onset of the 4-fan structure. At 750 mT the ratio is a bit higher than unity in contradiction with the calculated value which is less than unity. However, the intensity in  $\sigma$  and  $\pi$  channel is same up to 100 mT and starts going to higher values after this field. In case of circular dichroism also we have seen that after 50 mT circular dichroism starts increasing. Therefore, at 10 K we can expect phase co-existence to a larger extent compared to that of 100 K. This is also evident from the magnetization data, where initial magnetization curve at 10 K does not show as distinct features as that at higher temperatures.

From our experimental results, we can claim that distinct phase boundaries can not drawn based on mere magnetization data. Significant phase co-existence appears at low  $H$ . Above a certain  $H$  only the ( $0\ 0\ 1.5$ ) reflection remains. This will be discussed in next chapter.



## Chapter 6

# Magnetic structure in the ferroelectric phase

Almost a decade ago in the year 2005, Kimura *et al.*[3] found magnetic field driven ferroelectricity in the intermediate-III phase, that is in between  $H_5$  and  $H_6$  critical fields (see Fig. 4.10). In 2009 Chai *et al.* found that near room temperature,  $H$  driven ferroelectricity can be found at much lower field than that found earlier (see Fig. 6.1) [119]. For that, the sample was annealed in oxygen. Phase boundary from magnetization measurement in Fig. 6.1(b), the intermediate-III phase or proposed onset of ferroelectric phase *i.e.*  $H_5$ , is different compared to the phase diagram from magnetoelectric measurements in Fig. 6.1(a). Moreover, a 2-fan structure reported earlier in literature does not support magnetic field driven ferroelectricity as per inverse IDM mechanism. This is the classic example of  $H$  driven ferroelectricity in hexaferrite, but the spin structure in the FE phase is not yet solved. Therefore, a detailed investigation of the spin structure in the FE phase is needed. In most of the other hexaferrites, in the field driven ferroelectric phases, magnetic ordering with cycloidal components are reported [55, 58, 66, 126–128]. For example, in the case of  $\text{Ba}_2\text{Mg}_2\text{Fe}_{12}\text{O}_{22}$ , below 195 K the zero- $H$  magnetic structure is longitudinal conical and it transforms to slanted conical on application of a small  $H$  and thus, gives magnetic field induced ferroelectric polarization in accordance with inverse DM model [55]. Therefore, we used microscopic diffraction techniques to investigate the in-field magnetic structures of the samples. We used mostly BZY-2 samples for our measurements. To verify the phase diagram we have used the high field diffractometer of the beamline UE46\_PGM-1 in the Helmholtz-Zentrum Berlin. In Chapter 5 we discussed the low field metamagnetic phases, here we present the magnetic structure in the FE phase. In this chapter we will deal with magnetic field above  $H_4$  only.

As-grown surface as well as cleaved sample surfaces are used for soft X-ray diffraction

experiments. In all the experiments a horizontal scattering geometry is used. We will first discuss our results of horizontal magnet geometry in section 6.1, then vertical magnet geometry in section 6.2. We will present our numerical calculations in section 6.3 and finally with our correct model we will explain the experimental results in the section 6.4.

## 6.1 Horizontal magnet geometry

The high field chamber, as mentioned in section 3.5, consists of a horizontal magnet. In the case of high field measurements, the magnet is rotated so that the field remains perpendicular to  $[001]$  with tolerance of  $\pm 2^\circ$  for changes in omega by  $4^\circ$ . However, experiments are also performed with  $10^\circ$  angle between  $[001]$  and  $H$  and no significant difference is observed. In Chapter-5 we presented magnetic structures in low  $H$ .

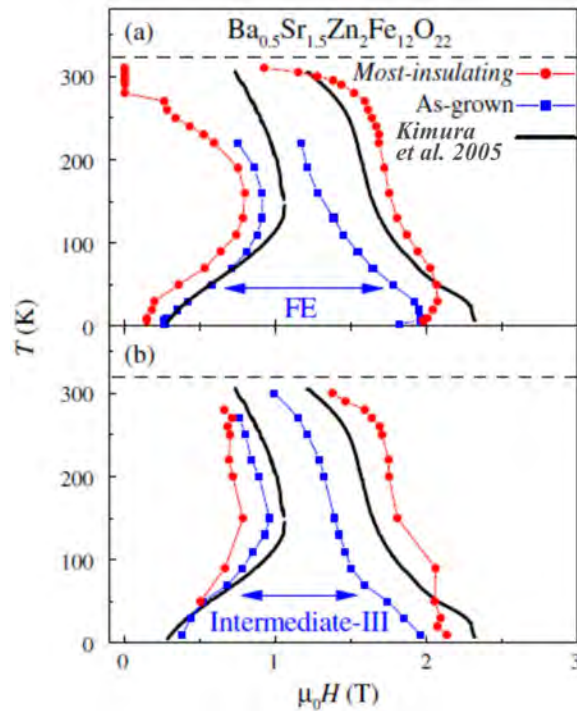


Fig. 6.1 Magnetolectric phase diagram of  $\text{Ba}_{0.5}\text{Sr}_{1.5}\text{Zn}_2\text{Fe}_{12}\text{O}_{22}$  from magnetolectric measurements from ref [119]. Black line is from ref [3] (M vs H), blue one is as-grown and red one is for sample after annealing in oxygen. Phase diagram was determined using the magnetolectric measurements. (b) Phase diagram from the magnetization measurements.

### 6.1.1 Energy dependence in magnetic field

Careful choice of resonance energy is very critical for resonance soft X-ray diffraction experiments. In Fig. 6.2 integrated intensity of  $(001.5)$  reflections at different photon energies are shown. Integrated intensities are calculated from Lorentzian fit of the reflections from

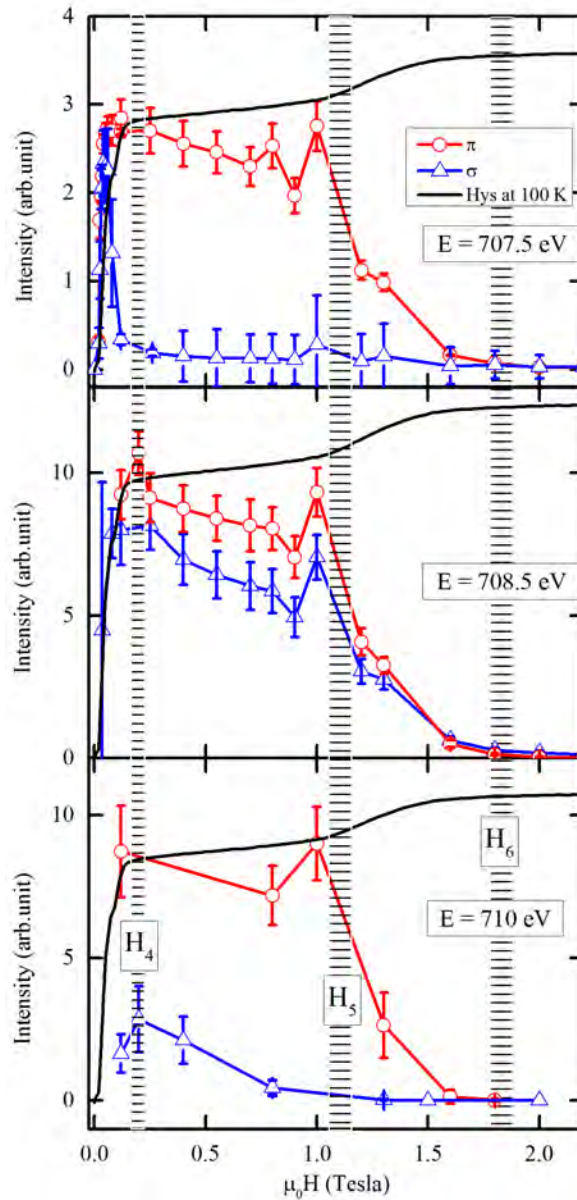


Fig. 6.2 Integrated intensity of  $(0\ 0\ 1.5)$  reflection from the Lorentzian fit of omega scans at different  $H$  for  $\pi$  and  $\sigma$  polarizations at 100 K. From the top at 707.5 eV, 708.5 eV and 710 eV resonance energy respectively. The horizontal bars represent various critical fields observed from the magnetization measurements.

$(0\ 0\ l)$  scans. In case of 707.5 eV, at fields higher than 0.06 T, the intensity in the  $\sigma$  channel comes down almost to zero whereas, for the  $\pi$  channel considerable intensity is observed up to 1.5 T, which is near the  $H_6$  critical field observed in magnetization measurements. For 708.5 eV energy, intensity in both the channels persists up to 1.5 T. However, the intensity for 707.5 eV experiments in  $\pi$  channel is also found to be 3 times smaller than that of 708.5

eV experiments. When 710 eV energy is used, the intensity in the  $\sigma$  channel also decreases considerably with increase in field like that of 707.5 eV experiment. This can be explained if we look at the energy scans at fixed Q very carefully.

In Fig. 6.3 intensity corresponding to energy 707.5 eV in the  $\sigma$  channel can be observed up to 80 mT (see the vertical green dashed line). Above 80 mT broad curve extending as low as 705 eV becomes very sharp and gives a maximum value at 708.5 eV (see the vertical pink dashed line). Only small intensity in the  $\sigma$  channel can be observed below 707.5 eV, but for the  $\pi$  channel even down to 710.5 eV intensity can be observed. Another maximum is observed for energy near 710 eV. For 710 eV also it is observed that the intensity in  $\sigma$  channel decreases comparatively more than that of 708.5 eV. The simulation of the energy spectra is beyond the scope of this thesis.

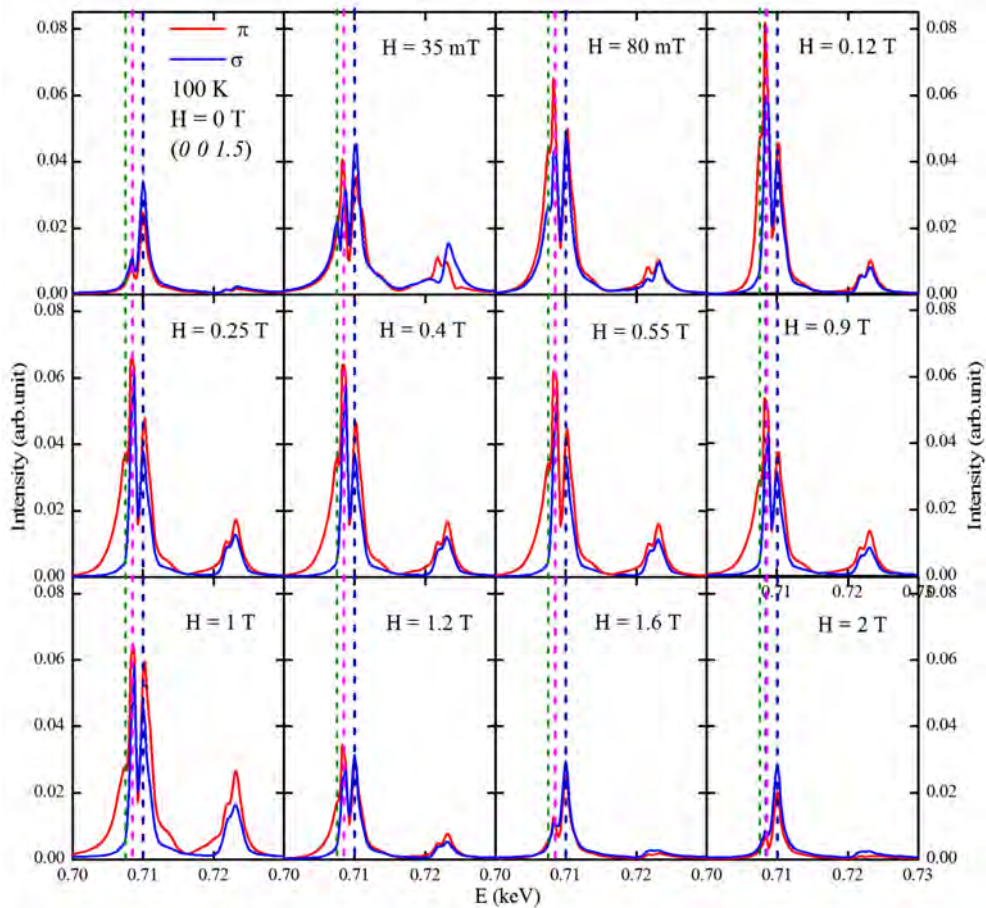


Fig. 6.3 Energy scans with fixed Q ( $0\ 0\ 1.5$ ) at different  $H$  at 100 K. Vertical dashed lines guide energy for the values as: olive - 707.5 eV, pink - 708.5 eV and navy blue - 710 eV.

In zero-field no reflection was observed at ( $0\ 0\ 1.5$ ). Therefore, the resonance enhancement in zero  $H$  can be considered to be from the reflectometry contribution from the shiny

surface of the sample. Complex magnetization dependence of the reflectometry contribution is neglected as the shape of the curve is similar at both zero  $H$  and at  $H = 3$  T. The spectra are replotted in Fig. 6.4 after subtracting the reflectometry contribution. After subtraction, the intensity in the  $\pi$  channel is found to be higher than that of  $\sigma$  channel all over the  $L_3$  edge. Therefore, we can use 708.5 eV and near 710-711 eV as reliable energies for our experiments above 80 mT.

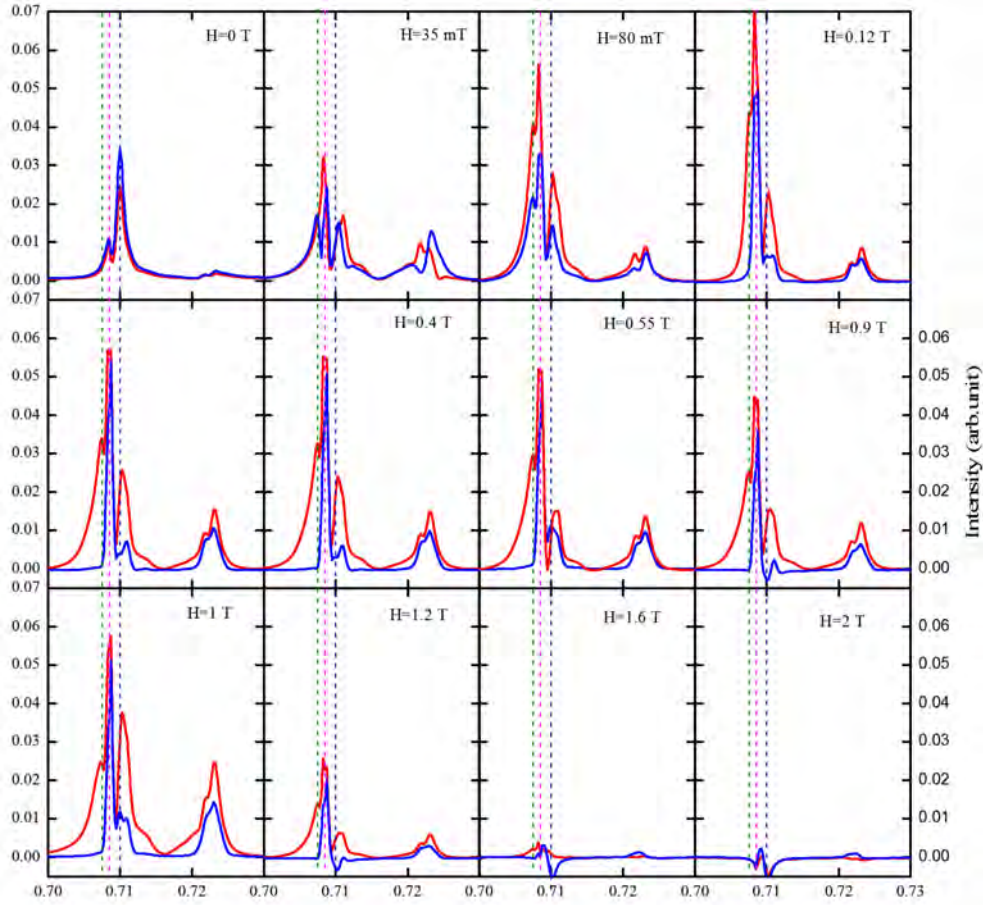


Fig. 6.4 Energy scans with fixed  $Q$  ( $0\ 0\ 1.5$ ) after subtracting the zero field E scans at 100 K. Vertical dashed lines guide energy for the values as: olive - 707.5 eV, pink - 708.5 eV and navy blue - 710 eV.

In the Fig. 5.7 of Chapter-5, we have seen that the intensity of the ( $0\ 0\ 1.5$ ) reflection starts appearing near 20 mT at 100 K, with equal intensity in  $\sigma$  and  $\pi$  channels. At the same time ( $0\ 0\ 2.25$ ) reflection was also present. This ( $0\ 0\ 2.25$ ) reflection is observed up to  $H$  close to  $H_3$ . Phase with only a ( $0\ 0\ 1.5$ ) reflection is found near  $H_4$  near 120 mT and above. The value of  $H_4$  was determined to be 0.16(2) T at 100 K from the magnetization

measurements (see Fig. 4.10). Individual intensities in both  $\pi$  and  $\sigma$  channels are found to be unchanged up to 1 T  $\approx H_5$  at 100 K and after that they start decreasing (see Fig. 6.5). Value of  $H_5$  was found to be 1.05(5) T at 100 K from magnetization measurements. Between 1 T and 1.2 T there are not enough data points to exactly determine the field region where the intensity starts decreasing. Therefore, it can be concluded that  $(0\ 0\ 1.5)$  reflection intensity starts decreasing near  $H_5$  and it disappears near  $H_6$  (1.78(5) T from  $M(H)$  measurements). To verify these results we measured at 10 K and found that here also the phase with only  $(0\ 0\ 1.5)$  reflection starts appearing near  $H_4$  (0.18(5) T from  $M(H)$  measurements) and disappears near  $H_6$  (2.20(5) T from  $M(H)$  measurements), see Fig. 6.6.

In Fig. 6.5(b), the ratio of  $I_\pi/I_\sigma$  is plotted along with the values normalized with the sum of intensity in both the channels.  $I_\pi/I_\sigma$  is found to be approximately same from 0.12 to 1.2 T and after that it starts decreasing. Values smaller than 1 are observed below 1.5 T but it can be due to small value of intensity as can be seen from the normalized values, (normalization by total intensity in  $\sigma$  and  $\pi$ ) which is indicated by black stars at the corresponding fields in Fig. 6.5 (b). At 10 K the average of  $I_\pi/I_\sigma$  is 1.66 (see Fig. 6.6). These values will be used later for quantitative analysis of different magnetic models.

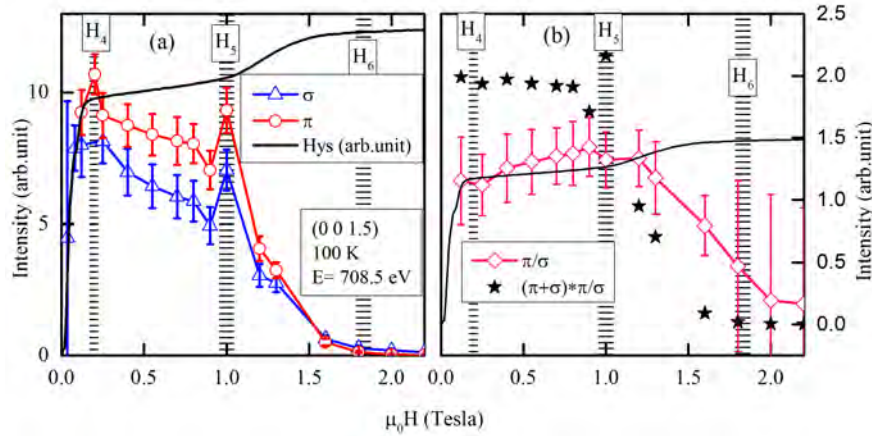


Fig. 6.5 (a) Integrated intensity from the Lorentzian fit of omega scans at different  $H$  for  $\pi$  and  $\sigma$  polarizations at 100 K and 708.5 eV. (b) Ratio normalized to total intensity and ratio between the intensities of  $\pi$  and  $\sigma$  in same scale. The initial magnetization curves at 100 K (arbitrary units) are shown for comparison. Horizontal bars are guide to the critical fields determined from the magnetization measurements.

We used circular polarization to determine the circular dichroism in diffraction. In Chapter-5 we have seen that the intensity of the  $(0\ 0\ 3-\delta)$  reflection depends upon the position on the sample and gives spin chiral domain configurations when the surface is mapped. Therefore, we used bigger beam spot of size  $400\ \mu\text{m} \times 400\ \mu\text{m}$  to collect intensity in omega scans and  $(0\ 0\ l)$  scans to get an average circular dichroism.

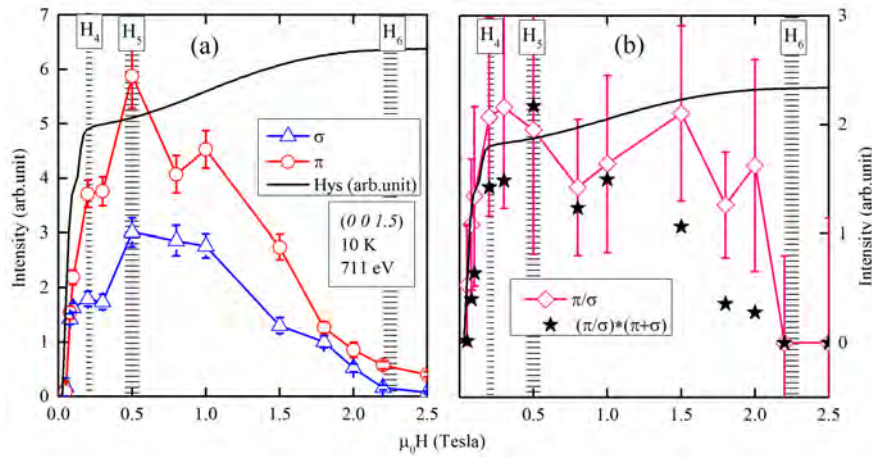


Fig. 6.6 (a) Integrated intensity from the Lorentzian fit of  $(0\ 0\ l)$  scans at different  $H$  for  $\pi$  and  $\sigma$  polarizations at 10 K and 711 eV. (b) Ratio normalized to total intensity and ratio between the intensities of  $\pi$  and  $\sigma$ . Initial magnetization curves at 10 K (arbitrary unit) are shown for comparison. Horizontal bars are guide to the critical fields determined from the magnetization measurements.

From Fig. 6.7 we can see that intensity of the  $(0\ 0\ 1.5)$  reflection follows a similar trend as that is observed for  $\sigma$  and  $\pi$  polarization at 100 K. The total intensity ( $P+M$ ) remains the same up to 1 T, but afterwards at 1.2 T it decreases 55 % and at 1.8 T it vanishes. Ratio between  $P$  and  $M$  and their difference is normalized with total intensity is approximately constant between  $H_4$  and shortly below  $H_6$ . The ratio  $P/M$  is 1.38 and average relative difference normalized to intensity is 16.%.

At 10 K the intensity of  $(0\ 0\ 1.5)$  reflection also starts to decrease above  $H_5$  and it vanishes near  $H_6$  as shown in Fig. 6.8. The  $P/M$  ratio is found out to be 2.04 and the relative difference normalized to total intensity is found out to be 34.%.

The two experiments were performed on as grown sample surfaces. Another experiment was carried out on a cleaved surface. For cleaving, the sample is glued to a metal piece and the sample holder and then a sudden force is applied. In Fig. 6.9 integrated intensities from the omega scans for  $P$  and  $M$  polarizations at 10 K in low  $H$  are plotted. It can be seen that a maximum intensity plateau is reached in much lower field than  $H_4$ , in fact it appears near  $H_2$ . Normalized difference and total intensity in  $P$  and  $M$  also remain almost flat after  $H_2$ . This can be due to some magnetization history in the sample and will be addressed in later sections. For as-grown surface also we repeated our experiments and found similar observations.

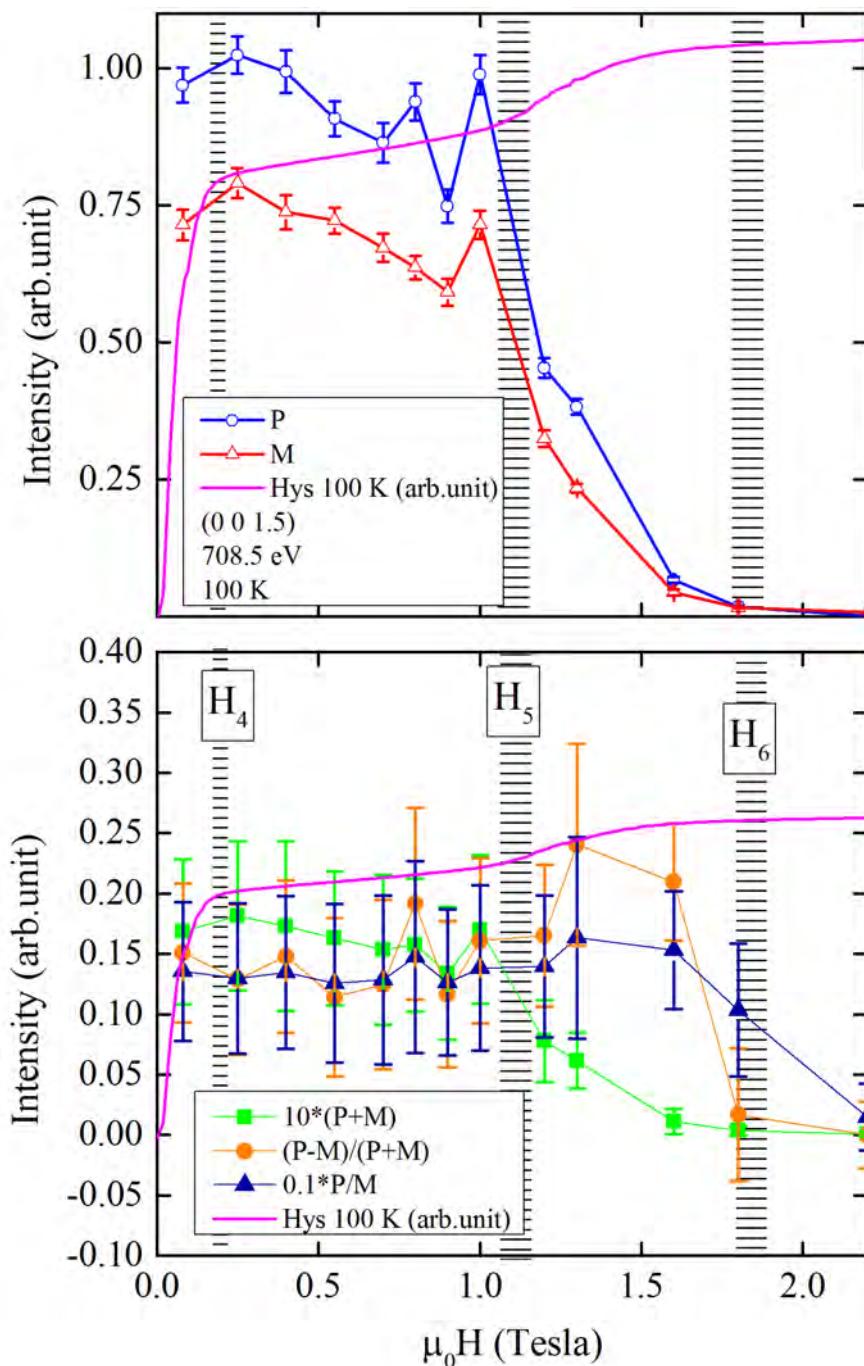


Fig. 6.7 *Top*: Integrated intensity from the Lorentzian fit omega scans at different  $H$  for  $P$  and  $M$  polarizations at 100 K and 708.5 eV. *Bottom*: difference normalized to total intensity and ratio between the intensities of  $P$  and  $M$ . Initial magnetization curves at 100 K (arbitrary unit) are shown for comparison. Horizontal bars are guide to the critical fields determined from the magnetization measurements.

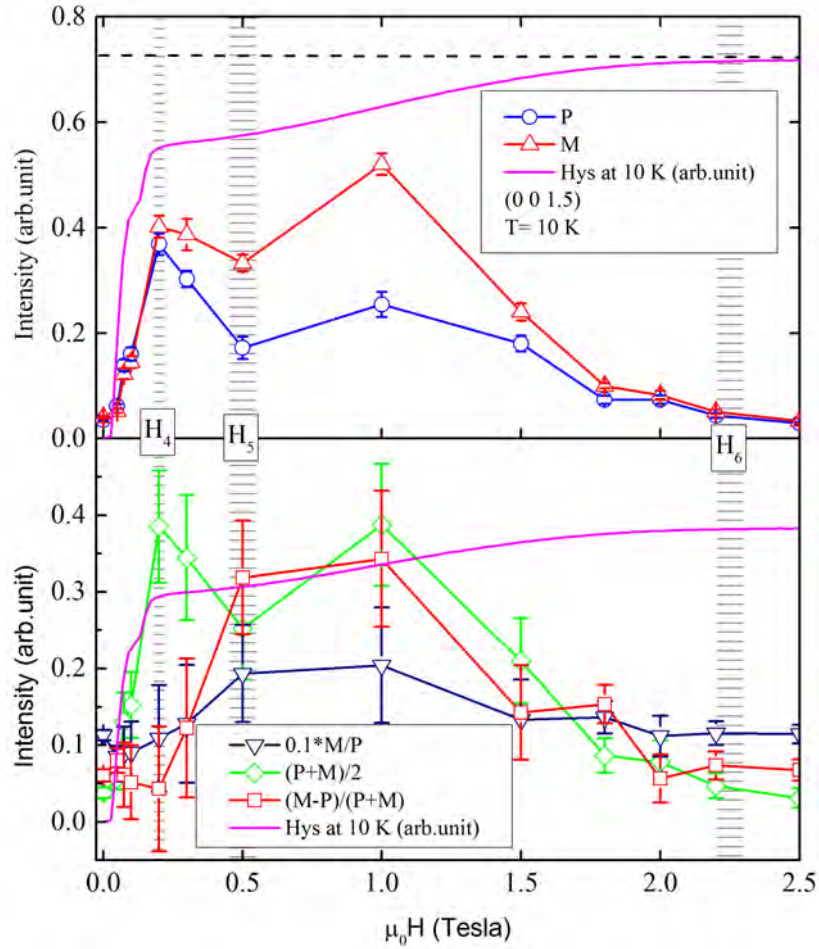


Fig. 6.8 *Top*: Integrated intensity from the Lorentzian fit  $(0\ 0\ l)$  scans at different  $H$  for  $P$  and  $M$  polarizations at 10 K and 711 eV. *Bottom*: difference normalized to total intensity and ratio between the intensities of  $P$  and  $M$ . Initial magnetization curves at 10 K (arbitrary unit) are shown for comparison. Horizontal bars are guide to the critical fields determined from the magnetization measurements.

### 6.1.2 Discussion

In the previous neutron diffraction studies on Al substituted  $\text{Ba}_{0.5}\text{Sr}_{1.5}\text{Zn}_2(\text{Fe}_{1-x}\text{Al}_x)_{12}\text{O}_{22}$  [66] and  $\text{Ba}_2\text{Mg}_2\text{Fe}_{12}\text{O}_{22}$  [65] Y-type hexaferrites, in the entire ferroelectric phase a  $(0\ 0\ l.5)$  reflection was present. In the case of Al substituted samples in the field driven ferroelectric phase the field region for FE overlaps with appearance of the propagation vector  $k_1 = (0\ 0\ l.5)$ . The incommensurate propagation vector  $k_2 = (0\ 0\ \delta)$  disappears in the magnetic field region where ferroelectric polarization appears [56] and  $k_1$  appears. In the case of  $\text{Ba}_2\text{Mg}_2\text{Fe}_{12}\text{O}_{22}$  three different ferroelectric phases were found where FE-3 phase contains only the  $(0\ 0\ l.5)$  propagation vector along  $(0\ 0\ l)$ . The other two ferroelectric phases contain  $(00.75)$  along with  $(0\ 0\ l.5)$  and  $(001)$  with  $(00\delta)$  incommensurate propagation. Therefore,

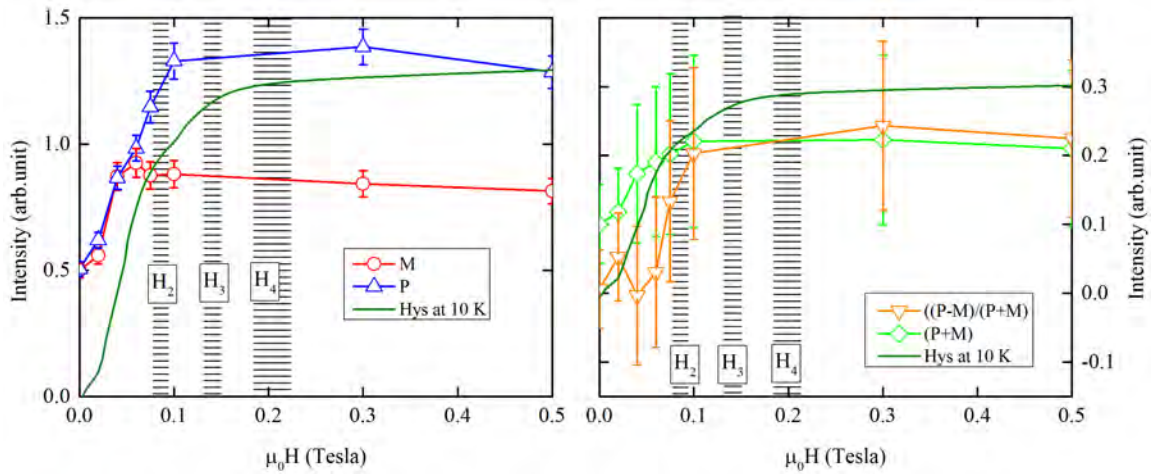


Fig. 6.9 *Left*: Integrated intensities from the Lorentzian fitted omega scans at different  $H$  at 10 K in a cleaved sample. *Right*: Sum of the integrated intensity in  $P$  and  $M$  channels, difference of  $P$  and  $M$  normalized to total intensity and ratio between  $P$  and  $M$  is plotted. Horizontal bars are guide to different metamagnetic critical fields measured by DC magnetization measurements.

we will try to find the relationship between our  $(0\ 0\ 1.5)$  reflections in soft X-ray diffraction and magnetic field driven macroscopic polarization in our sample.

From the above field dependence of the intensity of the  $(0\ 0\ 1.5)$  reflection, it can be seen that at all temperatures the intensity appears around  $H_2$  and  $H_3$  (with  $(0\ 0\ 2.25)$  reflection) and it becomes maximum above  $H_4$  and starts disappearing above  $H_5$ . No other anomalies are observed between  $H_4$  and  $H_5$  indicating that there is not phase transition between  $H_4$  and  $H_5$ . Therefore, onset of the field dependent polarization should be near  $H_4$  in contrast to the proposed  $H_5$  (intermediate-III) by Kimura *et al.*[3]. Measurements performed by Chai *et al.* indicate that with increasing resistivity of the samples in much lower  $H$ , polarizations can be obtained [119]. However, it is still higher than  $H_4$ . We observed the commensurate  $(0\ 0\ 1.5)$  reflections at much lower field. Like other Y-type hexaferrite mentioned above, if the phase with commensurate  $(0\ 0\ 1.5)$  is to be responsible for magnetic field driven ferroelectricity then according to our scattering data, polarization should appear at much lower  $H$  than that observed previously. We will discuss the lower boundary of FE phase in later sections.

Moreover, since the intensity of  $(0\ 0\ 1.5)$  starts to decrease above  $H_5$ , the region between  $H_5$  and  $H_6$  *i.e.*, intermediate-III can not be the only field driven ferroelectric phase. Intermediate-III phase can be considered as the transient phase connecting ferrimagnetic phase and intermediate-II. In other words, intermediate-II and intermediate-III are same phase, where intermediate-II is the onset of ferrimagnetic phase. The metamagnetic transition at  $H_5$  should be associated with the spin canting angle which causes the decrease in

intensity in  $(0\ 0\ 1.5)$  reflection.

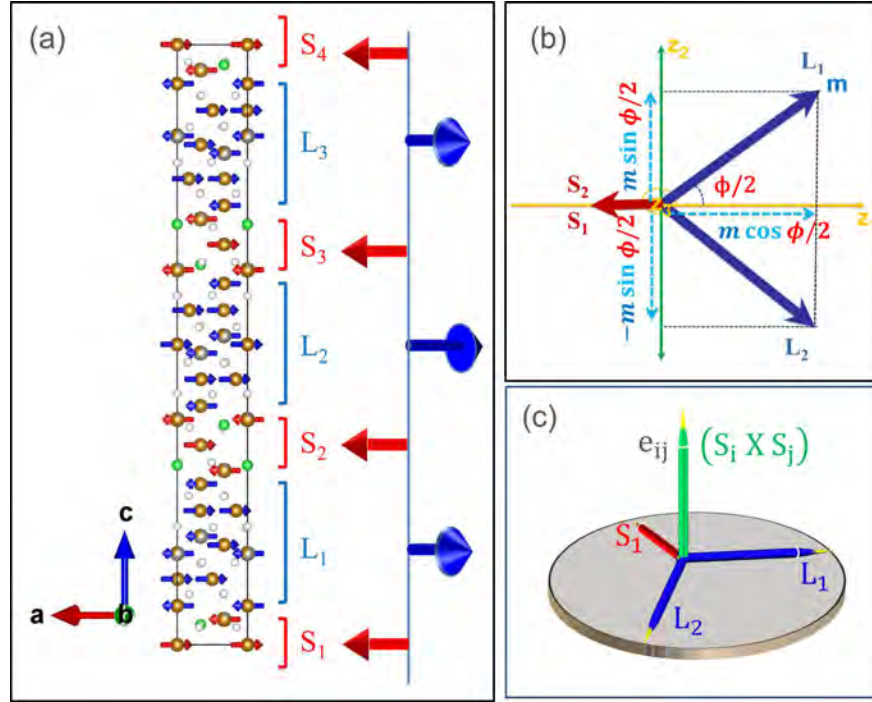


Fig. 6.10 (a) 2-fan structure for  $x = 0$  in  $\text{Ba}_2 - x\text{Sr}_x\text{Zn}_2\text{Fe}_{12}\text{O}_{22}$  with crystal structure and spin blocks (section 2.4.3). Schematic of the proposed 2-fan magnetic structures in intermediate-II and intermediate-III [3, 61]. (b) Schematic of the magnetic structure in 2 dimension with components of moments in three Cartesian co-ordinates  $z_1$ ,  $z_2$  and  $z_3$  as defined in Fig. 3.5. (c) Schematic explaining the propagation vector and the cross product of spin blocks. We refer to this model as model-A.

Let us consider the magnetic structures proposed previously [3, 6, 61]. The proposed 2-fan proper screw structure is schematically represented in Fig. 6.10. We will refer to it as model-A. In this model no clear distinction was proposed between intermediate-II and intermediate-III, but a change in the turn angle in the intermediate-III phase is considered as a transient phase connecting ferrimagnetic and intermediate-II phase [61]. However, both the magnetic structures are incompatible with a macroscopic polarization induced by IDM mechanism, as explained in section 2.3 in Chapter-2.

### 6.1.3 Intensity calculations and circular dichroism mapping

The following assumptions and rules are followed for the calculation of intensity and various dichroisms. We used various parameters to fit our models and a python program for calculating the intensity.

- The block spin model is assumed to be valid and within each block spins are collinear

(see section 2.4.3).

- Within each block the ferrimagnetic arrangements are there as explained in Fig. 2.18.
- Site (Fe vs Zn) occupancies are taken into consideration from Table. 4.2
- For structure factor calculations the actual positions of the atoms within the blocks are considered.

The structure factor for the magnetic satellite is given by the Eq. 3.25. We can write  $f^{XRMS}$  with the help of matrix given in Eq. 3.25. Now we calculate the structure factor for individual atoms in the  $3/2$  of the cell (the periodicity for  $(0\ 0\ 1.5)$  satellite reflection) structure factor contributions for  $\sigma \rightarrow \pi$ ,  $\pi \rightarrow \pi$  and  $\pi \rightarrow \sigma$  channels. In the appendix we calculated, for individual spin blocks for all the polarizations, the structure factor contributions which are finally summed up for calculating the total structure factor. Circular dichroism and linear dichroism are calculated by Eq. 3.28 and Eq. 3.29.

From Eq. 3.28 we see that a basic requirement for circular dichroism is a non zero intensity in the  $\pi \rightarrow \pi$  channel as well as in  $\sigma \rightarrow \pi$  channel. Linear dichroism is not simply the difference between total intensity in  $\pi$  and  $\sigma$  channels but is also the contrast between  $\sigma \rightarrow \pi$  and  $\pi \rightarrow \sigma$  channel, which can give rise to position dependence. The linear dichroism will be discussed in the experiments with vertical magnets.

#### 6.1.4 Model-A (2-fan structure)

We calculated the Intensity of  $(0\ 0\ 1.5)$  and relative circular dichroism (Rel\_Circ) to check whether the proposed structure is compatible with our results. We define angle  $\phi$  to be the angle between adjacent large spin blocks, *i.e.* between  $L_1$  and  $L_2$ . Since  $\sigma \rightarrow \sigma$  is zero for incoming sigma channel, intensity in total incoming  $\sigma$  channel is due to  $\sigma \rightarrow \pi$  and according to the matrix equation Eq. 3.25, it is sensitive to moment component along  $z_1$  and  $z_3$ . In model-A  $z_3$  component is zero, and hence,  $\sigma \rightarrow \pi$  and  $\pi \rightarrow \sigma$  have equal intensity where, we probe moments in  $z_1$  direction only. In the  $\pi \rightarrow \pi$  channel we are sensitive to moments in  $z_2$  direction, where only L-blocks contribute.

In the  $z_1$  direction there is only ferrimagnetic contribution from both the L and S spin blocks which gives magnetic intensity in  $(0\ 0\ 3n)$  reflections but not in  $(0\ 0\ 1.5)$ . Therefore, there is no intensity in the  $\sigma \rightarrow \pi$  and in  $\pi \rightarrow \sigma$  channels. In  $z_2$  direction only large spin blocks contribute to  $(0\ 0\ 1.5)$  reflections with magnetic cell equal to  $2/3$  of  $c$ . Therefore, we have non-zero intensity only in the  $\pi \rightarrow \pi$  channel in our calculations and is shown in Fig. 6.11. As stated above, with zero intensity in the  $\sigma \rightarrow \pi$  channel Rel\_circ is also not observed. Since this model can not explain the experimental circular dichroism, this model

is clearly not compatible with our data for the field regions both in the intermediate-II and intermediate-III.

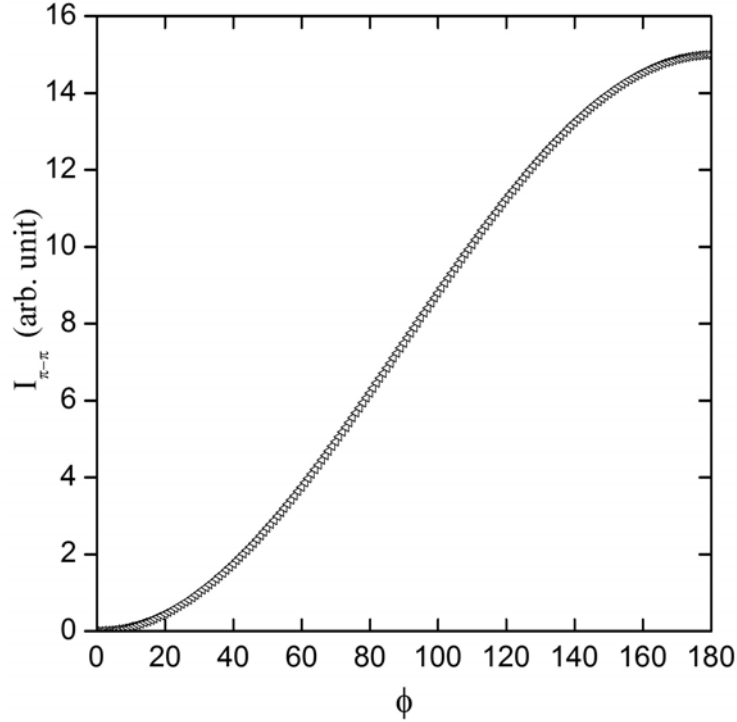


Fig. 6.11 Calculated  $I_{\pi \rightarrow \pi}$  for  $(0\ 0\ 1.5)$  satellite as a function of  $\phi$  for model-A.

To fit our experimental data as well as an  $H$  induced FE polarization we need to employ other more complex magnetic models. A simple model which can explain  $H$  induced FE polarization is a transverse conical model proposed for other hexaferrite compositions [55, 58, 66, 126–128]. For that we need the experimental values of Rel\_Circ and some additional parameters. We have seen in Chapter-5 that circular dichroism is a position dependent phenomenon, therefore, we mapped the surface in the presence of different magnetic fields. Fig. 6.12 shows maps of the intensity of the  $(0\ 0\ 1.5)$  reflection at 10 K in different  $H$ . In the first row, intensity maps of  $(0\ 0\ 1.5)$  reflection are shown at different  $H$  for  $P$  polarizations. Peak intensities of both 0.5 T and 1 T are comparable, but at 1.5 T it reduces significantly. In the second row, intensity maps are shown for  $M$  polarization showing distinct regions of high intensity.

From Fig. 6.12 a strong sample position dependence of the diffracted intensity for circularly polarized light is seen, which is different for  $P$  and  $M$  polarizations. Therefore, a more reliable value Rel\_Circ is extracted from the individual maps. The extracted values of Rel\_circ, according to formula 3.28, as a function of sample position are plotted in Fig. 6.13. We see two distinct regions with Rel\_circ having positive and negative values. The

size of the region with one chiral domain has sharp changes at the boundary with higher values of Rel\_circ for 0.5 T and 1 T compared to that of 1.5 T. For all the fields a particular shape of the spin chiral domains is observed. This shape is retained in all the high field measurements.

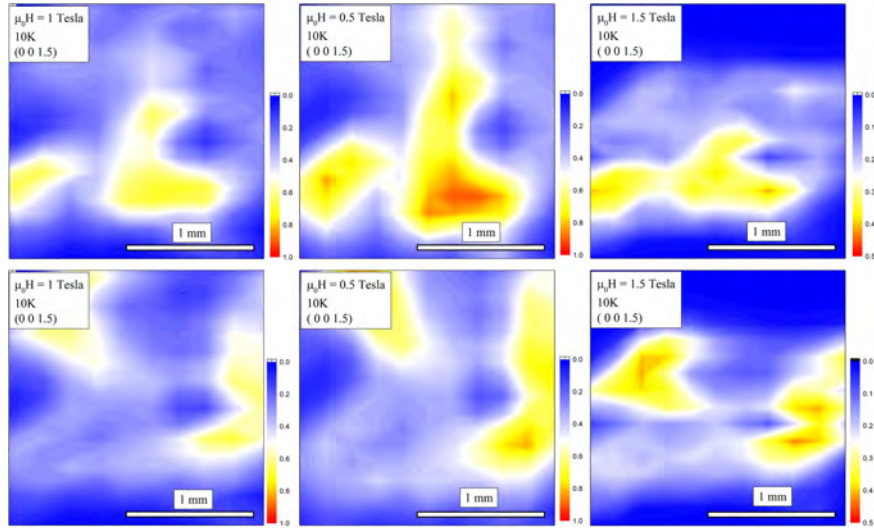


Fig. 6.12 Position dependence of individual intensities of circular  $P$  and  $M$  polarizations at 10 K in different fields for  $(0\ 0\ 1.5)$ . Color bar indicates intensity in arbitrary unit.

From the map of the sample it is evident that when we measure the field dependence of intensity with omega scans or  $(0\ 0\ l)$  scans using a wide beam, in a particular field we will get a domain average of the intensity depending on the beam spot size used. The size of the region with higher intensity, for a particular polarization, is not the same at all the fields. Therefore, we calculated the average of first 50 highest data points (experimental Y-scans) from the map of the surface for relative circular dichroism and this can be seen in Table 6.1. The difference between the Rel\_Circ extracted from the maps and that from omega scans with larger beam spot is very high at 100 K. We obtained 16 % circular dichroism from omega scans whereas for our map we got an average of 32.5%. This is not the case when we used a smaller beam spot where, in case of 10 K data we get  $\approx 32.5\%$  from map and 34(8)% from  $(0\ 0\ l)$  scans. A larger beam spot gives a domain average of circular dichroism with the intensity in  $P$  and  $M$  channels are coming partly from the regions with higher positive or higher negative relative circular dichroism. Therefore, we will use the average values from the maps in all the position dependent parameters. To verify our results we used another sample which is much smaller compared to the previous sample and mapped its surface. In this sample Rel\_Circ is observed to be divided into positive and negative regions almost diagonally (see Fig. 6.15). Therefore, if the incoming beam is hitting the middle of the sample then it can have contribution from both the positive and negative regions. Lower

values of relative circular dichroism in Fig. 6.7 are thus due to the contribution from both the spin chiral domains.

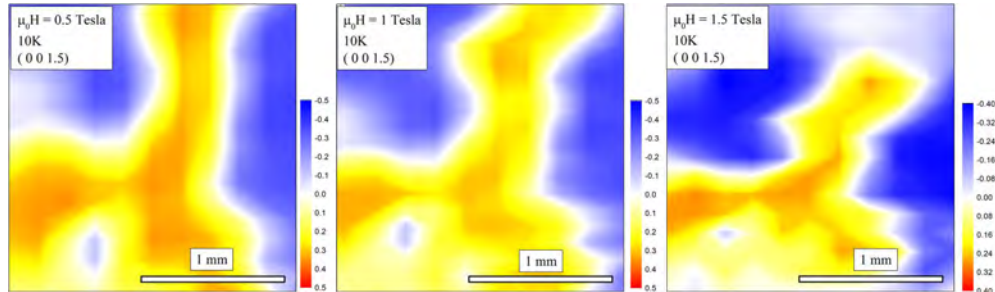


Fig. 6.13 Position dependence of the relative circular dichroism  $(P-M)/(P+M)$  at 10 K in different fields for  $(0\ 0\ 1.5)$  reflections. Color bar indicates  $(P-M)/(P+M)$ .

It is difficult to explain why a particular domain configuration is observed in the sample used. It may have some domain wall pinning effect by defects in the sample, which leads to the particular domain configuration. The sample was heated several times to 350 K, which is above the spin-reorientation temperature, and mapping for relative circular dichroism at 1 T yielded the same domain configuration. Higher than the saturation field ( $> 4$  T) was applied and the after that also mapping produces same domain configuration at 1 T. Therefore, we can conclude that neither of thermal nor magnetic hysteresis effect is there in the spin chiral domains. This is also visible from the magnetization curves, where no hysteresis is observed at higher field in the magnetic field vs moment and 1 T temperature dependent field cooling and field warming measurements, as discussed in Chapter-4.

Interestingly, when we reversed the field direction and measured the intensity in  $P$  and  $M$  channel as a function of sample position, we found that the domains with higher  $P$  or  $M$  are not the same for positive field but they exchange positions. In Fig. 6.14 we show the intensity maps for  $P$  and  $M$  polarizations at 1 T and -1 T field. Map for 1 T for  $P$  polarization is similar to that of  $M$  polarization for -1 T and vice versa. This is clearly visible in the relative circular dichroism maps (top figure). Positive circular dichroism regions become negative and negative circular dichroism regions become positive on reversing the field direction (see the color bar). Since in the domain configuration we did not observe any hysteresis, either thermal or magnetic, we checked this behavior with a different sample.

We reversed the field at 100 K also and found that the domain configuration is again inverted on reversing the field direction. The maps on the right of Fig. 6.15 show that in the case of this sample also upon reversing the field the relative circular dichroism changes sign. Moreover, the domains are smeared out at 1.2 T compared to that at 0.4 T and 0.8 T, which was also observed in the previous sample. Therefore, changing sign of the spin chiral

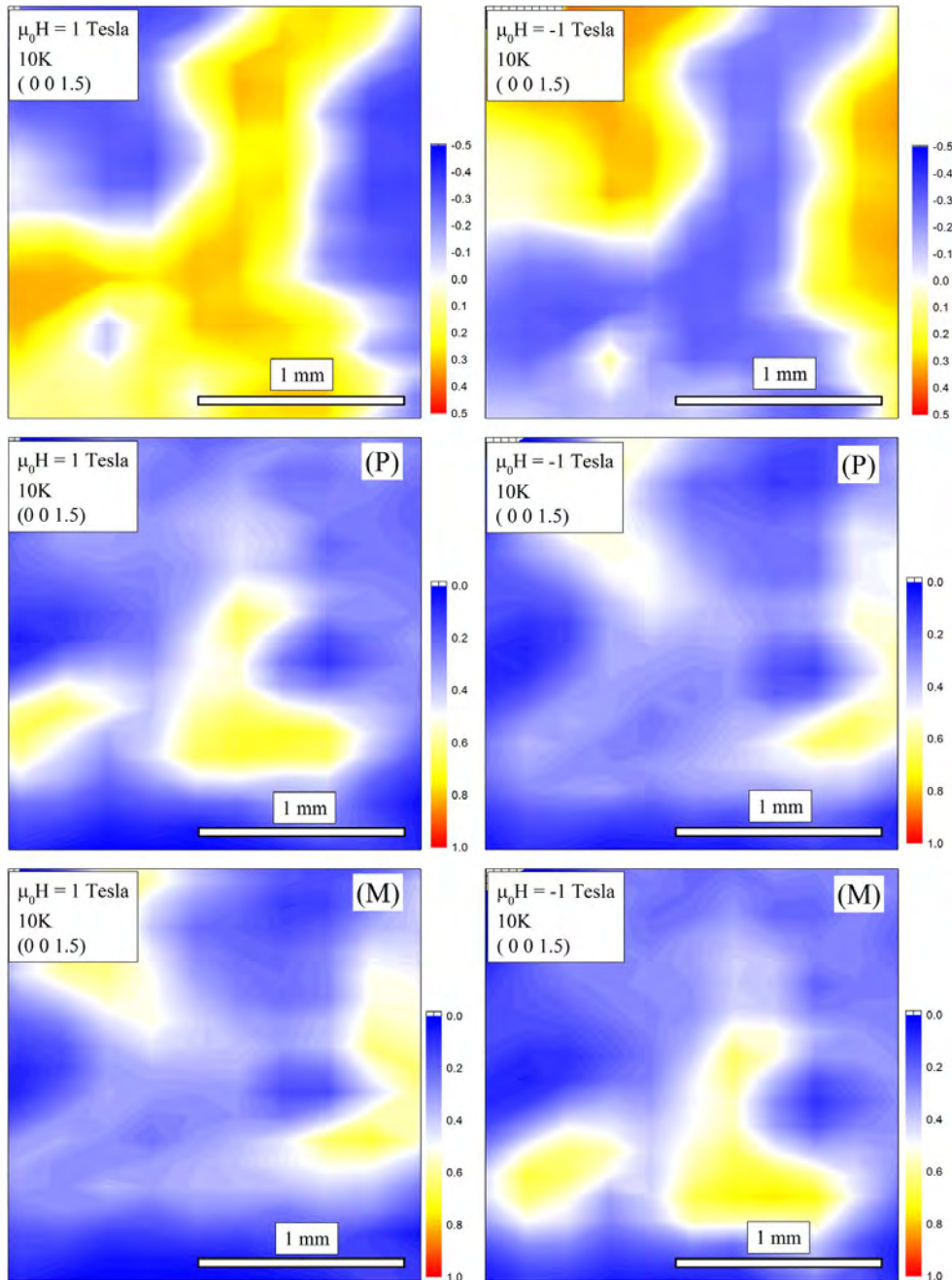


Fig. 6.14 Intensity map for: (*Bottom:*)  $P$  polarization, (*Middle:*)  $M$  polarization and (*Top:*) relative circular dichroism for field (*Left:*) 1 Tesla and (*Right:*) negative 1 Tesla. Color bar indicates  $(P - M)/(P + M)$  for top and rest intensity in arbitrarily unit.

domains is not sample specific but intrinsic. At the same field of 0.4 T we saw that domains are larger at 4 K compared to the domains at 100 K.

We used a cleaved sample and a larger beam spot to verify whether circular dichroism changes sign on reversing field direction. We carefully did omega scans on the sample in

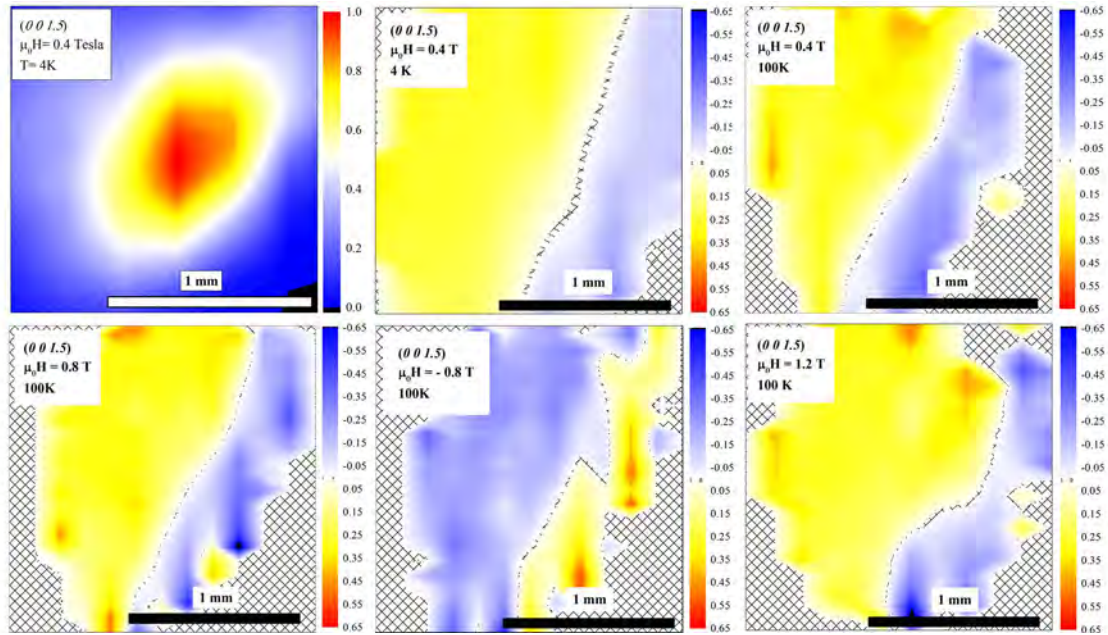


Fig. 6.15 Relative circular dichroism map at 0.4, 0.8, 1.2 and -ve 0.8 T at 100 K. Color bar indicates  $(P-M)/(P+M)$ . The hatched regions are the regions with extremely low intensity.

different fields at 10 K using energy 710.6 eV. Between measurements the field was ramped from positive to negative direction. In the Fig. 6.16 it can be seen that the blue curve for  $M$  polarization is higher in positive field and becomes lower to that of  $P$  polarization in negative field direction. Close observation of the data reveals that in the positive field direction the difference in  $P$  and  $M$  starts appearing near  $H_2$  but in the negative field direction it starts appearing at near  $H_4$ .  $H_2$  and  $H_4$  values are from virgin magnetization curves, therefore, magnetic history of the sample has an influence on the stability of the particular magnetic structure of the sample. This can also be seen in Fig. 6.17, where circular dichroism is observed in the sample for  $(0 0 1.5)$  reflection in low field region (65 mT), when ramping the field from a higher field.

We did a crude experiment on the sample used for measurements at 100 K. We fixed the detector at the  $2\theta$  and  $\omega$  corresponding to  $(0 0 1.5)$ , varied the magnetic field at a ramp rate of 4 mT per second and collected the data at 0.4 seconds intervals. Although in this type of measurements sample positions as well as field values are not very accurate, magnetic phase transitions can be visualized with certain error bars with more data points. In Fig. 6.18 we plotted the time scans for all the four polarizations. Left side measurements are performed for ramping fields from positive to negative directions. For both, in  $\sigma$  and  $\pi$  channels near the critical field,  $H_1$  intensity starts jumping up ( $H_1$  is not shown in the graph because its value is very small). After that it reaches a maximum and reduces down to another minimum. There is a hysteresis observed in this region when we compare to that

of the curves at right hand side. The features in the curves are not important as such measurements of intensity are not very reliable but the position in  $H$  definitely shows hysteresis between  $H_3$  and  $H_1$ . These anisotropic contributions are also visible in the magnetization measurements, where a small loop opening is seen between  $H_2$  and  $H_4$  region but it vanishes at  $H = 0$  (see inset of Fig. 6.16).

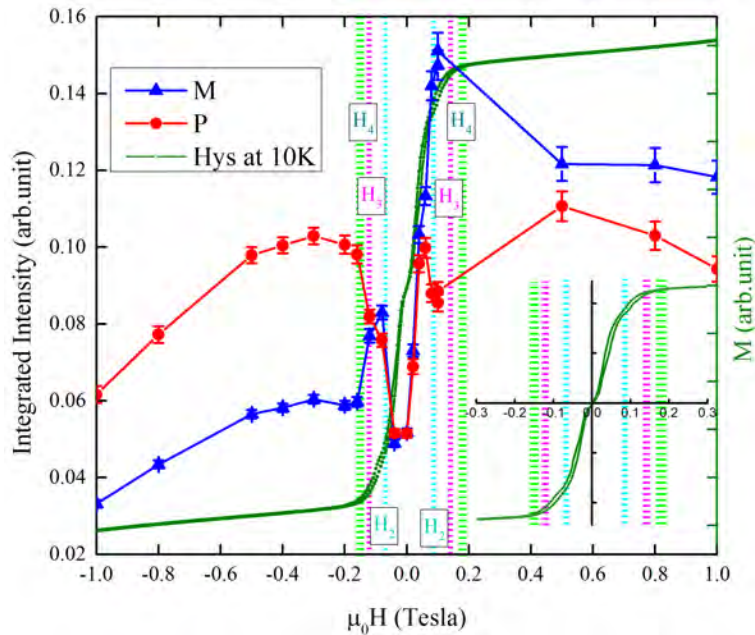


Fig. 6.16 Integrated intensity from the omega scans on a cleaved sample at 10 K using 710.6 eV for  $P$  and  $M$  polarization. Horizontal bars indicate different critical fields from the magnetization measurements. Hysteresis loop at 10 K (arbitrary unit) is also shown as a reference.

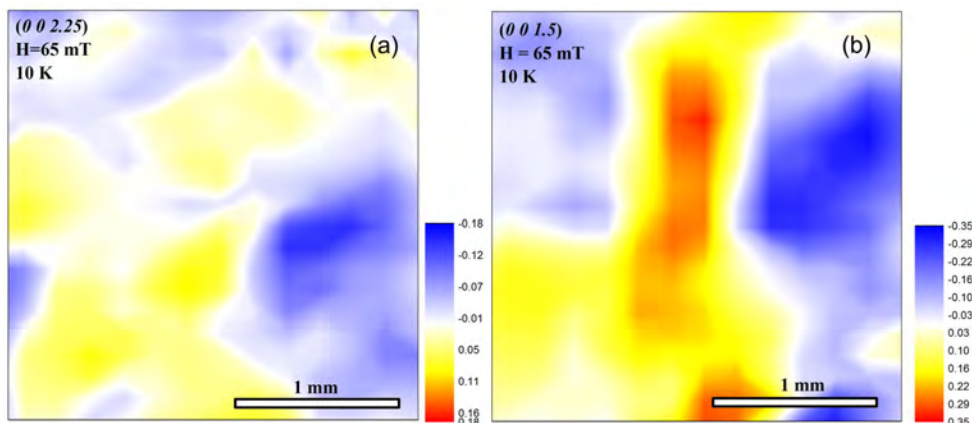


Fig. 6.17 (a) Spin-chiral domain patterns at 10 K in  $H = 65$  mT for  $(0 0 2.25)$  reflection and (b) for  $(0 0 1.5)$  reflection after coming from 3.5 T. Contrast is given by  $\frac{P-M}{P+M}$ .

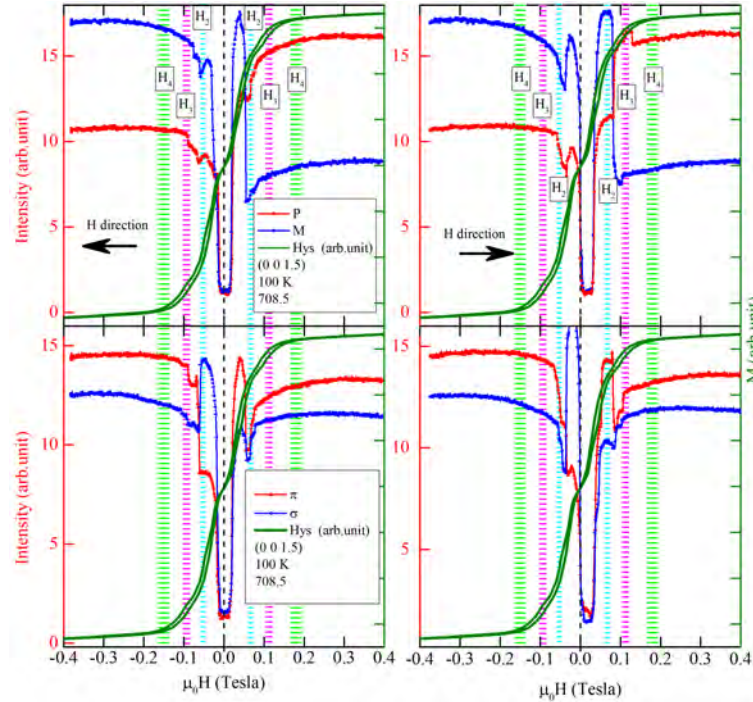


Fig. 6.18 Plot of intensity vs.  $H$  for linear and circular polarizations at 100 K while the field is sweeping. For this measurement, detector and omega are fixed at (0 0 1.5) reflections and magnetic field is varied. (Left:) for ramping field from positive to negative direction and (Right:) for reverse direction. Horizontal bars represent different critical fields measured by magnetization measurements.

## 6.2 Vertical magnet geometry

We also used a vertical permanent magnet of field strength  $0.3 \pm 0.02$  T (measured with a hall probe at the center of both the pole pieces) in the sample of dimension 3 mm for our experiment in the zero-field chamber and this is explained graphically in Fig. 3.8. This field value is between  $H_5$  and  $H_6$ . With the permanent magnet we have higher heat loss because the big pole pieces of magnets were attached to the cryostat. This limits our base temperature to 15 K only. We oriented the sample using higher energy X-rays and only (0 0 1.5) reflection could be reached within the limitations of dark angle of our setup.

It was interesting to see that no circular dichroism is observed in the vertical field geometry in the (0 0  $l$ ) scans as can be seen in Fig. 6.19(a). We mapped portions of the sample for circular dichroism and found that the entire sample surface does not have circular dichroism as can be seen from Fig. 6.19(b). Intensity in  $\sigma$  channel was found to be 4 times higher than that of in the  $\pi$  channel. Mapping of the sample surface for linear dichroism *i.e.*  $(I_\pi - I_\sigma)/(I_\pi + I_\sigma)$  produces the same shape domains as was observed in the case of circular dichroism in horizontal magnetic field and is shown in Fig. 6.19(d).

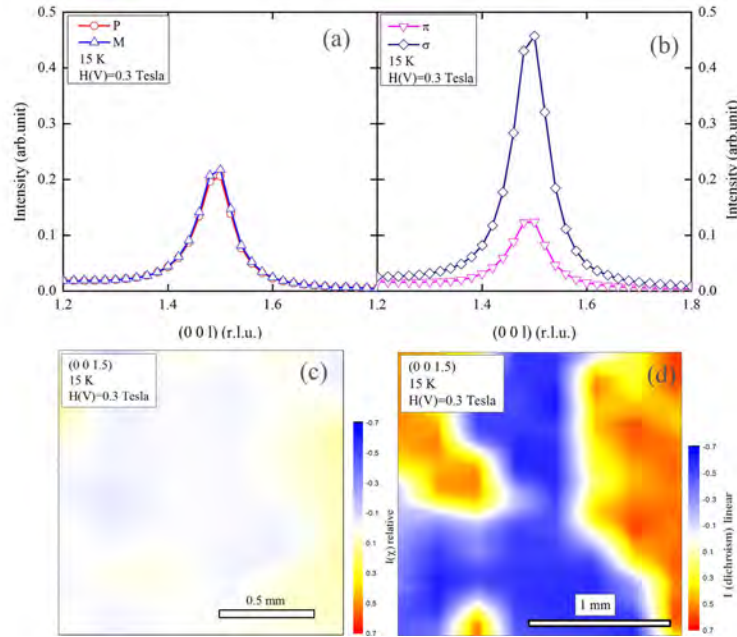


Fig. 6.19 (a)  $(00l)$  scans for  $P$  and  $M$  polarization, (b) same for  $\sigma$  and  $\pi$  polarizations, (c) map of the sample surface for relative circular dichroism where color bar indicates  $(P-M)/(P+M)$  and (d) is map of the sample for relative linear dichroism, where, color bar indicates values of  $(I_\pi - I_\sigma)/(I_\pi + I_\sigma)$  at 15 K.

We mapped the sample for linear dichroism as a function of temperature and found that the same domain configuration can be obtained up to 300 K, see Fig. 6.20. As the temperature is increased, the value of relative linear dichroism starts to decrease. Domain configurations also start to become more diffuse compared to that of 15 K. At 300 K most of the sample is occupied by -ve values of Rel\_Lin and *i.e.* the  $\sigma$  channel intensity is higher than that of the  $\pi$  channel.

To understand the difference between horizontal and vertical field geometry let us go back to the scattering geometry in Fig. 3.5 of Chapter-3. We have  $z_1, z_2$  and  $z_3$  along  $U_1, U_2$  and  $U_3$  directions respectively. Now, as shown in Fig. 6.21, for example, for the model-A we can put the large spin block  $L_1$  in the plane containing  $z_1$  and  $z_2$  with an angle  $\phi/2$  with  $z_1$ . The total moment in the large spin blocks starts moving towards field direction with increasing field whereas small spin blocks are in the opposite direction at saturation point. In a horizontal scattering geometry horizontal  $H$  is along  $z_1$  direction whereas a vertical  $H$  is along  $z_2$  direction. With our direction of  $k$  fixed, the modulated moments in  $z_1$  direction in horizontal field are now modulated in the  $z_2$  direction.

We have seen from Eq. 3.28 that the circular dichroism is related to the  $\sigma \rightarrow \pi$  and  $\pi \rightarrow \pi$  channels. From Eq. 3.29, we can see that linear dichroism is related to the  $\sigma \rightarrow \pi$  and  $\pi \rightarrow \sigma$  channels. For linear dichroism we need contrast between moment components

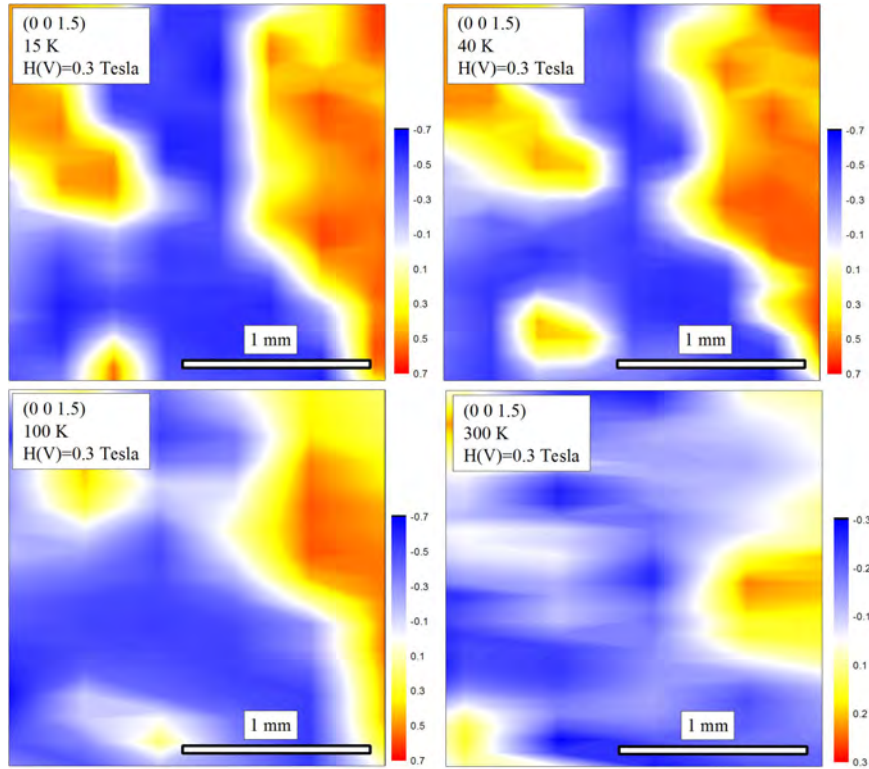


Fig. 6.20 Map of linear dichroism in vertical field geometry at 15 K, 40 K, 100 K and at 300 K for (0 0 1.5) reflection. Color bar indicates  $(I_\pi - I_\sigma)/(I_\pi + I_\sigma)$ .

in the two directions in the scattering plane *i.e.* along  $z_1$  and  $z_3$  directions. Both of them are responsible for moments in the  $z_3$  direction. With  $z_3 = 0$  for model-A we also can not have linear dichroism in vertical field geometry. This implies that there should be a component of moment in  $z_3$  direction which is parallel to  $\vec{Q}$  and therefore to the  $c$ -axis.

In the following we will consider few simple models, which might fit our linear and circular dichroism data.

## 6.3 Calculations on possible models

### 6.3.1 Model-B

Now let us consider our first model after the 2-fan model, the model-B, where the large spin blocks are tilted towards the  $c$ -axis *i.e.* our  $z_3$  direction with an angle  $\alpha$  with  $c$ -axis. The small spin blocks are kept the same as for the model-A, see Fig. 6.22. We consider the projections of L-blocks in the  $c$ -direction and in the plane perpendicular to it given by  $m \cos \alpha$  and  $m \sin \alpha$ . This  $m \sin \alpha$  makes an angle  $\phi/2$  with the  $z_1$  axis. The components of moment in the  $z_1$  and  $z_2$  directions are  $m \sin \alpha \cos \phi/2$  and  $m \sin \alpha \sin \phi/2$  respectively. In the case of horizontal magnet geometry, field is applied in the  $z_1$  direction and in the

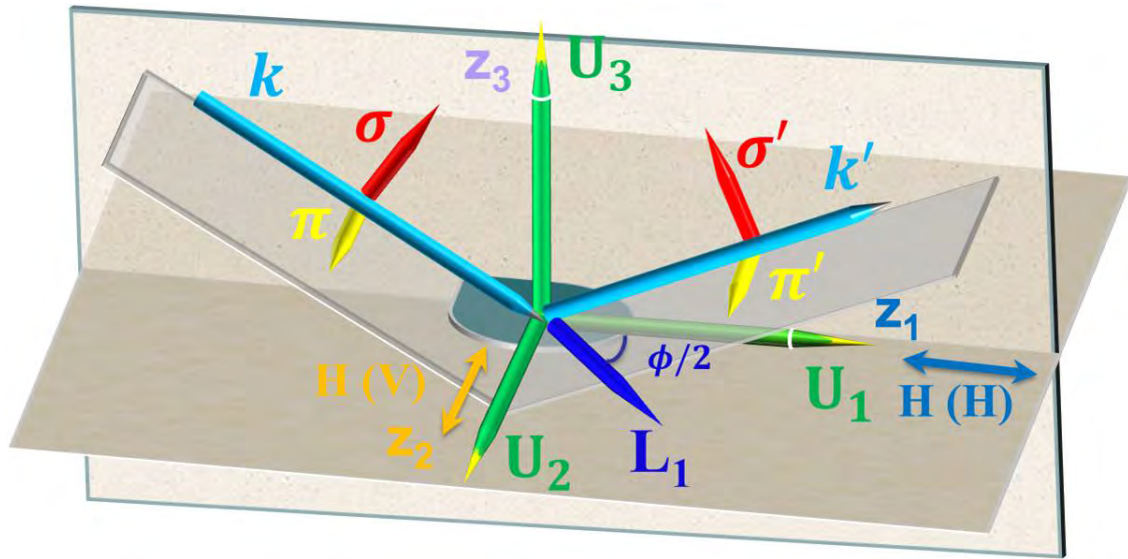


Fig. 6.21 Scattering geometry for both horizontal and vertical field is explained graphically. For horizontal field  $H(H)$  it is in the  $z_1$  direction whereas for vertical field  $H(V)$ , the field is along  $z_2$  direction. For  $H(H)$  the large spin blocks (only  $L_1$  shown) have angle  $\phi/2$  with  $z_1$  direction whereas this angle becomes  $(\pi/2 - \phi/2)$  for vertical field. Following conclusion can be seen from the scattering geometry:  $(\sigma' \times \sigma) = 0$ ,  $(\sigma' \times \pi) = \hat{k} = f_{\pi \rightarrow \sigma}$ ,  $(\pi' \times \sigma) = -\hat{k}' = f_{\sigma \rightarrow \pi}$ ,  $(\pi' \times \pi) = \hat{k}' \times \hat{k} = f_{\pi \rightarrow \pi}$ .

Table 6.1 Summary of experimental parameters for Rel\_circ and Rel\_Lin at different  $H$  and  $T$  for both the horizontal and vertical field experiments

Field (H)					Circular $H$ (H)	Linear $H$ (H)	Circular $H$ (V)	Linear $H$ (V)
4 K	10 K	15 K	40 K	100 K				
	0.0065							
		0.3					0	60.3
			0.3				0	56.4
				0.3			0	51.4
				0.4	42.3	0		
0.4					34.9	0		
	0.5				31.7	0		
				0.8	37.1	0		
				-0.8	39.0	0		
	1				32.5	0		
	-1				31.7	0		
	1.5				26.5	0		

case of vertical field geometry, field is applied in the  $z_2$  direction. Magnetic modulation perpendicular to  $z_1$  now moves by  $\pi/2$  towards  $z_2$ . Therefore, we exchange the axes  $z_1$

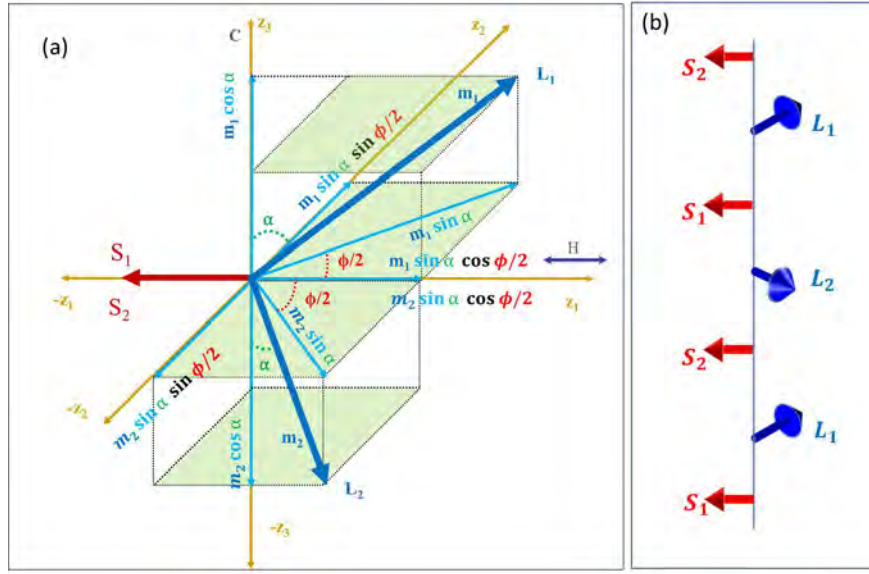


Fig. 6.22 (a) Schematic representation of model-B, where the small spin blocks are same as model-A but large spin blocks are tilted at angle  $\alpha$  with  $c$ -axis. Components of magnetic moments are also shown in the figure. (b) In the unit cell the periodicity of the spin blocks are represented.

and  $z_2$  for calculations of the structure factors in vertical and horizontal magnet geometry. Structure factor calculation details can be found in Appendix-B.

If we look at the Eq. 3.28, it is the contrast between real part of the structure factor in  $\sigma \rightarrow \pi$  times the imaginary part in  $\pi \rightarrow \pi$  and real part of the structure factor in  $\pi \rightarrow \pi$  times the imaginary part in  $\sigma \rightarrow \pi$  that gives circular dichroism. For circularly polarized light ( $\sigma + i\pi$ ) the real and imaginary part of the light have a phase shift of  $\pi/2$  or both are  $\cos$  and  $\sin$  functions. Now if we consider the moments as localized in the center of each block, with moment components  $z_2$  and  $z_3$  in L-blocks, we can have finite intensities in  $\sigma \rightarrow \pi$  and  $\pi \rightarrow \pi$  channels but for a circular polarized light real and imaginary parts have the same phase shift. Therefore,  $P$  and  $M$  polarization can not have contrast in this model. Therefore, we can not have circular dichroism in horizontal field in this model also. This rules out model-B also from our probable models. Numerical calculations on the intensity, circular and linear dichroism can be found in Appendix-B.3. However, linear dichroism in the vertical field (Rel\_Lin) can be observed in this model (see Fig. B.1).

### 6.3.2 Model-C

Considering both the vertical magnet and horizontal magnet geometry for model-B, we can summarize that with the  $z_3$  component of moment for large spin blocks we can have linear dichroism in the vertical field geometry but we fail to account for the experimentally

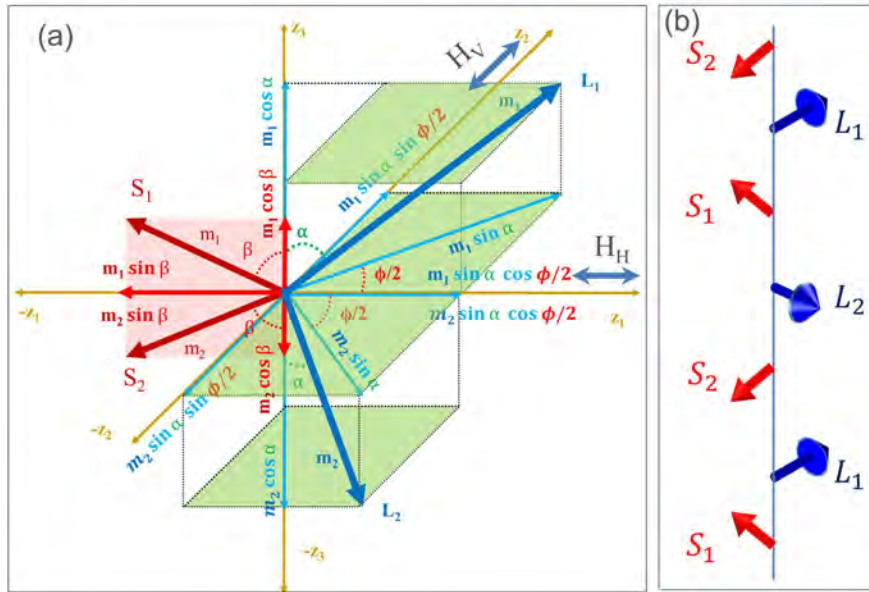


Fig. 6.23 (a) Schematic representation of model-C. The small spin blocks are rotated in the  $c$ -direction of the crystallographic axis with an angle  $\beta$  and large spin blocks are the same as in model-B. Components of magnetic moments in all the three  $z$ -directions are also shown. (b) In the unit cell the periodicity of the spin blocks are represented.

observed circular dichroism in the horizontal field. The contrast between real part of the structure factor in  $\sigma \rightarrow \pi$  times the imaginary part in  $\pi \rightarrow \pi$  and real part of the structure factor in  $\pi \rightarrow \pi$  times the imaginary part in  $\sigma \rightarrow \pi$  is zero when we have contrast between  $z_2$  and  $z_3$  present at the same position. Therefore, to have circular dichroism we need this contrast at two positions, in the unit cell, which are not multiples of  $\pi$ . The small spin blocks have to be modulated as well to circular dichroism in the horizontal field geometry. We consider model-C as shown in Fig. 6.23. We add a component of the small spin blocks in the  $c$ -direction of the crystallographic axis with the same periodicity of  $(0\ 0\ 1.5)$ . Magnetic moment in small spin blocks makes an angle  $\beta$  with the  $z_3$  axis.

Now we have three angle parameters dependence *i.e.*  $\phi$ ,  $\alpha$  and  $\beta$  in model-C. In Appendix-B.4 our numerical calculations on model-C for intensity in individual channels and various quantities  $Rel\_Circ$ ,  $Rel\_Lin$  and  $I_\pi/I_\sigma$  are presented. In this model, for horizontal field geometry, we have both  $Rel\_Circ$  and  $Rel\_Lin$  for wide angular dependence. We picked out the values across a very broad range of angles  $\phi$ ,  $\alpha$  and  $\beta$  which satisfies a wide range of experimental values. For that we considered  $0.2 \leq Rel\_Circ \leq 0.7$  and plotted the range of angles observed in Fig. 6.24. We can see that  $Rel\_Circ$  can be observed only up to  $\phi \leq 60$  and  $70 \leq \alpha$ . We restrict  $I_\pi/I_\sigma$  ratio in the range  $1. \leq I_\pi/I_\sigma \leq 5$  and obtained an area as shown in Fig. 6.24(b). In both the cases we get a wide range of values for  $\beta$  as can be seen

from the color-bar. Filtering out the values which satisfy the above two conditions we found the region shown in Fig. 6.24(c).

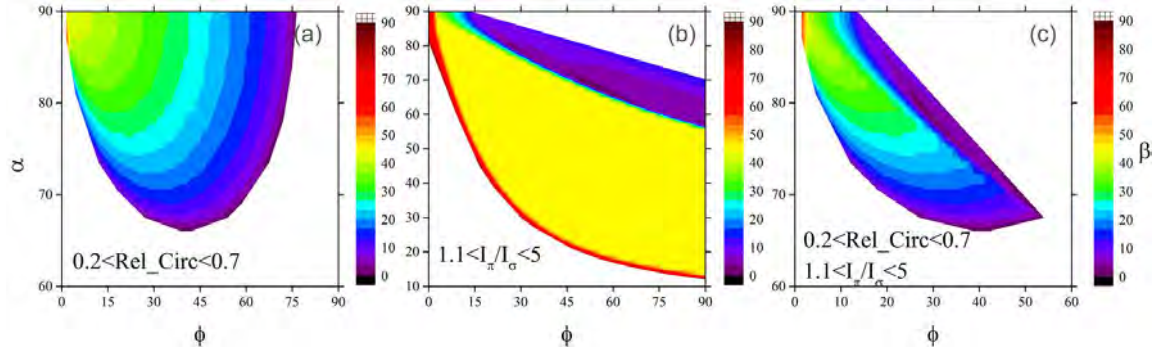


Fig. 6.24 Calculated slices of the range of  $\phi$ ,  $\alpha$  and  $\beta$  for values of (a) Rel\_circ, (b)  $I_{\pi}/I_{\sigma}$  as indicated in the figure. (c) Combinations of both the parameters for model-C.

For vertical magnet geometry various parameters with angular dependence are shown in Appendix B.6.  $I_{\sigma \rightarrow \pi}$  and  $I_{\pi \rightarrow \sigma}$  have a strong angular dependence whereas  $I_{\pi \rightarrow \pi}$  is zero. This gives us the angular dependence of Rel\_Lin values. Now we choose the range of Rel\_lin as  $0.2 \leq Rel\_Lin \leq 0.7$ . Incorporating this range into the solution for horizontal magnet we get the ranges of  $\phi$ ,  $\alpha$  and  $\beta$  as shown in Fig. 6.25. For a wide range of values for  $\phi$ ,  $\alpha$  and  $\beta$  we have a solution. It should be noted that we have chosen a large range (*i.e.* large experimental uncertainty) for the values of Rel\_Circ, Rel\_lin and  $I_{\pi}/I_{\sigma}$  to find the solution.

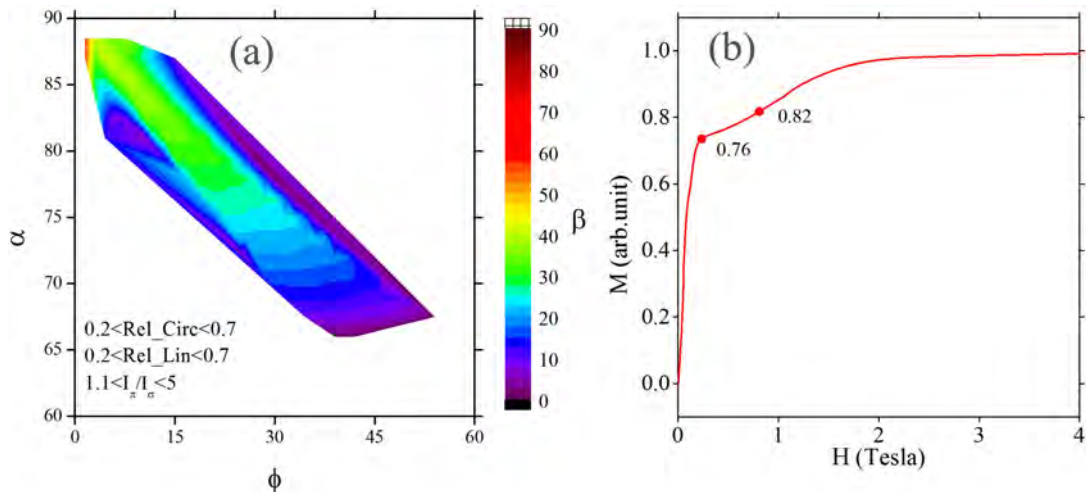


Fig. 6.25 Range of  $\phi$ ,  $\alpha$  and  $\beta$  after simultaneously incorporating the quantities Rel\_Circ, Rel\_Lin and  $I_{\pi}/I_{\sigma}$  as shown, with  $\phi$  and  $\alpha$  as the axes and  $\beta$  as the color bar. (b) Normalized initial magnetization curves at 100 K showing changes in values of  $M$  at  $H_4$  and  $H_5$ .

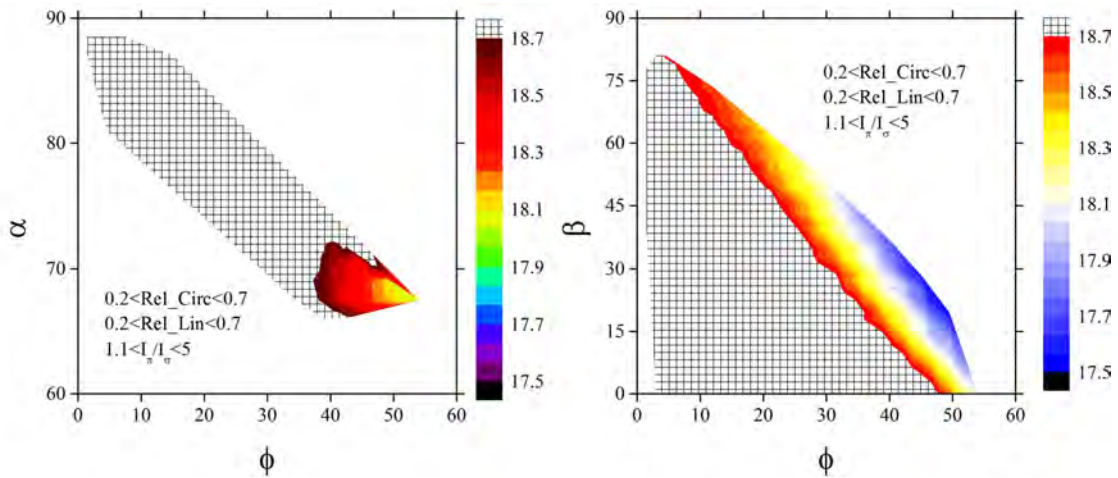


Fig. 6.26 Calculated moments for  $\phi$ ,  $\alpha$  and  $\beta$  values from the solution shown in Fig. 6.25. (a) as a function of  $\phi$  and  $\alpha$  with moment as color bar.

For the experimentally observed values of Rel\_Circ, Rel\_lin and  $I_\pi/I_\sigma$ , model-C is suitable. So far we have not considered the change in magnetic moments. We calculated the magnetizations for the values of  $\phi$ ,  $\alpha$  and  $\beta$  found in the solution and plotted this in Fig. 6.26. Most of the solutions for model-C show magnetization above the saturation moment value of  $18.6 \mu_B/F.U.$  (sparse region shows values above the saturation magnetization). From Fig. 6.25(b) we see that in  $H_4$  and  $H_5$ , 82% ( $15.25 \mu_B/F.U.$ ) and 76% change in magnetization are observed respectively. Calculated magnetization for all the values of  $\phi$ ,  $\alpha$  and  $\beta$  in the solution are well above these values and very close to saturation values. The smaller spin blocks are anti-parallel to the field direction. Now, for circular dichroism if we consider a c-component with angle  $\beta$ , then it serves our purpose to get Rel\_Circ for horizontal field, but we decrease the moment opposite to field direction with increase in  $\beta$ . Therefore, in this model also we can not have our solution.

### 6.3.3 Model-D: The correct spin structure

Contrast between  $z_2$  and  $z_3$  modulated moments at two different positions served our purpose in getting circular dichroism in model-C, but could not give us a suitable solution for the magnetic moments. A realistic model has to include both  $z_2$  and  $z_3$  components in both the large and small spin blocks. Therefore, we introduce model-D. The small spin blocks have a  $z_2$  component in model-D (horizontal field geometry). Each of the small spin block makes an angle  $\beta$  with the  $z_3$  axis. Like we did with large spin blocks in model-B, we make the projections of the small spin block moments along the c-axis and in the plane perpendicular to it ( $z_1 - z_2$  plane). Now, this projection makes an angle  $\gamma/2$  with the  $z_1$  axis.

Straight-forward solution is difficult in the case of model-D. We have four independent

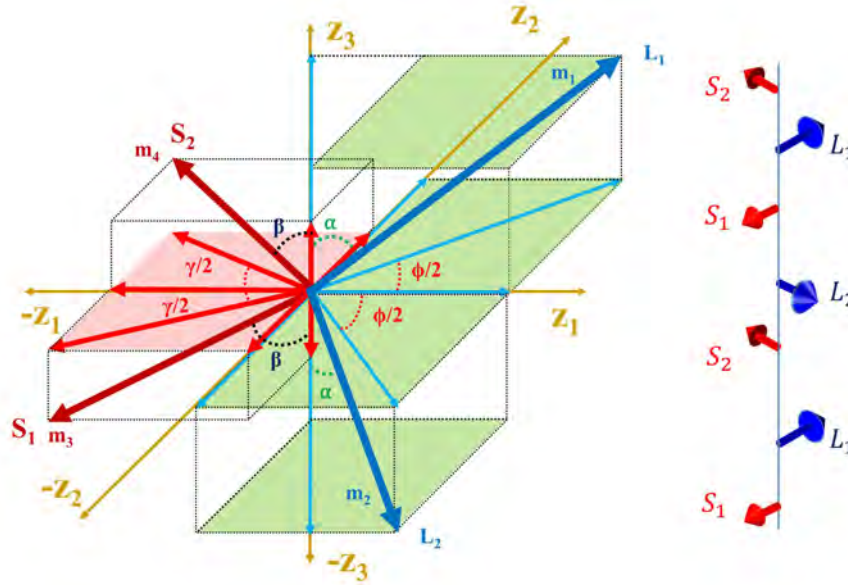


Fig. 6.27 Schematic representations of the model-D. Here, compared to model-C, a component of moment for the small spin block is added along  $z_2$  axis in horizontal magnet geometry. Small spin blocks make an angle  $\beta$  with the  $z_3$  axis and  $\gamma/2$  with the projections of it on the  $z_1 - z_2$  plane with  $z_1$  axis.

angles for which we need to calculate intensity and different parameters. We have calculated parameters such as  $Rel\_Circ$ ,  $I_\pi/I_\sigma$  for horizontal field and  $Rel\_Lin$  for vertical fields and identify values within certain tolerance limits using a programming script in Python. For this, let us consider values at 10 K from Table. 6.1. At 10 K, we have for horizontal field  $H = 0.5T$   $Rel\_Circ$  of 31.7 %. We do not have corresponding data for vertical field at 10 K and  $H$ . Therefore, we consider 15 K and  $H \approx 0.5 T$   $Rel\_Lin$  values. For that we added a tolerance of 10 % to each of the values, including magnetic moments. We kept  $Rel\_Lin$  in horizontal field and  $Rel\_Circ$  low for all the solutions and did not use any error bars as these values are close to zero.

In our experiments the net magnetic moments can be determined with the highest accuracy. Therefore we picked the values with the highest accuracy in magnetic moments. We saw in Fig. 6.25 that at  $H_4$  and  $H_5$  respectively, 75% and 82% of the saturation magnetic moment of  $18.6 \mu_B/(F.U.)$  is observed. Therefore, we extracted the values of various parameters from our calculations using a programming script as a function of all the four angles corresponding to magnetic moments in between  $H_3$  and  $H_4$ . To this we then added the additional requirements  $0.2 \leq Rel\_Circ \leq 0.7$ ,  $1. \leq I_\pi/I_\sigma \leq 5$  for horizontal magnet geometry and  $0.2 \leq Rel\_Circ \leq 0.7$  for vertical magnet geometry to extract the angular dependence. Values of  $\phi$  are found to have to be smaller than  $17^\circ$  to satisfy our solution for

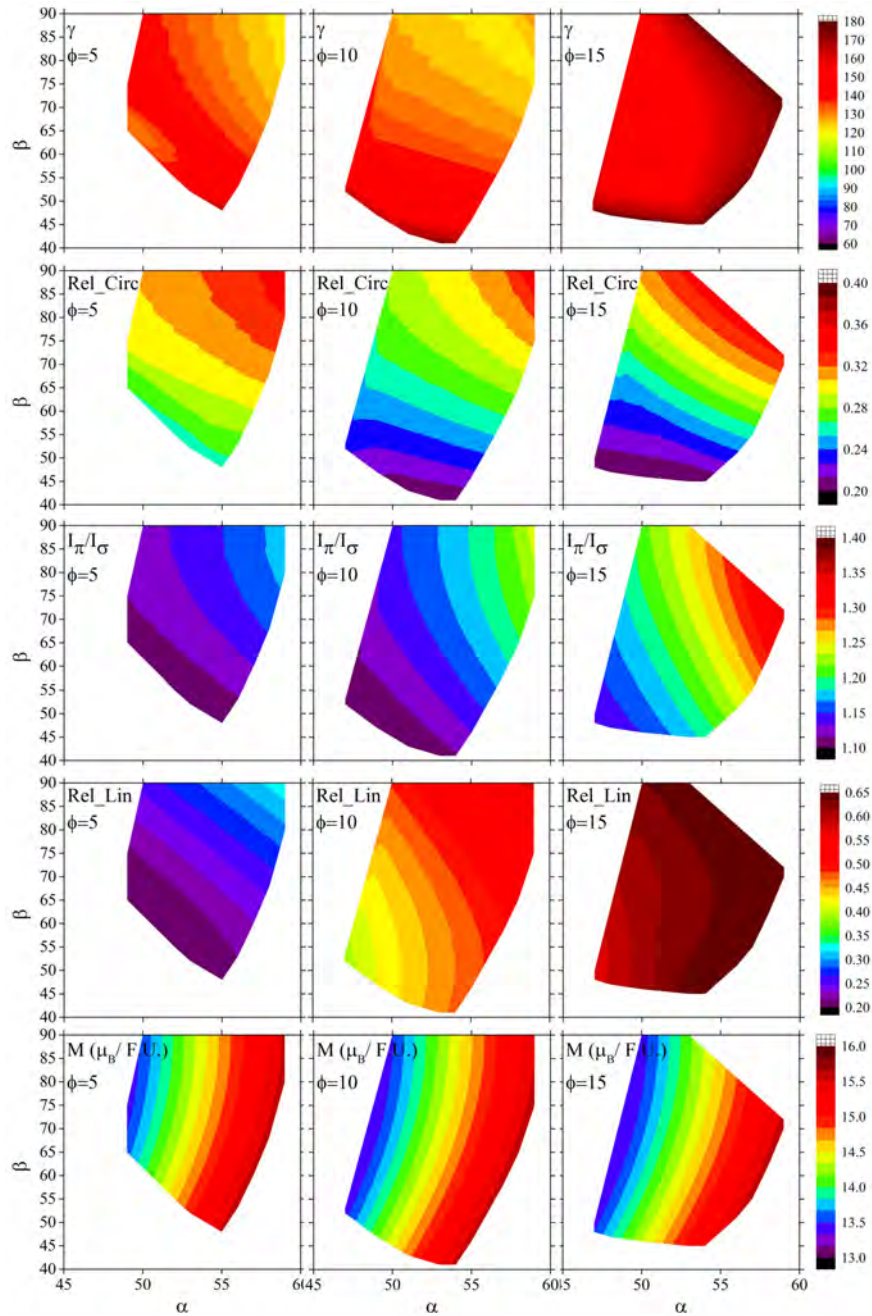


Fig. 6.28 Various parameters calculated for model-D for three different values of  $\phi$ ,  $5^\circ$ ,  $10^\circ$  and  $15^\circ$ , as a function of two out-of-plane angles  $\alpha$  and  $\beta$ , for L and S blocks. In the top panel, value of  $\gamma$  satisfying our solution is shown. For each  $\phi$  same color bars are used and are shown beside the  $\phi = 15^\circ$ .

all the quantities.

In Fig. 6.28 we have plotted various parameters as a function of  $\alpha$  and  $\beta$  as well as values of  $\gamma$  in the top panel for three different values of  $\phi$ :  $5^\circ$ ,  $10^\circ$  and  $15^\circ$  respectively.

Our broad solution criteria also restricts the other angles  $\alpha$ ,  $\beta$  and  $\gamma$  to non zero values. For  $\phi = 15^\circ$ , a broad range of values of the other angles are considered to swipe at a broader solution. The parameter range considered is:  $47^\circ \leq \alpha \leq 59^\circ$ ,  $45^\circ \leq \beta \leq 89^\circ$ ,  $96^\circ \leq \gamma \leq 178^\circ$ . Closer look in the plot reveals that for  $\phi = 15^\circ$  Rel\_lin is always above 50 % whereas we can obtain Rel\_Circ values ranging from 20 to 40 % for various values of the other three angles. Highest value of Rel\_Circ is found to be 40 %. With non-zero values of all four angles  $\phi$ ,  $\alpha$ ,  $\beta$  and  $\gamma$  we have a transverse conical spin structure. This T-conical spin structure not only gives the solution for our experimental microscopic properties but also fulfills the condition for  $H$  driven ferroelectricity by IDM mechanism (see section 2.3).

In other hexaferrite classes in the ferroelectric phase a transverse conical phase is proposed. When a small amount of Al is substituted for Fe, a longitudinal conical spin structure in the zero  $H$  transforms to a transverse conical phase with contributions from both spin blocks [66, 129]. For  $\text{Ba}_2\text{Mg}_2\text{Fe}_{12}\text{O}_{22}$  also transverse conical contributions from both the spin blocks were found in the ferroelectric phase [55, 65, 130].  $\text{Sr}_3\text{Co}_2\text{Fe}_{24}\text{O}_{41}$  system also has a transverse conical spin structure in the ferroelectric phase [58, 131]. All these hexaferrites exhibit magnetic field driven ferroelectricity by IDM mechanism. Our solution of producing a transverse conical structure in this classical hexaferrite is in line with the other hexaferrite systems showing  $H$  induced ferroelectricity.

We first sort our values corresponding to the data from the Table 6.1. For few field ranges we have plotted the values of  $\phi$ ,  $\alpha$ ,  $\beta$  and  $\gamma$  in Fig. B.7 in Appendix-B. Although we can see distinct changes in the values of angles near  $H_5$ , the error bars in the solutions are very large.

## 6.4 Experimental results in light of final model (model-D)

### 6.4.1 Boundary between different phases

We used a Mathematica 10.4 program to calculate our intensity and various parameters. In the Fig. B.8 of Appendix-B we plotted the values of the quantities Rel\_Circ, Rel\_Lin,  $I_\pi/I_\sigma$  and moment as a function of  $\alpha$ ,  $\beta$  and  $\gamma$  for three values of  $\phi=5^\circ$ ,  $10^\circ$  and  $15^\circ$ . All the values are interdependent. We need to find the solution for a particular set of experimental values. We used the same program to minimize the difference between experimental and simulated values of Rel\_Circ, Rel\_Lin,  $I_\pi/I_\sigma$  and moment by random search method. At 10 K (from Table. 6.1) we saw that from 0.5 T to 1 T our Rel\_Circ remains almost the same at 30(2)%. While ramping down  $H$ , we got almost the same values of Rel\_Circ at 65 mT (see Fig. 6.17). We solved for Rel\_Circ in the range of 30% (with tolerance of 5%) up to 1 T and higher for field of 26% (with 5% tolerance). We do not have experimental data on Rel\_Lin

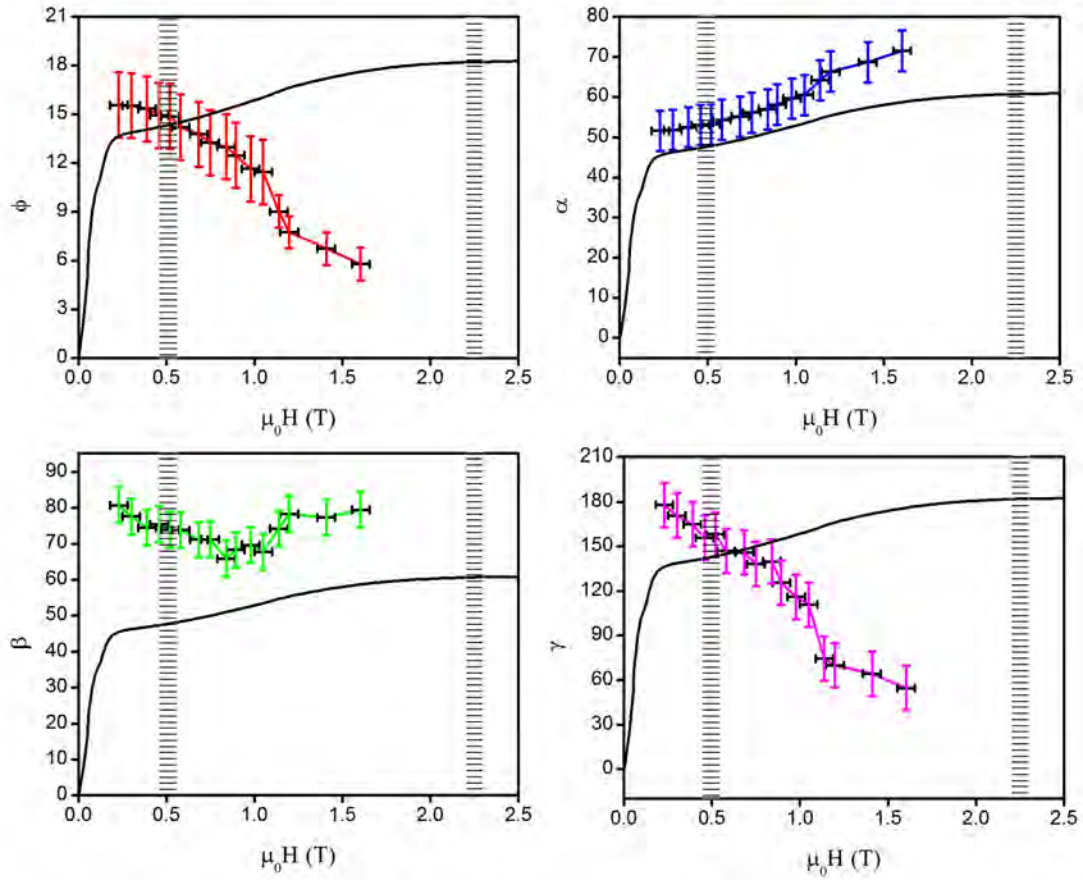


Fig. 6.29 Solution for model-D for  $\phi$ ,  $\alpha$ ,  $\beta$  and  $\gamma$  as a function of applied field below saturation field and above  $H_4$ . Values of the angles are calculated by simultaneously minimizing individual experimental parameters.

above 0.3 T. Therefore, we did not put tolerance in Rel\_Lin values. Magnetic moment is given a tolerance of 1%. Our solution for various values of  $H$  is shown in Fig. 6.29.

**Transition to ferrimagnetic phase** Let us first discuss the transition to ferrimagnetic phase from the transverse conical phase. With increasing  $H$ , the in-plane angle for large spin blocks *i.e.*  $\phi$  decreases near  $H_5$  and is sharper after 1 T. The in-plane angle from small spin blocks *i.e.*  $\gamma$  also follows the same trend. In case of out-of-plane angles for large spin blocks ( $\alpha$ ), it goes on increasing slowly from  $50^\circ$  at  $H_4$  to  $90^\circ$  as we increase  $H$ .  $\beta$  values decrease up to 1 T and then increases towards  $90^\circ$  with increasing  $H$ . From the trends in  $\phi$  and  $\gamma$  we can claim that  $H_5$  is the field region where the in-plane angle starts decreasing, but we have considerable out-of-plane contributions left. Thus, both the intermediate-II and intermediate-III phases can be considered as transverse conical phase. The relative approach of all the four angles towards ferrimagnetism is difficult to find as we do not have sufficient scattering data in this  $H$  region. Our speculation is that very close to saturation value the

spin structure remains transverse conical and first the in-plane angles approach zero and at the saturation point out-of-plane angle becomes close zero, i.e,  $\alpha$  and  $\beta$  approaches  $90^\circ$ .

### 6.4.2 Chirality inversion with reverse $H$

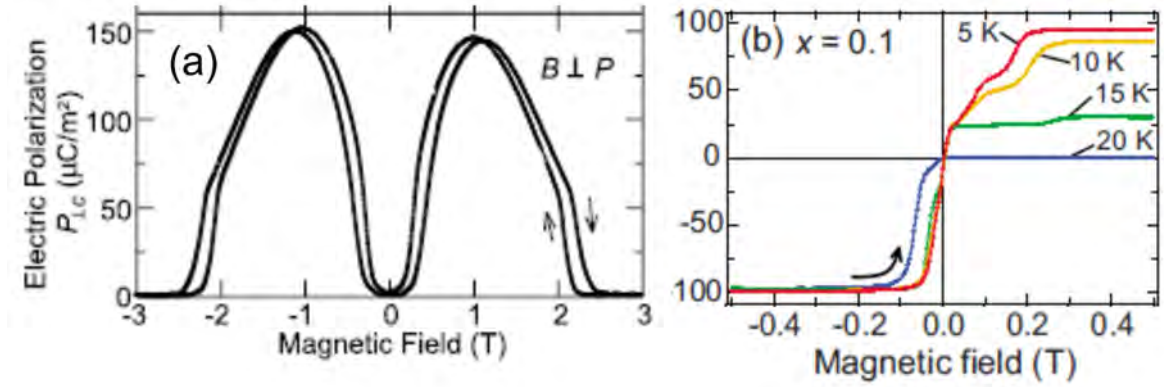


Fig. 6.30 Electric polarization as a function of applied  $H \perp c$  for (a)  $\text{Ba}_{0.5}\text{Sr}_{1.5}\text{Zn}_2\text{Fe}_{12}\text{O}_{22}$  from Kimura *et al.*[3] and (b) for  $\text{Ba}_2(\text{Mg}_{0.9}\text{Zn}_{0.1})_2\text{Fe}_{12}\text{O}_{22}$  from Ishiwata *et al.*[130].

In Chapter-5 we have seen that, near  $H_2$  the angle between the spin blocks becomes close to  $80^\circ$ (5). Above  $H_4$  it is difficult to calculate the angle as the phase corresponding to  $(0\ 0\ 1.5)$  starts contributing. Our solution above  $H_4$  shows that the L-spin block's in-plane (ab-plane) angle  $\phi$  decreases considerably while the S-spin block's in-plane angle ( $\gamma$ ) increases. Moreover, out-of-plane angles  $40^\circ$  ( $90^\circ - \alpha$ ) and  $10^\circ$  ( $90^\circ - \beta$ ) are found near  $H_4$ . This transition is accompanied by hysteresis as can be seen from the magnetization curves (Fig. 6.25(b)). Details of this hysteretic behavior are discussed below.

We have seen that our spin chiral domains are inverted upon reversal of the  $H$  direction (Fig. 6.15 and in Fig. 6.14). Let us consider the following situation as shown in table 6.2. The chirality term is  $(\vec{S}_1 \times \vec{S}_2)$  induced by IDM interaction (see section 2.3). For any magnetization direction in a multi-domain sample we have spin chiral domains with both the signs. Let us consider the condition shown by the first column in Table 6.2, where we have magnetization direction only upward while chirality is in both the directions. Now in negative  $H$  direction if we have  $M$  in the opposite direction and positive chirality is inverted implies that positive chirality becomes negative and vice-versa. From Eq. 2.11, we see that polarization induced by IDM mechanism is given by  $\vec{P} = \vec{e}_{12} \times (\vec{S}_1 \times \vec{S}_2)$  or we may write  $\vec{P} = \vec{e}_{12} \times \vec{c}$ . Let us consider the polarization is  $P$  for positive direction of  $H$ . Now, as  $H$  is inverted the domain population of both the chiralities get inverted in our experiment. Domains which are in positive direction become negative and vice-versa. This implies that the domain directions which are responsible for positive polarization are now in

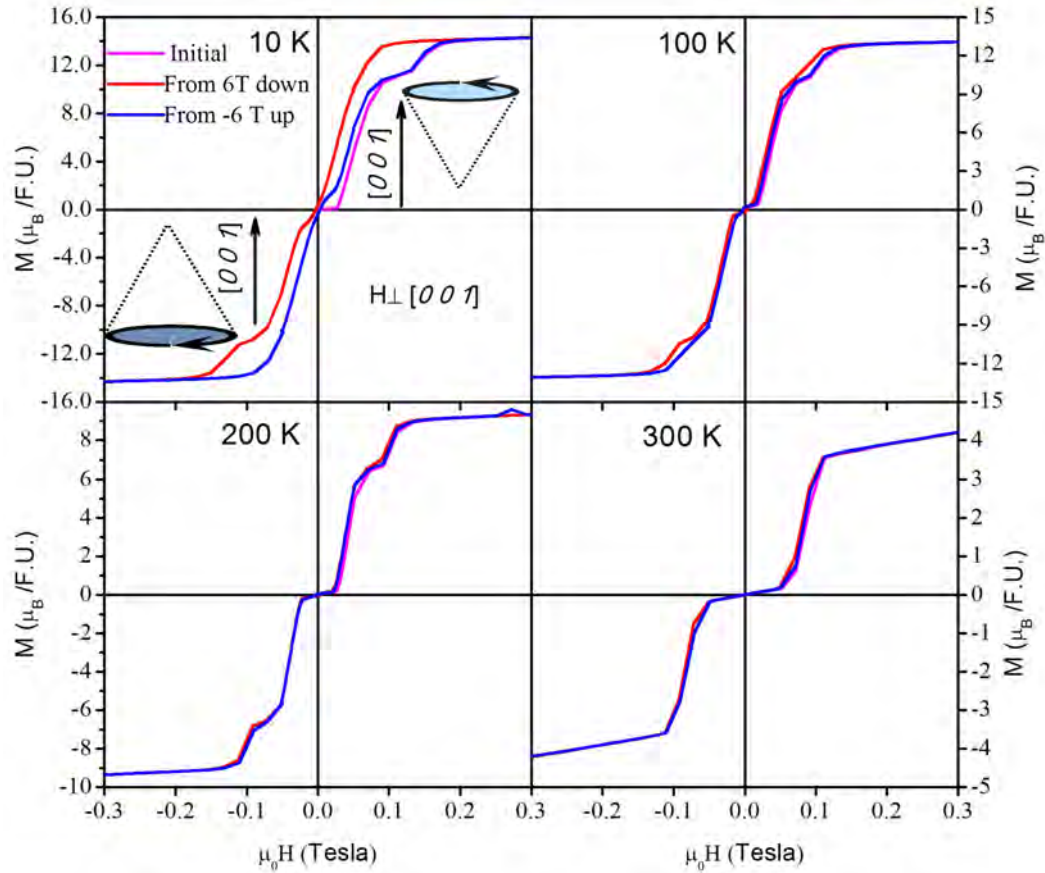


Fig. 6.31 Initial magnetization (pink), magnetization for decreasing field from 6 T (red) and magnetization for increasing field from -6 T (blue) curves at different temperatures.

negative direction and hence polarization should be  $-P$ , but according to the macroscopic measurements it is in the same direction [3]. This difference can be because of the difference in composition in our experiment compared to that of Kimura *et al.*

Table 6.2 Possible situation for magnetization and chirality ( $M\chi$ ) simultaneously present.

$M\chi$	$M$	$-M$
$\chi$	$\uparrow+$	$\downarrow-$
$\chi$	$\uparrow-$	$\downarrow+$

Chiral domains can be inverted if they are linked to the point where the field direction changes *i.e.* at  $H = 0$  (no coercivity). We have seen that when we measured in positive field direction from zero  $H$ , a non-chiral 4-fan phase is the connecting phase. The 4-fan structure was observed only for a small field range, above and below which it is mixed with the transverse conical and helical phases, both of which are chiral. However, all these

measurements were done in increasing field from zero  $H$ . In Fig. 6.17 we have seen that on ramping  $H$  from higher field we observed circular dichroism at 65 mT field also, which was the 4-fan phase range in the increasing field direction. We have measured very carefully some magnetization curves with 1 mT data interval to see if there is any hysteresis in the magnetization. We have plotted the hysteresis curves along with the initial magnetization curves in Fig. 6.31. In the initial magnetization curve (magenta) the step corresponding to 4-fan phase was observed. We can see clearly that metamagnetic steps corresponding to 4-fan phase are not present in the demagnetization curve (red) *i.e.* the magnetization measured while reducing  $H$  from 6 T down to 0 at 10 K. In the magnetization curve in the negative direction now there is the corresponding step, but the demagnetization curve does not show this step (blue). Therefore, we can claim that in the magnetic field switching process the 4-fan structure is not observed *i.e.* we have only the transverse conical and the helical phases. We can speculate that the chirality is linked between the transverse conical phase and the helical phase in the absence of 4-fan phase. Similar situation was observed in the case of  $\text{BaFe}_{12-x-\delta}\text{Sc}_x\text{Ma}_\delta\text{O}_{19}$  at 10 K, where a transverse conical domain wall was responsible for polarization reversal. However, at other temperatures the difference in magnetization and demagnetization is not that prominent (see Fig. 6.31) and therefore, no polarization switching can be predicted at higher temperatures. We speculate that minor loop tracing in magnetization measurement as well as in diffraction measurements after ramping from low  $H$  may provide different switching behavior.

### 6.4.3 The room temperature magnetoelectric

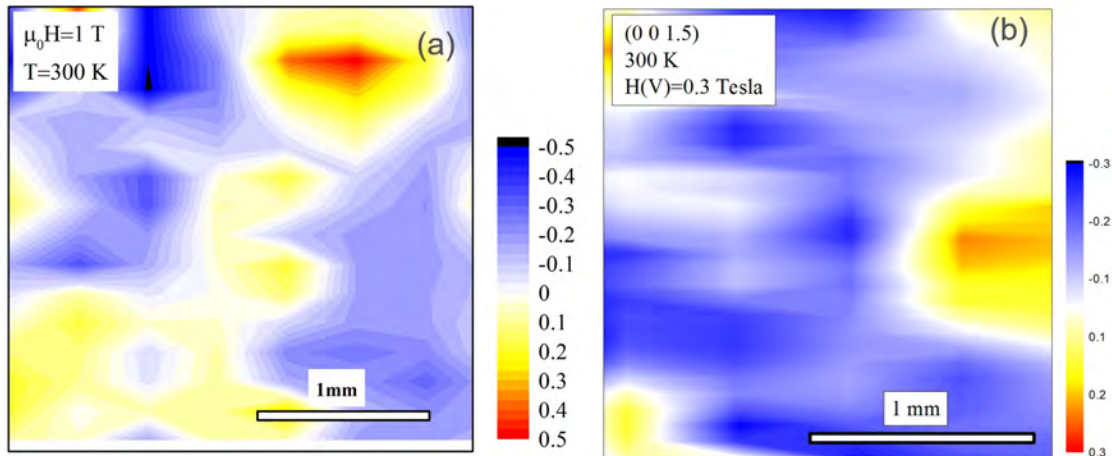


Fig. 6.32 Map of (a) Rel\_Circ at 300 K for horizontal magnet geometry and (b) Rel\_Lin at 300 K for vertical magnet geometry.

As the metamagnetic steps in magnetization curves were visible up to 300 K (see Fig.

4.8), we mapped the samples at 300 K for both the horizontal and vertical magnet geometries. Both these maps are shown in Fig. 6.32. At 300 K distinct domain configurations, similar to that observed at 10 K, were found in both the geometries. Therefore, we claim that magnetic field induced polarization can be expected to be observable up to 300 K. This indeed was observed in more resistive samples [119]. Therefore, apart from Z-type hexaferrites, our Y-type hexaferrites can be considered as room temperature magnetoelectric.

## 6.5 In field Neutron diffraction

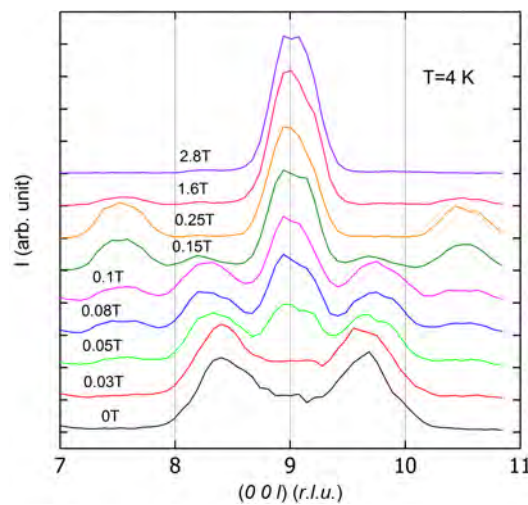


Fig. 6.33 Unpolarized neutron  $(0\ 0\ l)$  scans at 4 K in different vertical magnetic field. Measurements were carried out in increasing H.

In field Neutron diffraction experiments were carried in the two axis E4-diffractometer of the Helmholtz-Zentrum Berlin für Materialien und Energie. A vertical superconducting magnet is used in a horizontal scattering plane.  $(0\ k\ l)$  is our scattering plane with  $\lambda = 1.44\text{\AA}$ . Several samples were tested and in many samples reverse-obverse twinning was found. In Fig. 6.33 and 6.34 we have plotted  $(0\ 0\ l)$  scans at 4 K and 100 K in different magnetic fields. Nuclear reflections can be found obeying the conditions  $(-h+k+l=3n)$  ( $k_0$ ). Reflections corresponding to different propagations vectors  $(0\ 0\ 3n-\tau)$ ,  $(0\ 0\ 3/2)$  and  $(0\ 0\ 1/4)$  are labeled as  $k_1$ ,  $k_2$  and  $k_3$ . Along with this we have magnetic intensity in  $K_0$  at the nuclear reflection. At 4 K, where we measured in the increasing order of fields, the nuclear  $(0\ 0\ 9)$  reflection is difficult to resolve from the incommensurate  $k_1$  ( $\tau = 0.6$ ) satellite at  $H=0$  T. As the field increases to 0.05 T small intensity in the commensurate satellite corresponding to propagation vector  $k_2$  appears and another commensurate satellite corresponding to propagation vector  $k_3$  appears which is difficult to resolve from the incommensurate satellite. At 0.15 T onwards only the propagation  $k_2$  is found.

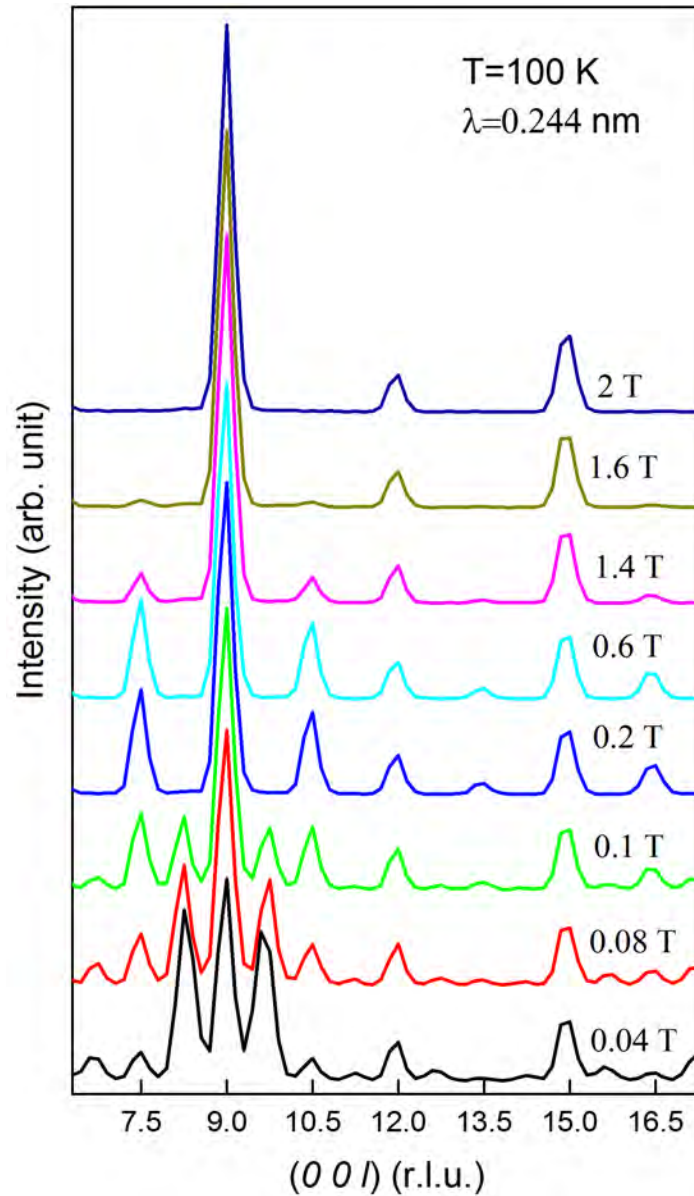


Fig. 6.34 Unpolarized neutron  $(0\ 0\ l)$  scans at 100 K in different vertical magnetic field. Measurements were carried out in decreasing H. Intensity of  $(0\ 0\ 7.5)$  is multiplied by 3

In another sample we measured in the decreasing H at 100 K. Unlike the previous sample we found sharp peaks in this sample. Therefore, this sample was used for further experiments, see Fig. 6.34. Near 1.6 T  $k_2$  satellite reflections starts appearing. Below 0.2 T additional  $k_3$  reflection is also found. It is interesting to find that this time we do not have any incommensurate reflection present.

Integrated intensities from Gaussian fits of the  $(0\ 0\ l)$  reflections at three different temperatures is shown in Fig. 6.35. Due to low detector resolution, the reflections corresponding to

$k_3$  are not possible to resolve from the incommensurate reflections. The  $(0\ 0\ 8.25)$  reflection was found to exist near 0.1 T ( $<0.2$  T) in all the temperatures. Considerable intensity for the reflections corresponding to  $k_2$  was found from 0.05T onwards in all the temperature. Due to the residual field in the superconducting magnet at low H the magnetic field below 0.1T has bigger uncertainty compared to high H values. Therefore, the boundary between the 4 fan and transverse conical phase is difficult to establish in this experiment. The reflections

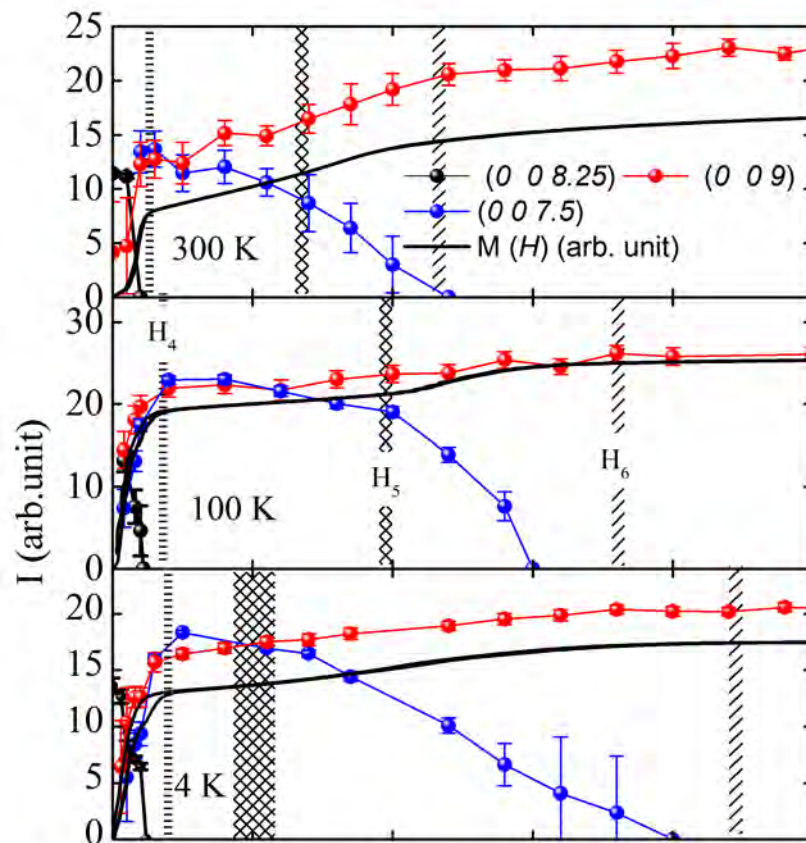


Fig. 6.35 Integrated intensity from the Gaussian fit of the reflections in unpolared neutron  $(0\ 0\ l)$  scans at three different temperatures 4 K, 100 K and 300 K. Magnetizations curve is also plotted as a reference.

corresponding to  $k_2$  starts becoming more intense near the  $H_4$  in all the cases and intensity starts decreasing near  $H_5$ . Other Y-type hexaferrite compositions studied by neutron diffractions having a  $K_2$  propagation has a transverse conical spin structure and are ferroelectric in that phase. For  $\text{Ba}_2\text{Mg}_2\text{Fe}_{12}\text{O}_{22}$  the Fe-II ferroelectric phase has only  $k_2$  propagation vector [65, 126, 130]. In  $\text{Ba}_{0.3}\text{Sr}_{1.7}\text{Co}_2\text{Fe}_{12}\text{O}_{22}$  and  $\text{Ba}_{0.5}\text{Sr}_{1.5}\text{Zn}_2(\text{Fe}_{1-x}\text{Al}_x)_{12}\text{O}_{22}$  also the commensurate  $k_2$  phase is the transverse conical ferroelectric phase [56, 66, 127]. In our case this commensurate phase is found at as low as 0.1 T or near  $H_4$  up to 300 K, see Fig.

6.35.

In the  $(0\ 0\ l)$  scans we did not get any additional information to what we have seen in our soft-x-ray data. In the following section we studied the scattering in perpendicular to  $(0\ 0\ l)$  direction in reciprocal space.

### 6.5.1 Neutron scattering in $(0\ k\ l)$ plane

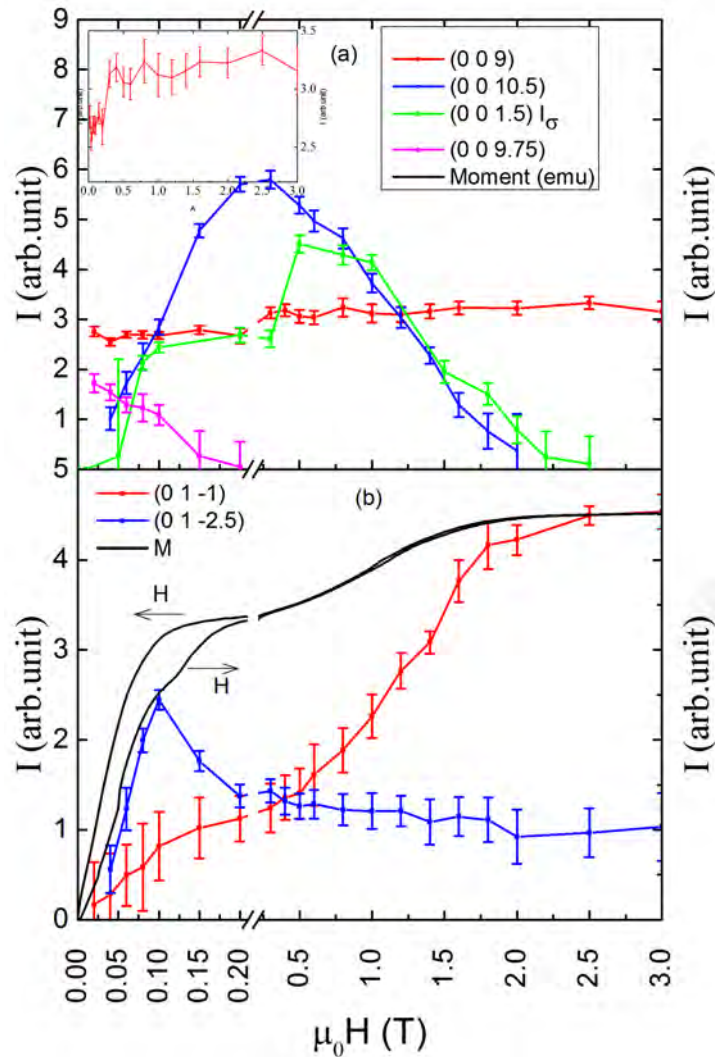


Fig. 6.36 Integrated intensity from the Gaussian fit of the omega scans for reflections along (a)  $(0\ 0\ l)$  and (b)  $(0\ l\ l)$  at 4 K as a function of applied  $H$ . Field is applied perpendicular to both  $(0\ 0\ l)$  and  $(0\ l\ l)$ . For reference intensity from the soft-x-ray experiment for  $\sigma$  polarization is also plotted in (a). Magnetization data is also shown in (b). In the inset of (a) enlarged view of  $(0\ 0\ 9)$  reflection is plotted.

In a good quality sample we carried out omega scans of few reflections in  $(0\ h\ l)$  plane.

The sample has small fraction of reverse-obverse twin. The nuclear and magnetic intensity of both the twins contributes for  $(0\ 0\ l)$  reflections but for  $(0\ 1\ l)$  reflections they are separated. Magnetic intensity in the  $(0\ 0\ l)$  reflections probe the moments in  $(h\ h\ 0)$  plane while modulated magnetic moments in  $[0\ 0\ l]$  direction will contribute to intensity in the  $(0\ h\ l)$  reflections but not to  $(0\ 0\ l)$ . Since our lattice parameter  $c$  ( $43.5\text{\AA}$ ) is large compared to  $a=b=5.86\text{\AA}$ , low  $Q$  reflections along  $(0\ h\ l)$  is perpendicular to the  $(0\ 0\ l)$ . In Fig. 6.36 (a) we saw that intensity of  $(0\ 0\ 10.5)$  follows similar trend as that of soft-x-ray resonance data (green). The intensity of the  $(0\ 0\ 9)$  reflection increases above 0.1 T (inset (a)) and becomes almost flat after 0.3 T indicating that the ferrimagnetic component perpendicular to  $(0\ 0\ l)$  remains approximately constant above 0.3 T. Thus we have almost non varying modulated moment in the  $ab$  plane. In (b) the magnetic intensity in the  $(0\ 1\ -1)$  nuclear reflection is found to increase sharply up to 0.12 T and then increases steadily. Combining with the variation along  $(0\ 0\ l)$  we can tell that this is due to the moment component along  $(0\ 0\ l)$ . The satellite  $(0\ 1\ -2.5)$  shows very interesting variation. Intensity of  $(0\ 1\ -2.5)$  increase sharply up to 0.12 Tesla, reaches a maximum and decreases steadily up to 2 T and then becomes flat again. In the ferrimagnetic phase we do not expect any satellite along  $c$ .

The presence of  $(0\ 1\ -2.5)$  in the saturation field is not unique to our sample. In  $\text{Ba}_{0.3}\text{Sr}_{1.7}\text{Co}_2\text{Fe}_{12}\text{O}_{22}$  and  $\text{Ba}_{0.5}\text{Sr}_{1.5}\text{Zn}_2(\text{Fe}_{1-x}\text{Al}_x)_{12}\text{O}_{22}$  also such behavior was reported [66, 127]. Since we do not have any satellite along  $(0\ 0\ l)$ , this can be only due to small tilt angle along  $c$ -direction still remaining in the sample, which predicts small reduction in saturation moments compared to calculated spin only moments. This is also evident from our soft-x-ray data, where the angles  $\alpha$  and  $\beta$  not seem to approach  $\pi/2$  compared to in-plane angles as we increase  $H$ , see Fig. 6.29.

Obvious question arises why we did not see any intensity in the  $(0\ 0\ 1.5)$  reflection. As the tilting of spins in  $c$ -direction causes modulated moments in  $z_3$  directions and should be observable in  $\sigma \rightarrow \pi$  and  $\pi \rightarrow \sigma$  channels. For that let us look back at the model-C. In Fig. B.3 for zero in plane angle *i.e.*  $\phi = 0$  we have almost negligible intensity in the  $\sigma \rightarrow \pi$  and  $\pi \rightarrow \sigma$  channels for smaller out of plane angle *i.e.*  $(\alpha, \beta \rightarrow 0)$ . Therefore, no intensity was observed in the soft-x-ray experiments in the  $(0\ 0\ 1.5)$  satellite. Our sample was exposed to high magnetic field before measurements. Although the measurements of omega scans were performed in increasing field order, previous magnetic history is found to influence the sample behavior. This is evident from the emergence of only  $(0\ 0\ 9.75)$  satellites and absence of incommensurate  $k_1$  satellite. The magnetization curves also showed the history in the sample, as can be seen from the loop opening near 0.2 T.

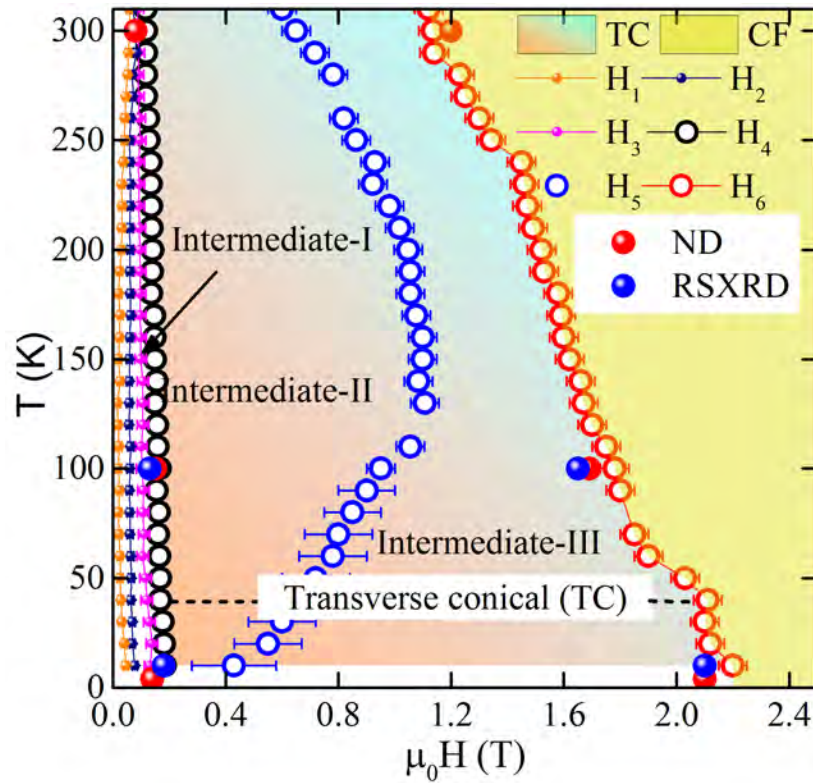


Fig. 6.37 H-T Phase diagram constructed using our magnetization, soft-x-ray diffraction and neutron diffraction data.

### 6.5.2 The phase diagram

Based on all our experimental data, magnetization, soft-x-ray diffraction and neutron scattering we constructed the H-T phase diagram of our sample which can be seen in Fig. 6.37. In the low field region we already saw that it is magnetic history dependent and various phases coexist. The intermediate-II phase which, in contrast to reported 2-fan structure earlier is found to be transverse conical phase with only  $k_2$  propagation. Therefore we claim it ferroelectric phase-I (FE-I). The difference with FE-II phase is that the  $k_2$  satellite intensity starts decreasing at this phase, but still remains ferroelectric. Thus FE-II phase can be considered as a transient phase or the onset of rapid transition to ferrimagnetic phase. The intermediate-II and intermediate-III both phases are found to be ferroelectric with transverse conical spin structure, which is contrary to the previously proposed phase diagram [3]. Moreover, the so called ferrimagnetic phase is also found to be modulated in c-direction. This needs high magnetic field studies to find out the field values where a collinear phase is reached. Therefore, our microscopic data proves that H-driven ferroelectricity in this type of hexaferrite is occurring at much lower field and can be observed near room temperature.



# Chapter 7

## Summary and outlook

In this thesis we carried out in-depth macroscopic as well as microscopic scattering studies on the Y-type hexaferrite  $[\text{Ba}_{(2-x)}\text{Sr}_x]\text{Zn}_2\text{Fe}_{12}\text{O}_{22}$ , the first hexaferrite to have magnetic field induced ferroelectricity. We have grown crystals of different compositions and compared their structural and macroscopic magnetic properties. This thesis provides, first time ever, a solution for spin structure in the ferroelectric phase. Most notably, the solved transverse conical spin structure is compatible with magnetic field induced ferroelectricity by IDM mechanism, which was the case for most of the hexaferrites.

Growth of single crystals of hexaferrite is a tricky business. As most of the hexaferrite classes have similar block arrangement, even small changes in thermodynamic and kinetic parameters can influence the growth remarkably. We were successful in synthesizing single crystals of  $[\text{Ba}_{(1-x)}\text{Sr}_x]\text{Zn}_2\text{Fe}_{12}\text{O}_{22}$  with three different  $x = 0.72, 1.18$  and  $1.4$ . Compositions with  $x$  values  $1.18$  and  $1.4$  show distinct metamagnetic steps in the easy plane magnetization curves ( $H \perp [001]$ ) indicating metamagnetic transitions, while for lower Sr content ( $x=0.72$ ) no such steps were observed. In Chapter-4 we have seen that the occupancies of Zn in the tetrahedral site are modified by the substitution of Sr for Ba. This change in occupation changes the average bond length at the boundary between Zn/Fe and O. This change happens to be in the boundary between the spin blocks which in turn effects the superexchange interaction in the spin block boundary. Thus, we get from ferrimagnetic to spin helix structures at zero  $H$  depending upon Sr content. It would be interesting to investigate more samples with different compositions to see the influence of Sr content on structural and magnetic changes in this type of hexaferrite.

The spin structures corresponding to metamagnetic phases were found to be consisting of phase mixtures at low  $H$ . Transverse conical structure is found to be present at very low  $H$ , mixed with a 4-fan structure in a wide field range. The transition of 4-fan to the transverse conical state is accompanied by hysteresis which disappears near zero  $H$ . No

circular dichroism is observed in the pure 4-fan structure at either of the satellites. This 4-fan structure is the connecting structure between the two chiral phases: the zero  $H$  helical and the high  $H$  transverse conical phases. In the demagnetization process the 4-fan structure is not observed and the zero  $H$  helical phase is reached from high  $H$  transverse conical phase. This causes a linkage between the two chiral phases in the demagnetization process.

We carried out extensive field dependent soft X-ray diffraction experiments to investigate the magnetic structure in the ferroelectric phase. Circular dichroism in horizontal fields and linear dichroism in vertical fields are not at all consistent with the proposed 2-fan spin structure. In 10 K to 300 K in no field range the proposed 2-fan structure in literature is found. We carried out numerical analysis of the various possible models and for the first time found that a transverse conical model is the best model that suits our diffraction data. As per IDM mechanism, spin induced ferroelectricity (see section 2.3) can not be possible in 2-fan spin structure proposed in the literature. Remarkably, as in the case of other magnetoelectric hexaferrite systems, our transverse conical spin structure is compatible with  $H$  induced polarization by IDM mechanism. It is for the first time the spin structure in the ferroelectric phase has been solved and found transverse conical structure.

Only the transverse conical structure is found to exist above the metamagnetic field  $H_4$ . Therefore, we claim that magnetic field induced ferroelectricity should be observable from  $H_4$  rather than from  $H_5$  as claimed by [3]. Our claim is supported by low  $H$  induced electric polarizations in the oxygen sintered highly resistive samples [119]. However, the field at which Chai *et al.* found field driven ferroelectricity is higher than the values of  $H_4$  obtained by magnetization measurements. Therefore, there is a scope that with increase in resistivity, polarization can be obtained at lower  $H$ . The reported 2-fan structures in intermediate-II and intermediate-III phases are found to be the same transverse conical phases. In the intermediate-III phase the in-plane angles start decreasing rapidly, causing a jump in the magnetization, but the structure still remains transverse conical.

Electrical polarization switching with magnetic field is one of the most interesting phenomenon in hexaferrites. In our system the mapped spin chiral domain configurations were inverted upon reversing the field direction. Chirality and polarization by IDM mechanism are related by  $\vec{P} = \vec{e}_{12} \times \vec{c}$ . Therefore, chirality switching should switch the polarizations, but experimentally, in a sample with different composition this has not been observed [3]. Also, in the same compound at two different temperatures, different switching behaviors were observed [57]. In the demagnetization process since the non-chiral 4-fan structure is not observed, the chirality in the high field transverse conical phase is assumed to be connected to the zero  $H$  helical phase. This may cause the chirality inversion upon reversing  $H$ . A clear insight can be obtained by performing more experiments at different  $H$  and

temperature.

We have seen that at 300 K, both linear dichroism in the vertical field and circular dichroism in horizontal field can be observed (see Fig. 6.32). Thus  $H$  induced polarization can be obtained at 300 K, which indeed was indicated by an earlier observation [119]. The metamagnetic signatures in our samples are found well above room temperature (318 K for BZY-2 and 303 K for BZY-3). This makes it a very good potential candidate for room temperature applications.

In our neutron diffraction experiment also we saw a transverse conical spin structure. In addition to that intensity in  $(0\ 1\ -2.5)$  reflection is observed up to 3 T vertical field which is above macroscopic saturation magnetization field. This indicates modulated moments in the  $c$ -direction is observed saturation field. Without in plane modulated components intensity in soft-x-ray resonance diffraction is too small to observe. This fact was for the first time addressed in this thesis. High field experiments are to be performed to see if the tilting angle goes to zero at high field.

Switching of chirality or magnetization by external electric field is desirable for magnetoelectric materials. Recently, magnetization switching by electric field was achieved in an M-type hexaferrite  $\text{SrCo}_2\text{Ti}_2\text{Fe}_8\text{O}_{19}$  [132]. In Al doped Y-type hexaferrite also it was found that magnetization can be switched with electric field [129].

It would be an interesting experiment to observe switching of chirality in electric field. So far we saw inversion of chirality at temperature 100 K and lower, but it would be interesting to see how Chirality changes at different temperatures and fields. Moreover, in good quality thin sample recently skyrmions have been reported [72, 133]. It will be interesting to see in our samples with spin polarized electron microscopy like Lorentz transmission electron microscopy. MFM or PFM studies can also be used to correlate the magnetic and ferroelectric domains. Model Hamiltonian calculations on different spin structures could give input to the stability of the structures.

Polarization analysis of neutron diffraction in a vertical magnetic field in horizontal scattering geometry can not distinguish between modulated moments in  $(0\ 0\ l)$  and in  $(h\ 0\ l)$  planes as both will give spin flip scattering. Therefore, in a horizontal external magnetic field half polarized neutron diffraction experiment may give valuable information. In our samples it was carried out very recently.

In a short, our proposed transverse conical spin structure model reveals that the  $H$  induced polarization is by IDM mechanism and can be observed at low  $H$  and can be extended to room temperature.



# References

- [1] Peter A. Gruenberg. Nobel lecture: From spin waves to giant magnetoresistance and beyond. *Rev. Mod. Phys.*, 80(4):1531–1540, December 2008.
- [2] Nicola A. Hill. Why are there so few magnetic ferroelectrics? *J. Phys. Chem. B*, 104:6694–6709, June 2000.
- [3] T. Kimura, G. Lawes, and A. P. Ramirez. Electric polarization rotation in a hexaferrite with long-wavelength magnetic structures. *Phys. Rev. Lett.*, 94:137201–, April 2005.
- [4] Tsuyoshi Kimura. Magnetoelectric hexaferrites. *Annu. Rev. Condens. Matter Phys.*, 3:93–110, February 2012.
- [5] N Momozawa, Y Yamaguchi, H Takei, and M Mita. Magnetic structure of  $(\text{Ba}_{1-x}\text{Sr}_x)_2\text{Zn}_2\text{Fe}_{12}\text{O}_{22}$  ( $x=0-1.0$ ). *J. Phys. Soc. Jpn.*, 54:771–780, February 1985.
- [6] A. J. Hearmon, R. D. Johnson, T. A. W. Beale, S. S. Dhesi, X. Luo, S.-W. Cheong, P. Steadman, and Paolo G. Radaelli. Magnetic fan structures in  $\text{Ba}_{0.5}\text{Sr}_{1.5}\text{Zn}_2\text{Fe}_{12}\text{O}_{22}$  hexaferrite revealed by resonant soft x-ray diffraction. *Phys. Rev. B*, 88:174413–, November 2013.
- [7] N Momozawa. Neutron diffraction study of helimagnet  $(\text{Ba}_{1-x}\text{Sr}_x)_2\text{Zn}_2\text{Fe}_{12}\text{O}_{22}$ . *J. Phys. Soc. Jpn.*, 55:4007–4013, November 1986.
- [8] N Momozawa and Y Yamaguchi. Field-induced commensurate intermediate phases in helimagnet  $(\text{Ba}_{1-x}\text{Sr}_x)_2\text{Zn}_2\text{Fe}_{12}\text{O}_{22}$  ( $x=0.748$ ). *J. Phys. Soc. Jpn.*, 62:1292–1304, April 1993.
- [9] A. M. Mulders, S. M. Lawrence, A. J. Princep, U. Staub, Y. Bodenthin, M. García-Fernández, M. Garganourakis, J. Hester, R. Macquart, and C. D. Ling. Circularly polarized soft x-ray diffraction study of helical magnetism in hexaferrite. *Phys. Rev. B*, 81:092405–, March 2010.
- [10] Y. Hiraoka, Y. Tanaka, T. Kojima, Y. Takata, M. Oura, Y. Senba, H. Ohashi, Y. Wakabayashi, S. Shin, and T. Kimura. Spin-chiral domains in  $\text{Ba}_{0.5}\text{Sr}_{1.5}\text{Zn}_2\text{Fe}_{12}\text{O}_{22}$  observed by scanning resonant x-ray microdiffraction. *Phys. Rev. B*, 84:064418–, August 2011.
- [11] Y. Hiraoka, Y. Tanaka, M. Oura, Y. Wakabayashi, and T. Kimura. The effect of field cooling on a spin-chiral domain structure in a magnetoelectric helimagnet  $\text{Ba}_{0.5}\text{Sr}_{1.5}\text{Zn}_2\text{Fe}_{12}\text{O}_{22}$ . *Journal of Magnetism and Magnetic Materials*, 384:160–165, June 2015.

- [12] John B Goodenough. Magnetism and chemical bond. Technical report, 1963.
- [13] Clarence Zener. Interaction between the  $d$ -shells in the transition metals. ii. ferromagnetic compounds of manganese with perovskite structure. *Phys. Rev.*, 82(3):403–405, May 1951.
- [14] P. G. de Gennes. Effects of double exchange in magnetic crystals. *Phys. Rev.*, 118:141–154, April 1960.
- [15] M. Imada, A. Fujimori, and Y. Tokura. Metal-insulator transitions. *Rev. Mod. Phys.*, 70(4):1039–1263, October 1998.
- [16] S. Jin, T. H. Tiefel, M. McCormack, R. A. Fastnacht, R. Ramesh, and L. H. Chen. Thousandfold change in resistivity in magnetoresistive la-ca-mn-o films. *Science*, 264:413–415, April 1994.
- [17] R. von Helmolt, J. Wecker, B. Holzapfel, L. Schultz, and K. Samwer. Giant negative magnetoresistance in perovskitelike  $\text{La}_{2/3}\text{Ba}_{1/3}\text{MnO}_3$  ferromagnetic films. *Phys. Rev. Lett.*, 71(14):2331–2333, October 1993.
- [18] B. D. Cullity and C. D. Graham. *Introduction to magnetic materials*. John Wiley & Sons, 2011.
- [19] S. Blundell. *Magnetism in condensed matter*. Oxford Univ. Press, 2001.
- [20] K Adachi, S Chikazumi, E Hirota, N Imamura, Y Ishikawa, Y Makino, Norio Miura, T Mizoguchi, Y Nakamura, and Y Sugita. *Physics and engineering applications of magnetism*, volume 92. Springer Science & Business Media, 2012.
- [21] Dmitry Zakharov, Hans-Albrecht Krug von Nidda, Mikhail Eremin, Joachim Deisenhofer, Rushana Eremina, and Alois Loidl. Anisotropic exchange in spin chains. In *Quantum Magnetism*, pages 193–238. Springer, 2008.
- [22] I. E. Dzyaloshinskii. On the magneto-electrical effect in antiferromagnets. *Soviet Physics JETP-USSR*, 10:628–629, 1960.
- [23] T Moriya. Anisotropic superexchange interaction and weak ferromagnetism. *Phys. Rev.*, 120:91–98, October 1960.
- [24] P. W. Anderson. New approach to the theory of superexchange interactions. *Phys. Rev.*, 115(1):2–13, July 1959.
- [25] V. E. Dmitrienko, E. N. Ovchinnikova, S. P. Collins, G. Nisbet, G. Beutier, Y. O. Kvashnin, V. V. Mazurenko, A. I. Lichtenstein, and M. I. Katsnelson. Measuring the dzyaloshinskii-moriya interaction in a weak ferromagnet. *Nat Phys*, 10:202–206, March 2014.
- [26] H. Schmid. Multi-ferroic magnetoelectrics. *Ferroelectrics*, 162:317–338, January 1994.
- [27] D Khomskii. Classifying multiferroics: Mechanisms and effects. *Physics*, 2:20, 2009.

- [28] K.F. Wang, J.-M. Liu, and Z.F. Ren. Multiferroicity: the coupling between magnetic and polarization orders. *Advances in Physics*, 58(4):321–448, June 2009.
- [29] T J Park, G C. Papaefthymiou, A J. Viescas, A R. Moodenbaugh, and S S. Wong. Size-dependent magnetic properties of single-crystalline multiferroic BiFeO<sub>3</sub> nanoparticles. *Nano Lett.*, 7:766–772, February 2007.
- [30] Jeroen van den Brink and Daniel I Khomskii. Multiferroicity due to charge ordering. *Journal of Physics: Condensed Matter*, 20(43):434217–, 2008.
- [31] N. Ikeda, H. Ohsumi, K. Ohwada, K. Ishii, T. Inami, K. Kakurai, Y. Murakami, K. Yoshii, Yoichi Mori, S. and Horibe, and H. Kito. Ferroelectricity from iron valence ordering in the charge-frustrated system LuFe<sub>2</sub>O<sub>4</sub>. *Nature*, 436:1136–1138, August 2005.
- [32] J. de Groot, K. Marty, M. D. Lumsden, A. D. Christianson, S. E. Nagler, S. Adiga, W. J. H. Borghols, K. Schmalzl, Z. Yamani, S. R. Bland, R. de Souza, U. Staub, W. Schweika, Y. Su, and M. Angst. Competing ferri- and antiferromagnetic phases in geometrically frustrated LuFe<sub>2</sub>O<sub>4</sub>. *Phys. Rev. Lett.*, 108:037206–, January 2012.
- [33] D Niermann, F Waschowski, J de Groot, M Angst, and J Hemberger. Dielectric properties of charge-ordered LuFe<sub>2</sub>O<sub>4</sub> revisited: the apparent influence of contacts. *Physical review letters*, 109:016405, 2012.
- [34] M. Angst. Ferroelectricity from iron valence ordering in rare earth ferrites? *physica status solidi (RRL)-Rapid Research Letters*, 7:383–400, 2013.
- [35] Mark S. Senn, Jon P. Wright, and J. Paul Attfield. Charge order and three-site distortions in the verwey structure of magnetite. *Nature*, 481(7380):173–176, January 2012.
- [36] S. Adiga. *Crystal growth and scattering studies on two Ferrites*. PhD thesis, RWTH Aachen, 2015.
- [37] Yoshinori Tokura, Shinichiro Seki, and Naoto Nagaosa. Multiferroics of spin origin. *Reports on Progress in Physics*, 77(7):076501, 2014.
- [38] T. Kimura, T. Goto, H. Shintani, K. Ishizaka, T. Arima, and Y. Tokura. Magnetic control of ferroelectric polarization. *Nature*, 426:55–58, November 2003.
- [39] T. Kimura. Spiral magnets as magnetoelectrics. *Annu. Rev. Mater. Res.*, 37:387–413, July 2007.
- [40] Yoshinori Tokura and Shinichiro Seki. Multiferroics with spiral spin orders. *Adv. Mater.*, 22(14):1554–1565, 2010.
- [41] Noriki Terada. Spin and orbital orderings behind multiferroicity in delafossite and related compounds. *Journal of Physics: Condensed Matter*, 26(45):453202, 2014.
- [42] K. Taniguchi, N. Abe, T. Takenobu, Y. Iwasa, and T. Arima. Ferroelectric polarization flop in a frustrated magnet MnWO<sub>4</sub> induced by a magnetic field. *Phys. Rev. Lett.*, 97(9):097203–, August 2006.

- [43] W Prellier, M P Singh, and P Murugavel. The single-phase multiferroic oxides: from bulk to thin film. *Journal of Physics: Condensed Matter*, 17:R803–, 2005.
- [44] S. Ishiwata, Y. Kaneko, Y. Tokunaga, Y. Taguchi, T. Arima, and Y. Tokura. Perovskite manganites hosting versatile multiferroic phases with symmetric and antisymmetric exchange strinctions. *Phys. Rev. B*, 81:100411–, March 2010.
- [45] V Yu Pomjakushin, M Kenzelmann, A Dönni, A B Harris, T Nakajima, S Mitsuda, M Tachibana, L Keller, J Mesot, H Kitazawa, and E Takayama-Muromachi. Evidence for large electric polarization from collinear magnetism in  $\text{TmMnO}_3$ . *New Journal of Physics*, 11:043019, 2009.
- [46] N. Lee, Y. J. Choi, M. Ramazanoglu, W. Ratcliff, V. Kiryukhin, and S.-W. Cheong. Mechanism of exchange striction of ferroelectricity in multiferroic orthorhombic  $\text{HoMnO}_3$  single crystals. *Phys. Rev. B*, 84(2):020101–, July 2011.
- [47] M Mostovoy. Ferroelectricity in spiral magnets. *Phys. Rev. Lett.*, 96:067601–, February 2006.
- [48] I. A. Sergienko and E. Dagotto. Role of the dzyaloshinskii-moriya interaction in multiferroic perovskites. *Phys. Rev. B*, 73:094434–, March 2006.
- [49] H Katsura, N Nagaosa, and Alexander V. Balatsky. Spin current and magnetoelectric effect in noncollinear magnets. *Phys. Rev. Lett.*, 95:057205–, July 2005.
- [50] S. Seki, Y. Yamasaki, Y. Shiomi, S. Iguchi, Y. Onose, and Y. Tokura. Impurity-doping-induced ferroelectricity in the frustrated antiferromagnet  $\text{CuFeO}_2$ . *Phys. Rev. B*, 75:100403, Mar 2007.
- [51] J. W. Cable, M. K. Wilkinson, E. O. Wollan, and W. C. Koehler. Neutron diffraction investigation of the magnetic order in  $\text{mni}_2$ . *Phys. Rev.*, 125:1860–1864, Mar 1962.
- [52] T. Goto, T. Kimura, G. Lawes, A. Ramirez, and Y. Tokura. Ferroelectricity and giant magnetocapacitance in perovskite rare-earth manganites. *Phys. Rev. Lett.*, 92:257201–, June 2004.
- [53] Y. Yamasaki, S. Miyasaka, Y. Kaneko, J.-P. He, T. Arima, and Y. Tokura. Magnetic reversal of the ferroelectric polarization in a multiferroic spinel oxide. *Phys. Rev. Lett.*, 96(20):207204–, May 2006.
- [54] T. Kimura, Y. Sekio, H. Nakamura, T. Siegrist, and A. P. Ramirez. Cupric oxide as an induced-multiferroic with high- $t_c$ . *Nat Mater*, 7:291–294, April 2008.
- [55] S Ishiwata, Y Taguchi, H Murakawa, Y Onose, and Y Tokura. Low-magnetic-field control of electric polarization vector in a helimagnet. *Science*, 319:1643–1646, 2008.
- [56] Sae Hwan Chun, Yi Sheng Chai, Yoon Seok Oh, Deepshikha Jaiswal-Nagar, So Young Haam, Ingyu Kim, Bumsung Lee, Dong Hak Nam, Kyung-Tae Ko, Jae-Hoon Park, Jae-Ho Chung, and Kee Hoon Kim. Realization of giant magnetoelectricity in helimagnets. *Phys. Rev. Lett.*, 104:037204–, January 2010.

- [57] Y. Tokunaga, Y. Kaneko, D. Okuyama, S. Ishiwata, T. Arima, S. Wakimoto, K. Kakurai, Y. Taguchi, and Y. Tokura. Multiferroic *m*-type hexaferrites with a room-temperature conical state and magnetically controllable spin helicity. *Phys. Rev. Lett.*, 105(25):257201–, December 2010.
- [58] Y Kitagawa, Y Hiraoka, T Honda, T Ishikura, H Nakamura, and T Kimura. Low-field magnetoelectric effect at room temperature. *Nat Mater*, 9(10):797–802, October 2010.
- [59] Sae Chun, Yi Chai, Byung-Gu Jeon, Hyung Kim, Yoon Oh, Ingyu Kim, Hanbit Kim, Byeong Jeon, So Haam, Ju-Young Park, Suk Lee, Jae-Ho Chung, Jae-Hoon Park, and Kee Kim. Electric field control of nonvolatile four-state magnetization at room temperature. *Phys. Rev. Lett.*, 108:177201–, April 2012.
- [60] G. Turner, B. Stewart, T. Baird, R.D. Peacock, and A.G. Cairns-Smith. Layer morphology and growth mechanisms in barium ferrites. *Journal of Crystal Growth*, 158(3):276–283, January 1996.
- [61] N Momozawa, Y Yamaguchi, H Takei, and M Mita. Modification of helix in  $(\text{Ba}_{1-x}\text{Sr}_x)_2\text{Zn}_2\text{Fe}_{12}\text{O}_{22}$  due to applied magnetic field. *J. Phys. Soc. Jpn.*, 54:3895–3903, October 1985.
- [62] Shigenori Utsumi, Daisuke Yoshiba, and Nobuyuki Momozawa. Superexchange interactions of  $(\text{Ba}_{1-x}\text{Sr}_x)_2\text{Zn}_2\text{Fe}_{12}\text{O}_{22}$  system studied by neutron diffraction. *J. Phys. Soc. Jpn.*, 76(3):034704–, February 2007.
- [63] J. Muller, A. Collomb, T. Fournier, I. Harrowfield, and D. Samaras. Composition and structure of some  $[\text{Ba}_{1-p}\text{Sr}_p]\text{ZnFe}_6\text{O}_{11}$  y-type hexagonal ferrites. *Journal of Magnetism and Magnetic Materials*, 102:305–313, December 1991.
- [64] A. Collomb, J. Muller, J.C. Guitel, and J.M. Desvignes. Crystal structure and zinc location in the  $\text{BaZnFe}_6\text{O}_{11}$  y-type hexagonal ferrite. *Journal of Magnetism and Magnetic Materials*, 78:77–84, January 1989.
- [65] S Ishiwata, D Okuyama, K Kakurai, M Nishi, Y Taguchi, and Y Tokura. Neutron diffraction studies on the multiferroic conical magnet  $\text{Ba}_2\text{Mg}_2\text{Fe}_{12}\text{O}_{22}$ . *Phys. Rev. B*, 81:174418–, May 2010.
- [66] H Lee, Y Song, J Chung, S H Chun, Y S Chai, K H Kim, M. Reehuis, K. Prokeš, and Mat’áš. Field-induced incommensurate-to-commensurate phase transition in the magnetoelectric hexaferrite  $\text{Ba}_{0.5}\text{Sr}_{1.5}\text{Zn}_2(\text{Fe}_{1-x}\text{Al}_x)_{12}\text{O}_{22}$ . *Phys. Rev. B*, 83:144425–, April 2011.
- [67] G. Albanese, M. Carbuicchio, A. Deriu, G. Asti, and S. Rinaldi. Influence of the cation distribution on the magnetization of y-type hexagonal ferrites. *Applied physics*, 7(3):227–238–, 1975.
- [68] Anthony R West. *Solid state chemistry and its applications*. John Wiley & Sons, 2007.
- [69] G. Dhanaraj, K. Byrappa, V. Prasad, and M. Dudley. *Springer handbook of crystal growth*. Springer Science & Business Media, 2010.

- [70] Y. Janssen, M. Angst, K.W. Dennis, R.W. McCallum, and P.C. Canfield. Differential thermal analysis and solution growth of intermetallic compounds. *Journal of Crystal Growth*, 285:670–680, December 2005.
- [71] N Momozawa, M Mita, and H Takei. Single crystal growth of  $(\text{Ba}_{1-x}\text{Sr}_x)_2\text{Zn}_2\text{Fe}_{12}\text{O}_{22}$  from high temperature solution. *Journal of Crystal Growth*, 83:403–409, June 1987.
- [72] X. Z. Yu, K. Shibata, W. Koshibae, Y. Tokunaga, Y. Kaneko, T. Nagai, K. Kimoto, Y. Taguchi, N. Nagaosa, and Y. Tokura. Thermally activated helicity reversals of skyrmions. *Phys. Rev. B*, 93:134417–, April 2016.
- [73] R. Takagi, Y. Tokunaga, T. Ideue, Y. Taguchi, Y. Tokura, and S. Seki. Thermal generation of spin current in a multiferroic helimagnet. *APL Mater.*, 4(3):032502, 2016.
- [74] M. McElfresh. *Fundamentals of magnetism and magnetic measurements*. Quantum Design, Inc., 6325 Lusk Boulevard, San Diego, CA 92121, USA, 1994.
- [75] Quantum design, <http://www.qdusa.com/>.
- [76] M. Bałanda. Ac susceptibility studies of phase transitions and magnetic relaxation: conventional, molecular and low-dimensional magnets. *Acta Physica Polonica A*, 124(6):964–976, 2013.
- [77] Ajoy K Ghatak and S Lokanathan. *Quantum mechanics: theory and applications*. Macmillan, 2004.
- [78] S. Blugel. *Scattering Methods for Condensed Matter Research: Towards Novel Applications at Future Sources*, chapter Scattering Theory: Born Series, pages A2.1–A2.29. Forschungszentrum Juelich, 2012.
- [79] M. Blume. Magnetic scattering of x rays (invited). *Journal of Applied Physics*, 57:3615–3618, 1985.
- [80] S W Lovesey. Magnetic photon scattering. *Journal of Physics C: Solid State Physics*, 20:5625–, 1987.
- [81] M. Blume and Doon Gibbs. Polarization dependence of magnetic x-ray scattering. *Phys. Rev. B*, 37(4):1779–1789, February 1988.
- [82] J. P. Hannon, G. T. Trammell, M. Blume, and Doon Gibbs. X-ray resonance exchange scattering. *Phys. Rev. Lett.*, 61(10):1245–1248, September 1988.
- [83] J. Bohr. Magnetic x-ray scattering: A new tool for magnetic structure investigations. *Journal of Magnetism and Magnetic Materials*, 83:530–534, January 1990.
- [84] S W Lovesey. Photon scattering by magnetic solids. *Reports on Progress in Physics*, 56:257–, 1993.
- [85] J. P. Hill and D. F. McMorrow. Resonant exchange scattering: Polarization dependence and correlation function. *Acta Crystallographica Section A*, 52:236–244, 1996.

- [86] D. Gibbs, D. E. Moncton, K. L. D'Amico, J. Bohr, and B. H. Grier. Magnetic x-ray scattering studies of holmium using synchrotron radiation. *Phys. Rev. Lett.*, 55:234–237, July 1985.
- [87] F. De Bergevin and M. Brunel. Observation of magnetic superlattice peaks by x-ray diffraction on an antiferromagnetic nio crystal. *Physics Letters A*, 39:141–142, April 1972.
- [88] F. de Bergevin and M. Brunel. Diffraction of x-rays by magnetic materials. i. general formulae and measurements on ferro- and ferrimagnetic compounds. *Acta Crystallographica Section A*, 37:314–324, 1981.
- [89] J. W. Kim, Y. Lee, D. Wermeille, B. Sieve, L. Tan, S. L. Bud'ko, S. Law, P. C. Canfield, B. N. Harmon, and A. I. Goldman. Systematics of x-ray resonant scattering amplitudes in  $rni_2ge_2$  ( $r = Gd, tb, dy, ho, er, tm$ ): The origin of the branching ratio at the  $l$  edges of the heavy rare earths. *Phys. Rev. B*, 72:064403–, August 2005.
- [90] T Bruckel. Scattering techniques ii: Magnetic x-ray scattering. *LECTURE MANUSCRIPTS OF THE SPRING SCHOOL OF THE INSTITUTE OF SOLID STATE RESEARCH*, 36:B5, 2005.
- [91] Gordon Leslie Squires. *Introduction to the theory of thermal neutron scattering*. Cambridge university press, 2012.
- [92] Varley F. Sears. Neutron scattering lengths and cross sections. *Neutron news*, 3(3):26–37, 1992.
- [93] Kim Lefmann. Neutron scattering: Theory, instrumentation, and simulation. *University Course*, page 12, 2010.
- [94] *Neutron Scattering: Lectures of the JCNS Laboratory Course Held at Forschungszentrum Jülich and the Research Reactor FRM II of TU Munich*, volume 27. Forschungszentrum Jülich, 2010.
- [95] R.H. Arendt. The molten salt synthesis of single magnetic domain  $BaFe_{12}O_{19}$  and  $SrFe_{12}O_{19}$  crystals. *Journal of Solid State Chemistry*, 8:339–347, December 1973.
- [96] A. Tauber, Samuel Dixon, and R. O. Savage. Improvement of the ferromagnetic resonance linewidth of single crystal ZnY ( $Ba_2Zn_2Fe_{12}O_{22}$ ) by a new growth technique. *Journal of Applied Physics*, 35(3):1008–1009, 1964.
- [97] L.M. Silber, E. Tsantes, and W.D. Wilber. Temperature dependence of ferromagnetic resonance linewidth in pure and substituted barium ferrite. *Journal of Magnetism and Magnetic Materials*, 54–57, Part 3:1141–1142, February 1986.
- [98] J.W. Nielsen and E.F. Dearborn. The growth of single crystals of magnetic garnets. *Journal of Physics and Chemistry of Solids*, 5:202–207, May 1958.
- [99] L. H. Brixner. Preparation of the ferrites  $BaFe_{12}O_{19}$  and  $SrFe_{12}O_{19}$  in transparent form1. *J. Am. Chem. Soc.*, 81(15):3841–3843, August 1959.

- [100] Arthur Tauber, J. A. Kohn, and R. O. Savage. Single crystal ferroxdure,  $\text{BaFe}_{12-2x}^{3+}\text{Ir}_x^{4+}\text{Zn}_x^{2+}\text{O}_{19}$ , with strong planar anisotropy. *Journal of Applied Physics*, 34(4):1265–1267, 1963.
- [101] M Nevřiva. Crystal growth of Mg- and Ti-substituted hexagonal ferrites from  $\text{PbO-B}_2\text{O}_3$  based melts. *Cryst. Res. Technol.*, 22:1225–1228, 1987.
- [102] J. Aidelberg, J. Flicstein, and M. Schieber. Cellular growth in  $\text{BaFe}_{12}\text{O}_{19}$  crystals solidified from flux solvent. *Journal of Crystal Growth*, 21:195–202, February 1974.
- [103] R. Varadinov, V. Nikolov, P. Peshev, I. Mitov, and Kh. Neykov. New solvents for the growth of substituted  $\text{BaFe}_{12}\text{O}_{19}$  single crystals from high-temperature solutions. *Journal of Crystal Growth*, 110(4):763–768, April 1991.
- [104] B. T. Shirk and W. R. Buessem. Temperature dependence of ms and k1 of  $\text{BaFe}_{12}\text{O}_{19}$  and  $\text{SrFe}_{12}\text{O}_{19}$  single crystals. *Journal of Applied Physics*, 40:1294–1296, 1969.
- [105] R. J. Gambino and F. Leonhard. Growth of barium ferrite single crystals. *Journal of the American Ceramic Society*, 44:221–224, 1961.
- [106] X. Obradors, A. Collomb, M. Pernet, D. Samaras, and J.C. Joubert. X-ray analysis of the structural and dynamic properties of  $\text{BaFe}_{12}\text{O}_{19}$  hexagonal ferrite at room temperature. *Journal of Solid State Chemistry*, 56:171–181, February 1985.
- [107] H. Machida, F. Ohmi, Y. Sawada, Y. Kaneko, A. Watada, and H. Nakamura. Magneto-optical properties and thermomagnetic recording of m-type ba-ferrites. *Journal of Magnetism and Magnetic Materials*, 54–57, Part 3(0):1399–1400, February 1986.
- [108] R.O. Savage and A. Tauber. Growth of complex single-crystal hexagonal ferrites. *Materials Research Bulletin*, 2:469–478, April 1967.
- [109] X. Obradors, X. Solans, A. Collomb, D. Samaras, J. Rodriguez, M. Pernet, and M. Font-Altaba. Crystal structure of strontium hexaferrite  $\text{SrFe}_{12}\text{O}_{19}$ . *Journal of Solid State Chemistry*, 72:218–224, February 1988.
- [110] Arthur Tauber, R. O. Savage, R. J. Gambino, and C. G. Whinfrey. Growth of single crystal hexagonal ferrites containing zn. *Journal of Applied Physics*, 33(3):1381–1382, 1962.
- [111] R. O. Savage and A. Tauber. Growth and properties of single crystals of hexagonal ferrites. *Journal of the American Ceramic Society*, 47:13–18, 1964.
- [112] Crysalis user manual. Technical report, Agilent Technologies, XRD Products.
- [113] Václav Petříček, Michal Dušek, and Lukáš Palatinus. Crystallographic computing system jana2006: general features. *Zeitschrift für Kristallographie-Crystalline Materials*, 229:345–352, 2014.
- [114] <http://abulafia.mt.ic.ac.uk/shannon/ptable.php>.
- [115] U. Enz. Magnetization process of a helical spin configuration. *Journal of Applied Physics*, 32:S22–S26, 1961.

- [116] TM Perekalina, VA Sizov, RA Sizov, II Yamzin, and RA Voskanyan. Helicoidal spin ordering in the hexagonal ferrite  $(\text{Sr}_{0.8}\text{Ba}_{0.2})_2\text{Zn}_2\text{Fe}_{12}\text{O}_{22}$ . *Soviet Journal of Experimental and Theoretical Physics*, 25:266, 1967.
- [117] N Momozawa, Y Nagao, S Utsumi, M Abe, and Y Yamaguchi. Cation distribution and helimagnetic structure of the  $\text{Ba}_2(\text{Zn}_{1-x}\text{Mg}_x)\text{Fe}_{12}\text{O}_{22}$  system as revealed by magnetization measurements and neutron diffraction. *J. Phys. Soc. Jpn.*, 70:2724–2732, September 2001.
- [118] Jung Tae Lim and Chul Sung Kim. Magnetic properties of Zn doped  $\text{Co}_2\text{Y}$  hexaferrite by using high-field mössbauer spectroscopy. *Journal of Applied Physics*, 115(17):–, 2014.
- [119] Y S Chai, S H Chun, S Y Haam, Y S Oh, Ingyu Kim, and Kee Hoon Kim. Low-magnetic-field control of dielectric constant at room temperature realized in  $\text{Ba}_{0.5}\text{Sr}_{1.5}\text{Zn}_2\text{Fe}_{12}\text{O}_{22}$ . *New Journal of Physics*, 11:073030, 2009.
- [120] P. A. Joy and S. K. Date. Comparison of the zero-field-cooled magnetization behavior of some ferromagnetic and ferrimagnetic systems. *Journal of Magnetism and Magnetic Materials*, 218(2-3):229–237, August 2000.
- [121] Y B Lee, J T Lim, and C S Kim. Investigation of  $\text{ba}_2\text{me}_2\text{fe}_{12}\text{o}_{22}$  ( $m = \text{co}, \text{zn}$ ) hexaferrite based on external magnetic field mössbauer spectroscopy. *Journal of the Korean Physical Society*, 65:1419–1422, 2014.
- [122] Fen Wang, Tao Zou, Li-Qin Yan, Yi Liu, and Young Sun. Low magnetic field reversal of electric polarization in a y-type hexaferrite. *Applied Physics Letters*, 100(12):–, 2012.
- [123] Eiichi Tsuji, Takahiro Kurasawa, Ichiro Yazawa, Hiroyuki Katoh, Nobuyuki Momozawa, Kohtaro Ishida, and Shunji Kishimoto. Polarization analysis of x-ray diffraction peaks from a hexagonal ferrite –anomaly of forbidden reflections—. *J. Phys. Soc. Jpn.*, 65(2):610–614, February 1996.
- [124] E. Schierle, V. Soltwisch, D. Schmitz, R. Feyerherm, A. Maljuk, F. Yokaichiya, D. N. Argyriou, and E. Weschke. Cycloidal order of 4f moments as a probe of chiral domains in  $\text{DyMnO}_3$ . *Phys. Rev. Lett.*, 105(16):167207–, October 2010.
- [125] A. Glavic, C. Becher, J. Voigt, E. Schierle, E. Weschke, M. Fiebig, and T. Brückel. Stability of spin-driven ferroelectricity in the thin-film limit: Coupling of magnetic and electric order in multiferroic  $\text{TbMnO}_3$  films. *Phys. Rev. B*, 88(5):054401–, August 2013.
- [126] H Sagayama, K Taniguchi, N Abe, T Arima, S Nishikawa, Yand Yano, Y Kousaka, J Akimitsu, M Matsuura, and K Hirota. Two distinct ferroelectric phases in the multiferroic  $\text{Ba}_2\text{Mg}_2\text{Fe}_{12}\text{O}_{22}$ . *Phys. Rev. B*, 80:180419–, November 2009.
- [127] H Lee, S Chun, K Shin, B Jeon, Y Chai, K Kim, J Schefer, H Chang, S Yun, T Joung, and J Chung. Helical magnetic order and field-induced multiferroicity of the  $\text{Co}_2\text{Y}$ -type hexaferrite  $\text{Ba}_{0.3}\text{Sr}_{1.7}\text{Co}_2\text{Fe}_{12}\text{O}_{22}$ . *Phys. Rev. B*, 86:094435–, September 2012.

- [128] S Ishiwata, Y Taguchi, H Murakawa, Y Onose, and Y Tokura. Magnetic-field control of electric polarization in a helimagnetic hexaferrite  $\text{Ba}_2\text{Mg}_2\text{Fe}_{12}\text{O}_{22}$ . *Journal of Physics: Conference Series*, 150:042073–, 2009.
- [129] Yi Sheng Chai, Sangil Kwon, Sae Hwan Chun, Ingyu Kim, Byung-Gu Jeon, Kee Hoon Kim, and Soonchil Lee. Electrical control of large magnetization reversal in a helimagnet. *Nat Commun*, 5:–, June 2014.
- [130] S. Ishiwata, Y. Taguchi, Y. Tokunaga, H. Murakawa, Y. Onose, and Y. Tokura. Electric polarization induced by transverse magnetic field in the anisotropy-controlled conical helimagnet  $\text{Ba}_2(\text{Mg}_{1-x}\text{Zn}_x)_2\text{Fe}_{12}\text{O}_{22}$ . *Phys. Rev. B*, 79:180408–, May 2009.
- [131] Minoru Soda, Taishi Ishikura, Hiroyuki Nakamura, Yusuke Wakabayashi, and Tsuyoshi Kimura. Magnetic ordering in relation to the room-temperature magneto-electric effect of  $\text{Sr}_3\text{Co}_2\text{Fe}_{24}\text{O}_{41}$ . *Phys. Rev. Lett.*, 106(8):087201–, February 2011.
- [132] Liaoyu Wang, Dunhui Wang, Qingqi Cao, Yuanxia Zheng, Haicheng Xuan, Jinlong Gao, and Youwei Du. Electric control of magnetism at room temperature. *Sci. Rep.*, 2:–, January 2012.
- [133] Xiuzhen Yu, Maxim Mostovoy, Yusuke Tokunaga, Weizhu Zhang, Koji Kimoto, Yoshio Matsui, Yoshio Kaneko, Naoto Nagaosa, and Yoshinori Tokura. Magnetic stripes and skyrmions with helicity reversals. *Proceedings of the National Academy of Sciences*, 109(23):8856–8860, 2012.

# Appendix A

## A.1 Crystal structure refinement parameters

Table A.1 BZY-1 atomic parameters

Atom	Atom type		x	y	z	Occ
Ba1	Ba2+	6c	0	0	0.298428(16)	0.295(3)
Sr1	Sr2+	6c	0	0	0.298428(16)	0.705(3)
Zn1	Zn2+	6c	0	0	0.37537(2)	0.143(10)
Fe1	Fe3+	6c	0	0	0.37537(2)	0.837(10)
Zn2	Zn2+	6c	0	0	0.152273(19)	0.684(11)
Fe2	Fe3+	6c	0	0	0.152273(19)	0.306(11)
Fe3	Fe3+	6c	0	0	0.06488(2)	1
Fe4	Fe3+	3b	0	0	0.5	1
Fe5	Fe3+	18h	0.50325(5)	0.49675(5)	0.109476(15)	1
Fe6	Fe3+	3a	0	0	0	1
O1	O2-	6c	0	0	0.41907(10)	1
O2	O2-	6c	0	0	0.19787(10)	1
O3	O2-	18h	0.1567(2)	-0.1567(2)	0.02875(6)	1
O4	O2-	18h	0.8282(2)	0.1718(2)	0.08412(6)	1
O5	O2-	18h	0.1806(2)	-0.1806(2)	0.13749(6)	1

Table A.2 BZY-1 thermal displacement parameters

Atom	U_11	U_22	U_33	U_12	U_13	U_23
Ba1	0.01375(11)	0.01375(11)	0.01516(19)	0.00687(6)	0	0
Sr1	0.01375(11)	0.01375(11)	0.01516(19)	0.00687(6)	0	0
Zn1	0.00674(17)	0.00674(17)	0.0050(3)	0.00337(8)	0	0
Fe1	0.00674(17)	0.00674(17)	0.0050(3)	0.00337(8)	0	0
Zn2	0.00574(15)	0.00574(15)	0.0060(2)	0.00287(8)	0	0
Fe2	0.00574(15)	0.00574(15)	0.0060(2)	0.00287(8)	0	0
Fe3	0.00665(14)	0.00665(14)	0.0060(2)	0.00332(7)	0	0
Fe4	0.00584(17)	0.00584(17)	0.0042(3)	0.00292(9)	0	0
Fe5	0.00594(12)	0.00594(12)	0.00600(18)	0.00368(10)	0.00002(4)	-0.00002(4)
Fe6	0.00825(18)	0.00825(18)	0.0050(3)	0.00413(9)	0	0
O1	0.0056(6)	0.0056(6)	0.0063(11)	0.0028(3)	0	0
O2	0.0072(6)	0.0072(6)	0.0061(12)	0.0036(3)	0	0
O3	0.0180(5)	0.0180(5)	0.0158(9)	0.0113(6)	-0.0032(3)	0.0032(3)
O4	0.0070(4)	0.0070(4)	0.0074(7)	0.0034(4)	0.0011(2)	-0.0011(2)
O5	0.0064(4)	0.0064(4)	0.0062(7)	0.0031(4)	-0.0003(2)	0.0003(2)

Table A.3 BZY-2 atomic parameters

Atom	Atom type		x	y	z	Occ
Ba1	Ba2+	6c	0	0	0.29930(2)	0.643(5)
Sr1	Sr2+	6c	0	0	0.29930(2)	0.357(5)
Zn1	Zn2+	6c	0	0	0.37581(4)	0.114(19)
Fe1	Fe3+	6c	0	0	0.37581(4)	0.886(19)
Zn2	Zn2+	6c	0	0	0.15231(4)	0.65(16)
Fe2	Fe3+	6c	0	0	0.15231(4)	0.35(19)
Fe3	Fe3+	6c	0	0	0.06505(4)	1
Fe4	Fe3+	3b	0	0	0.5	1
Fe5	Fe3+	18h	0.50323(10)	0.49677(10)	0.10963(3)	1
Fe6	Fe3+	3a	0	0	0	1
O1	O2-	6c	0	0	0.41959(18)	1
O2	O2-	6c	0	0	0.19792(18)	1
O3	O2-	18h	0.1573(4)	-0.1573(4)	0.02851(11)	1
O4	O2-	18h	0.8291(4)	0.1709(4)	0.08490(12)	1
O5	O2-	18h	0.1801(5)	-0.1801(5)	0.13756(11)	1

Table A.4 BZY-2 thermal parameters

Atom	U_11	U_22	U_33	U_12	U_13	U_23
Ba1	0.00887(19)	0.00887(19)	0.0127(3)	0.00443(10)	0	0
Sr1	0.00887(19)	0.00887(19)	0.0127(3)	0.00443(10)	0	0
Zn1	0.0039(4)	0.0039(4)	0.0036(5)	0.00194(19)	0	0
Fe1	0.0039(4)	0.0039(4)	0.0036(5)	0.00194(19)	0	0
Zn2	0.0035(5)	0.0035(5)	0.0047(5)	0.0018(2)	0	0
Fe2	0.0035(5)	0.0035(5)	0.0047(5)	0.0018(2)	0	0
Fe3	0.0042(3)	0.0042(3)	0.0044(5)	0.00210(16)	0	0
Fe4	0.0030(4)	0.0030(4)	0.0036(6)	0.0015(2)	0	0
Fe5	0.0032(3)	0.0032(3)	0.0052(3)	0.0022(2)	-0.00001(10)	0.00001(10)
Fe6	0.0048(4)	0.0048(4)	0.0035(6)	0.0024(2)	0	0
O1	0.0025(13)	0.0025(13)	0.005(2)	0.0012(6)	0	0
O2	0.0050(13)	0.0050(13)	0.005(2)	0.0025(7)	0	0
O3	0.0119(10)	0.0119(10)	0.0093(14)	0.0065(11)	-0.0028(5)	0.0028(5)
O4	0.0039(9)	0.0039(9)	0.0076(12)	0.0023(10)	0.0006(5)	-0.0006(5)
O5	0.0033(9)	0.0033(9)	0.0057(13)	0.0020(10)	-0.0002(5)	0.0002(5)

Table A.5 BZY-3 atomic parameters

Atom	Atom type		x	y	z	Occ
Ba1	Ba2+	6c	0	0	0.298707(13)	0.404(3)
Sr1	Sr2+	6c	0	0	0.298707(13)	0.596(3)
Zn1	Zn2+	6c	0	0	0.379(3)	0.117(2)
Fe1	Fe3+	6c	0	0	0.3748(4)	0.8549
Zn2	Zn2+	6c	0	0	0.15210(14)	0.660(3)
Fe2	Fe3+	6c	0	0	0.1528(3)	0.3316
Fe3	Fe3+	6c	0	0	0.06502(2)	1
Fe4	Fe3+	3b	0	0	0.5	1
Fe5	Fe3+	18h	0.50319(4)	0.49681(4)	0.109538(12)	1
Fe6	Fe3+	3a	0	0	0	1
O1	O2-	6c	0	0	0.41945(10)	1
O2	O2-	6c	0	0	0.19806(10)	1
O3	O2-	18h	0.1577(2)	-0.1577(2)	0.02849(7)	1
O4	O2-	18h	0.8293(2)	0.1707(2)	0.08446(6)	1
O5	O2-	18h	0.1797(2)	-0.1797(2)	0.13785(6)	1

Table A.6 BZY-3 thermal parameters

Atom	U <sub>11</sub>	U <sub>22</sub>	U <sub>33</sub>	U <sub>12</sub>	U <sub>13</sub>	U <sub>23</sub>
Ba1	0.01291(9)	0.01291(9)	0.01530(12)	0.00645(4)		0
Sr1	0.01291(9)	0.01291(9)	0.01530(12)	0.00645(4)		0
Zn1	0.006(5)	0.006(5)	0.01(2)	0.003(3)		0
Fe1	0.0065(9)	0.0065(9)	-0.002(3)	0.0032(5)		0
Zn2	0.0085(10)	0.0085(10)	0.0089(13)	0.0042(5)		0
Fe2	0.0014(17)	0.0014(17)	0.001(3)	0.0007(8)		0
Fe3	0.00766(10)	0.00766(10)	0.00686(15)	0.00383(5)		0
Fe4	0.00667(13)	0.00667(13)	0.00491(19)	0.00334(7)		0
Fe5	0.00632(8)	0.00632(8)	0.00645(10)	0.00375(8)		-0.00002(3)
Fe6	0.00869(14)	0.00869(14)	0.0055(2)	0.00435(7)		0
O1	0.0066(5)	0.0066(5)	0.0067(7)	0.0033(2)		0
O2	0.0069(5)	0.0069(5)	0.0071(7)	0.0034(2)		0
O3	0.0167(4)	0.0167(4)	0.0152(6)	0.0101(5)		0.0030(2)
O4	0.0072(3)	0.0072(3)	0.0081(4)	0.0034(4)		-0.00098(17)
O5	0.0069(3)	0.0069(3)	0.0070(4)	0.0032(4)	-0.000148(11)	0.00031(17)

# Appendix B

## Numerical calculations on various models

The intensity of a first harmonic magnetic reflection in dipole resonant condition can be written as:

$$I = \left(F^{XRMS}\right)^2 = \left|\sum f^{XRMS} e^{2\pi i Q r}\right|^2 \quad (\text{B.1})$$

where,  $f^{XRMS}$  is given by the following matrix:

$$\begin{aligned} f^{XRMS} &= \begin{vmatrix} \sigma \rightarrow \sigma & \pi \rightarrow \sigma \\ \sigma \rightarrow \pi & \pi \rightarrow \pi \end{vmatrix} \\ &= \begin{vmatrix} 0 & z_1 \cos \theta + z_3 \sin \theta \\ -z_1 \cos \theta + z_3 \sin \theta & -z_2 \sin 2\theta \end{vmatrix} \end{aligned} \quad (\text{B.2})$$

### B.1 4-fan structure

$\sigma$  to  $\pi^*$

$$\begin{aligned} S_1 &= m \cos(\phi/2) \cos(\theta) \\ L_1 &= -m \cos(\theta) \\ S_2 &= m \cos(\phi/2) \cos(\theta) \\ L_2 &= -m \cos(\phi) \cos(\theta) \\ S_3 &= m \cos(\phi/2) \cos(\theta) \\ L_3 &= -m \cos(\theta) \\ S_4 &= m \cos(\phi/2) \cos(\theta) \\ L_4 &= -m \cos(\phi) \cos(\theta) \end{aligned} \quad (\text{B.3})$$

$\pi$  to  $\sigma^*$

$$\begin{aligned}S_1 &= -m \cos(\phi/2) \cos(\theta) \\L_1 &= m \cos(\theta) \\S_2 &= -m \cos(\phi/2) \cos(\theta) \\L_2 &= m \cos(\phi) \cos(\theta) \\S_3 &= -m \cos(\phi/2) \cos(\theta) \\L_3 &= m \cos(\theta) \\S_4 &= -m \cos(\phi/2) \cos(\theta) \\L_4 &= m \cos(\phi) \cos(\theta)\end{aligned}\tag{B.4}$$

$\pi$  to  $\pi^*$

$$\begin{aligned}S_1 &= m \sin(\phi/2) \sin(2\theta) \\L_1 &= 0 \\S_2 &= -m \sin(\phi/2) \sin(2\theta) \\L_2 &= m \sin(\phi) \sin(2\theta) \\S_3 &= -2m \sin(\phi/2) \sin(2\theta) \\L_3 &= 0 \\S_4 &= m \sin(\phi/2) \sin(2\theta) \\L_4 &= -m \sin(\phi) \sin(2\theta)\end{aligned}\tag{B.5}$$

## B.2 Model-A

**Geometry: horizontal magnet**

$\sigma$  to  $\pi^*$

$$\begin{aligned}
 S_1 &= ([-z_1 \cos \theta + z_3 \sin \theta]) e^{2\pi i Q r} \\
 &= -z_1 \cos \theta . e^{2\pi i Q r} && Z_3=0 \\
 &= -[-m \cos [\phi / 2]] \cos \theta . e^{2\pi i Q r} && ; m \text{ is opposite to } z_1 \\
 &= m \cos \theta . e^{2\pi i Q r} && ; \phi = 0 \\
 L_1 &= -z_1 \cos \theta . e^{2\pi i Q r} \\
 &= -m \cos [\phi / 2] \cos \theta . e^{2\pi i Q r} && Z_3=0 \\
 S_2 &= m \cos \theta . e^{2\pi i Q r} \\
 L_2 &= -m \cos [\phi / 2] \cos \theta . e^{2\pi i Q r}
 \end{aligned}$$

$\pi$  to  $\sigma^*$

$$\begin{aligned}
 S_1 &= ([z_1 \cos \theta + z_3 \sin \theta]) e^{2\pi i Q r} \\
 &= z_1 \cos \theta . e^{2\pi i Q r} \\
 &= -m \cos [\phi / 2] \cos \theta . e^{2\pi i Q r} && ; m \text{ is opposite to } z_1, \phi = 0 \\
 &= -m \cos \theta . e^{2\pi i Q r} \\
 L_1 &= Z_1 \cos \theta . e^{2\pi i Q r} \\
 &= m \cos [\phi / 2] \cos \theta . e^{2\pi i Q r} \\
 S_2 &= -m \cos \theta . e^{2\pi i Q r} \\
 L_2 &= m \cos [\phi / 2] \cos \theta . e^{2\pi i Q r}
 \end{aligned}$$

$\pi$  to  $\pi^*$

$$\begin{aligned}
 S_1 &= -z_2 \sin 2\theta . e^{2\pi i Q r} \\
 &= -m \sin [\phi / 2] \sin 2\theta . e^{2\pi i Q r} \\
 &= 0 && ; \phi = 0, z_2=0 \\
 L_1 &= -z_2 \sin 2\theta . e^{2\pi i Q r} \\
 &= -m \sin [\phi / 2] \sin 2\theta . e^{2\pi i Q r} \\
 S_2 &= 0 \\
 L_2 &= m \sin [\phi / 2] \sin 2\theta . e^{2\pi i Q r} && \text{opposite to } z_2
 \end{aligned}$$

## B.3 Model-B

### Horizontal magnet geometry

**$\sigma$  to  $\pi$** 

$$\begin{aligned}
S_1 &= ([-z_1 \cos \theta + z_3 \sin \theta]) e^{2\pi i Qr} \\
&= -z_1 \cos \theta . e^{2\pi i Qr} && ; z_3 = 0 \\
&= m \cos [\phi / 2] \cos \theta . e^{2\pi i Qr} \\
&= m \cos \theta . e^{2\pi i Qr} && ; m \text{ is opposite to } z_1 \text{ and } \phi = 0 \\
L_1 &= [-z_1 \cos \theta + z_3 \sin \theta] e^{2\pi i Qr} \\
&= [-m \sin \alpha \cos \phi / 2 \cos \theta + m \cos \alpha \sin \theta] . e^{2\pi i Qr} \\
S_2 &= m \cos \theta . e^{2\pi i Qr} \\
L_2 &= ([-z_1 \cos \theta + z_3 \sin \theta]) e^{2\pi i Qr} \\
&= [-m \sin \alpha \cos \phi / 2 \cos \theta - m \cos \alpha \sin \theta] . e^{2\pi i Qr} && ; z_3 = -m \cos \alpha
\end{aligned}$$

 **$\pi$  to  $\sigma$** 

$$\begin{aligned}
S_1 &= ([z_1 \cos \theta + z_3 \sin \theta]) e^{2\pi i Qr} \\
&= z_1 \cos \theta . e^{2\pi i Qr} && ; z_3 = 0 \\
&= -m \cos [\phi / 2] \cos \theta . e^{2\pi i Qr} \\
&= -m \cos \theta . e^{2\pi i Qr} && ; \phi = 0, m \text{ is opposite to } z_1 \\
L_1 &= ([z_1 \cos \theta + z_3 \sin \theta]) e^{2\pi i Qr} \\
&= [m \sin \alpha \cos \phi / 2 \cos \theta + m \cos \alpha \sin \theta] . e^{2\pi i Qr} \\
S_2 &= -m \cos \theta . e^{2\pi i Qr} \\
L_2 &= ([z_1 \cos \theta + z_3 \sin \theta]) e^{2\pi i Qr} \\
&= [m \sin \alpha \cos \phi / 2 \cos \theta - m \cos \alpha \sin \theta] . e^{2\pi i Qr} && ; z_3 = -m \cos \alpha
\end{aligned}$$

 **$\pi$  to  $\pi$** 

$$\begin{aligned}
S_1 &= -z_2 \sin 2\theta . e^{2\pi i Qr} \\
&= 0 && ; \phi = 0, z_2 = 0 \\
L_1 &= -z_2 \sin 2\theta . e^{2\pi i Qr} \\
&= -m \sin \alpha \sin \phi / 2 \sin 2\theta . e^{2\pi i Qr} \\
S_2 &= 0 \\
L_2 &= -z_2 \sin 2\theta . e^{2\pi i Qr} \\
&= m \sin \alpha \sin \phi / 2 \sin 2\theta . e^{2\pi i Qr}
\end{aligned}$$

**Vertical magnet geometry** After exchanging  $z_1$  and  $z_2$ :

**$\sigma$  to  $\pi$**

$$\begin{aligned}
 S_1 &= ([-z_1 \cos \theta + z_3 \sin \theta]) e^{2\pi i Q r} \\
 &= 0 \quad ; \text{new } z_1 \text{ and } \phi = 0 \\
 L_1 &= [-z_1 \cos \theta + z_3 \sin \theta] e^{2\pi i Q r} \\
 &= [-m \sin \alpha \sin \phi / 2 \cos \theta + m \cos \alpha \sin \theta] . e^{2\pi i Q r} \\
 S_2 &= 0 \\
 L_2 &= ([-z_1 \cos \theta + z_3 \sin \theta]) e^{2\pi i Q r} \\
 &= [m \sin \alpha \sin \phi / 2 \cos \theta - m \cos \alpha \sin \theta] . e^{2\pi i Q r} \quad ; z_3 = -m \cos \alpha
 \end{aligned}$$

**$\pi$  to  $\sigma$**

$$\begin{aligned}
 S_1 &= ([z_1 \cos \theta + z_3 \sin \theta]) e^{2\pi i Q r} \\
 &= 0 \quad ; \phi = 0, \text{ new } z_1 = 0 \\
 L_1 &= ([z_1 \cos \theta + z_3 \sin \theta]) e^{2\pi i Q r} \\
 &= [m \sin \alpha \sin \phi / 2 \cos \theta + m \cos \alpha \sin \theta] . e^{2\pi i Q r} \\
 S_2 &= 0 \\
 L_2 &= ([z_1 \cos \theta + z_3 \sin \theta]) e^{2\pi i Q r} \\
 &= [-m \sin \alpha \sin \phi / 2 \cos \theta - m \cos \alpha \sin \theta] . e^{2\pi i Q r} \quad ; z_3 = -m \cos \alpha
 \end{aligned}$$

**$\pi$  to  $\pi$**

$$\begin{aligned}
 S_1 &= -z_2 \sin 2\theta . e^{2\pi i Q r} \\
 &= -m \sin 2\theta . e^{2\pi i Q r} \quad ; \phi = 0, z_2 = 0 \\
 L_1 &= -z_2 \sin 2\theta . e^{2\pi i Q r} \\
 &= m \sin \alpha \cos \phi / 2 \sin 2\theta . e^{2\pi i Q r} \\
 S_2 &= -m \sin 2\theta . e^{2\pi i Q r} \\
 L_2 &= -z_2 \sin 2\theta . e^{2\pi i Q r} \\
 &= m \sin \alpha \cos \phi / 2 \sin 2\theta . e^{2\pi i Q r}
 \end{aligned}$$

Calculated intensity for the model-B for horizontal magnet geometry is plotted in Fig. B.1. Intensities in  $\sigma \rightarrow \pi$  and  $\pi \rightarrow \sigma$  channels are similar and decrease with increase in  $\alpha$ . In both the channels intensity is almost independent of  $\phi$ . Higher  $\alpha$  indicates larger magnetic moment in the field direction and with smaller  $\phi$  it approaches ferrimagnetic structure. We

can conclude that in these two diagonal channels intensity is solely determined by the  $z_3$  component. Since there is no contrast between  $\sigma \rightarrow \pi$  and  $\pi \rightarrow \sigma$  intensities, Rel\_Lin is zero for all the values of  $\phi$  and  $\alpha$ . Higher value of Rel\_Lin near  $\alpha$  close to  $\pi/2$  can be explained on the basis of the smaller normalization factor, due to smaller values of intensity, which is an artifact in the calculations. Intensity in the  $\pi \rightarrow \pi$  channel changes diagonally towards higher values of both  $\phi$  and  $\alpha$ . The highest intensity is obviously found when moments are in the  $z_2$  direction.

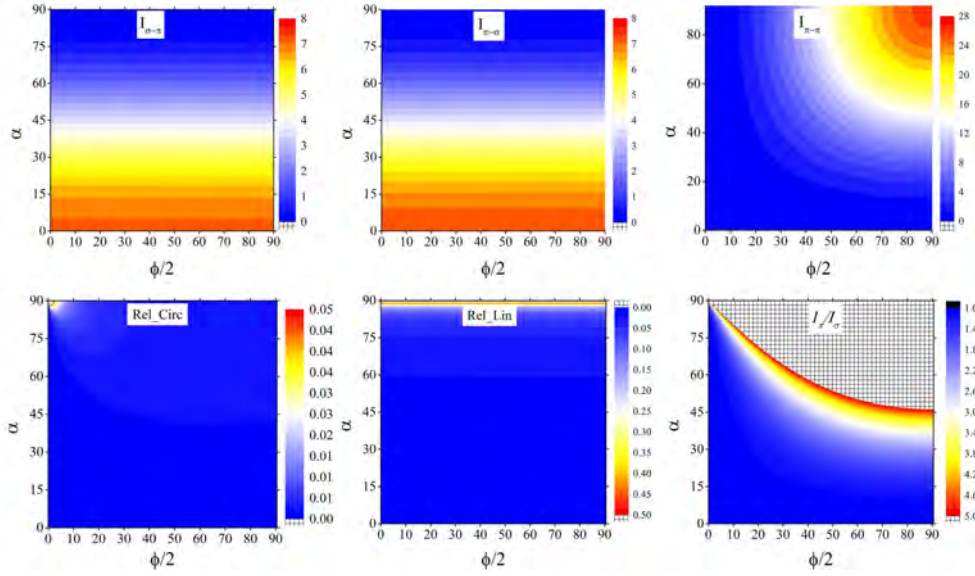


Fig. B.1 Model-B: Calculated intensities for the  $\sigma \rightarrow \pi$ ,  $\pi \rightarrow \sigma$  and  $\pi \rightarrow \pi$  channels for horizontal magnet geometry. In the bottom panels Rel\_Circ, Re\_Lin and  $I_{\pi}/I_{\sigma}$  are plotted as a function of  $\phi$  and  $\alpha$ . In the  $I_{\pi}/I_{\sigma}$  plot the values of  $I_{\pi}/I_{\sigma} > 5$  are shown by black sparse region.

In Fig. B.1 we also plotted the values of relative circular dichroism (Rel\_Circ), relative linear dichroism (Rel\_Lin) and ratio of intensities in  $\pi$  and  $\sigma$  channels ( $I_{\pi}/I_{\sigma}$ ). No Rel\_Circ can be found in the entire range of  $\alpha$  and  $\phi$  except in a small region near  $\alpha = 90^\circ$  and  $\phi = 0^\circ$ , which is also an artifact arising due to small values of intensity in  $\pi$  channel. In this case we have finite values of intensity in both  $\sigma \rightarrow \pi$  and  $\pi \rightarrow \pi$  channels at least in a certain range of  $\phi$  and  $\alpha$ , but Rel\_Circ is zero. If we look at the Eq. 3.28, it is not the intensity but the contrast between the real part of the structure factor in  $\sigma \rightarrow \pi$  times the imaginary part in  $\pi \rightarrow \pi$  and real part of the structure factor in  $\pi \rightarrow \pi$  times the imaginary part in  $\sigma \rightarrow \pi$ . For a circularly polarized light ( $\sigma + i\pi$ ) the real and imaginary parts of the light have a phase shift of  $\pi/2$  or both are cos and sin functions. As mentioned earlier, if we have moment component  $z_2$  and  $z_3$  we can have finite intensities in  $\sigma \rightarrow \pi$  and  $\pi \rightarrow \pi$  channels, but for a circular polarized light real and imaginary parts have the same phase shift. Therefore,  $P$

and  $M$  polarization can not have contrast in this model.

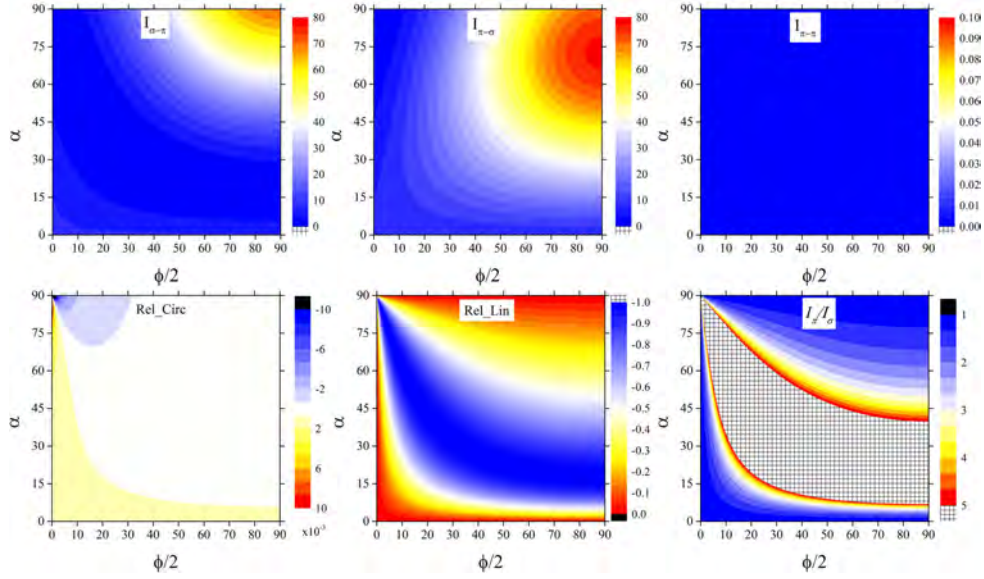


Fig. B.2 Model-B: Calculated intensities for the  $\sigma \rightarrow \pi$ ,  $\pi \rightarrow \sigma$  and  $\pi \rightarrow \pi$  channels for vertical magnet geometry. In the bottom panels Rel\_Circ, Re\_Lin and  $I_{\pi}/I_{\sigma}$  is plotted as a function of  $\phi$  and  $\alpha$ . In the  $I_{\pi}/I_{\sigma}$  plot the values of  $I_{\pi}/I_{\sigma} > 5$  are shown by black sparse region.

In Fig. B.2 we have plotted the intensity of the individual channels for vertical field geometry. Compared to horizontal magnet geometry, in vertical magnet intensity is both  $\alpha$  and  $\phi$  dependent for  $(I_{\sigma \rightarrow \pi})$  and  $(I_{\pi \rightarrow \sigma})$ . In the case of vertical magnet geometry, magnetic modulations are shifted by  $\pi/2$  from that of horizontal magnets in  $z_1$  direction. Now our new  $z_1$  for vertical magnet is the  $z_2$  in horizontal magnet, and directions are given by a right handed co-ordinate system. Contributions from both the large spin blocks in the magnetic unit cell contribute opposite to each other in  $z_1$  direction, as well as that for  $z_3$ . Therefore, we have a contrast in our new  $z_1$  and  $z_3$  moment directions. This gives us a difference in intensities in  $\sigma \rightarrow \pi$  and  $\pi \rightarrow \sigma$  channels. Highest intensity in this case for both  $\sigma \rightarrow \pi$  and  $\pi \rightarrow \sigma$  was observed for higher values of both  $\phi$  and  $\alpha$ . This indicates that in the case of vertical magnet higher component of moments in the new  $z_1$  (which is the  $z_2$  direction) in horizontal magnet favors both the diagonal channel intensities. However, unlike in case of horizontal magnet, here intensity maps are not the same *i.e.*  $\phi$ ,  $\alpha$  dependence is not the same for both the channels and intensity is both  $\alpha$  and  $\phi$  dependent.

In case of vertical magnet geometry we do not get any circular dichroism except for the artifact near  $\phi = 0^\circ$  and  $\alpha = 90^\circ$ . Interestingly, in a wide range of  $\alpha$  and  $\phi$  linear dichroism is observed. The  $I_{\pi}/I_{\sigma}$  ratio becomes very huge in the regions as shown in Fig. B.2. Therefore, altogether this model-B could not explain the circular dichroism observed in horizontal field

geometry and accounts for no common regions in  $\phi$  and  $\alpha$  for experimentally observed  $I_\pi/I_\sigma$  ratio and Rel\_Lin.

## B.4 Model-C

### Horizontal magnet geometry

#### $\sigma$ to $\pi$

$$\begin{aligned}
 S_1 &= ([-z_1 \cos \theta + z_3 \sin \theta]) e^{2\pi i Q r} \\
 &= [-(-m \sin \beta) \cos \theta + m \cos \beta \sin \theta]. e^{2\pi i Q r} \\
 &= [m \sin \beta \cos \theta + m \cos \beta \sin \theta]. e^{2\pi i Q r} \\
 L_1 &= ([-z_1 \cos \theta + z_3 \sin \theta]) e^{2\pi i Q r} \\
 &= [-m \sin \alpha \cos \phi / 2 \cos \theta + m \cos \alpha \sin \theta]. e^{2\pi i Q r} \\
 S_2 &= ([-z_1 \cos \theta + z_3 \sin \theta]) e^{2\pi i Q r} \\
 &= [-(-m \sin \beta \cos \theta) + (-m \cos \beta \sin \theta)] \quad ; z_3, z_1 \text{ oppositedirection} \\
 &= [m \sin \beta \cos \theta - m \cos \beta \sin \theta] \\
 L_2 &= ([-z_1 \cos \theta + z_3 \sin \theta]) e^{2\pi i Q r} \\
 &= [-m \sin \alpha \cos \phi / 2 \cos \theta - m \cos \alpha \sin \theta]. e^{2\pi i Q r} \quad ; z_3 = -m \cos \alpha
 \end{aligned}$$

#### $\pi$ to $\sigma$

$$\begin{aligned}
 S_1 &= ([z_1 \cos \theta + z_3 \sin \theta]). e^{2\pi i Q r} \\
 &= [-m \sin \beta \cos \theta + m \cos \beta \sin \theta]. e^{2\pi i Q r} \quad ; z_1 \text{ oppositedirection} \\
 L_1 &= ([z_1 \cos \theta + z_3 \sin \theta]) e^{2\pi i Q r} \\
 &= [m \sin \alpha \cos \phi / 2 \cos \theta + m \cos \alpha \sin \theta]. e^{2\pi i Q r} \\
 S_2 &= ([z_1 \cos \theta + z_3 \sin \theta]) e^{2\pi i Q r} \\
 &= [-(m \sin \beta \cos \theta) + (-m \cos \beta \sin \theta)] \quad ; z_3, z_1 \text{ oppositedirection} \\
 &= [-m \sin \beta \cos \theta - m \cos \beta \sin \theta] \\
 L_2 &= ([z_1 \cos \theta + z_3 \sin \theta]) e^{2\pi i Q r} \\
 &= [m \sin \alpha \cos \phi / 2 \cos \theta - m \cos \alpha \sin \theta]. e^{2\pi i Q r} \quad ; z_3 = -m \cos \alpha
 \end{aligned}$$

**$\pi$  to  $\pi$** 

$$\begin{aligned}
S_1 &= -z_2 \sin 2\theta . e^{2\pi i Qr} \\
&= 0 \\
L_1 &= -z_2 \sin 2\theta . e^{2\pi i Qr} \\
&= -m \sin \alpha \sin \phi / 2 \sin 2\theta . e^{2\pi i Qr} \\
S_2 &= 0 \\
L_2 &= -z_2 \sin 2\theta . e^{2\pi i Qr} \\
&= m \sin \alpha \sin \phi / 2 \sin 2\theta . e^{2\pi i Qr}
\end{aligned}$$

**Vertical magnet geometry** **$\sigma$  to  $\pi$** 

$$\begin{aligned}
S_1 &= ([-z_1 \cos \theta + z_3 \sin \theta]) e^{2\pi i Qr} \\
&= m \cos \beta \sin \theta \quad ; \text{new } z_1 = 0 \text{ and } \phi = 0 \\
L_1 &= [-z_1 \cos \theta + z_3 \sin \theta] e^{2\pi i Qr} \\
&= [-m \sin \alpha \sin \phi / 2 \cos \theta + m \cos \alpha \sin \theta] . e^{2\pi i Qr} \\
S_2 &= -m \cos \beta \sin \theta \\
L_2 &= ([-z_1 \cos \theta + z_3 \sin \theta]) e^{2\pi i Qr} \\
&= [m \sin \alpha \sin \phi / 2 \cos \theta - m \cos \alpha \sin \theta] . e^{2\pi i Qr} \quad ; z_3 = -m \cos \alpha
\end{aligned}$$

 **$\pi$  to  $\sigma$** 

$$\begin{aligned}
S_1 &= ([z_1 \cos \theta + z_3 \sin \theta]) e^{2\pi i Qr} \\
&= m \cos \beta \sin \theta \quad ; \phi = 0, \text{ new } z_1 = 0 \\
L_1 &= ([z_1 \cos \theta + z_3 \sin \theta]) e^{2\pi i Qr} \\
&= [m \sin \alpha \sin \phi / 2 \cos \theta + m \cos \alpha \sin \theta] . e^{2\pi i Qr} \\
S_2 &= -m \cos \beta \sin \theta \\
L_2 &= ([z_1 \cos \theta + z_3 \sin \theta]) e^{2\pi i Qr} \\
&= [-m \sin \alpha \sin \phi / 2 \cos \theta - m \cos \alpha \sin \theta] . e^{2\pi i Qr} \quad ; z_3 = -m \cos \alpha
\end{aligned}$$

$\pi$  to  $\pi$

$$\begin{aligned}
 S_1 &= -z_2 \sin 2\theta . e^{2\pi i Q r} \\
 &= -m \sin \beta \sin 2\theta . e^{2\pi i Q r} \\
 L_1 &= -z_2 \sin 2\theta . e^{2\pi i Q r} \\
 &= m \sin \alpha \cos \phi / 2 \sin 2\theta . e^{2\pi i Q r} \\
 S_2 &= -m \sin \beta \sin 2\theta . e^{2\pi i Q r} \\
 L_2 &= -z_2 \sin 2\theta . e^{2\pi i Q r} \\
 &= m \sin \alpha \cos \phi / 2 \sin 2\theta . e^{2\pi i Q r}
 \end{aligned}$$

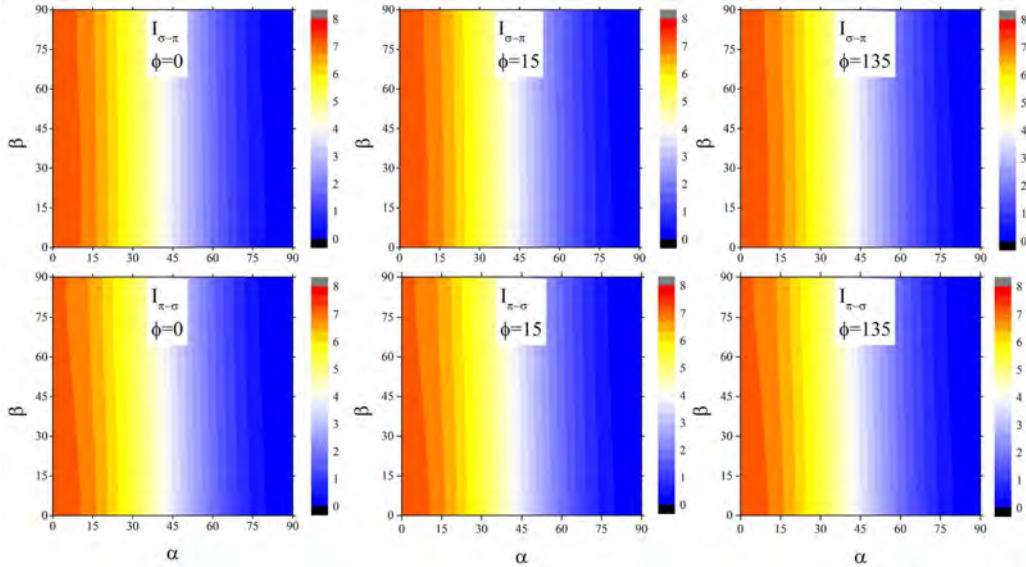


Fig. B.3 Calculated intensity of model-C for horizontal field in the  $\sigma \rightarrow \pi$  and  $\pi \rightarrow \sigma$  channel as a function of angles  $\alpha$  and  $\beta$  at various values of  $\phi$ . Color bars scale with the corresponding values.

Calculations of various parameters in this case is not as straight forward as is the case of model-A and model-B. In model-C we have three parameters  $\phi$ ,  $\alpha$  and  $\beta$ . Therefore, we calculate the intensity parameters for each  $\phi$  by varying  $\alpha$  and  $\beta$ .

Fig. B.3 shows the intensity in  $\sigma \rightarrow \pi$  and  $\pi \rightarrow \sigma$  channels for selected values of  $\phi$  and as a function of  $\alpha$  and  $\beta$  for horizontal field geometry. Intensity in  $\sigma \rightarrow \pi$  and  $\pi \rightarrow \sigma$  has only small difference for all  $\phi$  which is not visible in the intensity map and there should not be any Rel\_Lin. We also did not observe any Rel\_Lin experimentally. For both the spin blocks pairs, L1 and L2 and S1 and S2, have equal contributions towards  $z_1$ . In  $z_3$  direction in both the pairs each one contributes opposite to the other. Thus the sum and difference of

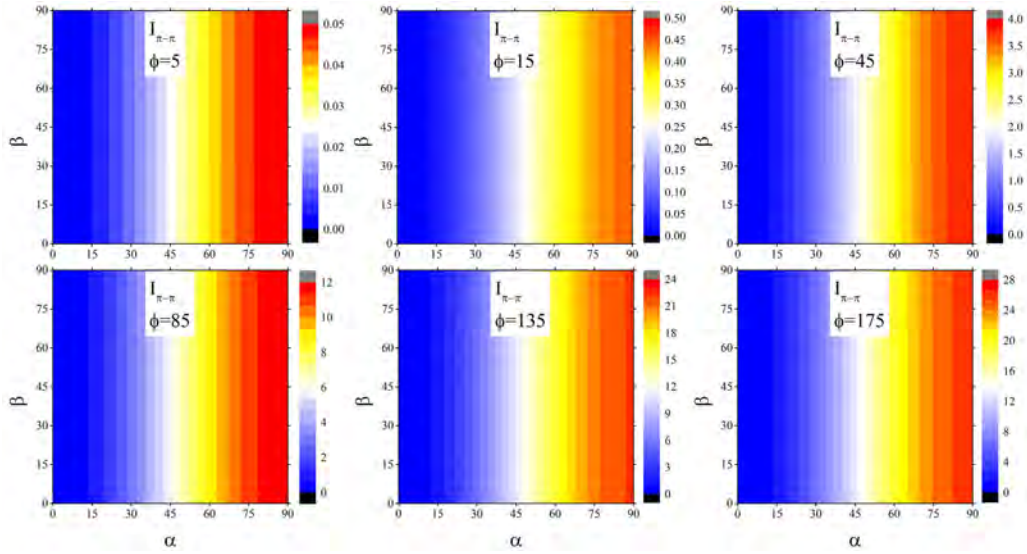


Fig. B.4 Calculated intensity of model-C for horizontal field in the  $\pi \rightarrow \pi$  channel as a function of angles  $\alpha$  and  $\beta$  at various values of  $\phi$ . Color bars scale with the corresponding values.

contributions in  $z_1$  and  $z_3$  are equal. Our calculations also show equal intensities for  $\sigma \rightarrow \pi$  and  $\pi \rightarrow \sigma$ . In the  $\pi \rightarrow \pi$  channel for  $\phi = 0^\circ$  no intensity is observed. This is obvious that with no  $z_2$  component intensity in this channel is zero. As the value of  $\phi$  increases the  $z_2$  component also increases and the intensity in  $\pi \rightarrow \pi$  channel starts increasing, see Fig. B.4.

We have plotted various parameters calculated from model-C, as a function of  $\alpha$  and  $\beta$  for various values of  $\phi$ , in Fig. B.5. From the intensity calculations we have already seen that for  $\phi = 0$ , intensity in  $\pi \rightarrow \pi = 0$ . Since, for Rel\_Circ we need finite intensity in  $\pi \rightarrow \pi$  channel, for  $\phi = 0$  we cannot see any circular dichroism for all values of  $\alpha$  and  $\beta$ . For a small change in  $\phi = 5^\circ$  circular dichroism appears. Highest value of circular dichroism is found when  $\alpha$  goes to  $\pi/2$  and the value of  $\beta$  is small. Rel\_Circ dichroism with a value of 0.7 can be observed in this region. However, for a wide range of  $\beta$  Rel\_Circ in the range of 0.2 to 0.7 is observed. As we increase  $\phi$  to  $15^\circ$  the region with circular dichroism increases to lower values of  $\alpha$ . At  $\phi = 45^\circ$  the highest value of Rel\_Circ decreases to below 0.3 but small circular dichroism is extended for lower values of  $\alpha$ . With further increase in  $\phi$ , value of circular dichroism decreases. We have plotted the  $I_\sigma/I_\pi$  ratio up to a value of  $I_\sigma/I_\pi = 5$ . Some very high values of  $I_\sigma/I_\pi$  are observed, which we indicate by the white regions in the curve. With small increase in  $\phi$  value above  $0^\circ (=1$  for  $\phi = 0)$  the ratio increases. Highest value of the ratio is observed near  $\alpha, \beta \rightarrow \pi/2$ . With higher  $\phi$ ,  $\alpha, \beta \rightarrow \pi/2$  region gives values much higher than 5 (which are shown as cross-dashed region in the plot).

Now let us look at the vertical field geometry. In this case, as mentioned earlier,  $z_1$  and  $z_2$  are exchanged. In Fig. B.6 we plotted the individual intensities  $I_{\sigma \rightarrow \pi}$  and  $I_{\pi \rightarrow \sigma}$  with the

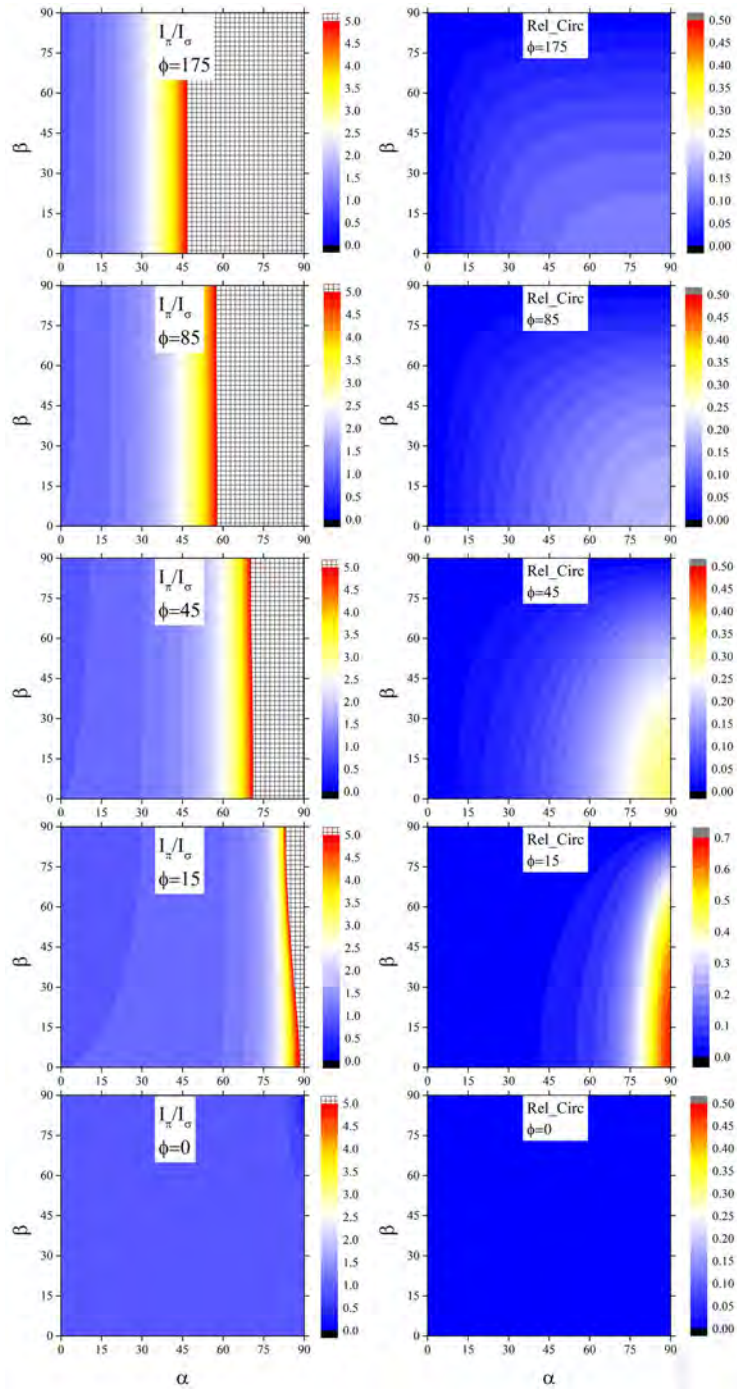


Fig. B.5 Calculated  $I_{\pi}/I_{\sigma}$  ratio and Rel\_Circ of model-C for horizontal field as a function of angles  $\alpha$  and  $\beta$  at various values of  $\phi$ . Color bars scale with the corresponding values.

same color bars for the same values of  $\phi$ . In case of both the diagonal channels  $\sigma \rightarrow \pi$  and  $\pi \rightarrow \sigma$  intensity increases as we increase  $\phi$ . For a particular  $\phi$ , intensity has huge variation along  $\alpha$  but a very small change is observed along  $\beta$ . For  $\phi = 0^\circ$  we can see that in both

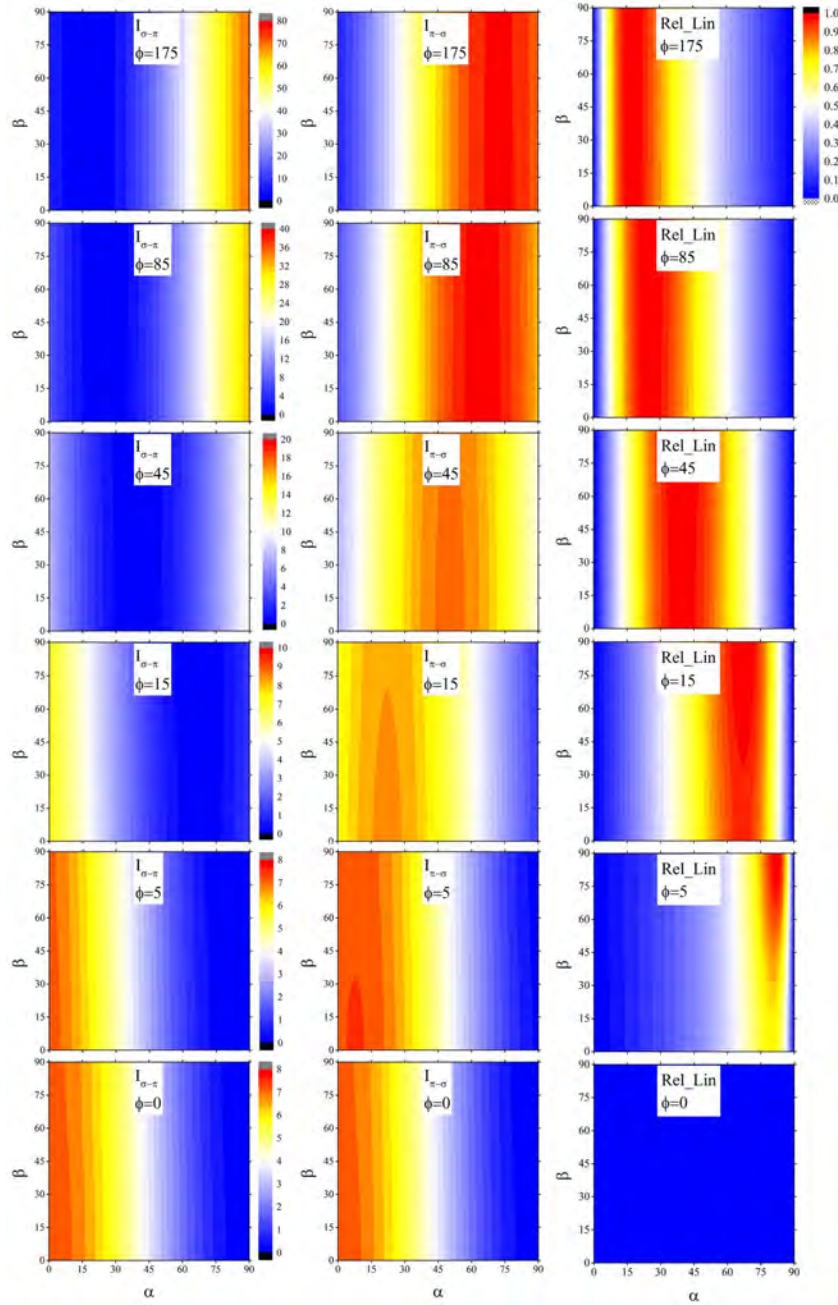


Fig. B.6 Intensity in the  $\sigma \rightarrow \pi$ ,  $\pi \rightarrow \sigma$  and calculated for vertical field geometry of model-C for different values of  $\phi$  as indicated in the figure. For  $I_{\sigma \rightarrow \pi}$  and  $I_{\pi \rightarrow \sigma}$  same color bars are used for the same values of  $\phi$ . Rel\_Lin is plotted in the right hand side with the same color bar for all values of  $\phi$ .

the channels  $\sigma \rightarrow \pi$  and  $\pi \rightarrow \sigma$  highest intensity is observed at  $\alpha = 0$  and it decreases with increase in  $\alpha$ . As  $\phi$  is increased, the pattern of relative intensities changes differently for both the channels. Intensity in both the channels are independent of  $\beta$ . This indicates

that for linear dichroism the angle of the small spin blocks with the c-axis has no influence. Small  $\beta$  dependence is observed for  $\phi = 5^\circ$  and the small values are due to the artifact caused by small values of individual intensities. For both the intensities small blocks in the new  $z_1$  direction, or the perpendicular to  $H$  direction, do not have moment component. Therefore, it is obvious that Rel\_Lin is independent of  $\beta$ . The value of  $\alpha$  is the controlling factor for the linear dichroism.

Intensity in the  $\pi \rightarrow \pi$  channel is negligible for the entire regions of  $\phi$ ,  $\alpha$  and  $\beta$ . Along  $z_2$  *i.e.* in the field direction there is only ferrimagnetic contribution, so there is no intensity in the  $\pi \rightarrow \pi$  channels. Without  $\pi \rightarrow \pi$  intensity we can not have Rel\_Circ. For the entire range of  $\phi$ ,  $\alpha$  and  $\beta$  no Rel\_Circ is observed.

As can be seen in Fig. B.6, Rel\_Lin values can reach as high values as  $\approx 1$ . There is no Rel\_Lin for  $\phi = 0^\circ$ .  $z_2$  component for L-blocks are essential for relative linear dichroism also. For  $\phi = 5^\circ$  we can see that regions with very high Rel\_lin start appearing at  $\alpha$  value around  $80^\circ$ . As we further increase in  $\phi$  the highest value region moves towards lower  $\alpha$ .

## B.5 Model-D

### Horizontal magnet

$\sigma$  to  $\pi$

$$\begin{aligned}
 S_1 &= ([-z_1 \cos \theta + z_3 \sin \theta]) e^{2\pi i Q r} \\
 &= [-m \sin \beta \cos(\gamma/2) \cos \theta - \cos \beta \sin \theta] \cdot e^{2\pi i Q r} \\
 L_1 &= ([-z_1 \cos \theta + z_3 \sin \theta]) e^{2\pi i Q r} \\
 &= [-m \sin \alpha \cos(\phi/2) \cos \theta + m \cos \alpha \sin \theta] \cdot e^{2\pi i Q r} \\
 S_2 &= [-m \sin \beta \cos(\gamma/2) \cos \theta + \cos \beta \sin \theta] \cdot e^{2\pi i Q r} \\
 L_2 &= ([-z_1 \cos \theta + z_3 \sin \theta]) e^{2\pi i Q r} \\
 &= [-m \sin \alpha \cos(\phi/2) \cos \theta - m \cos \alpha \sin \theta] \cdot e^{2\pi i Q r} \quad ; z_3 = -m \cos \alpha
 \end{aligned}$$

**$\pi$  to  $\sigma$** 

$$\begin{aligned}
S_1 &= [z_1 \cos \theta + z_3 \sin \theta] \cdot e^{2\pi i Q r} \\
&= [m \sin \beta \cos(\gamma/2) \cos \theta - \cos \beta \sin \theta] \cdot e^{2\pi i Q r} \\
L_1 &= ([z_1 \cos \theta + z_3 \sin \theta]) e^{2\pi i Q r} \\
&= [m \sin \alpha \cos(\phi/2) \cos \theta + m \cos \alpha \sin \theta] \cdot e^{2\pi i Q r} \\
S_2 &= [m \sin \beta \cos(\gamma/2) \cos \theta + \cos \beta \sin \theta] \cdot e^{2\pi i Q r} \\
L_2 &= ([z_1 \cos \theta + z_3 \sin \theta]) e^{2\pi i Q r} \\
&= [m \sin \alpha \cos(\phi/2) \cos \theta - m \cos \alpha \sin \theta] \cdot e^{2\pi i Q r} \quad ; z_3 = -m \cos \alpha
\end{aligned}$$

 **$\pi$  to  $\pi$** 

$$\begin{aligned}
S_1 &= -z_2 \sin 2\theta \cdot e^{2\pi i Q r} \\
&= m \sin \beta \sin(\gamma/2) \sin 2\theta \cdot e^{2\pi i Q r} \\
L_1 &= -z_2 \sin 2\theta \cdot e^{2\pi i Q r} \\
&= -m \sin \alpha \sin(\phi/2) \sin 2\theta \cdot e^{2\pi i Q r} \\
S_2 &= -m \sin \beta \sin(\gamma/2) \sin 2\theta \cdot e^{2\pi i Q r} \\
L_2 &= -z_2 \sin 2\theta \cdot e^{2\pi i Q r} \\
&= m \sin \alpha \sin(\phi/2) \sin 2\theta \cdot e^{2\pi i Q r}
\end{aligned}$$

**Vertical magnet geometry** **$\sigma$  to  $\pi$** 

$$\begin{aligned}
S_1 &= ([-z_1 \cos \theta + z_3 \sin \theta]) e^{2\pi i Q r} \\
&= m[-\sin \beta \sin(\gamma/2) \cos \theta - \cos \beta \sin \theta] \cdot e^{2\pi i Q r} \quad ; \text{new } z_1 = m \sin \gamma \\
L_1 &= [-z_1 \cos \theta + z_3 \sin \theta] e^{2\pi i Q r} \\
&= [-m \sin \alpha \sin(\phi/2) \cos \theta + m \cos \alpha \sin \theta] \cdot e^{2\pi i Q r} \\
S_2 &= m[\sin \beta \sin(\gamma/2) \cos \theta + \cos \beta \sin \theta] \cdot e^{2\pi i Q r} \\
L_2 &= ([-z_1 \cos \theta + z_3 \sin \theta]) e^{2\pi i Q r} \\
&= [m \sin \alpha \sin(\phi/2) \cos \theta - m \cos \alpha \sin \theta] \cdot e^{2\pi i Q r} \quad ; z_3 = -m \cos \alpha
\end{aligned}$$

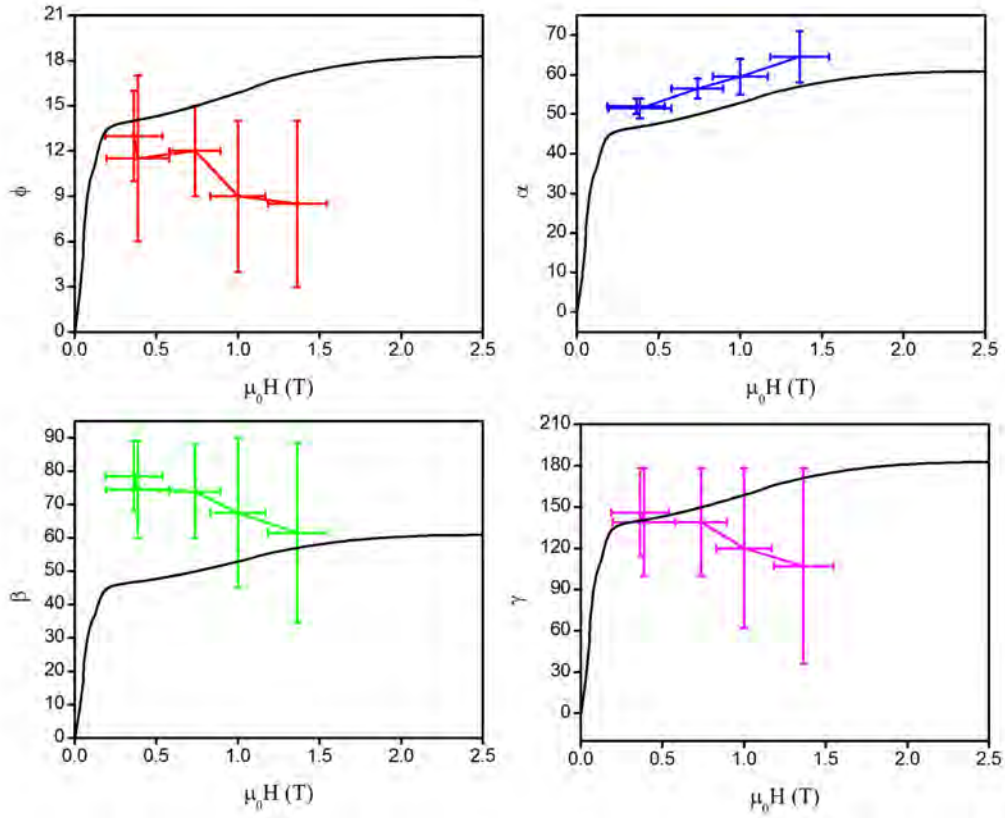


Fig. B.7 Solution for model-D for  $\phi$ ,  $\alpha$ ,  $\beta$  and  $\gamma$  for applied field below saturation field and above  $H_4$

$\pi$  to  $\sigma$

$$\begin{aligned}
 S_1 &= ([z_1 \cos \theta + z_3 \sin \theta]) e^{2\pi i Q r} \\
 &= m[\sin \beta \sin(\gamma/2) \cos \theta - \cos \beta \sin \theta] \cdot e^{2\pi i Q r} \quad ; \text{ new } z_1 = m \sin(\gamma/2) \\
 L_1 &= ([z_1 \cos \theta + z_3 \sin \theta]) e^{2\pi i Q r} \\
 &= [m \sin \alpha \sin(\phi/2) \cos \theta + m \cos \alpha \sin \theta] \cdot e^{2\pi i Q r} \\
 S_2 &= m[-\sin \beta \sin(\gamma/2) \cos \theta + \cos \beta \sin \theta] \cdot e^{2\pi i Q r} \\
 L_2 &= ([z_1 \cos \theta + z_3 \sin \theta]) e^{2\pi i Q r} \\
 &= [-m \sin \alpha \sin(\phi/2) \cos \theta - m \cos \alpha \sin \theta] \cdot e^{2\pi i Q r} \quad ; z_3 = -m \cos \alpha
 \end{aligned}$$

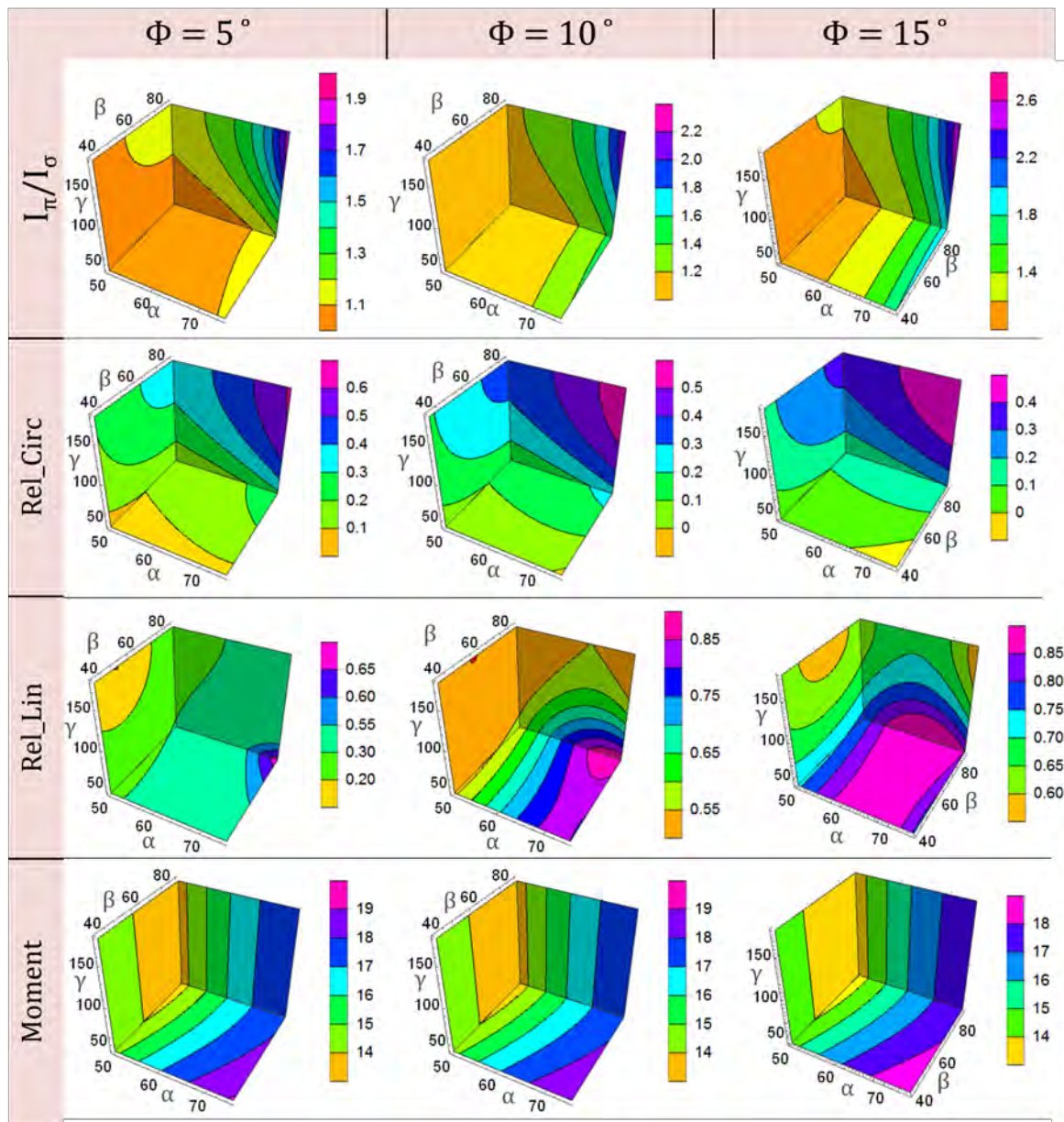


Fig. B.8 Calculated values of Rel\_Circ, Rel\_Lin,  $I_\pi/I_\sigma$  and moment (using a Wolfram mathematica 10.4 program) as a function of  $\alpha$ ,  $\beta$  and  $\gamma$  for three values of  $\phi=5^\circ$ ,  $10^\circ$  and  $15^\circ$ .

$\pi$  to  $\pi$

$$\begin{aligned} S_1 &= -z_2 \sin 2\theta \cdot e^{2\pi i Qr} \\ &= -m \sin \beta \cos(\gamma/2) \sin 2\theta \cdot e^{2\pi i Qr} \\ L_1 &= -z_2 \sin 2\theta \cdot e^{2\pi i Qr} \\ &= m \sin \alpha \cos(\phi/2) \sin 2\theta \cdot e^{2\pi i Qr} \\ S_2 &= -m \sin \beta \cos(\gamma/2) \sin 2\theta \cdot e^{2\pi i Qr} \\ L_2 &= -z_2 \sin 2\theta \cdot e^{2\pi i Qr} \\ &= m \sin \alpha \cos(\phi/2) \sin 2\theta \cdot e^{2\pi i Qr} \end{aligned}$$

# List of figures

2.1	Atomic magnetism (a) Orbital magnetic moment (b) Spin only moment. . .	4
2.2	Different types of anti-ferromagnetism in a cubic lattice due to positive and negative values of $J$ in the nearest and the next nearest neighbors. . . . .	5
2.3	Different intermediate steps in super-exchange interactions. Intermediates (d) and (e) are spin forbidden transitions. . . . .	5
2.4	Mechanism of double exchange. . . . .	6
2.5	Competing ferromagnetic and anti-ferromagnetic interactions between $J_1$ and $J_2$ , leading to helical magnetic order [19]. . . . .	8
2.6	Schematic of (a) Symmetric anisotropic exchange (b) Antisymmetric anisotropic exchange interactions. Blue lines represent transitions with the excited state due to SO coupling while the red arrows represent electron hopping via the transfer integral. There can be some other excited states also. Only one excited state is represented here. (c) Possible hopping and transfer processes when two magnetic atoms a and b are connected via a non magnetic atom c. Redrawn after [21]. . . . .	9
2.7	Multiferroics: coupling between different order parameters. . . . .	12
2.8	Mechanism of multiferroicity [37]. . . . .	13
2.9	Inverse DM interaction. . . . .	14
2.10	Different types of spiral orders. . . . .	15
2.11	Spin current mechanism of multiferroicity after [49]. . . . .	16
2.12	Different close packed layers in hexaferrite. Gray colored atoms are oxygen, greens are alkaline earth metals and brown are transition metals. . . . .	19
2.13	B-S and RS blocks in M-type hexaferrite. . . . .	20
2.14	Polyhedra in M-type hexaferrite. . . . .	21
2.15	$B_2S_4$ and T-S model for Y type hexaferrite. . . . .	22
2.16	Transition metals sites in Y-type hexaferrite. . . . .	23
2.17	Crystal structure of Z-type and U-type hexaferrite. . . . .	24

2.18	(a) Crystal and spin structure of $[\text{Ba}_{(1-x)}\text{Sr}_x]_2\text{Zn}_2\text{Fe}_{12}\text{O}_{22}$ in the ferrimagnetic phase. On the left side of the structure, crystallographic T and S blocks are shown as discussed in 2.4.2. On the right side, small S (red) and large L (blue) spin blocks are shown. (b) First 12 layers of atoms along $[001]$ . (c) Expanded region of the boundary between spin blocks. (d) Enlarged view of the boundary region without the spins. . . . .	25
3.1	(a) Mechanisms of solid state reactions (b) Lowering of melting point on mixing different constituents (c) Temperature profile in the crystal growth, and (d) Schematics of crystal growth inside a platinum crucible. . . . .	29
3.2	Schematics of an optical floating zone crystal growth chamber from [69]. . .	30
3.3	(a) Configuration of SQUID detection coils in a SQUID magnetometer (b) SQUID output voltage as a function of scan length of the sample and (c) DC SQUID with two Josephson Junctions. . . . .	31
3.4	Diffraction [78]. . . . .	35
3.5	Scattering geometry, coordinate system with polarization. . . . .	37
3.6	(a) Schematic of Thomson scattering and (b) X-ray resonance scattering. . .	38
3.7	(a) Different scans used to measure the reciprocal lattice vector length and intensity (b) Two permanent end-stations, the XUV diffractometer and the high-field diffractometers in the UE46_PGM-1 beamline. . . . .	44
3.8	<i>Left:</i> Schematic of high field chamber with the openings of the magnets. <i>Right:</i> Schematic of permanent magnet assembly in the zero field chamber. . . . .	45
4.1	BaO:ZnO = 1:1 plane single crystal fields. Inset shows the composition tetrahedron for BaO:ZnO plane. From: [110]. . . . .	50
4.2	Some of the as grown crystals with $[001]$ perpendicular to the plane of the paper. . . . .	52
4.3	(a) Different Fe/Zn-O bond lengths and (b) Partial occupancies of Zn(1) and Zn(2) for BZY-1, BZY-2 and BZY-3. $x$ is given in the formula $\text{Ba}_{1-x}\text{Sr}_x\text{ZnFe}_6\text{O}_{11}$	55
4.4	(a) DC magnetization vs applied external magnetic measurements of all the three samples $H \perp [001]$ , normalized to magnetization at 6 T at 10 K. Inset (a) shows the enlarged view of low field region. (b) Magnetization at 6 Tesla as a function of temperature. . . . .	56

- 4.5 DC Magnetization vs applied external magnetic measurements of BZY-1 in  $H \perp [001]$  as well as  $H \parallel [001]$ . (a) ZFC and FC curves for  $H \parallel [001] = 10$  mT and ZFC for  $H \perp [001]$ . (b) comparison of initial magnetization curves near the transition temperature for  $H \perp [001]$ . . . . . 58
- 4.6 (below) DC Magnetization vs applied external magnetic measurements of BZY-3 in both  $H \perp [001]$  (black) and  $H \parallel [001]$  (red) configuration. The dots indicate the threshold fields where the magnetization curves, measured both parallel and perpendicular directions, meet. (above) Variation of threshold field  $H_{th}$  with T. . . . . 59
- 4.7 DC Magnetization vs applied external magnetic measurements of BZY-2 and BZY-3 in a SQUID magnetometer, normalized over magnetization at 6 Tesla. For BZY-2 and BZY-3, both perpendicular to  $[001]$  and parallel to  $[001]$   $H$  is applied. Inset shows the enlarged region of low applied  $H$  in positive quadrant. . . . . 60
- 4.8 (a) Initial magnetization curves of both BZY-2 and BZY-3 samples for  $H \perp [001]$ . Red dots indicate  $H_5$  and blue dots indicate  $H_6$ . Dots are put with accuracy of eyes. . . . . 61
- 4.9 Magenta curve shows the  $M$  vs  $H \perp [001]$  at 200 K (initial magnetization). Red curve shows the first derivative of  $M_{\perp}$  and the blue curve shows the second derivative. Horizontal grid lines are the broad metamagnetic transitions. Black dotted lines are the extrapolation of regions where  $M_{\perp}$  has the steepest change. The crossing points are considered to be the points of metamagnetic transitions. . . . . 62
- 4.10 Metamagnetic fields (a)  $H_1, H_2, H_3$  and  $H_4$  and (b)  $H_5$  and  $H_6$  are plotted against temperature for BZY-2 (left) and BZY-3 (right). Error bars indicate the broadness of transitions as determined by the first and second derivatives of initial magnetization. . . . . 63
- 4.11 Initial magnetization curves near spin reorientation temperature of BZY-2 and BZY-3. Inset for both cases show the high  $H$  regions. . . . . 64
- 4.12 Zero-field-cooled curves (red), field-cooled curves measured while warming curves (green) and field-cooled curves measured while cooling curves (blue) at different applied  $H \perp [001]$  for BZY-2. Vertical dotted pink line corresponds to the  $T_p$  of the ZFC curve at 332 K and the black line is at 318 K (determined as the spin reorientation temperature from the initial magnetization curves). Bottom right figure shows enlarged view of the  $T_p$  region. . . . . 66

4.13	Initial magnetization curves near $T_p$ . <i>Left</i> : for BZY-2 and <i>Right</i> : for BZY-3. Inset shows the expanded region near low field. . . . .	66
4.14	(a) Real and (b) Imaginary part of the AC magnetic susceptibility of BZY-2. Inset shows the region near ordering temperature. . . . .	67
4.15	ZFC (red), FCW (green) and FCC (blue) at different applied $H \perp [0 0 1]$ for BZY-3. Vertical dotted pink line corresponds to the ZFC curve at 331 K and the black line is at 303 K, determined as the spin reorientation temperature from the initial magnetization curves. Bottom right figure shows enlarged view of the $T_p$ region. . . . .	68
4.16	(a) Real and (b) Imaginary part of the AC magnetic susceptibility of BZY-3. Inset shows the region near ordering temperature. . . . .	68
5.1	$(0 0 l)$ scan at 10 K with 711 eV energy (a) with $\pi$ and $\sigma$ polarizations and (b) with $P$ and $M$ polarizations, (right:) temperature dependence of incommensurate satellite with nuclear $(0 0 3)$ reflection, intensity and position in reciprocal space. . . . .	72
5.2	<i>Left</i> : $(0 0 l)$ scans at different temperatures with neutron of wavelength $\lambda = 2.31 \text{ \AA}$ . <i>Right</i> : temperature dependence of incommensurate satellite with nuclear $(0 0 9)$ reflection, intensity and position in reciprocal space are shown. . . . .	74
5.3	(a) change in propagation vector with temperature for both neutron and X-ray measurements, with X-ray $(0 0 3 \pm \delta)$ is measured, while with neutron $(0 0 9 \pm \delta)$ is measured. The ratio of $(0 0 3 - \delta)/(0 0 3 + \delta)$ is also plotted (pink curve) with a different scale (rightside). (b) Turn angle ( $\phi$ ) calculated from X-ray and neutron experiments (c) $H_1$ field from magnetic measurement with temperature. . . . .	75
5.4	Energy scans with fixed Q at $H = 0$ . (a) and (b) are energy scans for $\sigma$ and $\pi$ polarizations at $Q = (0 0 1.5)$ and $Q = (0 0 3 - \delta)$ respectively. (c) and (d) are for $P$ and $M$ polarizations with the same Q respectively. . . . .	76
5.5	$(0 0 l)$ scans at different magnetic fields at 100 K with $\sigma$ and $\pi$ polarizations of incoming photons. . . . .	78

- 5.6 Integrated intensity from the Lorentzian fitted peaks of  $(0\ 0\ l)$  scans as shown in Fig. 5.5. (a) Incommensurate  $(0\ 0\ 3-\delta)$ , commensurate  $(0\ 0\ 0.75)$  and  $(0\ 0\ 1.5)$  reflections with  $\pi$  polarization. Initial magnetization curves at 100 K (arbitrary unit) are also shown for comparison. Horizontal gray bars refer to the metamagnetic transition fields at 100 K as explained in the previous chapter. (b) same as (a), but with  $\sigma$  polarization and (c), (d) and (e) are individual reflections shown separately. All measurements are performed in increasing field after zero-field cooling. Error in  $H$  is  $\approx 5$  mT. . . . . 79
- 5.7 (a) Some of the  $(0\ 0\ l)$  scans at different magnetic fields at 10 K and  $E = 711$  eV. (b) Integrated intensity from the Lorentzian fitted peaks of  $(0\ 0\ l)$ . Incommensurate  $(0\ 0\ 3-\delta)$  reflection with both  $\sigma$  and  $\pi$  polarizations, initial magnetization curves at 10 K (arbitrary unit) are also shown for comparison. Horizontal gray bars refer to the metamagnetic transition fields at 10 K as explained in the previous chapter. (c) is the same as (b) with  $(0\ 0\ 2.25)$  (d) with  $(0\ 0\ 1.5)$  reflections. All measurements are performed in increasing field after zero-field cooling. Error in  $H$  is  $\approx 5$  mT. . . . . 80
- 5.8 Integrated intensity by Lorentzian fitting of the omega scans for  $\sigma$  and  $\pi$  polarizations. Initial magnetization curves at 10 K (arbitrary unit) are also shown for comparison. (a) and (b) are integrated intensities at different field of  $(0\ 0\ 3-\delta)$ ,  $(0\ 0\ 2.25)$  and  $(0\ 0\ 1.5)$  with  $\pi$  and  $\sigma$  polarization respectively. In (c), (d), and (e) individual reflections are shown separately for both the polarizations. . . . . 81
- 5.9 Various fan structures reported in the literature. Large ( $L_k$ ) and small ( $S_k$ ) are stacked as  $L_k S_k L_{k+1} S_{k+1} \dots$  for  $k = 1, 2, 3, \dots$  . . . . . 81
- 5.10 Component of spin block moments ( $\perp c$ )  $L$  and  $S$  of 4-fan structure along field direction and perpendicular to it. Corresponding satellite reflections due to the components are also shown. . . . . 83
- 5.11 Calculated intensity as a function of  $\phi$  for 4-fan structure for both (a)  $(0\ 0\ 2.25)$  (b)  $(0\ 0\ 1.5)$  reflections and (c) ratio of intensities of the  $(0\ 0\ 1.5)$  in  $\sigma$  channel to that of  $(0\ 0\ 2.25)$  in  $\pi$  channel. . . . . 84
- 5.12 (a) and (b) are maps of the sample surface with  $M$  and  $P$  polarizations respectively. (c) is the map of the ratio between  $P$  and  $M$  over the sample surface and (d) is difference between  $P$  and  $M$  normalized by their sum  $(\frac{P-M}{P+M})$ . . . . . 85
- 5.13 (a) Same as Fig. 5.12 (d), (b) after applying saturation magnetic  $H$ . . . . . 86

- 5.14 Integrated intensity from the Lorentzian fitted peaks of  $(0\ 0\ l)$  scans. (a) Incommensurate  $(0\ 0\ 3-\delta)$ , commensurate  $(0\ 0\ 0.75)$  and  $(0\ 0\ 1.5)$  reflections with circular  $p$  polarization. Initial magnetization curves at 100 K (arbitrary unit) is also shown for comparison. Horizontal gray bars refer to the metamagnetic transition fields at 100 K as explained in the previous chapter. (b) is the same as (a) with circular  $M$  polarization. (c), (d) and (e) are individual reflections shown separately for both the polarizations with  $I_{\chi} = \frac{I(P)-I(M)}{I(P)+I(M)}$ . . . . . 87
- 5.15 Integrated intensity by Lorentzian fitting of the omega scans for  $P$  and  $M$  polarizations. Initial magnetization curves at 10 K (arbitrary unit) are also shown for comparison. (a) and (b) are integrated intensities at different fields of  $(0\ 0\ 3-\delta)$ ,  $(0\ 0\ 2.25)$  and  $(0\ 0\ 1.5)$  with  $P$  and  $M$  polarization respectively. In (c), (d), and (e) the individual reflections are shown separately for both the polarizations. . . . . 88
- 5.16 The ratios on intensities in the  $\sigma$  and  $\pi$  channels for  $(0\ 0\ 1.5)$  reflection and ratio of intensity of  $(0\ 0\ 1.55)$  and  $(0\ 0\ 2.25)$  reflections in the  $\pi$  channels for different  $H$  at 100 K and 10 K. . . . . 88
- 6.1 Magnetoelectric phase diagram of  $\text{Ba}_{0.5}\text{Sr}_{1.5}\text{Zn}_2\text{Fe}_{12}\text{O}_{22}$  from magnetoelectric measurements from ref [119]. Black line is from ref [3] ( $M$  vs  $H$ ), blue one is as-grown and red one is for sample after annealing in oxygen. Phase diagram was determined using the magnetoelectric measurements. (b) Phase diagram from the magnetization measurements. . . . . 92
- 6.2 Integrated intensity of  $(0\ 0\ 1.5)$  reflection from the Lorentzian fit of omega scans at different  $H$  for  $\pi$  and  $\sigma$  polarizations at 100 K. From the top at 707.5 eV, 708.5 eV and 710 eV resonance energy respectively. The horizontal bars represent various critical fields observed from the magnetization measurements. . . . . 93
- 6.3 Energy scans with fixed  $Q$   $(0\ 0\ 1.5)$  at different  $H$  at 100 K. Vertical dashed lines guide energy for the values as: olive - 707.5 eV, pink - 708.5 eV and navy blue - 710 eV. . . . . 94
- 6.4 Energy scans with fixed  $Q$   $(0\ 0\ 1.5)$  after subtracting the zero field  $E$  scans at 100 K. Vertical dashed lines guide energy for the values as: olive - 707.5 eV, pink - 708.5 eV and navy blue - 710 eV. . . . . 95

- 6.5 (a) Integrated intensity from the Lorentzian fit of omega scans at different  $H$  for  $\pi$  and  $\sigma$  polarizations at 100 K and 708.5 eV. (b) Ratio normalized to total intensity and ratio between the intensities of  $\pi$  and  $\sigma$  in same scale. The initial magnetization curves at 100 K (arbitrary units) are shown for comparison. Horizontal bars are guide to the critical fields determined from the magnetization measurements. . . . . 96
- 6.6 (a) Integrated intensity from the Lorentzian fit of  $(0\ 0\ l)$  scans at different  $H$  for  $\pi$  and  $\sigma$  polarizations at 10 K and 711 eV. (b) Ratio normalized to total intensity and ratio between the intensities of  $\pi$  and  $\sigma$ . Initial magnetization curves at 10 K (arbitrary unit) are shown for comparison. Horizontal bars are guide to the critical fields determined from the magnetization measurements. . . . . 97
- 6.7 *Top*: Integrated intensity from the Lorentzian fit omega scans at different  $H$  for  $P$  and  $M$  polarizations at 100 K and 708.5 eV. *Bottom*: difference normalized to total intensity and ratio between the intensities of  $P$  and  $M$ . Initial magnetization curves at 100 K (arbitrary unit) are shown for comparison. Horizontal bars are guide to the critical fields determined from the magnetization measurements. . . . . 98
- 6.8 *Top*: Integrated intensity from the Lorentzian fit  $(0\ 0\ l)$  scans at different  $H$  for  $P$  and  $M$  polarizations at 10 K and 711 eV. *Bottom*: difference normalized to total intensity and ratio between the intensities of  $P$  and  $M$ . Initial magnetization curves at 10 K (arbitrary unit) are shown for comparison. Horizontal bars are guide to the critical fields determined from the magnetization measurements. . . . . 99
- 6.9 *Left*: Integrated intensities from the Lorentzian fitted omega scans at different  $H$  at 10 K in a cleaved sample. *Right*: Sum of the integrated intensity in  $P$  and  $M$  channels, difference of  $P$  and  $M$  normalized to total intensity and ratio between  $P$  and  $M$  is plotted. Horizontal bars are guide to different metamagnetic critical fields measured by DC magnetization measurements. 100
- 6.10 (a) 2-fan structure for  $x = 0$  in  $\text{Ba}_{2-x}\text{Sr}_x\text{Zn}_2\text{Fe}_{12}\text{O}_{22}$  with crystal structure and spin blocks (section 2.4.3). Schematic of the proposed 2-fan magnetic structures in intermediate-II and intermediate-III [3, 61]. (b) Schematic of the magnetic structure in 2 dimension with components of moments in three Cartesian co-ordinates  $z_1$ ,  $z_2$  and  $z_3$  as defined in Fig. 3.5. (c) Schematic explaining the propagation vector and the cross product of spin blocks. We refer to this model as model-A. . . . . 101

6.11	Calculated $I_{\pi \rightarrow \pi}$ for $(0\ 0\ 1.5)$ satellite as a function of $\phi$ for model-A. . . . .	103
6.12	Position dependence of individual intensities of circular $P$ and $M$ polarizations at 10 K in different fields for $(0\ 0\ 1.5)$ . Color bar indicates intensity in arbitrary unit. . . . .	104
6.13	Position dependence of the relative circular dichroism $(P-M)/(P+M)$ at 10 K in different fields for $(0\ 0\ 1.5)$ reflections. Color bar indicates $(P-M)/(P+M)$ . . . . .	105
6.14	Intensity map for: ( <i>Bottom:</i> ) $P$ polarization, ( <i>Middle:</i> ) $M$ polarization and ( <i>Top:</i> ) relative circular dichroism for field ( <i>Left:</i> ) 1 Tesla and ( <i>Right:</i> ) negative 1 Tesla. Color bar indicates $(P - M)/(P + M)$ for top and rest intensity in arbitrarily unit. . . . .	106
6.15	Relative circular dichroism map at 0.4, 0.8, 1.2 and -ve 0.8 T at 100 K. Color bar indicates $(P-M)/(P+M)$ . The hatched regions are the regions with extremely low intensity. . . . .	107
6.16	Integrated intensity from the omega scans on a cleaved sample at 10 K using 710.6 eV for $P$ and $M$ polarization. Horizontal bars indicate different critical fields from the magnetization measurements. Hysteresis loop at 10 K (arbitrary unit) is also shown as a reference. . . . .	108
6.17	(a) Spin-chiral domain patterns at 10 K in $H = 65$ mT for $(0\ 0\ 2.25)$ reflection and (b) for $(0\ 0\ 1.5)$ reflection after coming from 3.5 T. Contrast is given by $\frac{P-M}{P+M}$ . . . . .	108
6.18	Plot of intensity vs. $H$ for linear and circular polarizations at 100 K while the field is sweeping. For this measurement, detector and omega are fixed at $(0\ 0\ 1.5)$ reflections and magnetic field is varied. ( <i>Left:</i> ) for ramping field from positive to negative direction and ( <i>Right:</i> ) for reverse direction. Horizontal bars represent different critical fields measured by magnetization measurements. . . . .	109
6.19	(a) $(0\ 0\ l)$ scans for $P$ and $M$ polarization, (b) same for $\sigma$ and $\pi$ polarizations, (c) map of the sample surface for relative circular dichroism where color bar indicates $(P-M)/(P+M)$ and (d) is map of the sample for relative linear dichroism, where, color bar indicates values of $(I_{\pi} - I_{\sigma})/(I_{\pi} + I_{\sigma})$ at 15 K. . . . .	110
6.20	Map of linear dichroism in vertical field geometry at 15 K, 40 K, 100 K and at 300 K for $(0\ 0\ 1.5)$ reflection. Color bar indicates $(I_{\pi} - I_{\sigma})/(I_{\pi} + I_{\sigma})$ . . . . .	111

- 6.21 Scattering geometry for both horizontal and vertical field is explained graphically. For horizontal field  $H(H)$  it is in the  $z_1$  direction whereas for vertical field  $H(V)$ , the field is along  $z_2$  direction. For  $H(H)$  the large spin blocks (only  $L_1$  shown) have angle  $\phi/2$  with  $z_1$  direction whereas this angle becomes  $(\pi/2 - \phi/2)$  for vertical field. Following conclusion can be seen from the scattering geometry:  $(\sigma' \times \sigma) = 0$ ,  $(\sigma' \times \pi) = \hat{k} = f_{\pi \rightarrow \sigma}$ ,  $(\pi' \times \sigma) = -\hat{k}' = f_{\sigma \rightarrow \pi}$ ,  $(\pi' \times \pi) = \hat{k}' \times \hat{k} = f_{\pi \rightarrow \pi}$ . . . . . 112
- 6.22 (a) Schematic representation of model-B, where the small spin blocks are same as model-A but large spin blocks are tilted at angle  $\alpha$  with c-axis. Components of magnetic moments are also shown in the figure. (b) In the unit cell the periodicity of the spin blocks are represented. . . . . 113
- 6.23 (a) Schematic representation of model-C. The small spin blocks are rotated in the c-direction of the crystallographic axis with an angle  $\beta$  and large spin blocks are the same as in model-B. Components of magnetic moments in all the three z-directions are also shown. (b) In the unit cell the periodicity of the spin blocks are represented. . . . . 114
- 6.24 Calculated slices of the range of  $\phi$ ,  $\alpha$  and  $\beta$  for values of (a) Rel\_circ, (b)  $I_\pi/I_\sigma$  as indicated in the figure. (c) Combinations of both the parameters for model-C. . . . . 115
- 6.25 Range of  $\phi$ ,  $\alpha$  and  $\beta$  after simultaneously incorporating the quantities Rel\_Circ, Rel\_Lin and  $I_\pi/I_\sigma$  as shown, with  $\phi$  and  $\alpha$  as the axes and  $\beta$  as the color bar. (b) Normalized initial magnetization curves at 100 K showing changes in values of  $M$  at  $H_4$  and  $H_5$ . . . . . 115
- 6.26 Calculated moments for  $\phi$ ,  $\alpha$  and  $\beta$  values from the solution shown in Fig. 6.25. (a) as a function of  $\phi$  and  $\alpha$  with moment as color bar. . . . . 116
- 6.27 Schematic representations of the model-D. Here, compared to model-C, a component of moment for the small spin block is added along  $z_2$  axis in horizontal magnet geometry. Small spin blocks make an angle  $\beta$  with the  $z_3$  axis and  $\gamma/2$  with the projections of it on the  $z_1 - z_2$  plane with  $z_1$  axis. . . . 117
- 6.28 Various parameters calculated for model-D for three different values of  $\phi$ ,  $5^\circ$ ,  $10^\circ$  and  $15^\circ$ , as a function of two out-of-plane angles  $\alpha$  and  $\beta$ , for L and S blocks. In the top panel, value of  $\gamma$  satisfying our solution is shown. For each  $\phi$  same color bars are used and are shown beside the  $\phi = 15^\circ$ . . . . . 118
- 6.29 Solution for model-D for  $\phi$ ,  $\alpha$ ,  $\beta$  and  $\gamma$  as a function of applied field below saturation field and above  $H_4$ . Values of the angles are calculated by simultaneously minimizing individual experimental parameters. . . . . 120

6.30	Electric polarization as a function of applied $H \perp c$ for (a) $\text{Ba}_{0.5}\text{Sr}_{1.5}\text{Zn}_2\text{Fe}_{12}\text{O}_{22}$ from Kimura <i>et al.</i> [3] and (b) for $\text{Ba}_2(\text{Mg}_{0.9}\text{Zn}_{0.1})_2\text{Fe}_{12}\text{O}_{22}$ from Ishiwata <i>et al.</i> [130]. . . . .	121
6.31	Initial magnetization (pink), magnetization for decreasing field from 6 T (red) and magnetization for increasing field from -6 T (blue) curves at different temperatures. . . . .	122
6.32	Map of (a) Rel_Circ at 300 K for horizontal magnet geometry and (b) Rel_Lin at 300 K for vertical magnet geometry. . . . .	123
6.33	Unpolarized neutron $(0\ 0\ l)$ scans at 4 K in different vertical magnetic field. Measurements were carried out in increasing H. . . . .	124
6.34	Unpolarized neutron $(0\ 0\ l)$ scans at 100 K in different vertical magnetic field. Measurements were carried out in decreasing H. Intensity of $(0\ 0\ 7.5)$ is multiplied by 3 . . . . .	125
6.35	Integrated intensity from the Gaussian fit of the reflections in unpolarized neutron $(0\ 0\ l)$ scans at three different temperatures 4 K, 100 K and 300 K. Magnetizations curve is also plotted as a reference. . . . .	126
6.36	Integrated intensity from the Gaussian fit of the omega scans for reflections along (a) $(0\ 0\ l)$ and (b) $(0\ 1\ l)$ at 4 K as a function of applied H. Field is applied perpendicular to both $(0\ 0\ l)$ and $(0\ 1\ l)$ . For reference intensity from the soft-x-ray experiment for $\sigma$ polarization is also plotted in (a). Magnetization data is also shown in (b). In the inset of (a) enlarged view of $(0\ 0\ 9)$ reflection is plotted. . . . .	127
6.37	H-T Phase digram constructed using our magnetization, soft-x-ray diffraction and neutron diffraction data. . . . .	129
B.1	Model-B: Calculated intensities for the $\sigma \rightarrow \pi$ , $\pi \rightarrow \sigma$ and $\pi \rightarrow \pi$ channels for horizontal magnet geometry. In the bottom panels Rel_Circ, Re_Lin and $I_\pi/I_\sigma$ are plotted as a function of $\phi$ and $\alpha$ . In the $I_\pi/I_\sigma$ plot the values of $I_\pi/I_\sigma > 5$ are shown by black sparse region. . . . .	154
B.2	Model-B: Calculated intensities for the $\sigma \rightarrow \pi$ , $\pi \rightarrow \sigma$ and $\pi \rightarrow \pi$ channels for vertical magnet geometry. In the bottom panels Rel_Circ, Re_Lin and $I_\pi/I_\sigma$ is plotted as a function of $\phi$ and $\alpha$ . In the $I_\pi/I_\sigma$ plot the values of $I_\pi/I_\sigma > 5$ are shown by black sparse region. . . . .	155
B.3	Calculated intensity of model-C for horizontal field in the $\sigma \rightarrow \pi$ and $\pi \rightarrow \sigma$ channel as a function of angles $\alpha$ and $\beta$ at various values of $\phi$ . Color bars scale with the corresponding values. . . . .	158

---

B.4	Calculated intensity of model-C for horizontal field in the $\pi \rightarrow \pi$ channel as a function of angles $\alpha$ and $\beta$ at various values of $\phi$ . Color bars scale with the corresponding values. . . . .	159
B.5	Calculated $I_\pi/I_\sigma$ ratio and Rel_Circ of model-C for horizontal field as a function of angles $\alpha$ and $\beta$ at various values of $\phi$ . Color bars scale with the corresponding values. . . . .	160
B.6	Intensity in the $\sigma \rightarrow \pi$ , $\pi \rightarrow \sigma$ and calculated for vertical field geometry of model-C for different values of $\phi$ as indicated in the figure. For $I_{\sigma \rightarrow \pi}$ and $I_{\pi \rightarrow \sigma}$ same color bars are used for the same values of $\phi$ . Rel_Lin is plotted in the right hand side with the same color bar for all values of $\phi$ . . . . .	161
B.7	Solution for model-D for $\phi$ , $\alpha$ , $\beta$ and $\gamma$ for applied field below saturation field and above $H_4$ . . . . .	164
B.8	Calculated values of Rel_Circ, Rel_Lin, $I_\pi/I_\sigma$ and moment (using a Wolfram mathematica 10.4 program) as a function of $\alpha$ , $\beta$ and $\gamma$ for three values of $\phi=5^\circ$ , $10^\circ$ and $15^\circ$ . . . . .	165



# List of tables

2.1	Different hexaferrites with their structural blocks . . . . .	18
2.2	Different types of $\text{Fe}^{3+}/\text{Zn}^{2+}$ in unit cell of $\text{Ba}_2\text{Zn}_2\text{Fe}_{12}\text{O}_{22}$ . . . . .	24
2.3	Superexchange interaction in the first 12 layers of the unit cell from $z = 0$ , for $x = 0$ . Numbers in superscript represent the layer number and that in parentheses represent Wyckoff positions. . . . .	25
3.1	Resonance enhancement of scattering amplitude for some elements. Weak =1, medium = $10^2$ and strong $> 10^3$ . . . . .	40
4.1	Composition of starting materials used for crystal growth (composition in mole%), details parameters can be found in Appendix-A. . . . .	51
4.2	Composition and partial occupancies of Zn(1) and Zn(2) from single crystal X-ray diffraction refinements at room temperature . . . . .	53
4.3	Different transition metal-O bond lengths from single crystal X-ray refinements of samples BZY-1, BZY-2, BZY-3 at room temperature. $x$ is given in the formula $\text{Ba}_{1-x}\text{Sr}_x\text{Zn}_{1-p}\text{Fe}_{6+p}\text{O}_{11}$ . . . . .	54
5.1	Comparison of the ratio of intensities of our experiment to that of experimental and calculated one by Mulders <i>et al.</i> [9] . . . . .	74
5.2	Different satellite reflections observed for different fan structures and comparison with reference [6]. In this reference, apart from main phase satellites other satellites were also found, indicating mixture of phases. . . . .	77
6.1	Summary of experimental parameters for Rel_circ and Rel_Lin at different $H$ and $T$ for both the horizontal and vertical field experiments . . . . .	112
6.2	Possible situation for magnetization and chirality ( $M\chi$ ) simultaneously present.	122
A.1	BZY-1 atomic parameters . . . . .	145
A.2	BZY-1 thermal displacement parameters . . . . .	146

A.3	BZY-2 atomic parameters . . . . .	146
A.4	BZY-2 thermal parameters . . . . .	147
A.5	BZY-3 atomic parameters . . . . .	147
A.6	BZY-3 thermal parameters . . . . .	148